

https://dspace.org/

An integrated geological and geophysical study of the Deblin Copper Mine are in Kombat South, Southern Otavi mountain land, Northern Namibia

Shilunga, Josia Tulongeni

2018

https://hdl.handle.net/10539/26956

Shilunga, Josia Tulongeni, (2018) An integrated geological and geophysical study of the Deblin Copper Mine area in Kombat South, Southern Otavi Mountain Land, Northern Namibia, University of the Witwatersrand, Johannesburg, https://hdl.handle.net/10539/26956.

Downloaded from a DSpace repository. https://dspace.org/

An Integrated Geological and Geophysical Study of the Deblin Copper Mine area in Kombat South, Southern Otavi Mountain Land, Northern Namibia



Josia Tulongeni Shilunga (1252952)

School of Geosciences, University of the Witwatersrand, Johannesburg

2018

Supervisors: Prof. Judith Kinnaird and Prof. Susan Webb

A Dissertation submitted to the Faculty of Science, University of the Witwatersrand, Johannesburg, in fulfillment of the requirements for the degree of Master of Science.

Declaration

I declare that this dissertation my own work, unaided work. It is being submitted for the Degree of Master of Science at the University of the Witwatersrand, Johannesburg. It has not been submitted before for any degree or examination at any other University.



Josia Tulongeni Shilunga

28th day of February 2018 in Johannesburg.

Abstract

The Deblin Copper Mine is located at the transition between the Swakop rift-basin and the carbonate platform of the Otavi Mountain Land. Copper and zinc mineralization occurs mainly in carbonate host rocks close to a major thrust fault underlain by bimodal metavolcanics with mineralized quartz-calcite veins. Copper sulphides of chalcopyrite and bornite occur as disseminated and vein-type mineralization associated with sphalerite and pyrite. The area is characterized by outcrops of carbonates and limited metavolcanics. Wall rock alterations include sericitization and chloritization of metavolcanics, as well as silicification and dolomitization of carbonates. Vein type mineralization is characterized by a relatively narrow range of sulphur isotopes ($\delta^{34}S$ = -4.9‰ to +6.0‰) compared to that of disseminated sulphides ($\delta^{34}S$= -9.99‰ to +3.63‰). The two sulphur isotope ranges suggest that both magmatic and sedimentary sulphur sources were involved in the genesis of the deposit. Geochemical and petrological data suggest that the metavolcanic rocks in the area formed as alkali basalts in an oceanic island geotectonic setting. Magnetic data revealed concealed faults which may have acted as conduits for mineralizing hydrothermal fluids. The deposit shows ore forming processes associated with both VMS and MVT-type mineralization.

Acknowledgements

Firstly, I would like to express my sincere gratitude to my supervisor Prof. Judith Kinnaird and co-supervisor Prof. Susan Webb for giving me an invaluable opportunity to undertake this research and for your continuous support and patience throughout the entire research period. Your guidance helped me all the time of research. The doors to your offices were always open whenever I had a question about my research or writing. Besides my supervisors, I would like to thank Prof. Frederich Kamona for initiating this interesting research project, the Kombat South research project and for your endless support, advice, assistance in the field and willingness to answers. My humble gratitude to Dr. Teklay Mengist and Prof. Paul Nex for their tireless support, discussions and contributions to this research. Special thanks to Dr. Branko Corner, Mr. Gregory Symons, Dr. Stephanie Scheiber-Enslin, Dr. Ben Hayes and Prof. Gordon Cooper and for their guidance in processing and interpretation of geophysical data. Many thanks to those I shared the postgraduate research office with over the years at the University of the Witwatersrand (Seeiso Moshoeshoe, Kofi Acheampong and Blessing Chinamora). Many thanks to my colleagues and officemates at the University of Namibia: Dr. Absai Vatuva, Mr. Harris Martin and Mr. Mbili Tshiningayamwe for your encouragement. I am grateful to all the professors and lecturers of the School of Geosciences at the University of the Witwatersrand for the assistance and advice on certain aspects of my research work. I would like to extend my gratitude to all my colleagues in the Geology Department, University of Namibia for your support to help me complete this research.

This project would not have been possible without the financial support of the Geology Department, University of Namibia. Special thanks to Dr. Ansgar Wanke and Prof. Benjamin Mapani for your great efforts in helping me secure this funding from the University of Namibia. Additional funding was generously provided by the Hugh McKinstry Fund of the Society of Economic Geologists Foundation, Inc.

I would like to thanks Sabre Resources Namibia for fieldwork support including access to the study area and drill cores. Special thanks go to Mr. Crispen Mutizwa and his entire crew at the Kombat exploration camp for the support during the fieldwork of my research. Thanks to the Geological Survey of Namibia for providing the high resolution aeromagnetic data. Geophysical data acquisition would not have been possible without the field equipment support of Gregory Symons Geophysics. I am grateful to Mr. Gregory Symons for generously allowing me to use your

GSM-19 Overhauser magnetometer. Acknowledgements are owed to the School of Geosciences for the access to the Oasis Montaj, Geosoft and Arc Map softwares. Many thanks go to Caiphas Majola, Sam and Joe Aphane for the assistance with the preparations of polished thin sections. Thanks also go to the technical staff at Wits School of Geosciences Earth Lab for the help with XRF and ICP-MS analyses. I gratefully acknowledge Mr. Phillemon Kambonde for assistance in the field when collecting ground magnetic data. Many thanks to Mr. Mike Butler at iThemba Laboratories in Johannesburg for the sulphur isotope analyses. Special thanks to the Wits Economic Geology Research Institute (EGRI) office for the administrative and logistical assistance during my research. Sincere thanks are due to Mrs. Johanna Kaluwapa, Mr. Gabriel Nghikongelwa and Ms. Josephine Hamutoko for the administrative support during the preparations of field work.

I thank all my friends for the great support during this project, just to mention a few: Frans Shafudah, Samuel Nengola, Lisias Negonga, Frank Twite, Moses Angombe, Haikela Endifenge, Sinskus Amwiigidha, Tangi Nepolo, Hallelujah Ekandjo, Fenni Iyambo and Nailoke Shilunga. Special thanks to my friends Paskalia Ndapandula Neingo and Nghimwenavali David for the great hospitality and logistical support for the entire time I was in Johannesburg. Many thanks for your endless support and for always pushing me, especially when times were tough.

Finally, I must express my very profound gratitude to my family for your understanding and for providing me with consistent support and continuous encouragement throughout my years of researching and writing this dissertation. I thank you for your patience and for believing in me even though dealing with rocks does not make a lot of sense to you.

Table of Contents

Declaration ii
Abstract iii
Acknowledgements iv
List of Figures ix
List of Tables xxiii
Chapter 1 1
Introduction 1
1.1 Background 1
1.2 Location of the study area 1
1.3 The Research Problem 2
1.4 Aim and Objectives 3
1.5 Research Methodology 4
Chapter 2 5
Regional Geology 5
2.1 Geological Setting of the Otavi Mountain Land 5
2.1.1 The Damara Belt 5
2.1.2 Geology of the Otavi Mountain Land 13
2.1.3 Summary 25
Chapter 3 27
Local Geology 27
3.1 Introduction 27
3.2 Previous Work 27
3.3 Current Work 30
3.3.1 Methodology 31
3.3.2 Local Stratigraphy 32
3.3.3 Petrographic Description of the Local Stratigraphy 33
3.4 Discussion 67
Chapter 4 74
Mineralization of the Deblin Copper Mine area 74
4.1 Introduction 74

4.2 Previous Work 74
4.3 Current Work 78
4.3.1 Methodology 78
4.3.2 Hypogene Mineralization 79
4.3.3 Types of Mineralization 81
4.3.4 Ore Mineralogy and Textures 85
4.3.5 Supergene Enrichment 90
4.4 Discussion 91
Chapter 5 95
Sulphur Isotopic Studies of the Deblin ores 95
5.1 Introduction 95
5.2 Previous Work 95
5.3 Current Work 97
5.3.1 Methodology 97
5.3.2 Sulphur Isotope Geochemistry 97
5.4 Discussion 100
Chapter 6 103
Whole Rock Geochemistry 103
6.1 Introduction 103
6.2 Methodology 103
6.3 Data 104
6.4 Element mobility and chemical alteration assessment 109
6.5 Trace element geochemistry 111
6.6 Tectonic implications 116
6.7 Discussion 118
Chapter 7 120
Geophysical Study of the Deblin Copper Mine area 120
7.1 Introduction 120
7.2 Previous Geophysical Work 121
7.2.1 Southern Otavi Mountain Land……121
7.2.2 Kombat South: Deblin Copper Mine Area……...124

7.3 Structural geological analysis 125
7.4 Magnetic Susceptibility Data 130
7.4.1 Equipment and Data Collection 132
7.4.2 Magnetic Susceptibility Data Analysis 128
7.4.3 Interpretation of the magenetic sucsceptibility data 138
7.5 Regional aeromagnetic data analysis of the Southern Otavi Mountain Land 140
7.5.1 Aeromagnetic data 140
7.5.2 Image processing and enhancement of aeromagnetic data 140
7.5.3 Interpretation of geophtsical aeromageneic data 153
7.6 Ground Magnetic Survey of the Deblin Copper Mine Area 159
7.6.1 Ground magnetic survey parameters and configuration 159
7.6.2 Equipment 163
7.6.3 Software 163
7.6.4 Data Collection 159
7.6.5 Data Processing 165
7.6.6 Interpretation of the ground magnetic data 184
7.7 Discussion 188
Chapter 8 192
Discussion and Conclusion 192
References 199
Appendices 210
Appendix A 210
Appendix B 233
Appendix C 234
Appendix D 237
Appendix E 240
Appendix F 249

List of Figures

Figure 1.1. Location map of the study area on the northeastern margin of the Damara Belt (taken from Miller, 1983 and Borg, 2000). The open green box represents the Otavi Mountain Land. Bottom left inset shows location of Namibia. 2

Figure 2.1 Map of the Brasiliano and Pan-African orogens showing the position of the Neoproterozoic Damara Orogen, Kalahari and Congo cratons as well as other orogenic belts (after Gray et al., 2008, Miller, 2008). 6

Figure 2.2 The location and architecture of the Damara Belt. (A) Simplified map of the Neoproterozoic Pan-African belt systems in southern and central Africa showing the intracontinental Damara Belt and the coastal Kaoko and Gariep Belts (after Gray et al., 2008; Miller, 2008). (B) Simplified map of the Damara Belt showing the tectonostratigraphic zones (taken from Corner, 2008 and Miller, 2008). The X-Y line represents a cross section shown on Figure 2.4. 7

Figure 2.3 Lithostratigraphy and correlation across the Damara Belt with approximate deposition age for the Damara Sequence (modified after Miller, 2008). The vertical thickness of the sequence is not to scale. 11

Figure 2.4 Generalized pre-orogenic section across the Damara Belt (from X to Y as shown in Figure 2.2b) with a simplified stratigraphic compilation showing basal, initial rift grabens, the syn-rift Nosib Group and the post-rift units of the Otavi, Swakop and Mulden groups (modified after Borg, 2000). 12

Figure 2.5 Geology of the Otavi Mountain Land with locations of major deposits and some prospects (modified after Söhnge, 1957; Kamona and Günzel, 2007 and map of 1:250,000 of the Geological Survey of Namibia). Generally, the Tsumeb type consists of sulphide ores containing Cu, Pb, Zn, Ag, As, Ge, Cd and Ga, whereas the Berg Aukas type contains primarily Pb-Zn and V sulphide ores with little Cu. 14

Figure 2.6 Geological map showing the regional architecture of the Otavi Mountain Land metallogenic province, the main base metal deposits (Mississippi Valley Type), the Deblin Cu Mine and other Cu prospects in the southern Otavi Mountain Land (modified after Kamona and Günzel, 2007 and map of 1:250 000 of the Geological Survey of Namibia). 22

Figure 3.1 Regional geological map of the southern Otavi Mountain Land with the Askevold Trend defined by Cu prospects closely related to the Askevold Formation volcanics. Taken from the 1: 250,000 of the Geological Survey of Namibia (2008). The black dotted line indicates the Askevold Trend. The black box shows the local study area (Figure 3.4). 28

Figure 3.2 Stratigraphic column for the accepted Otavi Mountain Land stratigraphy with mineral deposits of Kamona and Günzel (2007)..... 29

Figure 3.3 Stratigraphic column for the study area and comparison with the accepted Otavi Mountain Land stratigraphy with mineral deposits of Kamona and Günzel (2007). 33

Figure 3.4 Detailed geological map of the area around the Deblin Copper Mine constructed at the scale of 1:2,500. In addition, the map shows the location of the twelve hand samples and three boreholes drilled in the study area. This geological map was constructed from the outcrop geology. 35

Figure 3.5 Lithological logs of the three boreholes from the Deblin Copper Mine area. A) DBDD0001 lithological log showing the succession of both the Nosib Group metavolcanic rocks and Otavi Group dolomites, and the location of the copper sulphide mineralization in the stratigraphy. Grid reference: 758547 mE, 7814734 mN. B) DBDD0002 lithological log showing the succession of both the Nosib Group metavolcanic rocks and Otavi Group dolomites, and the location of the copper sulphide mineralization in the stratigraphy. Grid reference: 758547 mE, 7814735 mN. C) DBDD0002 lithological log. This borehole intersected solely the Nosib Group metavolcanic rocks. Note the lack of a mineralized unit. Grid reference: 757600 mE, 7814885 mN. 36

Figure 3.6 Cross-section of the three boreholes from the Deblin Copper Mine area showing their orientations. The drill holes were plotted with Leapfrog Geo 3.1 and digitized in ArcMap 10.2.2. 37

Figure 3.7 Lithological logs of the three boreholes (DBDD0001, DBDD0002 and DBDD0003) from the Deblin Copper Mine area showing sample localities. 44

Figure 3.8 Photographs of the tuff. A) Half drill core of the tuff with frequent quartz-calcite veins. DBDD0003: 39.20 m – 39.40 m – DB3S10. B) Half drill core of the tuff with quartz-calcite veins and numerous calcite vugs. DBDD0003: 67.40 m – 67.60 m – DB3S14. Magnetic pen for scale. 46

Figure 3.9 The tuff mineralogy, grain size and textural relationships. A) Randomly oriented fine-grained plagioclase, very fine-grained quartz and medium-grained calcite (XPL). DBDD0003: 39.20 m – 39.40 m – DB3S10-D17a. B) Fine-grained microcline overgrown by biotite and fine-grained calcite grains (XPL). DBDD0003: 47.28 m – 47.48 m – DB3S13-D18d. C) Coarse-grained plagioclase replaced by finer-grained calcite and sericite. The biotite grain is replaced by calcite (XPL). DBDD0003: 75.04 m – 75.24 m – DB3S15-D141d. D) Frequent very fine-to fine-grained

plagioclase overgrown by calcite (XPL). DBDD0003: 34.20 m – 34.40 m – DB3S9-D131b. (XPL= crossed-polarized light; PPL= plane-polarized light). 47

Figure 3.10 Spaced foliation in the tuff. A) S-C fabric with C-shear band foliation transecting the sericite dominated main foliation (S-foliation) during shearing (XPL) and B) same image shown in plane-light (PPL). DBD0003: 39.20 m – 39.40 m - DB3S10-D17c. C) Carbonates and plagioclase constitute the microlithons of the sericite cleavage domain (XPL). DBD0003: 39.20 m – 39.40 m - DB3S10-D17e. D) Sinuous cleavage made up of sericite. Biotite overgrowth on sericite (XPL). Conspicuous calcite overgrowths over the foliation. DBDD0003: 75.04 m – 75.24 m – DB3S15-D140c. The white lines define S and C surfaces. (XPL= crossed-polarized light; PPL= plane-polarized light). 48

Figure 3.11 Multiple mineral overgrowths in the tuff. A) Calcite grains are cut through by the foliation. While calcite grains exhibit undulose extinction, the micas display kinked microfolds (XPL). DBDD0003: 47.28 m – 47.48 m – DB3S13-D18a. B) Coarse-grained calcite overgrowth over the foliation (sericite). This is the opposite of what is in 'image A' (XPL). DBDD0003: 85.60 m – 85.80 m – DB3S18-D19c. C) Medium-grained plagioclase replaced by fine-grained calcite, biotite and chlorite (XPL). DBDD0003: 76.24 m – 76.44 m - DB3S16-D27c. D) Plagioclase overgrown by calcite and sericite. Sericite, in contrast, is overgrown by calcite (XPL). DBDD0003: 85.60 m- 85.80 m – DB3S18-D19d. The white line defines S1 foliation. (XPL= crossed-polarized light; PPL= plane-polarized light). 49

Figure 3.12 More observations of calcite overgrowths over other mineral phases. A) Plagioclase overgrown by calcite and sericite (XPL). DBDD0003: 58.00 m – 58.20 m – DB3S20-D139a. B) Ubiquitous plagioclase replacement by calcite (XPL). DBDD0003: 34.20 m – 34.40 m – DB3S9-D130b. C) Chlorite overgrowth over the foliation, whereas biotite enclosed in a calcite grain is not altered (PPL) and D) same image in crossed-nicols (XPL) DBDD0003: 75.04 m – 75.24 m – DB3S15-D142c. The white and black lines defines S1. (XPL= crossed-polarized light; PPL= plane-polarized light). 50

Figure 3.13 Photographs of the chlorite schist. Grid reference: 758343 mE; 781477 mN. A) Chlorite schist exposed in the exploration trench. Geological hammer for scale in the photograph. B) Hand specimen of the chlorite schist with flecks of malachite and ubiquitous quart-calcite veins, DB1b. Magnetic pen for scale in the photograph. 51

Figure 3.14 Mineral assemblage of the chlorite schist. A) Plagioclase rich pocket surrounded by carbonates and chlorite. Chlorite overgrows the primary minerals (micas) (PPL). DBDD0003: 3.73 m – 3.93 m - DB3S1-D124a. B) Micaceous spaced foliation overgrown by chlorite and fine-grained calcite (PPL). DBDD0003: 4.15 m – 4.35 m - DB3S2-D126a. C) Chlorite overgrowths. Also, the foliation is overgrown by carbonates. (PPL). Grid reference: 758268 mE; 7814999 mN:

DB7a-D31a. D) Calcite overgrown by chlorite (PPL). 758268 mE, 7814999 mN: DB7a-D32b. The white line defines S1. (XPL= crossed-polarized light; PPL= plane-polarized light). 52

Figure 3.15 Calcareous, moderately-weathered mafic metavolcanic outcrop with kink folds. Grid reference: 759554 mE, 7814668 mN. Geological hammer for scale to the right of the photograph. 53

Figure 3.16 Mineral assemblage of the mafic metavolcanic rock. A) Fine-grained carbonate and quartz grains constitute the microlithon, whereas sericite makes up the cleavage domain of the foliation observed in this sample (XPL). Grid reference: 759552 mE; 7814663 mN – DB8a-D33b. B) Carbonate overgrowth on sericite in the cleavage domain (XPL). DBDD0001: 138.10 m – 138.30 m - DB1S20-D30a. C) Chlorite overgrows both the disjunctive foliation (sericite) and quartz-calcite veins (XPL). DBDD0001: 138.10 m – 138.30 m - DB1S20-D80a. D) Chlorite overprinting the foliation (S1) and other mineral phases (XPL). DB10a-40a. The white line defines S1. (XPL= crossed-polarized light; PPL= plane-polarized light). 54

Figure 3.17 Field photographs of the agglomerate outcrop (5 x 4 m). Grid reference: 758747 mE, 7814817 mN. A) Poorly exposed agglomerate outlined in red. This unit is concealed by younger sediments. B) Deformed mafic clasts of the agglomerate that are elongated along strike. The pen for scale in the centre of the photograph. 55

Figure 3.18 Photographs of the agglomerate in drill cores. A) The drill cores exhibit fresh, though chloritized agglomerate with a foliated matrix and fine grained mafic clasts of the agglomerate. The unit is cross-cut by abundant quartz-calcite veins. DBDD0001: 146.60 m – 151.33 m depth. B) Frequent sub-rounded mafic clasts and quartz-calcite veins in the agglomerate. DBDD001: 161.30 m – 161.50 m - DB1S23. The coin for scale in the photograph. 56

Figure 3.19 Mineral assemblage and textural relationships in the agglomerate unit. A) Chlorite overgrowth on calcite grains (PPL). DBDD0002: 109.70 m – 109.90 m - DB2S19-D26. B) Mafic clasts separated by biotite-rich cleavage domain and cross-cut by quartz-calcite veins (XPL). DBDD0001: 161.30 m – 161.50 m - DB1S23-D9h. C) Lens-shaped quartz-calcite veins with a mica-fish morphology as a result of shearing (XPL). DBDD0001: 145.00 m – 145.20 m – DB1S21-D83a. D) S-C fabric in the agglomerate with the C-plane transecting the main foliation (S-plane). DBDD0001: 161.30 m – 161.50 m - DB1S23-D9e. (XPL= crossed-polarized light; PPL= plane-polarized light). The white line defines the C-shear band and S-plane. 58

Figure 3.20 Photographs of the felsic volcanic breccia. Grid reference: 758342 mE, 7815085 mN. A) Cross-cutting quartz veins with malachite stains. B) Fine-grained pink fragments held together by a dark grey fine-grained silica cement. Geological hammer and magnetic pen for scale in the photographs. 59

Figure 3.21 Field image and photomicrograph of the pyritic dolomite. A) Pyritic dolomite outcrop with frequent chert bands oriented in different directions. Grid reference: 759899 mE; 7814741 mN. B) Photomicrograph of the chloritized pyritic dolomite with an anhedral pyrite grain (XPL). Grid reference: 758497 mE, 7814882 mN: DB2b-D36e. (XPL=crossed-polarized light). Geological hammer and camera lens cover for scale in the photographs. 59

Figure 3.22 Photographs of the grey limestone. A) Contact between the limestone and the underlying pyritic dolomite. The grey limestone has dolomite bands close to its contact with the pyritic dolomite. Grid reference: 760059 mE, 7814656 mN. B) Cross-bedding in the grey limestone. Grid reference: 759832 mE, 7814629 mN. Geological hammer and pencil for scale in the photographs. 60

Figure 3.23 Figure 3.23 Banded limestone outcrop showing microfolds cross-cut by quartz-calcite veins. Grid reference: 759548 mE; 7814447 mN. Camera lens cover used for scale in the photograph.. 61

Figure 3.24 Intensely-weathered calcareous phyllite with brown oxidized idiomorphic cubic pyrite grains. Grid reference: 759985mE; 7814520mN. Geological hammer for scale in the photograph. 62

Figure 3.25 Images of the silicified dolomite in drill cores and outcrop. A) Silicified dolomite with outstanding thin and thick quartz-calcite veins. DBDD0001: 100.65 m – 105.31 m depth. B) Stromatolites in the silicified dolomite drill cores. DBDD0001: 117.00 m – 119.00 m depth. C) Silicified dolomite outcrop with deformed stromatolites and brown weathering colour. Grid reference: 759363 mE, 7814342 mN. Camera lens cover and ruler for scale in the photograph.. 63

Figure 3.26 Silicified dolomite mineralogy and textures. A) Mosaic texture defined by both fine- and coarse-grained quartz and carbonate minerals (XPL). DBDD0002: 35.27 m – 35.47 m - DB2S4-D11a. B) Carbonate and quartz grains (XPL). DBDD0002: 73.40 m – 73.60 m – DB2S12-D14d. C) Coarse grained quartz-calcite veins with sulphides (XPL). DBDD0001: 3.75 m – 3.95 m – DB1S1-D1b. D) Cross-cutting relation of two quartz-calcite veins. The north-northeast trending vein is displaced by the north-northwest trending vein, which also host sulphides (XPL). DBDD0001: 3.75 m – 3.95 m – DB1S1-D1a. (XPL= crossed-polarized light). 64

Figure 3.27 Sericite in the silicified dolomite and mineral overgrowths. A) Foliation, S1 made up of largely sericite (XPL). Additional observations show carbonate overgrowth over sericite in the cleavage domain. DBDD0002: 73.40 m – 73.60 m – DB2S12-D14c. B) Fine-grained quartz in the quartz-calcite vein and minor distinct sericite cleavage domains (XPL). DBDD0001: 82.59 m – 82.59 m - DB1S11-D4b. 64

Figure 3.28 Dolomite breccia. A) Dolomite breccia with deformed stromatolites. DBDD0001: 9.14 m – 13.15 m depth. B) Clast-supported dolomite breccia. The clasts are silicified. DBDD0001: 15.84 m – 16.04 m – DB1S4. Coin for scale in the photograph. 65

Figure 3.29 Textural characteristics of the dolomite breccia. A) Dilation in the dolomite breccia as a result of the deformation of the quartz and carbonates (PPL) and B) same image shown in crossed-nicols (XPL). DBDD0002: 13.70 m – 13.90 m – DB2S2-D10a. 66

Figure 3.30 Field images of the diamictite: A) Diamictite with large angular carbonate clasts. B) A banded iron-rich layer within the diamictite. The outcrop exhibits a red colour due to ferruginous material. Both A-and B-photographs represent the outcrop in the northwestern part of the study area. Grid reference: 758810 mE, 7814791 mN. C) Diamictite with limestone and dolomite fragments in a brown calcareous matrix. The matrix of the dolomite weathers to brown. Grid reference: 759157 mE, 7814229 mN. D) Poorly exposed diamictite layer (~60 cm) with dolomitic depositional layers intercalated with the pyritic dolomite. Grid reference: 759653 mE, 7814678 mN. The photographs in C and D represent the outcrop in the southern part of the study area. Geological hammer and pen for scale in the photographs.. 67

Figure 3.31 Stratigraphic column for the study area and comparison with the accepted Otavi Mountain Land stratigraphy with mineral deposits of Kamona and Günzel (2007). 68

Figure 3.32 Regional geological map of the southern Otavi Mountain Land with the updated stratigraphy based on the petrological data from the Deblin Copper Mine area (Figure 3.3). The updated stratigraphy is indicated with a red rectangular box. Modified after the 1: 250,000 maps of Smit (1959) and the Geological Survey of Namibia (2008). 70

Figure 4.1 The Deblin Copper Mine concrete-lined circular shaft, grid reference 758551 mE, 7814737 mN 76

Figure 4.2 Cross section at the Deblin Copper Mine showing the modelled orebody morphology, structural interpretation, orientation of the drill holes DBDD0001 and DBDD0002 and drill targets (Golden Deeps Limited, 2013). 78

Figure 4.3 Lithostratigraphic logs from the Deblin Mine area showing the four ore-bearing horizons. DBDD0001 has a maximum depth of 170.5 m and intersected three mineralized zones in the agglomerate, silicified dolomite and dolomite breccia. DBDD0002, by contrast, has a maximum depth of 120 m and records two mineralized zones located in the silicified dolomite and dolomite breccia. Drill hole DBDD0001 is located at 758547 mE, 7814734 mN, whereas drill hole DBDD0002 is located at 758547 mE, 7814735 mN 80

Figure 4.4 Disseminated chalcopyrite grains (enclosed in black circles) in the dolomite breccia. DBDD0001: 45.41 m – 46.20 m. 82

Figure 4.5 Pyrite disseminations in the agglomerate below the contact and vein type mineralization with chalcopyrite in the silicified dolomite above the contact. DBDD0001: 137.41 m – 139.50 m. The quartz-calcite veins in the agglomerate are not mineralized. 83

Figure 4.6 Stringer chalcopyrite cross-cut by later chalcopyrite veinlet in the silicified dolomite. DBDD0001: 82.20 m – 82. 40 m - DB1S10. 83

Figure 4.7 Chalcopyrite-bearing quartz-calcite veins, chalcopyrite veinlets and minor chalcopyrite disseminations in the silicified dolomite. DBDD0002: 59.15 m - 59.40 m. 84

Figure 4.8 Drill core images of silicified dolomite showing vein type mineralization. A) Quartz-calcite vein-hosted chalcopyrite mineralization. DBDD0002: 84.00 m - 84.20 m - DB2S12. B) Convoluted chalcopyrite and pyrite bands, discrete euhedral pyrite grains in the matrix and a fabric-parallel quartz-calcite vein with chalcopyrite mineralization along the margin of the vein. DBDD0002: 72.62 m - 72.82 m – DB2S11. 84

Figure 4.9 Photograph and photomicrograph of the folded sulphides in the silicified dolomite. A) Polydirectional, highly folded fine-grained chalcopyrite and pyrite veinlets. DBDD0001: 54.78 m – 54.98 m – DB1S7 (bottom sample); DBDD0001: 109.67 m – 109.87 m – DB1S15 (top sample). B) Highly folded chalcopyrite. DBDD0001 109.67 m – 109.87 m - DB1S15-D61 (Reflected Light). 85

Figure 4.10 Reflected light photomicrographs showing chalcopyrite textures and replacements. A) Successive replacement of pyrite by corroded chalcopyrite. Also shown is both chalcopyrite and chalcopyrite cut by later sphalerite. DBDD0001: 137.22 m – 137.42 m – DB1S17-D69a (silicified dolomite). B) Corroded chalcopyrite veinlets. DBDD0001: 136.61 m – 136.81 m – DB1S16-D63e (silicified dolomite). C) Chalcopyrite veinlets infilling fine cracks of pyrite. DBDD0001: DBDD0002: 96.52 m – 96.71 m – DB2S17-D118c (silicified dolomite). The pinkish color in the pyrite grain is caused by the wrong field of light of the camera. D) Chalcopyrite largely replacing pyrite groundmass. DBDD0002: 59.87 m – 60.07 m – DB2S9-D104d (silicified dolomite). 86

Figure 4.11 Reflected light photomicrographs showing replacement patterns of pyrite A) Fractured pyrite with minor chalcopyrite and sphalerite infills. DBDD0001: 137.73 m – 137.93 m – DB1S18-D75c (agglomerate). B) Outstanding fractures in pyrite with slivers of sphalerite and gangue minerals. DBDD0001: 139.10 m – 139.30 m – DB1S20-D80f (mafic metavolcanic). C) Highly corroded pyrite with cracks invaded by gangue minerals. Grid reference: 758497 mE, 7814882

mN – DB2b-D37 (pyritic dolomite). D) Colloform texture of goethite (formerly pyrite) and replacement of chalcopyrite by goethite. DBDD0001: 46.80 m – 47 m – DB1S6-D47g (dolomite breccia). 87

Figure 4.12 Reflected light photomicrographs showing the sphalerite texture and replacements. A) Goethite with colloform texture along the margins of quartz-calcite veins. DBDD0001: 46.80 m – 47 m – DB1S6-D47f (dolomite breccia). B) Sphalerite replacing both pyrite and chalcopyrite, whereas chalcopyrite is replacing pyrite. DBDD0001: 60.70 m – 60.88 m – DB1S9-D50c (dolomite breccia). C) Pyrite enclosed in sphalerite as a consequence of pyrite replacement by sphalerite. DBDD0001: 82.20 m – 82.40 m – DB1S10-D55e (silicified dolomite). D) Chalcopyrite groundmass transected by a network of sphalerite veinlets. Please note that sphalerite in this image appears light bluish because image was taken in the wrong field of light. DBDD0001: 46.80 m – 47 m – DB1S6-D46c (dolomite breccia). 86

Figure 4.13 Reflected light photomicrographs showing textures and replacement patterns of bornite and covellite. A) Bornite veins cut-across chalcopyrite matrix. DBDD0002: 59.36 m – 59.56 m – DB2S7-D99d (silicified dolomite). B) Fractured bornite replacing chalcopyrite. In addition, the fractures in bornite are infiltrated by gangue minerals. DBDD0002: 59.36 m – 59.56 m – DB2S7-D100b (silicified dolomite). C) Fine-grained covellite replacing tarnished chalcopyrite. DBDD0001: 60.70 m – 60.88 m – DB1S9-D50a (breccia dolomite). D) Sporadic fine-grained covellite replacing chalcopyrite. DBDD0001: 109.67 m – 109.87 m – DB1S15-D61e (silicified dolomite). 89

Figure 4.14 Field images of the exploration trenches showing supergene enrichment of malachite. A) A 20 m long, 4m wide and 1.5 to 2 m deep pink volcanic breccia exploration trench. B) Volcanic breccia outcrop with malachite in cross-cutting quartz veins. Grid reference: 758342 mE, 7815085 mN. C) A 12 m long, 5 m wide and ~8 m deep silicified dolomite exploration trench. D) Malachite and quartz-calcite veins hosted in a highly oxidized silicified dolomite. Grid reference 758747 mE, 7814817 mN. 90

Figure 4.15 Paragenetic sequence of sulphide minerals and supergene minerals as defined by mineral assemblages and textures. 92

Figure 5.1 Sulphur isotope ratios ($\delta^{34}S_{CDT}$) in sulphides and sulphate of the major deposits in the Otavi Mountain Land (OML). Taken from Kamona and Günzel (2007). 96

Figure 5.2 Variation of sulphur isotope ratios ($\delta^{34}S_{CDT}$) in sulphides of the Deblin Copper Mine and Kombat deposit. 97

Figure 5.3 Sulphur isotope ratios ($\delta^{34}S_{CDT}$) in the major deposits in the Otavi Mountain Land (OML), central African Copper belt and Kupferschiefer. Data taken from Dechow & Jensen (1965), Sawlowicz (1989) and Kamona and Günzel (2007). 101

Figure 6.1 Bivariate plots of Loss on Ignition (LOI) versus selected major elements and Large Ion Lithophile Elements (LILE). The Rb, Sr and Pb plots do not show any correlations. A) The plot of the Loss on Ignition with CaO displays a positive trend. B) The Loss on Ignition vs SiO_2 exhibits a negative trend. C) The LOI vs total alkali content (K_2O+Na_2O) plot. D) The LOI vs Rb plot. E) The LOI vs Sr plot. F) The LOI vs Pb plot. 110

Figure 6.2 Geochemical classification of the metavolcanic rocks of the Askevold Formation using the Nb/Y-Zr/Ti diagram of Pearce (1996). The samples plot within the alkali basalt field, although one sample plots close to the basalt field. 111

Figure 6.3 Bivariate graphs of Zr versus selected HFSE and REE showing positive correlations. A) The Zr vs Ti plot. B) The Zr vs Nb plot. C) The Zr vs Ce plot. D) The Zr vs Sm plot. 112

Figure 6.4 Chondrite-normalized REE patterns of the metavolcanic samples from the area around the Deblin Copper Mine, with subtle positive and negative Eu anomalies. Normalization values and the order of the elements are taken from Sun and McDonough (1989). 113

Figure 6.5 Plots of Eu/Eu* vs A) TiO_2 and B) Nb showing positive trends..... 114

Figure 6.6 Primitive mantle-normalized spider diagrams. A) Primitive mantle-normalized multi-element patterns of the metavolcanic samples from the area around the Deblin Copper Mine. B) A comparison of the primitive mantle-normalized spider diagrams of the N-MORB and Oceanic Island Basalts (OIB) average values. All normalization values and the order of the elements are taken from Sun and McDonough (1989). 115

Figure 6.7 Oceanic Island Basalt (OIB)-normalized multi-element patterns of the metavolcanic samples from the area around the Deblin Copper Mine. Normalization values and the order of the elements are taken from Sun and McDonough (1989). 116

Figure 6.8 Basalt tectonic discrimination diagrams. A) The majority of the metavolcanic samples plot in the within-plate lavas field. B) Metavolcanic samples plot within the oceanic islands field on the La/Yb-Nb/La diagram of Hollocher et al. (2012). 117

Figure 7.1 Regional aeromagnetic map of Namibia, 1: 1 000 000 scale. A) The airborne magnetic anomaly map (nT) of Namibia, with the International Geomagnetic Reference Field at the time of acquisition removed. B) Pattern of magnetic lineaments representing regional geological features,

derived from (A). The red open boxes in both maps show the location of the Otavi Mountain Land. Both maps are modified after Eberle et al., (1995). 123

Figure 7.2 Regional geological map of the southern Otavi Mountain Land showing the AA'-CC' lines of the cross-sections shown on Figure 7.3. Modified after Smit (1959) and the Geological Survey of Namibia (2008). 126

Figure 7.3 Cross-sections of the showing interpreted structural architecture of the southern Otavi Mountain Land…… 127

Figure 7.4 Geological map of the Deblin Copper Mine are showing the AA'-CC' lines for the cross-sections shown on Figure 7.5…… ……128

Figure 7.5 Cross-sections showing interpreted structural architecture of the Deblin Copper Mine area……...130

Figure 7.6 A photograph of the handheld SM 20 magnetic susceptibility meter. 131

Figure 7.7 Detailed geological map of the Deblin Copper Mine area showing the distribution of the magnetic susceptibility values of different rock types. 132

Figure 7.8 Histograms of in situ measured magnetic susceptibility data of the Askevold Formation lithologies..... 133

Figure 7.9 Magnetic susceptibility log for drill hole DBDD0001. The high values of the agglomerate suppress the variations in the overlying carbonates. 134

Figure 7.10 Magnetic susceptibility log for drill hole DBDD0002. The high values of the agglomerate suppress the variations in the overlying carbonates. 135

Figure 7.11 Magnetic susceptibility log for drill hole DBDD0003 showing low values. 136

Figure 7.12 Histograms of in situ measured magnetic susceptibility data of the Chuos Formation lithologies..... 137

Figure 7.13 Magnetic stratigraphic column of the Deblin Copper Mine area. The diamictite is magnetic where it is associated with a banded iron formation and non-magnetic where the banded iron formation is absent. 139

Figure 7.14 TMI map of the aeromagnetic data of the southern Otavi Mountain Land (OML). 142

Figure 7.15 Sunshaded TMI map of the aeromagnetic data of the southern Otavi Mountain Land. 143

Figure 7.16 The application of upward continuation of the total magnetic intensity (TMI) aeromagnetic data of the southern Otavi Mountain Land by various heights. A) The TMI data shows details of the surface and near surface magnetic sources. B) The TMI data upward continued by 20 m. C) The TMI data upward continued by 50 m. D) The TMI data upward continued by 80 m. Notably, the higher the amount of upward continuation, the smoother the TMI data become. 144

Figure 7.17 Application of the RTP operator to the TMI aeromagnetic data of the southern Otavi Mountain Land. Note that the RTP image has subtle north-south flight line noise (very clear in the sunshaded image). The flight line noise is evident in the northern part of the map.. 146

Figure 7.18 Decorrugated RTP map. The flight line noise observed in Figure 7.17 is completely removed and the image appears smooth. 147

Figure 7.19 Figure 7.19 1st VD map with enhanced shallow structures. Note the presence of high frequency noise.. 148

Figure 7.20 Processed TDR map showing shallow crustal features. 149

Figure 7.21 Figure 7.21 Processed THDR showing the edges of the magnetic bodies 150

Figure 7.22 Processed AS map showing the edges of the magnetic bodies. Please note that the geological continuity is destroyed. 152

Figure 7.23 Residual filtering are applied to the aeromagnetic data to selectively remove the regional magnetic field. The residual magnetic field map shows magnetic response of the shallower bodies..... 152

Figure 7.24 Regional geological map of the southern Otavi Mountain Land showing the extensive sand cover and limited rock exposure as well as mappable structural features. Modified after Smit (1959) and the Geological Survey of Namibia (2008)..... 154

Figure 7.25 RTP map of the southern Otavi Mountain Land showing the magnetic anomalies in relation to copper deposits in the region. 155

Figure 7.26 TDR map showing the response of different magnetic rock types, shallow regional crustal structures and the three different domains in the southern Otavi Mountain Land. 156

Figure 7.27 Interpreted solid geological map of the southern Otavi Mountain Land with the major east-west-trending thrust faults and shallow structural NE-trending faults as well as folds. 158

Figure 7.28 Sampling stations along the survey lines on the satellite image. The maps shows the location of the base station and drill holes. DBDD0003 does not appear on this map because it is outside the survey area. 160

Figure 7.29 Detailed local geological map with survey lines in both areas with known geology and areas with the sand cover. 160

Figure 7.30 Photos of the magnetometers that were used to conduct the ground magnetic survey in the Deblin Copper Mine area. A) The Geometrics 856 proton precession magnetometer (Base station) and B) GSM-19 Overhauser magnetometer (Rover). 162

Figure 7.31 The 69 survey lines of the ground magnetic survey with the line spacing of 25 m. The survey lines have different lengths due to limited access of some parts of the survey area. 164

Figure 7.32 Base station. A) The field survey operator setting the base station. B) The base station magnetometer taking readings on an auto cycle mode 165

Figure 7.33 Diurnal variation plot for day 1. The Julian day is 344. The survey lasted for 253.5 minutes.. 167

Figure 7.34 Diurnal variation plot for day 2. The Julian day is 346. The survey lasted for 605 minutes.. 168

Figure 7.35 Diurnal variation plot for day 3. The Julian day is 347. The survey started after midday and lasted for 231.5 minutes. 168

Figure 7.36 Diurnal variation plot for day 4. The Julian day is 348. The survey lasted for 277 minutes. 169

Figure 7.37 Diurnal variation plot for day 5. The Julian day is 349. The survey lasted for 398.5 minutes. 170

Figure 7.38 Diurnal variation plot for day 6. The Julian day is 350. The survey lasted for 514.5 minutes. 170

Figure 7.39 Diurnal variation plot for day 7. The Julian day is 351. The survey lasted for 229 minutes.. 171

Figure 7.40 Figure 7.40 Plots for diurnal variations for all the days. 172

Figure 7.41 Profiles of the selected survey lines: Line 1400 and 1800. 174

Figure 7.42 2D presentation of magnetic profiles of the 34 infill survey lines. The red dotted line represents the area with a trend of positive anomalies, whereas the red dot represents the location of the Deblin Copper Mine shaft. The trend of the anomalies indicate the strike of magnetic units.. 174

Figure 7.43 Comparison of Total Magnetic Intensity (TMI) maps gridded with A) minimum curvature and B) kriging methods..... 175

Figure 7.44 TMI maps gridded with different set of lines. A) All survey lines (69 lines). B) The first 35 lines. C) The 34 infill lines. D) A combination of two grids (B and C).. 177

Figure 7.45 Reduced to Pole (RTP) and first vertical derivative (1st VD) maps of the merged grids with line noise, which is obvious in the sunshaded maps. The red spot in the images represent the Deblin Mine shaft. The inclination and declination for the shaded images are 45° and 45°, respectively.. 177

Figure 7.46 Total Magnetic Intensity (TMI) map of the Deblin Mine area with the magnetic data sampling points. The Earth's declination and inclination are -9.4 and -61.9, respectively. The red dot represents the location of the Deblin Copper Mine shaft. 178

Figure 7.47 The Total Magnetic Intensity (TMI) data upward continued by 5 m. Notice how the TMI data is smoothed. The red dot represents the location of the Deblin Copper Mine shaft... 179

Figure 7.48 Ground magnetic data of the Deblin Copper Mine area. A) Is the Total Magnetic Intensity (TMI) image and B) is the Reduced to Pole (RTP) image of the TMI data with anomalies lying directly on top of their sources. 179

Figure 7.49 The application of the first vertical derivative (1VD) to the Deblin Copper Mine ground magnetic data. A) Reduced to Pole (RTP) map; B) 1VD map showing the shallow linear structures. 180

Figure 7.50 The application of the tilt derivative to the ground magnetic of the Deblin Copper Mine area. A) Reduced to Pole (RTP) map and B) the tilt horizontal derivative (TDR) which clearly maps shallow linear structures.. 181

Figure 7.51 Contact mapping of the magnetic units using A) total horizontal derivatives (THDR) and B) analytic signal (AS). The maps show contacts of the magnetic maps. The continuity of the stratigraphy is preserved in the THDR map and destroyed in the AS map.. 181

Figure 7.52 Residual filter spectral analysis of the TMI of the Deblin Copper Mine area. Cut-off frequency is 2.0.. 182

Figure 7.53 Residual filter applied to the ground magnetic data of the Deblin Copper Mine area. A) RTP map showing the total magnetic field of all the shallow and deep underground magnetic sources; B) Residual magnetic field map showing magnetic response of shallow seated sources; C) 1st VD of the residual magnetic field showing shallow linear structures; D) TDR of the residual magnetic field showing shallow linear structures with a high resolution. 183

Figure 7.54 Detailed geological map of the Deblin Copper Mine showing the extensive sand cover, rock outcrops and inferred structures. 184

Figure 7.55 Interpreted RTP map showing the magnetic response of the rocks from the Deblin Copper Mine area and positions of the major thrust fault and northeast-oriented faults..... 185

Figure 7.56 Interpreted TDR map showing the magnetic anomalies of the different magnetic units and the locations of the east-west-trending thrust fault and the shallow northeast-trending faults. 186

Figure 7.57 Interpreted solid geological map of the Deblin Copper Mine with the major east-west-trending thrust fault and shallow structural NE-trending faults..... 188

Figure 7.58. A conceptual cross-section model across the Deblin Copper Mine are showing a set of thrust faults along which metal-bearing basinal fluids were introduced into the carbonate host rocks.. 191

List of Tables

Table 2.1 The stratigraphy of the Otavi Mountain Land with stratigraphic positions of the main deposits and prospects (Kamona and Günzel, 2007). The Otavi Group is dominated by shallow marine carbonates with stromatolites whereas the Mulden Group rocks are mainly the siliciclastic sediments……16

Table 2.2 A summary of different characteristics of the Tsumeb-type and Berg Aukas-type mineralization (after Lombaard et al., 1986; Innes and Chaplin, 1986; Hughes, 1987; Misiewicz, 1988; Pirajno and Joubert 1993; Laukamp, 2006; Kamona and Günzel, 2007)……..….25

Table 3.1 Lithological log sheet of DBDD0001 with the detailed description of all the intersected units……38

Table 3.2 Lithological log sheet of DBDD0002 with the detailed description of all the intersected units……40

Table 3.3 Lithological log sheet of DBDD0003 with the detailed description of all the intersected units……42

Table 5.1 Sulphur isotope ratios (permil δ^{34}SCDT) of sulphide minerals from the Deblin Copper Mine and Kombat deposit……..99

Table 6.1 Whole-rock major element compositions of metavolcanic rocks from the area around the Deblin Copper Mine. The major element concentrations are in wt.% and were analyzed by X-ray fluorescence spectrometry……105

Table 6.2 Whole-rock trace element and REE compositions of metavolcanic rocks from the area around the Deblin Copper Mine. Trace element and REE concentrations are in ppm and were analyzed by Inductively Coupled Plasma-Mass Spectrometry (ICP-MS)……..105

Table 6.3 Chondrite-normalized ratios of selected REEs of the metavolcanic rocks from the area around the Deblin Copper Mine……..107

Table 6.4 Geochemical compositions of the Askevold Formation SE of Otavi in Miller's report (as cited in Miller, 2008). Major element concentrations are in wt.% whereas trace element and REE concentrations are in ppm……...108

Table 7.1 Survey parameters for the ground magnetic survey……...159

Table 7.2 Summary of the data collections dates……...163

Chapter 1

Introduction

1.1 Background

This study is part of the Kombat South research project, which aims to apply geological and geophysical techniques to gain a better understanding of the geology of the area in the southern part of the Otavi Mountain Land. The main objective is to develop models that can be applied in the identification and location of economic mineral occurrences in Namibia. The Kombat South research project is part of a collaborative effort between the University of Namibia (UNAM) and the Geological Survey of Namibia (GSN) on the geological and geophysical characterization of metallogenic zones in Namibia. The project is coordinated by Prof A.F. Kamona (UNAM) and Mr. I. Kahimise (GSN). This study uses field geological mapping, geochemical (whole rock and sulphur isotopes) methods and geophysical methods, primarily aeromagnetic and ground magnetic data, and magnetic susceptibility data to determine the style of copper mineralization and its structural setting in the area around the historical Deblin Copper Mine (Neuwerk Cu-deposit), in the southern part of the Otavi Mountain Land.

1.2 Location of the study area

The study area is situated on farm Neuwerk 507 in northern Namibia (Figure 1.1), about 5 km south of the Otavi Valley Syncline and on the southern margin of the Otavi Mountain Land (Figure 1.1). The area lies about 60 km south of Tsumeb Mine (Cu-Pb-Zn-Ga-Ge-Ag deposit) and 15 km southwest of Kombat Mine (Cu-Pb-Zn deposit) (Figure 1.1), which closed in 1996 and 2008, respectively. The area is under the Exclusive Prospecting License (EPL) 3743 owned by Golden Deeps Limited to prospect for base metals in the Otavi Mountain Land. The term Deblin Copper Mine used in this dissertation relates to the shaft that was developed at the Neuwerk Cu deposit, which was discovered by Falconbridge Exploration Limited in 1970. Falconbridge Exploration Limited (as cited in Adamson, 1976) described the Deblin Copper Mine as a small body of base metal mineralization with an estimated tonnage of 260 000 t at 2.6% Cu (Adamson, 1976; Schneider and Seeger, 1992 in Kamona and Günzel, 2007; Golden Deeps Limited, 2012).

Subsequently, Falconbridge Exploration Limited developed a 2 m diameter concrete-lined circular shaft but no mineralization was encountered (Adamson, 1976, Golden Deeps Limited, 2012). In 1975, the shaft was affected by a strong flood event and hence the mine development stopped without any production records (Adamson, 1976; Golden Deeps Limited, 2012).

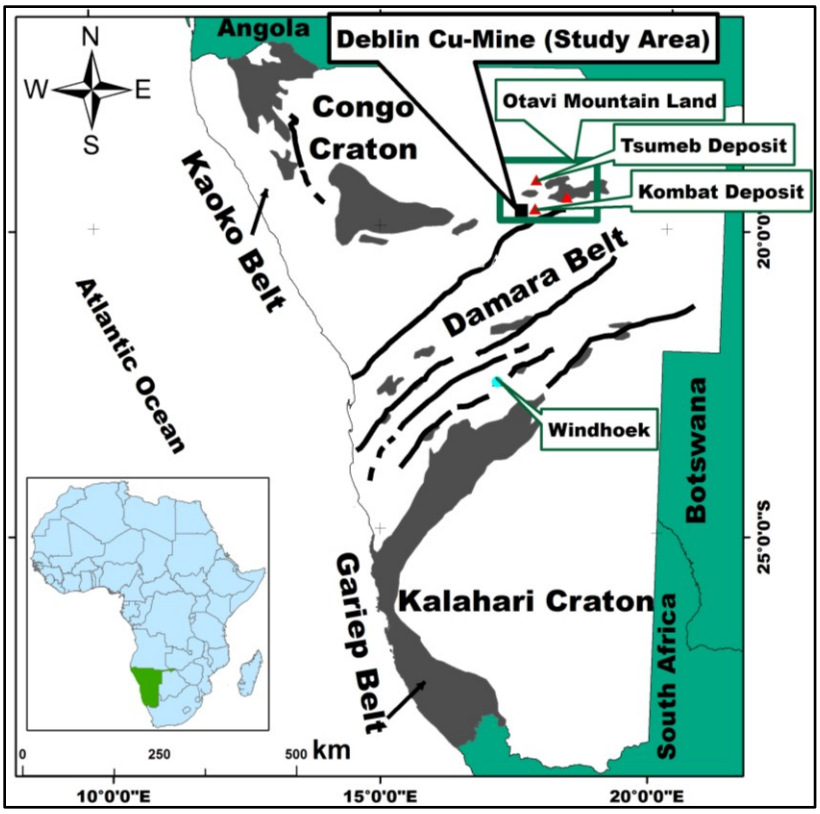


Figure 1.1. Location map of the study area on the northeastern margin of the Damara Belt (taken from Miller, 1983 and Borg, 2000). The open green box represents the Otavi Mountain Land. Bottom left inset shows location of Namibia.

1.3 The Research Problem

The southern Otavi Mountain Land, including the area around the Deblin Copper Mine, preserves valuable records of the tectonic development and associated base metal mineralization (Smit, 1959; Adamson, 1976; Petzel, 1991; Kamona and Günzel, 2007; Golden Deeps Limited, 2013) in the northern Damara Orogen. The recognition of the importance of the southern Otavi Mountain Land geology in the base metal evolution of northern Damara belt has been developed through extensive studies by several researchers, over several decades (Smit, 1959; Schaum 1960; Adamson, 1976; Miller, 1983; Petzel, 1991; Kamona & Günzel, 2007; Golden Deeps Limited,

2013; Nangolo, 2014). Structures in the central and northern Otavi Mountain Land appear to indicate primary controls on metal-bearing hydrothermal fluid flow (Miller, 1983; Pirajno and Joubert, 1993; Deane, 1995; Laukamp, 2006). Although the geological setting and mineralization of various base metal deposits in the Otavi Mountain Land including the Nosib Group volcanic-hosted deposits have been studied in detail (Smit, 1959; Lombaard *et al.*, 1986; Nangolo, 2014; Innes and Chaplin, 1986; Hughes, 1987; Misiewicz, 1988; Petzel, 1991; Chadwick, 1993; Chetty, 1998) the geological framework and mineralization in the Deblin Copper Mine area is unclear due to the extensive Cenozoic sand cover. In addition, major geological structures and underlying lithologies are concealed by the Otavi Group carbonates. As a consequence, little is known about the structural framework and mineralization in the study area and existing geological map structures are largely inferred. Moreover, there is limited geophysical data for the area which can be used in the identification and location of concealed structures and lithologies associated with copper mineralization.

The distribution of the stratigraphy of the area around the Deblin Copper Mine and its relationship with base metal mineralization is not well understood. Different authors interpreted the base metal mineralization style of the Deblin Copper Mine differently. As a result there are two contrasting ideas of the mineralization style of the Deblin Copper Mine. The early authors (Adamson, 1976; Petzel, 1991; Kamona and Günzel, 2007; Golden Deeps Limited, 2012) suggested that the Deblin Copper Mine is a volcanogenic massive sulphide (VMS) deposit with base metal sulphides located in the contact zone between sericite chlorite schist of the Askevold Formation and the overlying dolomite of the Abenab Subgroup. In contrast, recent petrographic studies by Golden Deeps Limited (2013) suggested a shear-hosted hydrothermal mineralization style with an Iron Oxide Copper and Gold (IOCG) style mineral assemblage hosted in the carbonates.

1.4 Aim and Objectives

This study aims to determine the copper mineralization style of the Deblin Copper Mine and to improve the existing local geological map. The objectives of the study are:

1. To produce a geological and structural map of the Deblin Copper Mine area based on geological mapping and magnetic survey data.

2. To establish the ore mineralogy and paragenetic sequence of sulphide mineralization in the Deblin Copper Mine area.
3. To establish the origin of sulphur in the sulphides from the Deblin Copper Mine.
4. To determine the geochemical characteristics and the possible tectonic setting of emplacement of the metavolcanic rocks of the Askevold Formation.

1.5 Research Methodology

The results of this study are based on geological and geophysical field data collected in the area around the Deblin Copper Mine. Fieldwork was undertaken between 27 May 2015 and 15 June 2015 and from 30 November 2015 to 17 December 2015. The geological data were collected on sporadic outcrops in the study area. Additional petrographic data were collected from three borehole cores that were drilled in the study area in 2013. The borehole cores were provided by Sabre Resources Namibia, a company that is exploring for base metals in the study area and other parts of the Otavi Mountain Land in collaboration with the Golden Deeps Limited.

Geological mapping and core lithological logging were used to create a new geological map and establish the local stratigraphy. Petrography and ore mineralogy were used to determine the host rock, main ore minerals and mineralization style. Sulphur isotope analyses were conducted to establish the source of sulphur in the sulphides, whereas whole rock geochemistry was used to establish the geotectonic setting of the metavolcanic rocks. Aeromagnetic data were used to understand the regional structural setting, while ground magnetic surveying was used to decipher the local structures and the distribution of the magnetic rocks. Magnetic susceptibility data were essential for understanding the magnetism of the rocks in the study area. Aeromagnetic data were provided by the Geological Survey of Namibia, whereas ground magnetic and magnetic susceptibility data were acquired during the second field session (30 November 2015 to 17 December 2015). Magnetic data were processed using the Oasis Montaj Geosoft software, version 8.3.

Chapter 2

Regional Geology

2.1 Geological Setting of the Otavi Mountain Land

2.1.1 The Damara Belt

The Pan-African Orogeny was responsible for the development of several Neoproterozoic orogenic belts of the Gondwana supercontinent in southern and central Africa (Miller, 1983; Porada, 1985; Hoffmann and Prave, 1996) (Figure 2.1). The Damara Orogen in Namibia represents the collision of the Angola-Congo and Kalahari cratons in Africa and the Rio de la Plata Craton in South America (Porada, 1985; Frimmel *et al.*, 1996; Gray *et al.*, 2008; Miller, 2008) (Figure 2.1). The Damara Orogen comprises three orogenic belts: (i) the Damara Belt (a north-east trending, intracontinental branch) (ii) the Kaoko Belt (a north-south trending coastal branch) and (iii) the Gariep Belt (a southern coastal branch) (Martin and Porada, 1977; Miller, 1983; Porada, 1985; Gray *et al.*, 2008) (Figure 2.1 and Figure 2.2A). However, Rapela *et al.* (2011) suggested that Kaoko and Gariep Belts formed from two different orogenic events. These three belts are considered to express a collisional triple junction (Martin and Porada, 1977; Miller, 1983; Porada, 1985; Borg, 2000; Gray *et al.*, 2008; Miller, 2008).

The Damara Belt represents an orogenic event that records the amalgamation of the former continental fragments of the Gondwana supercontinent (Miller, 1983; Hoffmann and Prave, 1996; Gray *et al.*, 2008), between the Kalahari and Congo Cratons (Hoffmann, 1983; Miller, 1983, 2008; Gray *et al.*, 2008) (Figure 2.1 and Figure 2.2). Aeromagnetic surveys indicate that the Damara Belt structural trends can be traced northeastward through northwestern Botswana (Rankin, 2014) and Zambia, and into the Katanga Succession of the Democratic Republic of the Congo (Miller, 1983; Gray *et al.*, 2008), as it extends under Kalahari Supergroup cover.

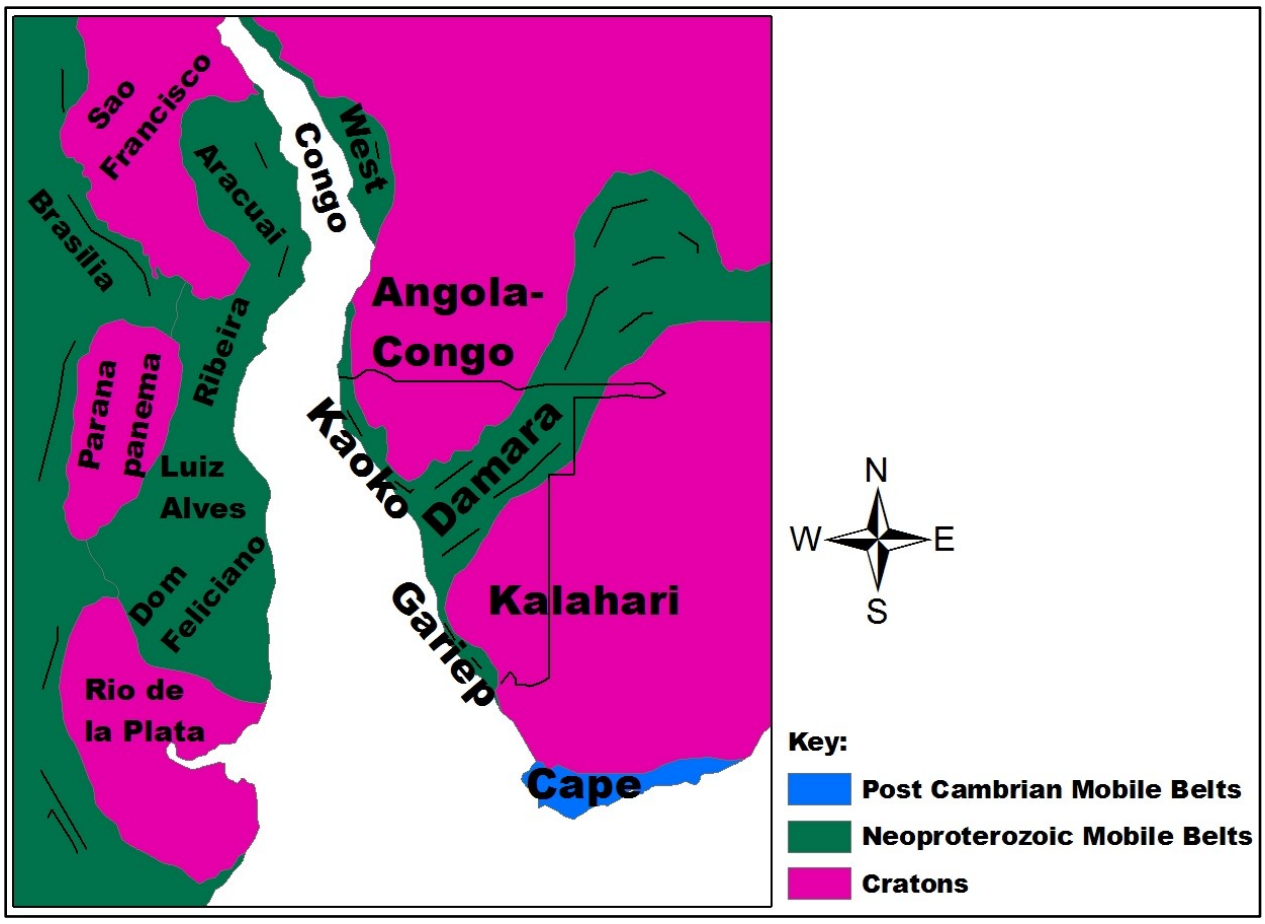


Figure 2.1 Map of the Brasiliano and Pan-African orogens showing the position of the Neoproterozoic Damara Orogen, Kalahari and Congo cratons as well as other orogenic belts (after Gray et al., 2008, Miller, 2008).

The Damara Belt has been extensively studied by both local and international researchers (Martin and Porada, 1977; Coward, 1981; Corner, 1983; Miller, 1983; Porada, 1985; Hoffmann and Prave, 1996; Corner, 2008; Miller, 2008; Gray *et al.*, 2008; Germs *et al.*, 2009; Rankin, 2014; Lehmann *et al.*, 2015). The Damara Belt is divided into seven contrasting tectonostratigraphic zones, on the basis of stratigraphy, structure, metamorphic grade, plutonic rocks, geochronology and aeromagnetic expressions (Miller, 1983, 2008). From north to south these are: the Northern Platform, Northern Margin Zone, Northern Zone, Central Zone, Southern Zone, Southern Margin Zone, and Southern Foreland (Corner, 2008; Miller, 2008) (Figure 2.2 and Figure 2.3). The zones are demarcated by major linear features, including faults, thrusts, lineaments, stratigraphic and metamorphic boundaries (Miller, 1983, 2008; Corner, 2008). The focus of this study is the

Northern Platform, which forms the northern margin of the Damara Belt, with less deformed carbonates than shown by other zones (Figure 2.2) (Miller, 2008).

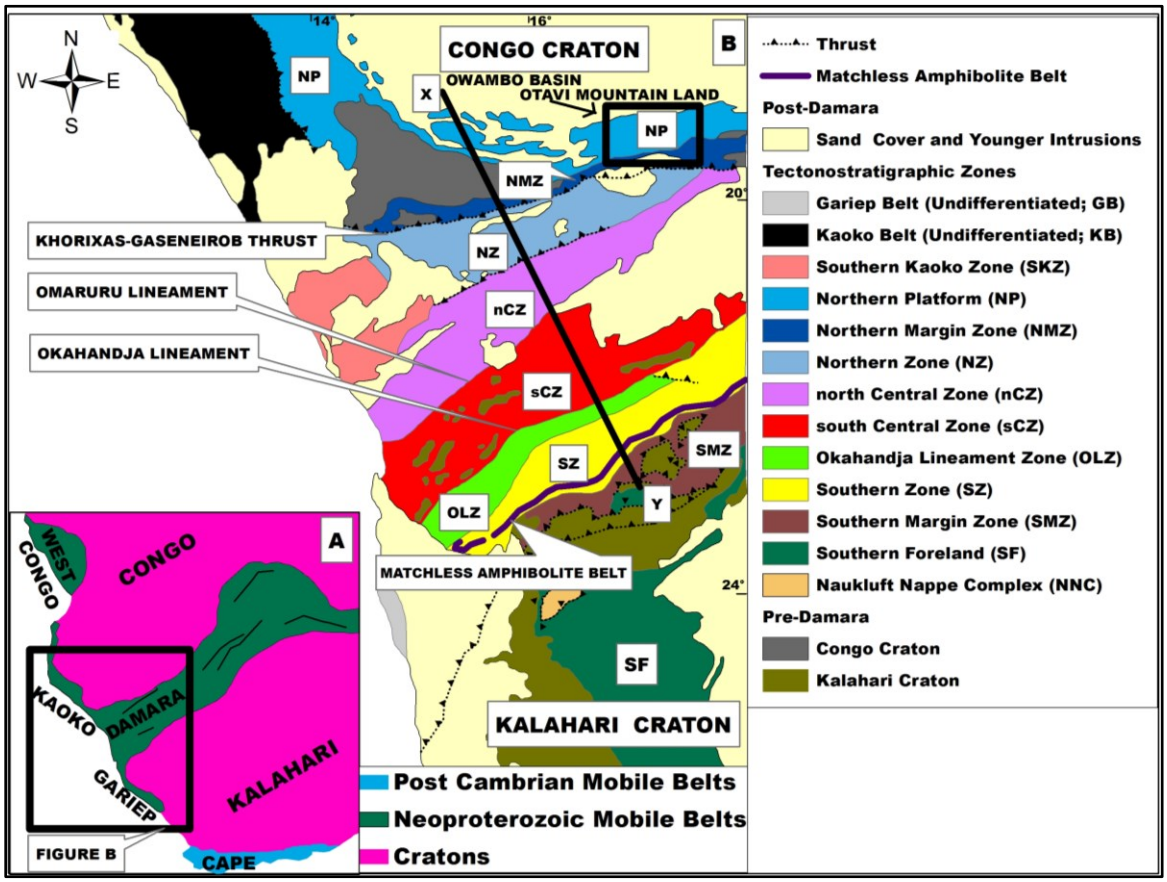


Figure 2.2 The location and architecture of the Damara Belt. (A) Simplified map of the Neoproterozoic Pan-African belt systems in southern and central Africa showing the intracontinental Damara Belt and the coastal Kaoko and Gariep Belts (after Gray et al., 2008; Miller, 2008). (B) Simplified map of the Damara Belt showing the tectonostratigraphic zones (taken from Corner, 2008 and Miller, 2008). The X-Y line represents a cross section shown on Figure 2.4.

According to Miller (2008), the Northern Platform is a broad shelf region bordering with both the Kaoko and Damara belts (Figure 2.2). The characteristic features of the Northern Platform include the thick, low grade platform carbonates of the Otavi Group overlain by molasse sediments of the Mulden Group (Figure 2.3 and Figure 2.4) and the presence of open folding (Miller, 1983). In addition, the east-west trending fold structures in the southern part of the Northern Platform are conspicuous in the magnetic data (Corner, 2008; Miller, 2008). Although the Northern Margin Zone is non-magnetic in general, it displays positive remanent magnetic anomalies in places,

ascribed to the presence of pyrrhotite in the Mulden Group phyllite and quartzite. While the Northern Margin Zone is characterized by molasse sediments, the Northern Zone is characterized by a southward transition into deep water facies rocks, syn-rift metasedimentary and volcanic rocks, low grade metamorphism and, highly deformed facies (Miller, 1983, 2008; Corner, 2008). Notably, the Northern Zone shows a strong magnetic signature attributed to the presence of a banded iron formation within the diamictite unit of the Chuos Formation (Figure 2.3) and to the mafic volcanic rocks of the Askevold Formation (Corner, 2008; Miller, 2008).

The Central Zone records the high-temperature-low-pressure conditions of the Damara Orogen and is characterized by sillimanite-cordierite metamorphic assemblages (Miller, 1983). The Central Zone is further subdivided into a north Central Zone and south Central Zone, both characterized by syn-to post-orogenic granitic plutons and dome structures. However, the magnetic signatures of the two zones are different. The north Central Zone consists of Karibib Formation carbonates and Kuiseb Formation schists (Figure 2.3) deformed in basin and dome structures (Miller, 2008) and down-thrown to the north of the Omaruru Lineament (Figure 2.2b) on a regional scale (Corner, 1983). Although the rocks of the north Central Zone are magnetically quiet, some fabric is noticeable in the high resolution aeromagnetic data (Corner, 1983, 2008). The south Central Zone, by contrast, is characterized by positive magnetic anomalies caused primarily by the mafic volcanic rocks of the Nosib Group, the Chuos Formation diamictites and the Meso- and Paleoproterozoic basement rocks (Corner, 2008; Miller, 2008). Corner (1983) observed that the Nosib Group formations are strongly magnetic where the metamorphic grades are high.

The Okahandja Lineament Zone is located between the Central Zone and Southern Zone (Corner, 1983, 2008; Miller, 1983; 2008) (Figure 2.2b). The Okahandja Lineament Zone marks major changes in the stratigraphic succession, structural style, age of early deformation, metamorphic records, aeromagnetic signatures and seismic characteristics of the lower crust (Corner, 1983; Miller, 1983). The Okahandja Lineament Zone together with the Southern Zone form the so-called Khomas Trough (Martin and Porada, 1977) (Figure 2.4). The Okahandja Lineament Zone is characterized by upright structures and a linear structural grain (Miller, 1983). The Okahandja Lineament Zone hosts the 350 km-long, post-tectonic, garnetiferous, two-mica Donkerhuk Granite batholith (Haack, 1983; Miller, 1983). Both the Okahandja Lineament Zone and the Southern Zone

contain one lithostratigraphic unit, the schistose Kuiseb Formation (Figure 2.3) (Miller, 1983), which is non-magnetic (Corner, 2008; Miller, 2008). The Southern Zone therefore has a quiet regional magnetic signature. However, there are some schist units in places that are magnetic and the magnetite quartzite associated with the Matchless Amphibolite Belt (Corner, 2008; Miller, 2008) (Figure 2.2b and Figure 2.4).

Miller (1983) described the Southern Margin Zone as consisting of intensely thrust pre-Damaran rocks in the southern part, while the northern part consists of thrust rocks of both Damara and pre-Damara Sequences (Figure 2.2b). In addition, the Southern Margin Zone is characterized by kyanite-chlorite-muscovite assemblages, which signal low-temperature-high-pressure metamorphic conditions (Kasch, 1983; Miller, 1983). The Southern Foreland is characterized by the Nama Group (Figure 2.3) rocks deposited on the stable Kalahari Craton and deformed along its margins in the north and west during the Damara Orogeny (Miller, 1983, 2008). The high-amplitude magnetic fabric and low magnetic signals, particularly in the high resolution aeromagnetic data in the Southern Margin Zone are associated with the Chuos Formation diamictite and the Nosib Group rocks, respectively (Corner, 2008; Miller, 2008). Aeromagnetic data show the continuation of the Southern Margin Zone regional structure and the folded northern edge of the Southern Foreland below the Kalahari Supergroup cover of northern Botswana into the Lufilian Arc where the Katangan rocks have been thrust southward (Miller, 1983, 2008; Rankin, 2014). The Damara Belt shows contrasting styles of metamorphism (Miller, 1983). While the Northern Platform and Northern Zone record less deformation and low grades of metamorphism, the south Central Zone, Southern Zone and Southern Margin Zone are the highly deformed zones of the Damara Belt (Germs *et al.*, 2009). The grade of metamorphism decreases progressively from upper amphibolite facies in the Okahandja Lineament Zone to greenschist facies in the Southern Margin Zone (Miller, 1983; Germs *et al.*, 2009).

The evolution of the Damara Belt is made up of several phases: continental rifting, ocean floor spreading, glaciation, subduction, collision, metamorphism and magmatism (Pirajno and Joubert, 1993; Miller, 2008). According to Miller (2008), the northeast-trending Damara Ocean formed during the spreading of the north-south Adamaster Ocean joining both Kaoko and Gariep belts. During this early stage of the evolution, two parallel northeast-trending rift basins formed: (i) the Northern Rift (Outjo Sea) in the Northern Zone and north Central Zone, and (ii) the Southern Rift

(Khomas Sea) in the Central Zone of the Damara Belt (Martin and Porada, 1977; Miller, 1983, 2008; Frimmel and Miller, 2009). These two rift basins formed about 746 ± 2 Ma ago (Hoffmann and Prave, 1996). Several rift shoulders gave way to numerous shelf regions during the early stages of the development of the Damara Belt (Miller, 2008). These rift shoulders include chiefly an elevated rift shoulder along the southern edge of the Northern Platform that formed the Northern Margin Zone and, a narrow shelf region, marginal to the deep Outjo Sea (Miller, 1983, 2008).

The Damara Sequence (Miller, 1983) (Figure 2.3 and Figure 2.4) is defined by a succession of siliciclastic and carbonate rocks that constitute part of the Damara Belt in both the Outjo and Khomas seas. This sequence includes felsic and mafic lavas, and sills with a U-Pb zircon age of 746 ±2 Ma (Hoffmann and Prave, 1996) that define the age of the basal successions. Deposition of the Damara Sequence during the Neoproterozoic lasted between at least 770 and 600 Ma (Miller, 1983; Hoffmann, 1983; Hoffmann and Prave, 1996). The main part of the rift was filled with high energy, coarse clastic and turbiditic sediments of the Nosib and Swakop groups, respectively (Miller, 1983, 2008) (Figure 2.4).

While rifting and spreading continued in the central part of the Damara Orogen, pure, post-rift, platform carbonate sediments (Otavi Group) (Figure 2.4) accumulated along the northern margin of the Northern Rift reaching a thickness of 4000 m (Hoffmann and Prave, 1996; Miller, 2008). Subsequently, extensive sea floor spreading in the central part of the Damara Orogen resulted in tholeiitic basaltic volcanism at ~700 Ma (Nagel, 1999) that formed a mid-oceanic ridge now represented as the Matchless Amphibolite Belt (Miller, 1983; Killick, 2000; Miller 2008) (Figure 2.4). The Matchless Amphibolite Belt is highly magnetic and it is associated with several Besshi-type Volcanogenic Massive Sulphide (VMS) Cu-Zn-(Ag-Au) deposits, which formed in a sea floor spreading environment (Killick, 2000; Miller, 2008).

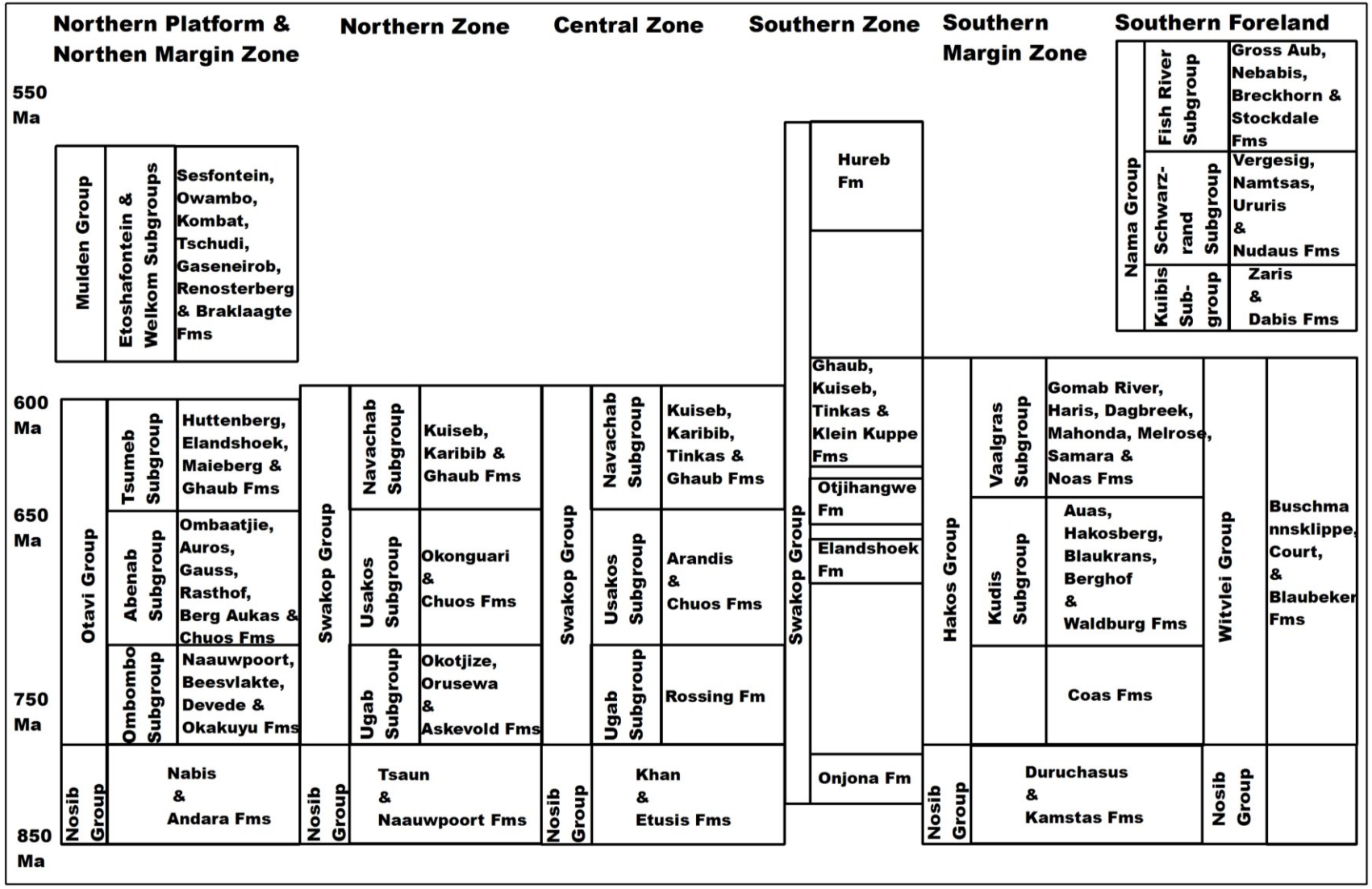


Figure 2.3 Lithostratigraphy and correlation across the Damara Belt with approximate deposition age for the Damara Sequence (modified after Miller, 2008). The vertical thickness of the sequence is not to scale.

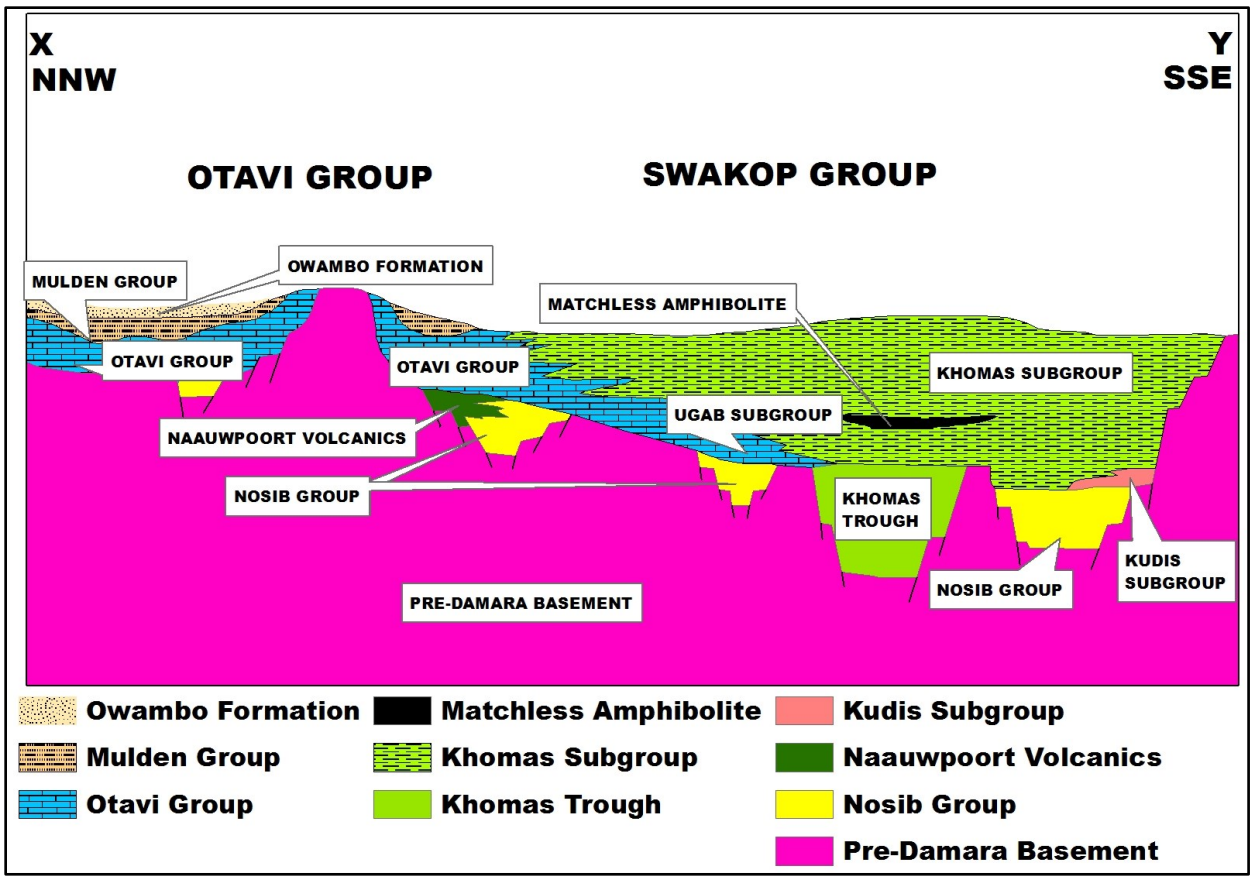


Figure 2.4 Generalized pre-orogenic section across the Damara Belt (from X to Y as shown in Figure 2.2b) with a simplified stratigraphic compilation showing basal, initial rift grabens, the syn-rift Nosib Group and the post-rift units of the Otavi, Swakop and Mulden groups (modified after Borg, 2000).

Although the Matchless Amphibolite Belt is made up of basalt relics with MORB (Mid Oceanic Ridge Basalt)-like chemistry and age of ~635 Ma (Foster *et al.*, 2015; Lehmann *et al.*, 2016) derived from the Kuiseb Formation schists in which the Matchless basalt emplaced, recent studies by Lehmann *et al.* (2016) suggested that the Amphibolite Matchless Belt is too young to suggest the breakup between the Congo and Kalahari Cratons.

Thereafter, two Neoproterozoic "Snowball-Earth" glaciation events resulted in the deposition of the older Chuos Formation (Sturtian) at about 750 Ma and the younger Ghaub Formation (Marinoan) with a constrained age of 635 ±1.2 Ma based on zircon dating (Hoffmann and Prave, 1996; Hoffmann *et al.*, 2004; Halverson *et al.*, 2005; Miller, 2008). Eventually, with the reversal of the plate motion, the Damara evolution ended with: (i) the subduction of the oceanic crust

towards the northwest under the Congo Craton, and (ii) the collision between the Congo and Kalahari Cratons (Coward, 1981; Miller, 1983; Porada, 1985; Gray et al., 2008; Miller, 2008; Germs *et al*., 2009). However, this has been challenged by Longridge *et al.* (2014) and Milani *et al.* (2015), who used geochemical evidence to show that there has not been pre-collisional subduction in the Damara Belt. The Congo and Kalahari Cratons collision, followed by crustal thickening is understood to have occurred between approximately 580 Ma and 540 Ma (Longridge *et al.*, 2014; Milani *et al.*, 2015).

2.1.2 Geology of the Otavi Mountain Land

Introduction

The Otavi Mountain Land is situated on the northeastern margin of the Damara Belt in the Northern Platform and Northern Zone. The Otavi Mountain Land is characterized by platform carbonates, which were deposited during the advanced stages of continental rifting, interrupted by the volcanism and subsequently affected by the Damara Orogeny and hydrothermal activity (Söhnge, 1957; Smit, 1959; Miller, 1983; Laukamp, 2006; Miller, 2008; Frimmel and Miller, 2009). The northern part of Otavi Mountain Land forms part of the Owambo Basin (Figure 2.2b) and the southern part is within the Northern Rift (Kamona and Günzel, 2007; Miller, 2008). The Otavi Mountain Land platform carbonates occur in generally east-west trending synclines and anticlines attributed to the folding and overturning of the Damara Sequence formations (Figure 2.5 and Table 2.1). The Otavi Mountain Land, and the geological units within, has been the subject of several geological studies resulting in different conceptual theories of its formation and mineralization styles. The first study of the geology and stratigraphy of the Otavi Mountain Land by Söhnge (1957) described it as a metallogenic province with stratigraphic controls on base metal mineralization.

Stratigraphy

The stratigraphy of the Otavi Mountain Land is predominantly composed of three major groups of the Damara Supergroup: (i) the Nosib Group with arenaceous clastics, (ii) the Otavi Group (a thick succession of carbonates) and (iii) the Mulden Group (a molasse succession) (Söhnge, 1957; Hedberg, 1979; Kamona and Günzel, 2007; Miller, 2008) (Figure 2.5 and Table 2.1). Early work on the Otavi Mountain Land stratigraphy was undertaken by Söhnge (1957) and Hedberg (1979),

who established the first regional stratigraphic framework for the Otavi Group in the Otavi Mountain Land in detail. Hoffman and Prave (1996) reviewed the stratigraphy of the Otavi Group with reference to the two glacial deposits predominantly the Chuos and Ghaub Formations and the associated cap carbonates. The geology and stratigraphy in the vicinity of the mining areas have been described by Lombaard *et al.* (1986), Innes and Chaplin (1986), Hughes (1987), Misiewicz (1988), Chadwick (1993), Chetty (1998), Chetty (2000) and Kamona and Günzel (2007).

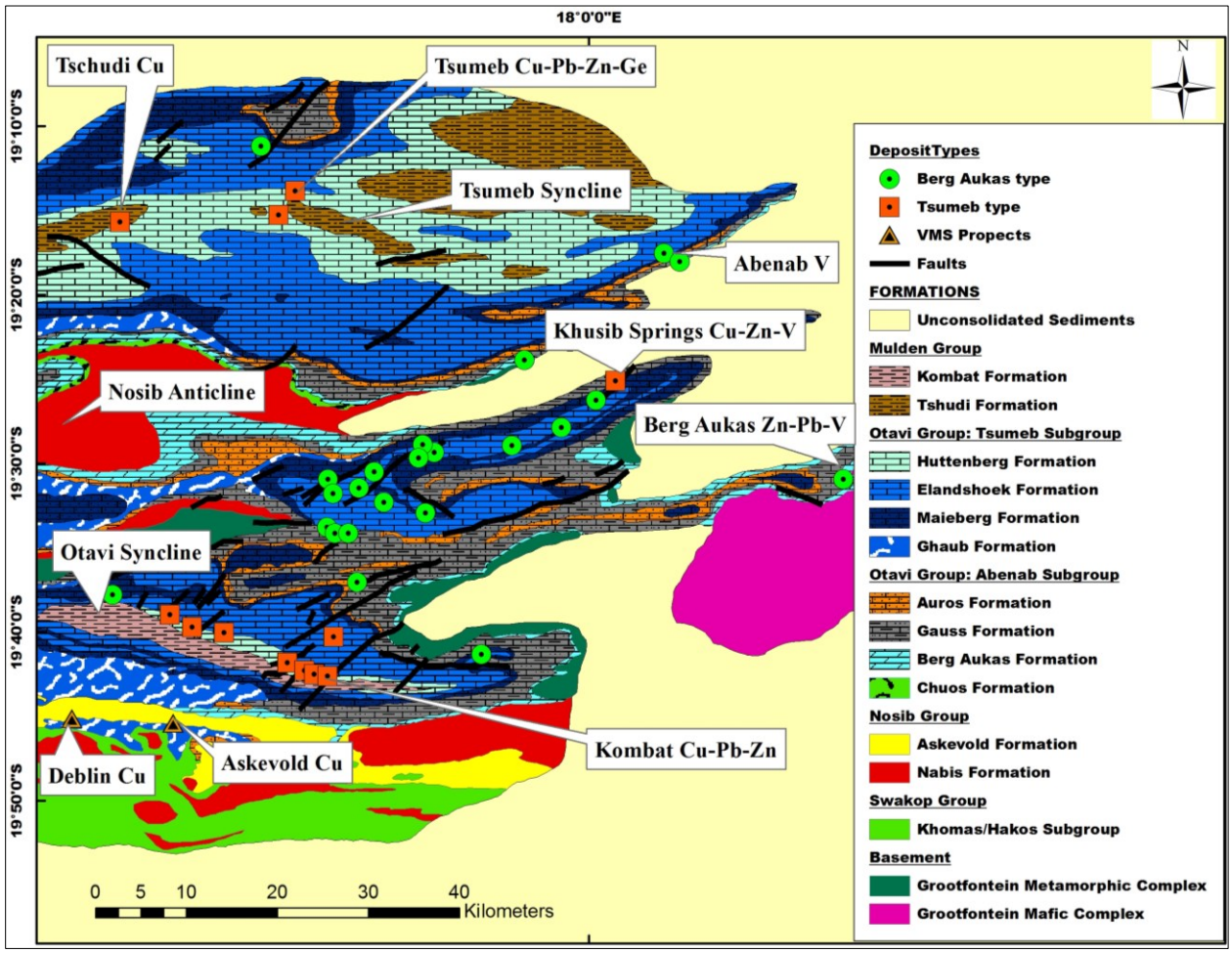


Figure 2.5 Geology of the Otavi Mountain Land with locations of major deposits and some prospects (modified after Söhnge, 1957; Kamona and Günzel, 2007 and map of 1:250,000 of the Geological Survey of Namibia). Generally, the Tsumeb type consists of sulphide ores containing Cu, Pb, Zn, Ag, As, Ge, Cd and Ga, whereas the Berg Aukas type contains primarily Pb-Zn and V sulphide ores with little Cu.

Paleoproterozoic Basement: Grootfontein Inlier

The basement rocks in the Otavi Mountain Land belong to the 1.946 ±299 Ma Grootfontein Inlier located on the southern Congo Craton (Miller, 2008). The Grootfontein Inlier is further subdivided into the older Grootfontein Mafic Body and the younger Grootfontein Metamorphic Complex (Misiewicz, 1988; Miller, 2008) (Figure 2.5 and Table 2.1). The Grootfontein Inlier is poorly exposed and its lithologies are given in Table 2.1.

Nosib Group

The Nosib Group unconformably overlies the basement rocks (Kamona and Günzel, 2007). The Nosib Group developed as a result of intracontinental rifting of the Congo Craton at approximately 756 Ma ago (Kamona and Günzel, 2007). According to Miller (2008), the basal Nosib Group of the Damaran Supergroup was deposited in two northeast-trending rifts, in half grabens formed between the two rifts and in fluviatile platform and shelf areas bordering the rifts in the Northern Platform and Southern Foreland. Kamona and Günzel (2007) contended that rifting and clastic sedimentation lasted until 746 Ma, when rift related volcanism produced bi-modal volcanic rocks in the Northern Rift of the Damara Orogen. The Nosib Group succession in the Otavi Mountain Land has been described in detail by Söhnge (1957), Botha (1960) and Porada (1985). The Nosib Group consists of Nabis and Askevold formations (Table 2.1) which are sporadically exposed in the central and southern parts of the Otavi Mountain Land (Kamona and Günzel, 2007; Miller, 2008). According to Söhnge (1957), the Nabis Formation in the Otavi Mountain Land is deposited in a series of east-west to northeast-trending basins. The Nabis Formation consists predominantly of basal conglomerate that reaches a thickness of about 400 m and interfingers with feldspathic sandstone in the upper part of the succession (Söhnge, 1957; Botha, 1960; Grobler, 1961). The overlying Askevold Formation occurs within the Northern Zone right up against the bounding fault of the Northern Rift (Miller, 2008). The Askevold Formation occurs as a metavolcanic unit limited to the southern part of the Otavi Mountain Land (Kamona and Günzel, 2007; Miller, 2008). The main lithologies of the Askevold Formation include epidotized basic volcanic rocks (epidosite), tuff (leucitite) and sericite-chlorite schist (Smit, 1959; Kamona and Günzel, 2007; Miller, 2008).

Table 2.1 The stratigraphy of the Otavi Mountain Land with stratigraphic positions of the main deposits and prospects (Kamona and Günzel, 2007). The Otavi Group is dominated by shallow marine carbonates with stromatolites whereas the Mulden Group rocks are mainly the siliciclastic sediments.

	GROUP		FORMATION	LITHOLOGY	DEPOSIT
543 Ma	Mulden	Etoshafontein Subgroup	Kombat	Slate, Phyllite, Sandstone	
			Tschudi	Arenite, Subgreywacke, Conglomerate	Tschudi Cu-(Ag)
	Otavi	Tsumeb Subgroup	Huttenberg	Dolostone, Oolite, Chert, Dolostone, Shale, Stromatolite, Chert, Breccia	Kombat Cu-Pb-(Zn) Tsumeb Pb-Cu-Zn-(Ge)
			Elandshoek	Dolostone, Chert, Breccia Dolostone	
			Maieberg	Dolostone Limestone Dolostone	Abenab V Khusib Springs Cu-Pb-Zn
620 Ma			Ghaub	Diamictite	
		Abenab Subgroup	Auros	Stromatolite, Chert, Limestone	Abenab West Pb-Zn-V
			Gauss	Breccia, Oolite Dolostone, Chert	Berg Aukas Zn-Pb-V
			Berg Aukas	Dolostone, Chert	
			Chuos	Diamictite	
	Nosib		Askevold	Tuff, Quartzite	Nosib Cu, Deblin Cu
			Nabis	Quartzite, Sandstone Conglomerate	
850 Ma	Grootfontein Metamorphic Complex			Diabase,Granite,Gneiss,Diorite,Gabbro,Serpentinite	
2500Ma	Grootfontein Mafic Body			Gabbro,Serpentinite	

Otavi Group

The Otavi Group forms the main succession in the Northern Platform (Miller, 1983) (Figure 2.4) and is dominated by a carbonate platform (Figure 2.5 and Table 2.1). The thickness of this group is estimated at about 4 km in outcrop and at about 6 km below the Cenozoic cover in the Owambo Basin (Hedberg, 1979; Miller, 1997). According to Miller (1983), the Otavi Group is the platform equivalent of the deep marine carbonate-bearing portions of the Swakop Group (Figure 2.3 and Figure 2.4). In the Otavi Mountain Land, the Otavi Group is subdivided into the Lower Abenab

and Upper Tsumeb Subgroups (Smit, 1959; Söhnge, 1975; Miller, 1983) (Figure 2.5 and Table 2.1).

a) The Abenab Subgroup

The Abenab Subgroup consists primarily of dolostone beds, but includes limestone, marl and shale, as well as the glacial deposit of the Chuos Formation diamictite (Kamona and Günzel 2007). In general, the Abenab Subgroup occurs in the central and southern parts of the Otavi Mountain Land (Figure 2.5). The Abenab Subgroup is subdivided into four formations (Söhnge, 1957; Hedberg, 1979; Kamona and Günzel, 2007; Miller, 2008). From oldest to youngest, these are the Chuos, Berg Aukas, Gauss and Auros Formations. The basal Chuos Formation (Table 2.1), formerly known as the Varianto Formation occurs in the central, western and southern parts of the Otavi Mountain Land (Kamona and Günzel 2007; Miller, 2008). The Chuos Formation unconformably overlies the Nosib Group or basement rocks (Miller, 2008). This glacial deposit is represented by a massive to poorly stratified diamictite with scattered and unsorted, polymict pebbles, cobbles and boulders derived from the underlying rocks of Nosib Group and basement granites (Miller, 2008). In addition, this formation consists of conglomeratic siltstone, feldspathic sandstone and banded iron formation (Söhnge, 1957; Hoffmann and Prave, 1996). The Chuos Formation diamictite was deposited during the Sturtian glaciation (Hoffmann and Prave, 1996; Hoffmann *et al.*, 2004; Halverson *et al.*, 2005), which was accompanied by volcanism dated at 746 ± 2 Ma (Hoffman et al., 1996) as shown by its andesitic and basaltic clasts in the matrix. The associated cap carbonates of the Berg Aukas Formation (Table 2.1) have been used in global correlations of the Sturtian glaciation by most researchers (Hoffmann et al., 2004; Halverson et al., 2005; Hoffman and Li, 2009). These cap carbonates are characterized by negative δ^{13}carbon anomalies, whereas the carbonate successions underlying the glacial deposits have high delta δ^{13}carbon (Frimmel *et al.*, 1996; Kennedy *et al.*, 1998; Hoffman and Li, 2009).

The Berg Aukas Formation consists of the basal laminated and banded grey dolostone (Söhnge, 1957; Kamona and Günzel, 2007, Miller, 2008), which were deposited directly onto the Chuos Formation during the flooding event that followed the Snowball Earth glaciation (Hoffmann and Prave, 1996). The laminated and banded grey dolostone is overlain by a light grey dolomite characterized by stromatolitic reef facies associated with reef debris and consisting of light grey

dolomite with sparry calcite cement and algal chert layers. The youngest unit of the Berg Aukas Formation is a black to dark grey banded and laminated dolostone rhythmite. The overlying Gauss Formation (Table 2.1) consists of a dark grey dolomicrite, light grey dolomicritic, light grey boundstone or dolo-arenite and oolite, laminated mudstone and light grey dolomicrite or dolo-arenite at the base (Chadwick, 1993). The successive Auros Formation (Table 2.1) is made up primarily of dolostone, limestone and shale (Kamona and Günzel, 2007). This formation is characterized by three to four upward cycles made up of shale horizons occurring with interbedded limestone and dolomite layers (Kamona and Günzel, 2007; Miller, 2008). Each cycle begins with marl and terminates with the stromatolitic tidal flat facies (Kamona and Günzel, 2007).

b) Tsumeb Subgroup

The Tsumeb Subgroup is made up of the basal Marinoan age glacial deposit of the Ghaub Formation, and subsequent carbonate formations of Maieberg, Elandshoek, and Hüttenberg (Figure 2.5 and Table 2.1). Each of these formations is divided into different units based on lithology (Söhnge, 1957). The units are labeled T2 to T8, following the usage of T for Tsumeb Subgroup. Unit T1 is accorded to the Ghaub Formation, whereas units T2 to T8 can be subdivided in two groups: (i) the lower T2-T4 sequence and (ii) the upper T5-T8 sequence (Miller, 2008). The Ghaub Formation unconformably extends across the Auros and Gauss Formations (Miller, 2008). The Ghaub Formation is defined principally by diamictite, conglomerate and minor shale, sandstone and dolomite (Miller, 2008). The diamictite of this Formation is characterized by unsorted boulders of predominantly dolomite, limestone and quartzite hosted in a fine-grained calcareous and dolomitic matrix (Kennedy et al., 1998; Hoffmann et al., 2004; Miller, 2008). The clasts are up to 1 m in diameter and can be striated. The succeeding Maieberg Formation is widely distributed within the Otavi Mountain Land (Kamona and Günzel, 2007). The base of the Maieberg Formation is made up of the Keilberg Member, which is the cap carbonate of the glaciogenic Ghaub Formation diamictite (Hoffmann and Prave, 1996; Hoffmann *et al.*, 2004; Halverson *et al.*, 2005; Hoffman and Li, 2009). Where the Keilberg Member lies directly in contact with the Ghaub Formation diamictite, it is thin and consists of a laminated dolomite. However, where the Ghaub Formation is missing, the Keilberg Member forms the basal Tsumeb Subgroup dolomite (Halverson et al., 2004; Hofmann at al., 2005). The top part of the Maieberg Formation is composed of the T2 limestone and T3 dolomite (Söhnge, 1957; Miller, 2008).

The Elandshoek Formation is highly karstic with an irregular blocky terrain. The Elandshoek Formation is persistent on the northern side of the Otavi Valley Syncline (Figure 2.5), where it reaches a thickness of approximately 1500 m (Miller, 2008). The Elandshoek Formation is conformably overlying the platy T3 dolomite of the Maieberg Formation and contains primarily largely uniform, light grey dolomite (Miller, 2008). This formation is subdivided into T4 and T5 dolomite units. The lower T4 dolomite unit is characterized by massive, light grey dolomite with layers of bedded to laminated dolomite. In contrast, the upper T5 dolomite unit is very uniform and consists of repetitive well bedded, medium to light grey, dolomite mudstone and grainstone with layers of massive dolomite. In addition, the T5 dolomite has a general medium grey to buff weathering colour (Miller, 2008). The T6, T7 and T8 units of the Huttenberg Formation constitute the uppermost part of the Tsumeb Subgroup. The T6 unit conformably follows the Elandshoek Formation and has a dolomite with conspicuous chert layers (Miller, 2008). The subsequent T7 unit is made up of dark grey, bedded, carbonaceous, dolomite mudstone or grainstone and alternating layers of light and dark grey dolomite mudstone or grainstone with minor limestone mudstone (Miller, 2008). This unit has subordinate thin shale beds and rare chert bands. The ensuing T8 dolomite is defined by light grey massive to medium-bedded dolomite mudstones and packstones with interbedded silicified oolite-oncolite beds, and wavy stratiform, domal, columnar stromatolites (Söhnge, 1957).

Mulden Group

The Mulden Group is unconformably to paraconformably overlying the Otavi Group (Figure 2.4 and Table 2.1) and formed from deposition of the erosional products of the Otavi Group (Hedberg, 1979; Miller, 2008). According to Miller (2008), the Mulden Group is syntectonic and was deposited between D_1 and D_2 phases of Damaran deformation in the Northern Platform. The Mulden Group rocks are eroded from the anticlinal areas of the central Otavi Mountain Land and deposited within the synclinal valleys (Figure 2.5) along the folded southern and western margins of the Northern Platform (Kamona and Günzel, 2007; Miller, 2008). In elevated margins of the Northern Platform, the Mulden Group rests directly on pre-Damara basement gneisses, whereas, in the Owambo Basin its rocks are extensively covered by the Karoo and Kalahari successions (Söhnge, 1957; Miller, 2008).

Like the Otavi Group, the Mulden Group is subdivided into two subgroups, chiefly the Etoshafontein and Welkom Subgroups accordingly (Miller, 2008) (Figure 2.3). While the siliciclastic Tschudi and Kombat Formations constitute the Etoshafontein Subgroup in the Otavi Mountain Land (Kamona and Günzel, 2007; Miller, 2008), the Welkom Subgroup is absent in the Otavi Mountain Land (Miller, 2008). The Tschudi Formation is further subdivided into a lower pelitic and an upper psammitic unit (Miller, 2008). The lower Tschudi Formation comprises dark grey shales, slates, feldspathic greywackes, marls, quartzite and interbedded, 2 m thick, conglomerate layers. The upper Tschudi Formation, by contrast, consists of immature sedimentary rocks. The typical Kombat Formation area is the Otavi Valley Syncline (Figure 2.5), where it overlies the Tschudi Formation (Kamona and Günzel, 2007). In this area, the Kombat Formation consists of the tightly folded, dark grey phyllite and silty to sandy phyllite, often pyrrhotitic or pyritic (Miller, 2008).

Deformation and Metamorphism

The Otavi Mountain Land is dominated by the Otavi Group carbonates in a foreland fold-and-thrust belt setting of the Damara Belt. The Otavi Mountain Land is located at the transition between the highly deformed and metamorphosed central part of the Damara Belt and the unmetamorphosed, less deformed molasse succession of the Owambo Basin in the north (Miller, 2008, 1983; Frimmel *et al.*, 2004) (Figure 2.2b). The Otavi Mountain Land underwent three regional deformation events during the pan-African Orogeny (Miller, 1983). The first deformational event, D_1 occurred at approximately 650 Ma marking the closure of the Proto-Atlantic with the formation of recumbent southeasterly vergent folds in the Kaoko Belt (Miller, 1983; Deane, 1995) and was responsible for the east-west shortening (Laukamp, 2006). As a consequence, highly deformed high grade rocks were thrust over the platform carbonates on the southwestern margin of the Congo Craton. The effects of this deformation are minimal in the Otavi Mountain Land (Deane, 1995). Lehmann *et al.* (2016) interpreted that D_1 north-south shortening event in the northern Damara Belt records an early stage of convergence between the Congo and Kalahari Cratons. According to Lehmann *et al.* (2016), the early convergence between the Congo and Kalahari Cratons occurred at ~590 Ma.

Previously, the second deformation event, D_2 was recorded at approximately 537 to 550 Ma (Deane, 1995), however recent work by Lehmann *et al.* (2016) demonstrated a new zircon age of 512 ±7 Ma for the D_2 activity, which appear to contradict the age of D_3, which is approximated at 530 Ma to 460 Ma as reported by Deane (1995). D_2 is the main deformational event in the Otavi Mountain Land (Deane, 1995; Laukamp, 2006; Miller, 2008). This was marked by the formation of the Damara Belt, which resulted in a north-south shortening of the Otavi Mountain Land (Miller, 1983; Deane 1995, Laukamp, 2006). Consequently, the northwest vergent folds and thrusts were developed and eventually formed the outstanding Otavi Valley Syncline (Figure 2.6) (Deane, 1995). The D_2 event was accompanied by a metamorphic event, M_1 (Kröner and Clauer, 1979; Deane, 1995) ranging from lower greenschist facies (Miller, 1983; Miller, 2008; Pirajno and Joubert, 1993; Deane, 1995) near the Kombat area (Figure 2.6) to zeolite and prehnite-pumpellyite facies for the Mulden Group rocks (Kröner and Clauer, 1979; Pirajno and Joubert, 1993). The metamorphic gradient in the Otavi Mountain Land diminishes northwards, coinciding with decreasing deformation (Smit, 1959; Söhnge, 1964; Miller, 1983; Pirajno and Joubert, 1993). The ensuing closure of the Khomas Sea with the subduction of the Kalahari Craton under the Sao-Francisco-Congo Craton caused the uplift and karstification of the Otavi Group rocks (Miller, 1983; Miller, 2008). The dominating structures associated with D_2 include the east-trending large folds, which are open to tight and upright to northward vergent in the southern Otavi Mountain Land (Coward, 1981). The distribution and the northward movement of the metalliferous hydrothermal fluids were facilitated by pre- to syn-D_2 structures as conduits. Additional remobilization of former base metal sulphide bodies into D_2-structures is evident from the Kombat (Innes and Chaplin, 1986; Deane, 1995) and Tsumeb (Hughes, 1979) deposits. The D_3 event formed large scale faults and dyke swarms attributed to the Paleozoic uplift and extension (Söhnge, 1957).

In general, the Otavi Mountain Land structures are oriented more or less east-west (Miller, 2008). This orientation is influenced by basement inliers (Miller, 1983). Folding in the Otavi Mountain Land is predominantly east-west striking and is associated with northward overturning of the strata (Smit, 1959; Pirajno and Joubert, 1993; Laukamp, 2006). According to Pirajno and Joubert (1993), a number of northward-trending faults and fractures, which are characteristic of the Damara Orogen occur throughout the Otavi Mountain Land (Figure 2.6). During the higher temperature

D_2 regime, Swakop Group rocks were thrust northwards onto lower temperature Mulden schists in the western Otavi Mountain Land (Miller, 1983). The F_2 folds along the southern margin were warped into doubly plunging anticlines and synclines during the late stages of east-west compression that ended D_2 in both the Kaoko Belt and the Northern Platform of the Damara Belt (Deane, 1995; Miller, 2008).

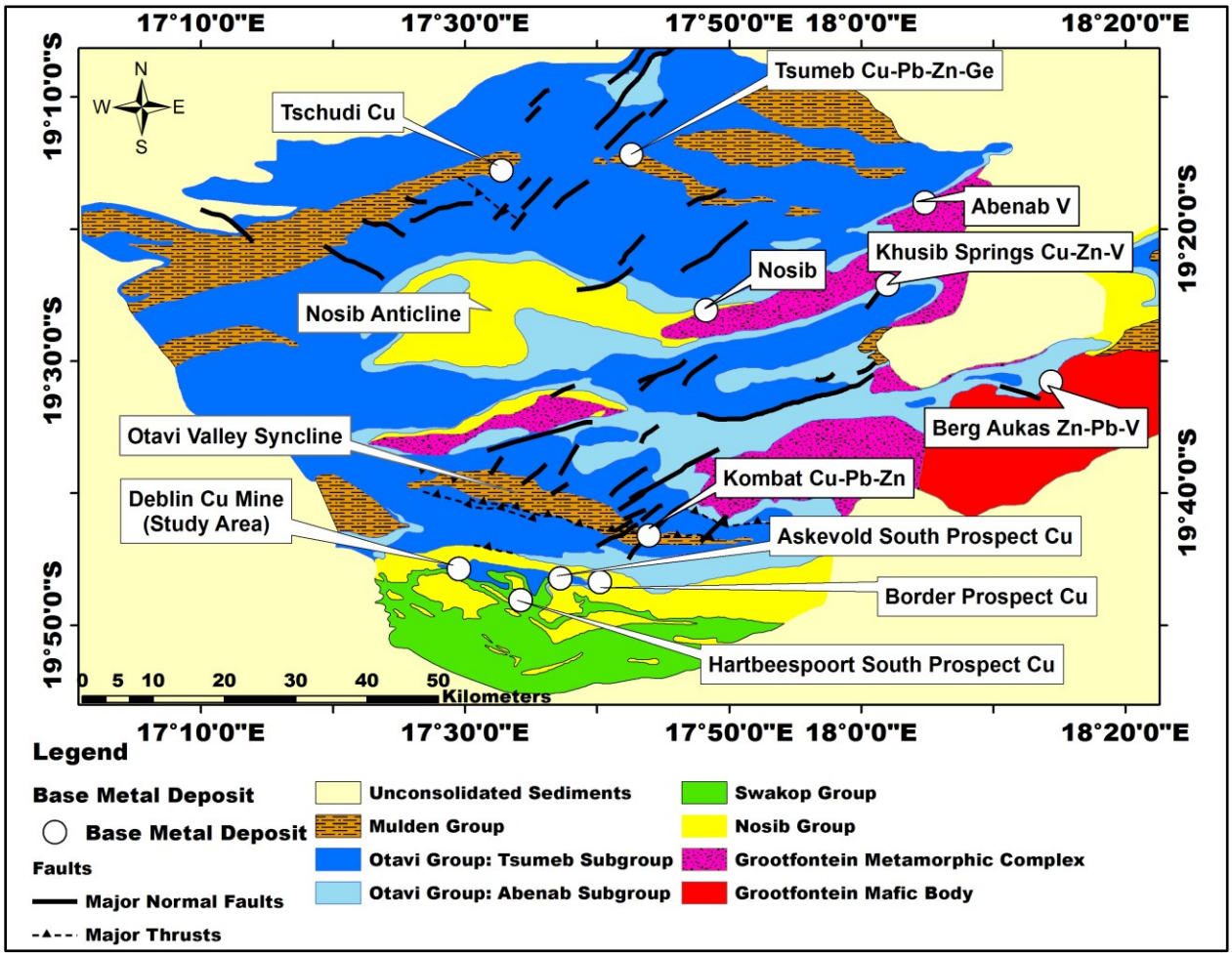


Figure 2.6 Geological map showing the regional architecture of the Otavi Mountain Land metallogenic province, the main base metal deposits (Mississippi Valley Type), the Deblin Cu Mine and other Cu prospects in the southern Otavi Mountain Land (modified after Kamona and Günzel, 2007 and map of 1:250 000 of the Geological Survey of Namibia).

Base Metal Mineralization

Base metal mineralization in the Otavi Mountain Land occurs throughout the Neoproterozoic Damara Supergroup units, including the basal Nosib Group, the middle Otavi Group and the uppermost Mulden Group (Emslie, 1979; Söhnge, 1957; Kamona and Günzel, 2007). Additionally, different styles of mineralization affected the Neoproterozoic rocks in the Otavi Mountain Land at various tectonic stages (Deane, 1995; Laukamp, 2004; Laukamp, 2006; Kamona and Günzel, 2007). The mineralization of key deposits in the Otavi Mountain Land was described in detail by Innes and Chaplin (1986), Lombaard et al. (1986), Misiewicz (1988), Frimmel et al. (1996) and Hughes (1987). Various genetic models have been proposed based on the nature of ore-forming solutions, metal sources and timing of mineralization to explain the origin of the hypogene sulphide ores in the Otavi Mountain Land (Hughes, 1987; Misiewicz, 1988; Pirajno and Joubert, 1993; Kamona and Günzel, 2007). Over 600 mineral occurrences of Cu-Pb-Zn-Ag sulphide mineralization and V-rich non-sulphide mineralization have been reported in the Otavi Mountain Land (Söhnge, 1957; Cairncross, 1997; Boni *et al.*, 2007). Most of the mineral occurrences are located in the Huttenberg Formation (52% of the occurrences) and the Gauss Formation (17% of the occurrences) (Table 2.1) of the Tsumeb and Abenab subgroups, respectively (Kamona and Günzel, 2007). The deposits that have proven to be economically viable with ore tonnage in the range of 0.5 to 30 Mt are all hosted in carbonate formations of the Otavi Group, chiefly, the Gauss (Berg Aukas Zn-Pb-V), the Auros (Abenab West Pb-Zn-V), the Maieberg (Abenab V and Khusib Springs Cu-Pb-Zn) and the Huttenberg (Tsumeb Pb-Cu-Zn-(Ge), Kombat (Cu-Pb-Zn) Formations (Kamona and Günzel, 2007) (Table 2.1). The distribution of these hydrothermal deposits in the Otavi Mountain Land is shown in Figure 2.5 and Figure 2.6. These deposits are good examples of the Mississippi Valley-Type (MVT) of mineralization.

a) Mineralization in the Nosib Group

The Nosib Group contains substantial occurrences of small, low-grade Cu deposits in conglomerate, sandstone, quartzite, tuff and agglomerate (Kamona and Günzel, 2007; Petzel, 1991). At the Deblin Copper Mine and Askevold South deposit (Figure 2.6), Cu is the major base metal with minor Au, whereas the Nosib Prospect (Figure 2.6) contains Cu and Ag with subordinate Pb and V mineralization.

b) Mineralization in the Otavi Group (Carbonate rock-hosted)

The carbonate-hosted mineral deposits in the Otavi Mountain Land represent multistage processes of ore genesis (Lombaard et al., 1986; Pirajno and Joubert, 1993; Frimmel et al., 1996). Pirajno and Joubert (1993) recognized at least three episodes. The first is marked by the low-temperature, high-salinity, Cu-poor, basinal fluids, which formed MVT deposits. The second episode is characterized by higher temperature and higher salinity, Cu-rich fluids (Pirajno and Joubert, 1993). The last stage is associated with recent weathering processes which locally caused the remobilization of the ores formed during the first two stages. Also, the last stage introduced non-sulphide Pb-Zn ores and V-ores in the Otavi Mountain Land (Boni *et al.*, 2007). The formation of these carbonate rock-hosted base metal deposits was thought to be controlled by karst structures, faults and shear zones as well as joints and fractures (Miller, 2008; Pirajno and Joubert, 1993; Laukamp, 2006; Laukamp, 2004; Lombaard *et al.*, 1986; Innes and Chaplin, 1986; Misiewicz, 1988; Deane, 1995).

The distribution of carbonate-hosted hydrothermal mineralization in the Otavi Mountain Land led to the identification of two broad types, namely Tsumeb type and Berg Aukas type (Lombaard et al., 1986; Innes and Chaplin, 1986; Hughes, 1987; Misiewicz, 1988; Pirajno and Joubert, 1993) (Table 2.2). The two deposit types were characterized on the basis of stratigraphic position (Table 2.1), mineralogy, metal association, lead and sulphur isotope characteristics and fluid inclusion data (Lombaard et al., 1986; Innes and Chaplin; Hughes, 1987; Misiewicz, 1988; Pirajno and Joubert, 1993) such that the Berg Aukas type are Pb-Zn-V ores derived from low temperature and high salinity basinal fluids whereas Tsumeb ores are complex and Cu-bearing and were formed from high temperature low salinity fluids.

a) Mineralization in the Mulden Group

The Tschudi deposit is located in the northwest part of the Otavi Mountain Land (Figure 2.6). The Tschudi deposit is the only known economic deposit hosted entirely in siliciclastic rocks, particularly in the medium-to fine-grained feldspathic arenites and sub-greywackes of the Mulden Group (Table 2.1). This deposit shows characteristics of MVT mineralization (Emslie, 1979; McKinney et al., 2009). The Tschudi deposit is likely to have formed from metal-bearing hydrothermal fluids that ascended through karst cavities in the Otavi Group carbonates and spread

within weakly cemented sandstone in the Mulden Group (McKinney et al, 2009). The Tschudi deposit is primarily a Cu-Ag deposit, with no significant Pb or Zn (McKinney et al., 2009). In addition, since the recorded Pb and Zn concentrations have values not more than 0.1%, the main economic metal target is solely Cu. This deposit is currently owned by Weatherly International Plc and was put into open pit operation in 2014.

Table 2.2 A summary of different characteristics of the Tsumeb-type and Berg Aukas-type mineralization (after Lombaard et al., 1986; Innes and Chaplin, 1986; Hughes, 1987; Misiewicz, 1988; Pirajno and Joubert 1993; Laukamp, 2006; Kamona and Günzel, 2007).

Tsumeb-type mineralization	**Berg Aukas-type mineralization**
Consists of complex sulphide ores containing Cu, Pb, Zn, Ag, As, Ge, Cd and Ga.	Consists of Pb-Zn and V sulphide ores and little or no Cu.
The known deposits are: Tsumeb Pb-Cu-Zn-(Ge) ; Kombat Cu-Pb-(Zn); Khusib Springs Cu-Zn-V	The known deposits are: Berg Aukas Zn-Pb-V deposits and Abenab West Pb-Zn-V.
Ore bodies are not stratabound and are confined to the upper part of the Tsumeb Subgroup. The ore bodies formed by copper bearing metamorphic fluids during the D_2 age event (syntectonic) and extended during D_3. Tsumeb type may contain remobilized material from Berg Aukas type.	Member of Mississippi Valley type deposits of pre-D_2 and is confined to the Abenab Subgroup. The main fluid source was basinal brines.
The mineralization is largely hosted in pipes that developed at cross junctions of different tectonic trends	The mineralization is largely hosted in carbonate breccias.
Tsumeb type is characterised by high temperature conditions and low salinity fluids.	Berg Aukas type is characterized by low temperature and high salinity basinal fluids

2.1.3 Summary

The Otavi Mountain Land is located on the northeastern margin of the Damara Belt. The Otavi Mountain Land contains platform carbonates, which were deposited during the advanced stages of continental rifting of the Damara belt evolution (Miller, 2008; Frimmel and Miller, 2009). The stratigraphy of the Otavi Mountain Land is made up of the Damara Sequence namely the Nosib Group, the Otavi Group and the Mulden Group (Söhnge, 1957; Hedberg, 1979; Kamona and Günzel, 2007; Miller, 2008). The Otavi Group is further divided into the Abenab and Tsumeb Subgroups and its platform carbonate deposition began after 746 Ma and ended between 630 and 550 Ma (Kamona and Günzel, 2007). The carbonate successions of the Abenab and Tsumeb

Subgroups consist of basal glacial deposits, namely the Sturtian Chuos Formation and Marinoan Ghaub Formation, respectively (Halverson *et al.*, 2005; Halverson *et al.*, 2007; Kamona and Günzel, 2007). The Otavi Group constitutes a large record for the Neoproterozoic for it preserves a complete carbonate record from the end of Sturtian glaciation to the middle of Ediacaran Period (Halverson *et al.*, 2007).

Base metal mineralization occurs in all the three groups (Kamona and Günzel, 2007). The Otavi Group is composed largely of carbonates and records several base metal deposits (Kamona and Günzel, 2007; Miller, 2008). The large base metal deposits such as the Berg Aukas and Tsumeb deposits hosted in the Otavi Group carbonates are good examples of the MVT-type of mineralization. The timing of MVT-type Pb-Zn deposits in the Otavi Group is not well constrained, however, based on radiometric age data the Cu-rich polymetallic Tsumeb-type deposits in the Otavi Mountain Land appears to have been concentrated after the peak of the Damara orogeny at around 530 Ma, which coincides with the 535 Ma peak of M_2 regional metamorphism (Kamona and Günzel, 2007; Miller, 2008).

Chapter 3

Local Geology

3.1 Introduction

The study area is located on the westernmost portion of the Askevold Trend (Figure 3.1) on the northeastern margin of the Damara Belt within the Northern Zone of Corner (2008) and Miller (2008). The study area covers a surface area of about 2 km^2. This area is characterized by thorn bushes, thick sand cover and has limited outcrop exposure. The thick extensive Cenozoic Kalahari Supergroup sand cover in the study area and limited surface geological data precluded researchers from fully understanding the stratigraphy and petrology.

For example, Adamson (1976), suggested that in the Deblin Copper Mine area, the Askevold Formation metavolcanic rocks are overlain by Gauss Formation dolomite units. However, on the regional geological map (Figure 3.1), the dolomite units in the Deblin Copper Mine area are shown to belong to both the Askevold and Chuos Formations, and the Gauss Formation is absent. Thus, it is not clear which formations of the Abenab Subgroup are present in the study area.

Although early workers (Söhnge, 1957; Kamona and Günzel, 2007; Miller, 2008) suggested that the Ombombo Subgroup facies (Figure 3.1) are absent in the southern Otavi Mountain Land and present only in the Kaokoveld, west of the Otavi Mountainland, local geologists (from the exploration companies in the Otavi Mountain Land) speculated that the carbonate rocks in the Deblin Copper Mine area belong to the Ombombo Subgroup. Therefore, a better understanding of the stratigraphic elements, including both exposed and concealed lithologies present in this area, developed through geological mapping, borehole lithological logging and petrography, could help improve the existing interpretation of the local geology.

3.2 Previous Work

Previous workers in the southern Otavi Mountain Land, have identified the Askevold Trend, in the Kombat South area and described the occurrence of base metal mineralization (Smit, 1959; Adamson, 1976; Petzel, 1991; Golden Deeps Limited, 2012, 2013). The Askevold Trend is a 30

km long east-west trending series of copper occurrences and geochemical anomalies (Golden Deeps Limited, 2012). From east to west, these copper prospects are: Askevold South Cu-Ba prospect, Border Post (Redrob) Cu prospect, and Neuwerk Cu prospect (Deblin Cu Mine) (Figure 3.1). These copper occurrences are thought to be associated with the rift-related mafic volcanic rocks of the Askevold Formation (Smit, 1959; Adamson, 1976; Petzel, 1991; Laukamp, 2006; Kamona and Günzel, 2007).

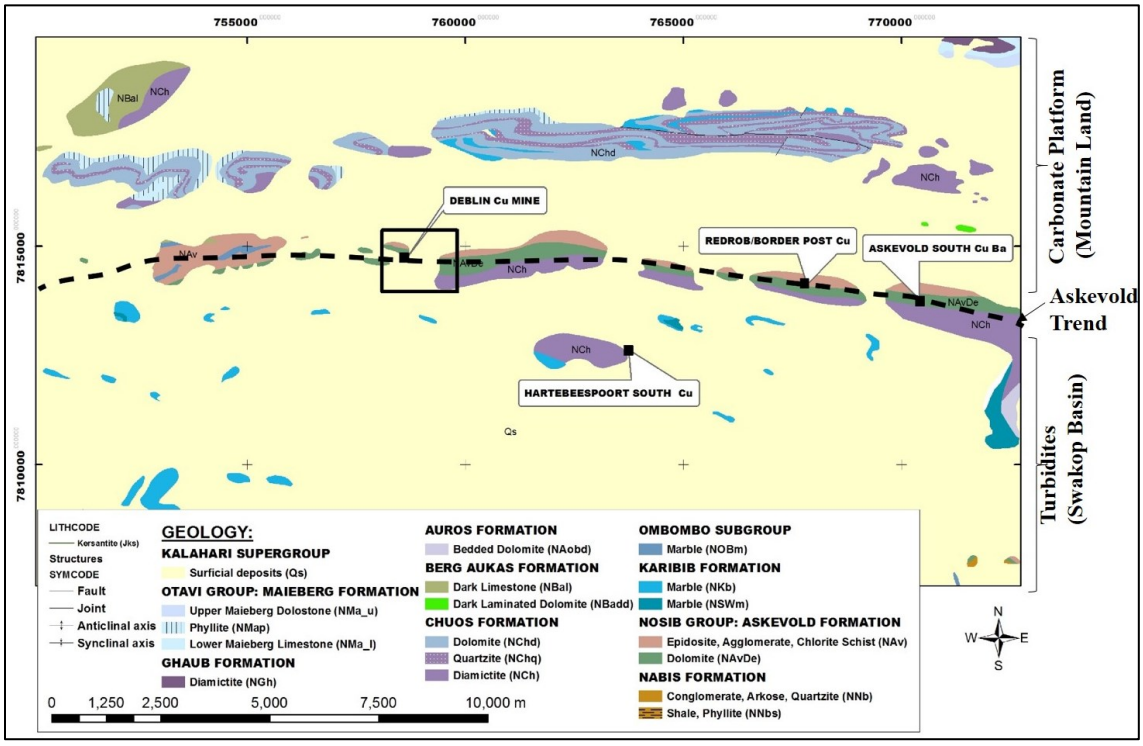


Figure 3.1 Regional geological map of the southern Otavi Mountain Land with the Askevold Trend defined by Cu prospects closely related to the Askevold Formation volcanics. Taken from the 1: 250,000 of the Geological Survey of Namibia (2008). The black dotted line indicates the Askevold Trend. The black box shows the local study area (Figure 3.4).

The occurrence of the volcanic-hosted base metal mineralization in the southern Otavi Mountain Land attracted a number of researchers and mineral prospectors. The local stratigraphy and geology of the southern Otavi Mountain Land was described in detail by Stahl (as cited in Schaum, 1960) when he advanced on the local stratigraphic work of Wagner (as cited in Smit, 1959) who investigated the area in 1910. Stahl (as cited in Schaum, 1960) described the local stratigraphy in this area and defined the diamictite unit as a conglomerate, which he grouped together with the

grits and quartzite of the Otavi Group. However, Schaum (1960) challenged the description of the conglomerate by Stahl (as cited in Schaum, 1960) and argued that the unit observed is instead a tillite. During his mapping work, Schaum (1960) suggested that there are two tillite (diamictite) horizons in this area, which he assigned to the Otavi Group. Today, these glacial deposits are referred to as the Chuos and Ghaub Formations (Figure 3.2). In addition, Stahl (as cited in Smit, 1959) established that the metamorphic grade across this area decreases from south to north.

Otavi Mountain Land Stratigraphy				
Group		**Formation**	**Lithology**	**Deposit**
MULDEN		Kombat	**Slate, Phyllite, Sandstone**	
		Tschudi	**Arenite, Subgreywacke, Conglomerate**	**Tschudi Cu-(Ag)**
OTAVI	**Tsumeb Subgroup**	Huttenberg	**Dolostone, Chert, Dolostone** **Shale, Stromatolite, Chert, Breccia**	**Kombat Cu-Pb-(Zn)** **Tsumeb Pb-Cu-Zn-(Ge)**
		Elandshoek	**Dolostone, Chert Breccia, Dolostone**	
		Maieberg	**Dolostone, Limestone, Dolostone**	**Abenab V, Khusib Springs Cu-Pb-Zn**
		Ghaub	**Diamictite**	
	Abenab Subgroup	Auros	**Chert, limestone**	**Abenab West Pb-Zn-V**
		Gauss	**Breccia** **Dolostone, Chert**	**Berg Aukas Zn-Pb-V**
		Berg Aukas	**Dolostone** **Chert**	
		Chuos	**Diamictite**	
NOSIB		Askevold	**Tuff, Quartzite**	**Nosib Cu, Askevold Cu**
		Nabis	**Quartzite, Sandstone, Conglomerate**	

Figure 3.2 Stratigraphic column for the accepted Otavi Mountain Land stratigraphy with mineral deposits of Kamona and Günzel (2007).

Smit (1959) mapped the southern Otavi Mountain Land on a regional scale and produced new information on the stratigraphy and structural framework of the area. He recognized the northwest and northeast trending faults; with or without noticeable displacements. Furthermore, Smit (1959) described in detail the epidotised basic volcanic unit of the Askevold Formation (Figure 3.2). The epidotised basic volcanic unit is referred to as an epidosite in the recent literature. Smit (as cited in Miller, 2008) initially referred to the Askevold Formation as the Kombat Suid Formation. Adamson (1976) investigated the geology of the Deblin Copper Mine area and described the local

petrology and the mineralization. According to Adamson (1976), the stratigraphy of the Deblin Copper Mine area comprises the older Askevold Formation of the Nosib Group overlain by the younger Gauss Formation of the Abenab Subgroup of the Otavi Group.

The lithologies include the hydrothermally altered, Askevold Formation schist unit with minor marble intercalations and the upper dolomite unit of the Abenab Subgroup. Adamson (1976) stated that the host rock of the Deblin Copper Mine is a sericitized and chloritized basic to acidic volcanic pyroclastic rock of the Askevold Formation. Later, Liedtke (1976) investigated the extent of the Askevold Formation volcanic rocks further east of the Deblin Copper Mine area to establish a new general stratigraphy and to assess the mineral potential of the volcanics. The petrology of the volcanic rocks of the Askevold Formation in this area has been subsequently studied in detail by Söhnge (1957), Smit (1959), Adamson (1976), Liedtke (1976) and Miller (2008). The Askevold Formation is understood to be composed of the green epidotised basic lava (epidosite) and dark greyish green sericite-chlorite schist, tuff (leucitite), schistose pyroclastic rocks and the agglomerate (Söhnge, 1957; Smit, 1959; Schaum, 1960; Adamson, 1976; Miller, 2008). The schistose rocks contain mainly various angular to rounded lithic fragments of quartzite as well as minerals including quartz and dolomite, with minor epidote, chlorite and amphibole (Smit, 1959; Miller, 2008).

3.3 Current Work

This chapter revises and updates the stratigraphy, and the petrology of the Deblin Copper Mine area using the most recently collected geological data and data compiled from the literature. This chapter focuses on the distribution and description of the local stratigraphy and geological features together with, the relationship between the copper mineralization and the host rocks. In addition, the chapter presents new petrographic data of the rocks from the study area. The new thin section petrographic data are used to supplement the lithological logging and geological mapping descriptions, and to elucidate the microstructures that are invisible at outcrop scale. Fieldwork was undertaken in the area around the Deblin Copper Mine and included geological mapping, sample collection, and drill core lithological logging. Subsequently, laboratory work primarily involving microscopy was conducted on the collected samples.

Poor rock exposure within the study area made it difficult to delineate the contacts between various different rock units. The study area comprises 11 mappable rock units at the scale of 1:2500. In addition, drilling revealed the existence of rock types that are not exposed in the area. For this reason, not all the rock types on the geological map (Figure 3.3) appear in the drill cores (Figure 3.4-3.6). The rock types in the study area correspond to traditional formations of the Otavi Mountain Land geology and have been documented here in detail. The metapelites and metabasalts from the study area have experienced greenschist facies metamorphism. Despite deformation and metamorphism, in most places, preserved primary structures, textures, composition and alteration allowed the identification of the carbonate rocks. As a result, the prefix "meta", which should precede the name of the carbonate rocks, is omitted for clarity. In the thin sections, the term carbonate has been used to represent both calcite and dolomite minerals.

Hydrothermal alteration is the most common characteristic feature in all the rock types from the study area. Carbonatization is the leading alteration type and is distinguished by late carbonate growths that overprint the primary minerals. Depictions in this chapter are later supplemented by mineralogical studies, whole rock geochemical and sulphur isotope analyses, and geophysical interpretations in the subsequent chapters to interpret the mineralization style of the Deblin Copper Mine area.

3.3.1 Methodology

a) Geological Mapping

Surface geological mapping was conducted over an area of about 1800 m x 1300 m during the first phase (27 May 2015 to 15 June 2015) of field geological data collection. Mapping was limited to outcrops and these cover no more than approximately 30% of the study area. Geological mapping was conducted to acquire all data exposed on the surface, including all petrological features, structural features and their orientations, and copper occurrences. These basic data were later integrated with magnetic data to establish the structural framework of this area. Geological mapping was conducted via traverses perpendicular to the strike of the rocks. In addition, rock samples were collected during mapping.

b) Drill Core Lithological Logging

Drill core lithological logging was undertaken during the first field session in the core yard of Sabre Resources Namibia. A total of three drill cores were logged for detailed description of the intersected lithologies including their mineralogy and other macroscopic petrographic features. In addition, lithological logging was undertaken to determine the location of the copper sulphide mineralization in the stratigraphy and ultimately guide the sampling process for geochemical analysis and petrographic studies. The logging techniques include the description of the lithological variations relative to depth, hydrothermal alterations, degree of weathering, mineralization and structures. The names of the boreholes are: DBDD0001, DBDD0002 and DBDD0003. The names are given by Sabre Resources Namibia and the abbreviation DBDD stands for Deblin Diamond Drillhole. It should be noted that, however, the first two boreholes, DBDD0001 and DBDD0002, are collared in the same place but drilled at different angles. DBDD0001 was drilled at an inclination of -72° with 0° azimuth and a maximum depth of 170.50 m, whereas DBDD0002 was drilled at an inclination of -60° with 0° azimuth and a maximum depth of 120.00 m. DBDD0003, located 947 m west from the first two boreholes was drilled at an inclination of -55° with 354.5° azimuth and a maximum depth of 90.60 m.

c) Petrography

A total of 75 fresh and least weathered representative samples were collected from the outcrops (12 samples) and drill cores (63 samples) during field work. These samples were selected for the petrographic studies. Subsequently, 115 polished thin sections were prepared and examined using petrological microscopes with both reflected and transmitted light at the Petrology Laboratory in the School of Geosciences, University of the Witwatersrand.

3.3.2 Local Stratigraphy

The stratigraphic succession of the study area is located close to the transition zone from Otavi Group facies to Swakop Group facies (Figure 3.1). These facies are underlain by volcanic rocks and clastic sediments of the Nosib Group (Figure 3.3). The local stratigraphy of the study area is subdivided into the older Askevold Formation of the Nosib Group and the younger Chuos Formation of the Otavi Group based on the petrological features (Figure 3.3). The Askevold Formation consists largely of schistose mafic and felsic metavolcanic rocks, whereas the Chuos Formation (Abenab Subgroup) is characterized by pyritic dolomite, grey limestone, banded

limestone, phyllite, silicified dolomite, dolomite breccia and diamictite as intercalations in association (Figure 3.3). The revised stratigraphy of the area around the Deblin Copper Mine area was constructed through geological mapping, lithological logging and petrographic descriptions.

The local stratigraphy from the new local geological map (Figure 3.3) was used to modify the regional geological map (Figure 3.4) in the area around the Deblin Copper Mine. On the regional geological map, the carbonates in the area around the Deblin Mine area were described as part of the Devon Carbonate Member of the Askevold Formation. However, detailed local geological mapping from this study identified more units such as the dolomite, limestone, phyllite and diamictite of the Chuos Formation (basal Otavi Group), which were previously collectively described as dolomite of the Devon Carbonate Member placed under the Askevold Formation of the Nosib Group.

Deblin Copper Mine Area				
Group		Formation	Lithology	Deposit
OTAVI	Abenab Subgroup	Chuos	Diamictite Dolomite Breccia Silicified Dolomite Phyllite Banded Limestone Grey Limestone Pyritic Dolomite	Deblin Cu
NOSIB		Askevold	Felsic Volcanic-Breccia Agglomerate Mafic Metavolcanic Chlorite-Schist Tuff	

Figure 3.3 Stratigraphic column for the study area and comparison with the accepted Otavi Mountain Land stratigraphy with mineral deposits of Kamona and Günzel (2007).

3.3.3 Petrographic Description of the Local Stratigraphy

The new geological map (Figure 3.4; Appendix F) of this area is dominated by carbonate rocks of the Abenab Subgroup (Chuos Formation) with minor metavolcanic rocks of the Askevold Formation. In addition to the lithologies displayed on the geological map, the lithologies that are not exposed in the study area are revealed by the drill holes (Figure 3.5) and their descriptions are given in Table 3.1-3.3. The dolomite in DBDD0001 is brecciated at different levels with depth and thus it appears to have more dolomite breccia zones than DBDD0002. This explains why the two closely collared drill holes show different rock types at the same depths (Figure 3.6). Drill core data were then combined with geological mapping data to determine the general geology and local stratigraphy of the study area. The sample localities are shown on the drill cores in Figure 3.7. The detailed descriptions of all the samples are given in Appendix A.

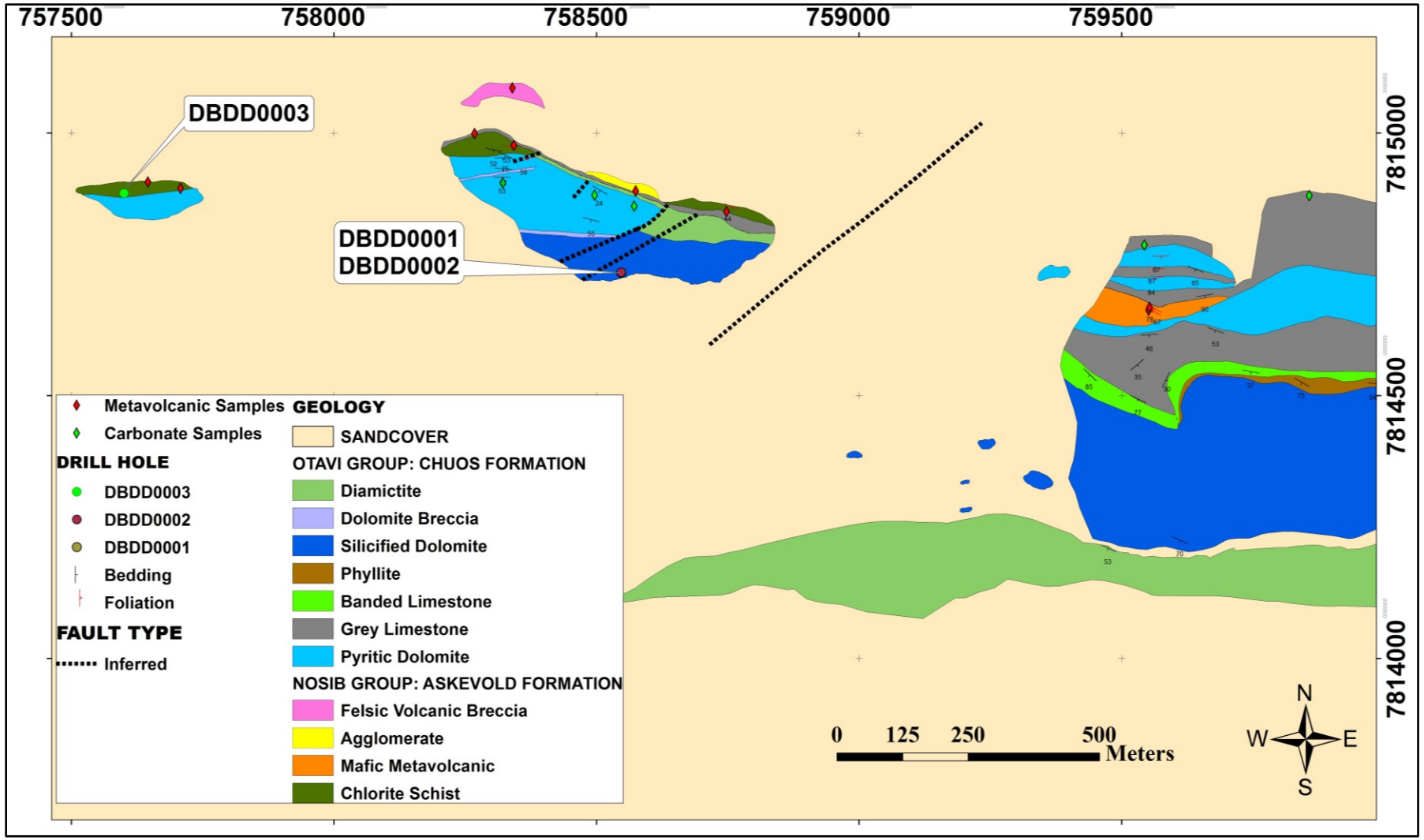


Figure 3.4 Detailed geological map of the area around the Deblin Copper Mine constructed at the scale of 1:2,500. In addition, the map shows the location of the twelve hand samples and three boreholes drilled in the study area. This geological map was constructed from the outcrop geology.

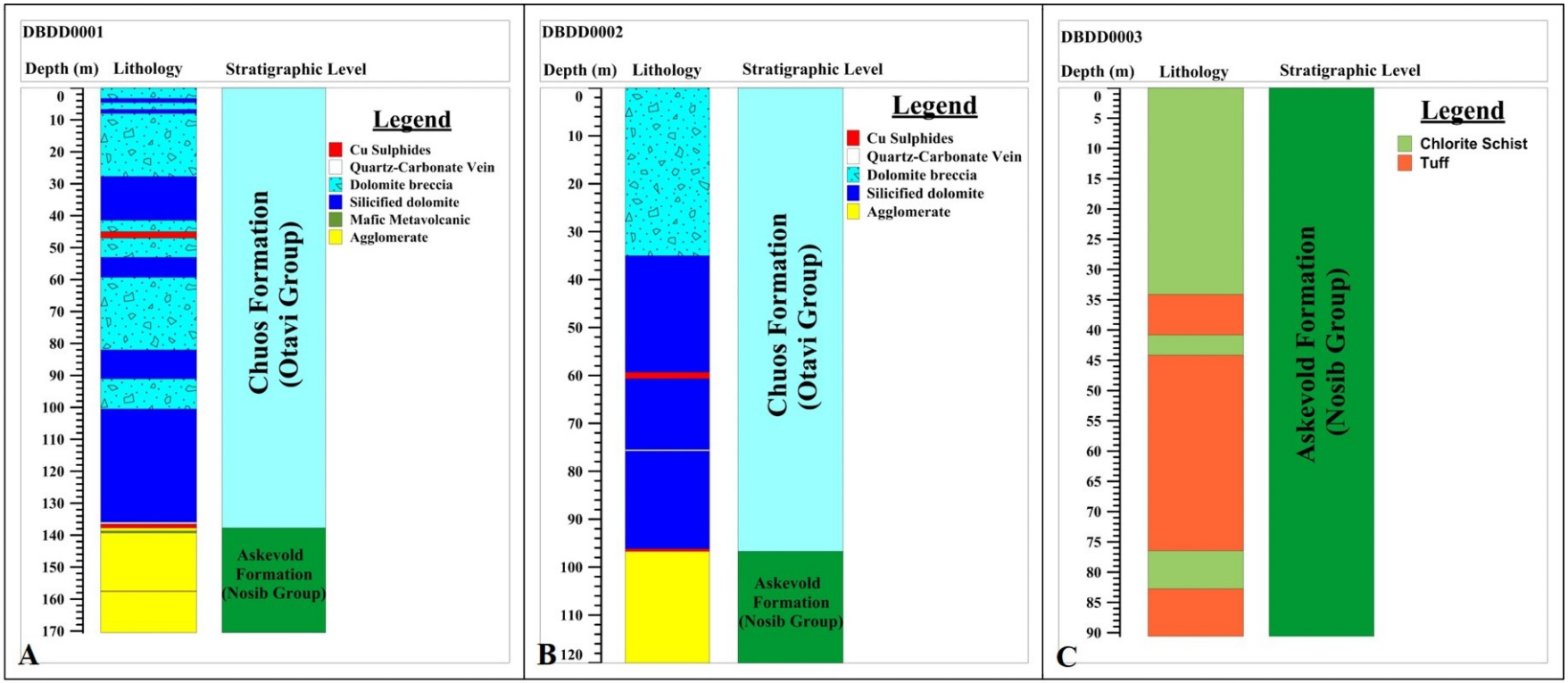


Figure 3.5 Lithological logs of the three boreholes from the Deblin Copper Mine area. A) DBDD0001 lithological log showing the succession of both the Nosib Group metavolcanic rocks and Otavi Group dolomites, and the location of the copper sulphide mineralization in the stratigraphy. Grid reference: 758547 mE, 7814734 mN. B) DBDD0002 lithological log showing the succession of both the Nosib Group metavolcanic rocks and Otavi Group dolomites, and the location of the copper sulphide mineralization in the stratigraphy. Grid reference: 758547 mE, 7814735 mN. C) DBDD0002 lithological log. This borehole intersected solely the Nosib Group metavolcanic rocks. Note the lack of a mineralized unit. Grid reference: 757600 mE, 7814885 mN.

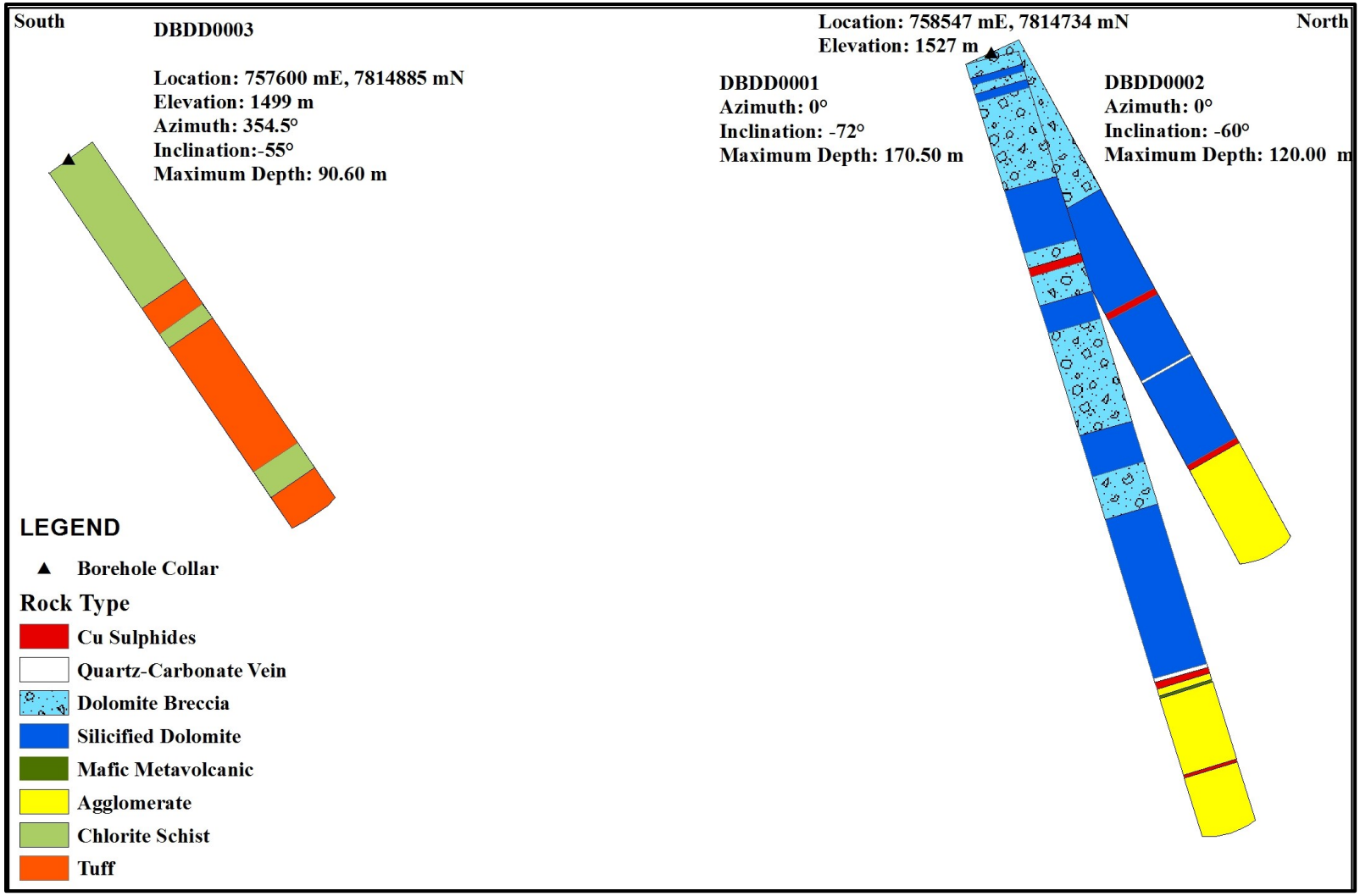


Figure 3.6 Cross-section of the three boreholes from the Deblin Copper Mine area showing their orientations. The drill holes were plotted with Leapfrog Geo 3.1 and digitized in ArcMap 10.2.2.

Table 3.1 Lithological log sheet of DBDD0001 with the detailed description of all the intersected units.

From (m)	To (m)	Lithology	Lithological Description	Colour	Texture	Weathering	Alteration Type	Sulphides	Structures
0.00	3.30	Dolomite breccia	Dolomite breccia with deformed stromatolites, oxidized calcite and quartz veins. In addition, the unit has a thick quartz-calcite vein with minor disseminations of pyrite grains between 3.14m and 3.21m depth.	Light grey	Fine-grained	Fresh	Carbonatization	Pyrite (2%)	Fractures
3.30	4.60	Silicified dolomite	Silicified dolomite with moderate thin quartz and calcite veins. Rare disseminations of pyrite are present throughout the unit.	Light grey	Fine-grained	Fresh	Silicification	Pyrite (3%)	Fractures
4.60	6.70	Dolomite breccia	Dolomite breccia with rare, thin quartz-calcite veins.	Light grey	Fine-grained	Fresh	Silicification		Fractures
6.70	8.03	Silicified dolomite	Silicified dolomite with minor calcite veins and fractures with oxidized surfaces. Minor malachite and pyrite occur within the rocks matrix.	Light grey	Fine-grained	Fresh	Silicification	Pyrite (3%)	Fractures
8.03	27.70	Dolomite breccia	Dolomite breccia with clasts size ranging from 0.5 cm to 4 cm, frequent quartz-calcite veins. The unit consists of stromatolites. Ubiquitous cross cutting carbonate veins occur between 14 m to 15 m depth. The fractures are filled with calcite linings. The unit records minor amounts of pyrite.	Light grey	Fine-grained	Fresh	Silicification	Pyrite (2%)	Fractures
27.70	41.47	Silicified dolomite	Silicified dolomite with various calcite veins and fractures filled with calcite. A 4 cm thick calcite vein with pyrite grains occurs at 31.91 m depth. In addition, there are minor grains of pyrite within the matrix.	Light grey	Fine-grained	Fresh	Silicification	Pyrite (3%)	Fractures
41.47	45.00	Dolomite breccia	Dolomite breccia with various fractures with oxidized surfaces.	Light grey	Fine-grained	Fresh	Silicification		Fractures

45.00	47.00	Cu Sulphides	Frequent chalcopyrite and subordinate pyrite hosted in quartz and quartz-calcite veins.	Light grey	Fine-grained	Fresh	Silicification	Chalcopyrite (10%) Pyrite (2%)	Fractures
47.00	53.00	Dolomite breccia	Dolomite breccia with various fractures with oxidized surfaces.	Light grey	Fine-grained	Fresh	Silicification		Fractures
53.00	59.32	Silicified dolomite	Silicified dolomite with patches of fresh and oxidized, brown pyrite grains.	Light grey	Fine-grained	Fresh	Silicification	Pyrite (4%)	Fractures
59.32	82.00	Dolomite breccia	Dolomite breccia with disseminations of pyrite between 64.50 m and 67.50 m depths.	Light grey	Fine-grained	Fresh	Silicification	Pyrite (3%)	Fractures
82.00	91.08	Silicified dolomite	Silicified dolomite with greenish chloritized thin (<cm thick) layers and pyrite grains.	Light grey	Fine-grained	Fresh	Chloritization	Pyrite (2%)	Fractures
91.08	100.50	Dolomite breccia	Dolomite breccia with rare disseminations of pyrite.	Light grey	Fine-grained	Fresh	Silicification	Pyrite (2%)	Fractures
100.50	135.93	Silicified dolomite	Silicified dolomite with frequent stromatolites and ubiquitous thick calcite veins (4 cm thick) between 100.50 m and 103.50m depths. Calcite vugs occur within the fractures. Rare pyrite grains occur at 133.50 m depth.	Light grey	Fine-grained	Fresh	Silicification	Pyrite (2%)	Fractures
135.93	136.58	Quartz-Calcite Vein	Thick quartz-calcite vein. The vein has both calcite and dolomite carbonate minerals.	White	Coarse-grained	Fresh	Silicification	Pyrite (4%)	Fractures
136.58	137.73	Cu Sulphides	Numerous vein type mineralization with chalcopyrite in the silicified dolomite.	Brown	Fine-grained	Fresh		Chalcopyrite (5%)	
137.73	138.71	Agglomerate	Deformed agglomerate rich in chlorite with weakly developed foliation, sub-rounded pebbles and patches of euhedral pyrite grains.	Green		Fresh	Chloritization (70%) Carbonatization (30%)	Pyrite (10%)	Foliation and Veins
138.71	139.30	Mafic Metavolcanic	Greenish, fine grained layer of the metavolcanic enriched in micas and chlorite.	Green	Fine-grained	Fresh	Chloritization (60%) Carbonatization (40%)		Foliation

139.30	157.50	Agglomerate	Deformed agglomerate rich in chlorite with weakly developed foliation, sub-rounded pebble.	Green	Fine-grained	Fresh	Chloritization (70%) Carbonatization (30%)		Foliation and Veins
157.50	157.62	Cu Sulphides	Minor amounts of chalcopyrite hosted in quartz-calcite veins.	Green	Fine-grained	Fresh		Chalcopyrite (2%)	
157.62	170.50	Agglomerate	Deformed agglomerate with sub to rounded elongated volcanic clasts. The unit in enriched in chlorite rich and have ubiquitous quartz-calcite veins. Pebbles range from <1 cm to 5 cm in the elongated direction.	Green	Fine-grained	Fresh	Chloritization (70%) Carbonatization (30%)		Foliation and Veins
End of Hole									

Table 3.2 Lithological log sheet of DBDD0002 with the detailed description of all the intersected units.

From (m)	To (m)	Lithology	Lithological Description	Colour	Texture	Weathering	Alteration Type	Sulphides	Structures
0.00	35.00	Dolomite breccia	Dolomite breccia with deformed stromatolites, frequent calcite and minor quartz veins consisting of minor pyrite grains. Manganese oxide staining occurs on the surface of the fractures.	Light grey	Fine-grained	Fresh	Carbonatization	Pyrite (2%)	Fractures
35.00	59.34	Silicified dolomite	Silicified dolomite consisting of various calcite veins and frequent deformed stromatolites. The unit has minor zones affected by brecciation and fractured along the quartz-calcite veins. Cross cutting quartz-calcite veins contain pyrite at 37.89 m depth. Frequent pyrite disseminations occur in the rock matrix between 42.88 m and 45.12 m depths, and also from 45.12 m to 55.85 m depths.	Light Grey	Fine-grained	Fresh	Silicification	Pyrite (3%)	Fractures

59.34	60.68	Cu Sulphides	Frequent chalcopyrite and minor amounts of pyrite in quartz-calcite veins within the silicified dolomite.	Light Grey	Fine-grained	Fresh	Silicification	Chalcopyrite (25%) Pyrite (20%)	Fractures and Veins
60.68	75.47	Silicified dolomite	Deformed silicified dolomite dominated by calcite veins and disseminations of pyrite in the rock matrix.	Grey	Fine-grained	Fresh	Silicification	Pyrite (5%)	Fractures
75.47	75.75	Quartz-Calcite Vein	Thick quartz-calcite vein. The vein has both calcite and dolomite carbonate minerals.	White	Coarse-grained	Fresh			Veins
75.75	96.18	Silicified dolomite	Deformed silicified dolomite with pyrite hosted in calcite veins aligned along the drill core and cut across bedding in some places.	Grey	Fine-grained	Fresh	Silicification	Pyrite (10%)	
96.18	96.71	Cu Sulphides	A small layer of chalcopyrite and pyrite disseminations at the bottom of the silicified dolomite.	Brown	Fine-grained	Fresh		Chalcopyrite (20%) and Pyrite (10%)	
96.71	120.00	Agglomerate	Deformed agglomerate with frequent quartz-calcite veins and sub-rounded mafic clasts hosted in a chlorite rich, highly foliated matrix. Most quartz-calcite veins cross cut each other. Coarse grains of pyrite are evident in the top part of this unit.	Green	Fine-grained	Fresh	Chloritization (70%) Carbonatization (30%)	Pyrite (5%)	Fractures, Foliation and Veins
End of Hole									

Table 3.3 Lithological log sheet of DBDD0003 with the detailed description of all the intersected units.

From (m)	To (m)	Lithology	Lithological Description	Colour	Texture	Weathering	Alteration Type	Sulphides	Structures
0.00	34.12	Chlorite Schist	Fine-grained chlorite schist dominated by chlorite with minor micas and quartz. In addition, the unit has frequent quartz-calcite veins and a strong foliation. Some quartz-calcite veins are parallel to the foliation, whereas some cross cut the foliation. Malachite linings occur along foliation planes between 2.70 m and 3.73 m depth. In addition, rare fine-grained pyrite grains occur in quartz-calcite veins between 12.70 m and 13.30 m depth. In places, pyrite grains are oxidized to brown.	Green	Fine-grained	Saprock	Chloritization	Pyrite (2%)	Fractures and Foliation
34.12	40.80	Tuff	Fine-grained tuff composed of micas, chlorite and calcite. The unit has a strong foliation and frequent calcite and quartz-calcite veins. In some places the veins are oxidized to brown. At 40.07 m depth, calcite and quartz-calcite veins exhibit cross-cutting relations.	Dark grey	Fine-grained	Fresh	Carbonatization		Fractures and Foliation
40.80	44.15	Chlorite Schist	Chlorite schist with weak foliation cross cut by quartz veins.	Light green	Fine-grained	Fresh	Chloritization		Foliation
44.15	76.45	Tuff	Fine-grained tuff with dark grey, thin mafic foliated layers and frequent calcite and quartz-calcite veins.	Dark grey	Fine-grained	Fresh	Carbonatization		Foliation
76.45	82.75	Chlorite Schist	Chlorite schist with weak foliation and frequent quartz veins	Light green	Fine-grained	Fresh	Chloritization		Foliation

82.75	90.60	Tuff	Tuff with thin mafic foliated layers, frequent calcite veins and subordinate quartz veins. The quartz and calcite veins gives the unit a white spotty appearance	Grey	Fine-grained	Fresh	Carbonatization		Foliation
End of Hole									

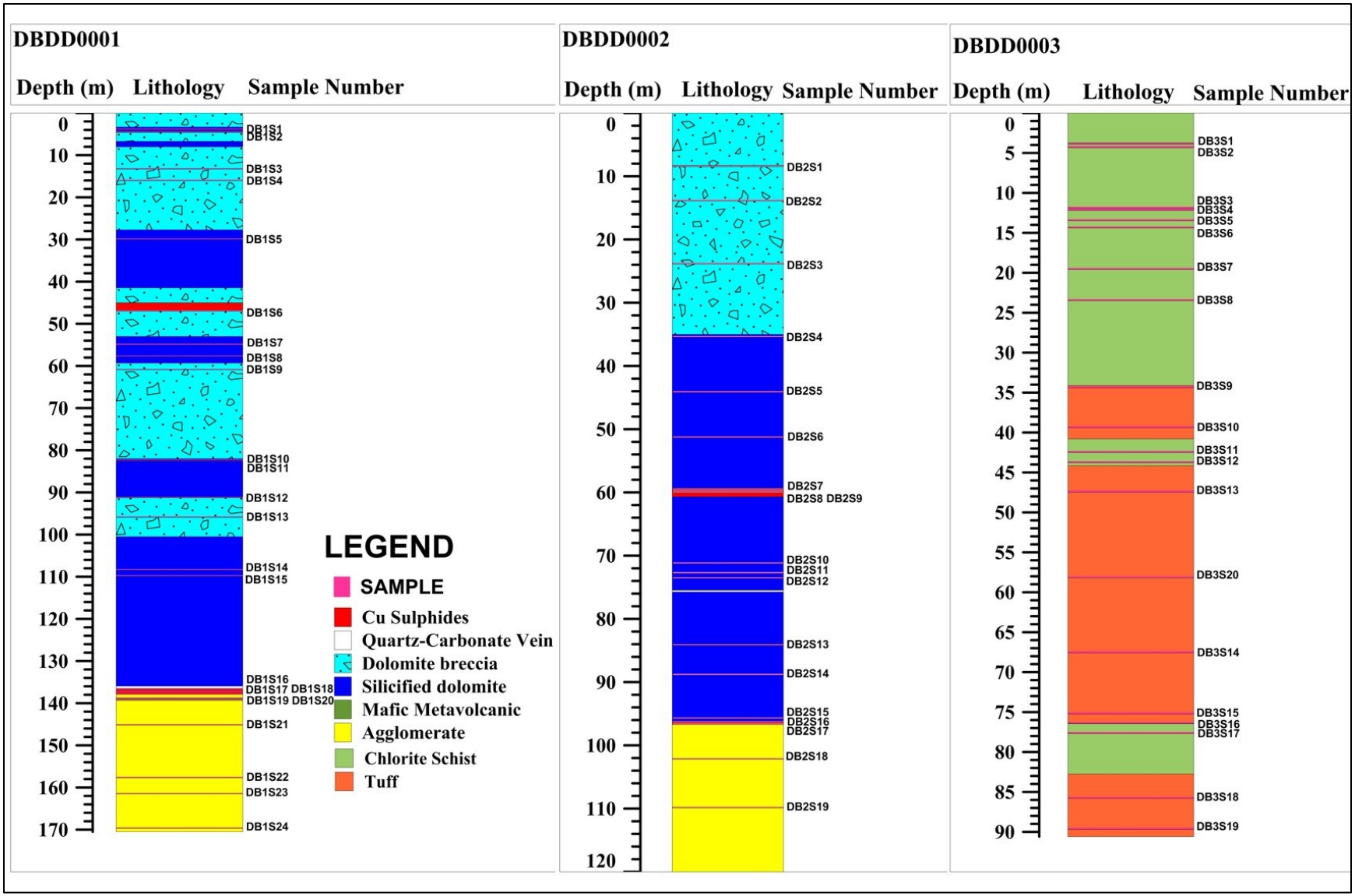


Figure 3.7 Lithological logs of the three boreholes (DBDD0001, DBDD0002 and DBDD0003) from the Deblin Copper Mine area showing sample localities.

Nosib Group

Askevold Formation

The Askevold Formation is a set of unexposed tuff, poorly exposed chlorite schist, mafic metavolcanic, agglomerate and felsic volcanic breccia. The descriptions of the Askevold Formation units are based on the well exposed, albeit limited outcrops, and drill cores.

Tuff

The tuff is not exposed in the study area and thus it does not appear on the detailed geological map. However, it was intersected in DBDD0003 at different intervals, alternating with the chlorite schist. These intervals are at the following depths: (i) 34.12 m to 40.80 m, (ii) 44.15 m to 76.45 m and (iii) 82.75 m to 90.60 m depths. Based on drill core observations, the tuff is dark grey, very fine-grained and highly foliated. This rock has frequent quartz-calcite veins (Figure 3.8). The tuff is fresh in hand specimen. The mineral composition is characterized by 35-40% sericite, 15-20% plagioclase, ~15% biotite, ~10% chlorite, 15-20 % carbonates (mainly calcite), ~7% quartz, and ~ 3% microcline. The opaque grains that are present as accessory minerals are primarily pyrite. Generally, different mineral grains of this rock vary in size and shape (Figure 3.9a-d). For instance, the grains of plagioclase are anhedral and are very fine-to fine-grained (0.088-0.25 mm) and in some samples the plagioclase grains are fine-to medium-grained (0.35-1.167 mm). The anhedral quartz grains are very fine-to fine-grained (0.088-0.162 mm) and medium-grained (0.117-0.35 mm) in some places. In addition, calcite is fine-to medium-grained (0.117-0.35 mm), although present as very fine-grains in places. Chlorite and the micas are very fine grained (0.041-0.098 mm).

In thin section, the tuff exhibits a well-developed widely spaced, sinuous foliation with poorly developed S-C fabrics defined by two foliations, labeled S and C (Figure 3.10a-b), both of which developed during a single deformation. The S-foliation is continuous and defined by mica foliation that curves towards an orientation parallel to the C-foliation. The C-foliation, in turn is a set of shear bands in the rock that develop parallel to the shear zone boundaries. This S-C fabric appear similar to extensional crenulation cleavages. The bedding (S_o) is not observed in this unit for it is completely obliterated by the primary foliation (S_1). The cleavage domains are made up chiefly of sericite (Figure 3.10). The microlithons are composed of quartz, carbonates and plagioclase (Figure 3.10c-d) as well as late biotite and chlorite stacks. Notably, coarse-grained biotite is not

always parallel to the foliation. This observation suggests the presence of late coarse-grained biotite growth, which overprinted the sericitic alteration (e.g. Figure 3.10d).



Figure 3.8 Photographs of the tuff. A) Half drill core of the tuff with frequent quartz-calcite veins. DBDD0003: 39.20 m – 39.40 m – DB3S10. B) Half drill core of the tuff with quartz-calcite veins and numerous calcite vugs. DBDD0003: 67.40 m – 67.60 m – DB3S14. Magnetic pen for scale.

The micaceous cleavage domains display a range of volume percentage between 60% and 70% (zonal foliation) defining a disjunctive foliation type. The spatial relation between cleavage domains is mainly anastomosing and there is a gradational transition between cleavage domains and microlithons. About 55% of the quartz and carbonate minerals population displays undulose extinction. Notably, some plagioclase grains are not deformed nor foliation-parallel indicating that they post-date the deformation responsible for the observed foliation. However, in other cases, plagioclase grains are slightly deformed and cut by the micas. The reason for the occurrence of the two scenarios of plagioclase is not well understood.

The tuff exhibits multiple types of alteration including carbonatization, chloritization and sericitization (Figure 3.11-3.12). The most prominent feature in this unit is the ubiquitous calcite grains that overgrow the foliation and all other mineral phases (Figure 3.11-3.12). Moreover, calcite grains and the micas replaced plagioclase (Figure 3.11d-3.12a-b), whereas calcite grains are overgrown by coarse-grained biotite and microcline in places. Chlorite occurs as overgrowths superimposed on other minerals such as the plagioclase and the micas although biotite hosted by calcite grains are protected from alteration (Figure 3.12c-d). The tuff records subordinate chloritization (5%) second after carbonatization (10%).

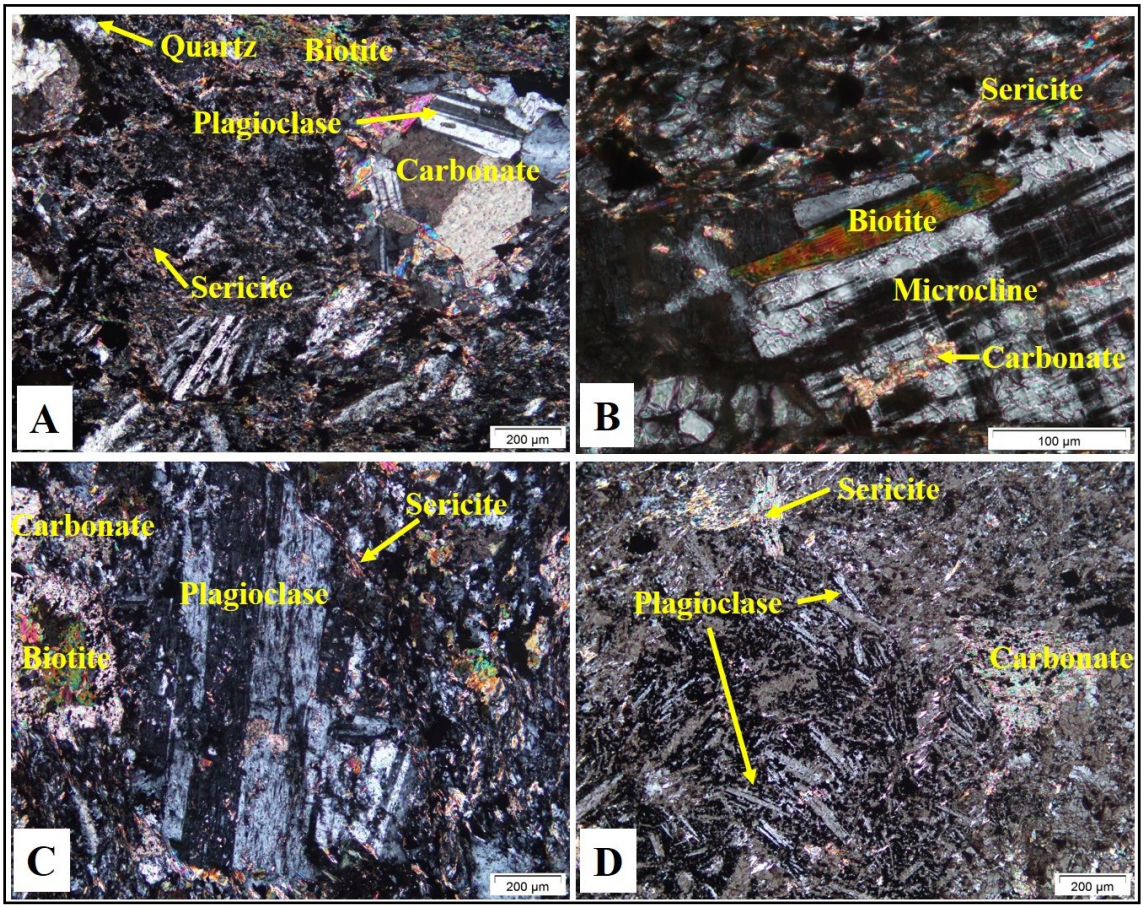


Figure 3.9 The tuff mineralogy, grain size and textural relationships. A) Randomly oriented fine-grained plagioclase, very fine-grained quartz and medium-grained calcite (XPL). DBDD0003: 39.20 m – 39.40 m – DB3S10-D17a. B) Fine-grained microcline overgrown by biotite and fine-grained calcite grains (XPL). DBDD0003: 47.28 m – 47.48 m – DB3S13-D18d. C) Coarse-grained plagioclase replaced by finer-grained calcite and sericite. The biotite grain is replaced by calcite (XPL). DBDD0003: 75.04 m – 75.24 m – DB3S15-D141d. D) Frequent very fine-to fine-grained plagioclase overgrown by calcite (XPL). DBDD0003: 34.20 m – 34.40 m – DB3S9-D131b. (XPL= crossed-polarized light; PPL= plane-polarized light).

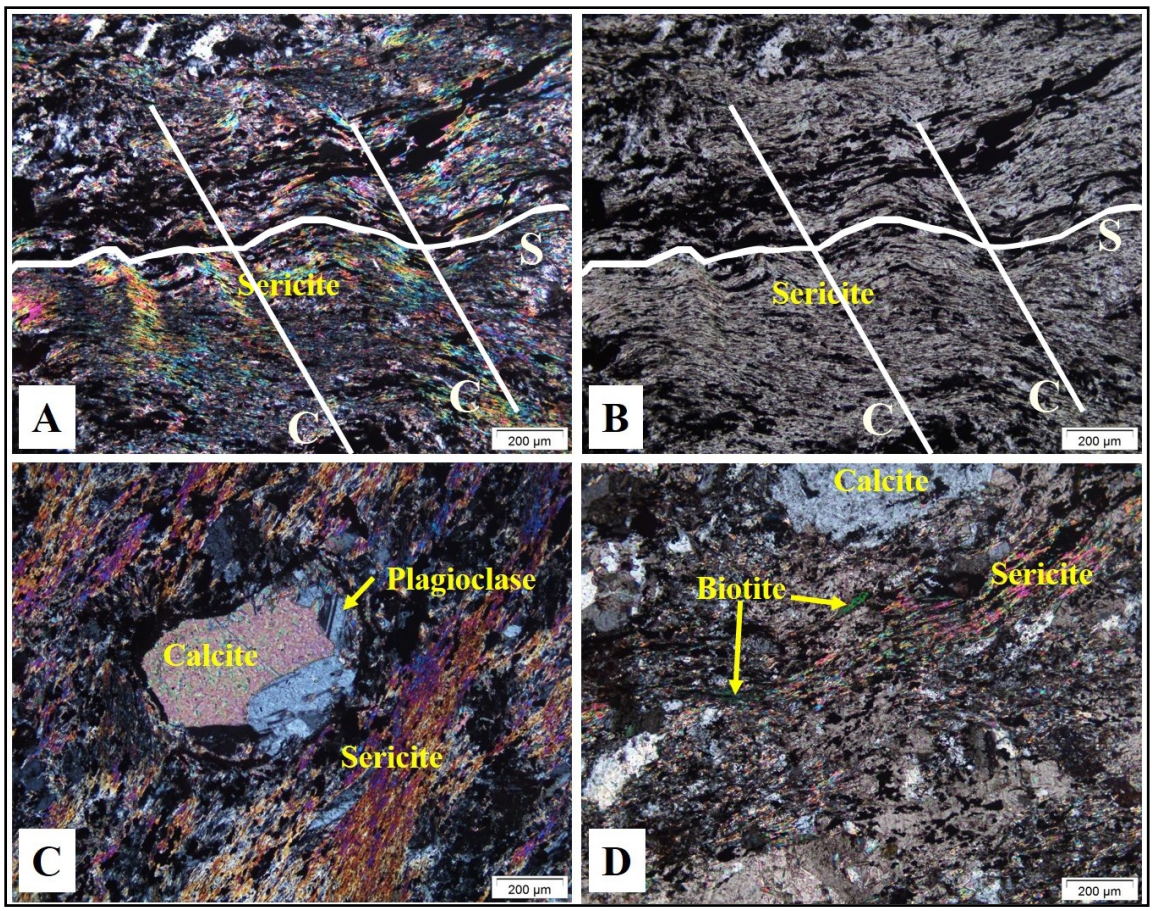


Figure 3.10 Spaced foliation in the tuff. A) S-C fabric with C-shear band foliation transecting the sericite dominated main foliation (S-foliation) during shearing (XPL) and B) same image shown in plane-light (PPL). DBD0003: 39.20 m – 39.40 m - DB3S10-D17c. C) Carbonates and plagioclase constitute the microlithons of the sericite cleavage domain (XPL). DBD0003: 39.20 m – 39.40 m - DB3S10-D17e. D) Sinuous cleavage made up of sericite. Biotite overgrowth on sericite (XPL). Conspicuous calcite overgrowths over the foliation. DBDD0003: 75.04 m – 75.24 m – DB3S15-D140c. The white lines define S and C surfaces. (XPL= crossed-polarized light; PPL= plane-polarized light).

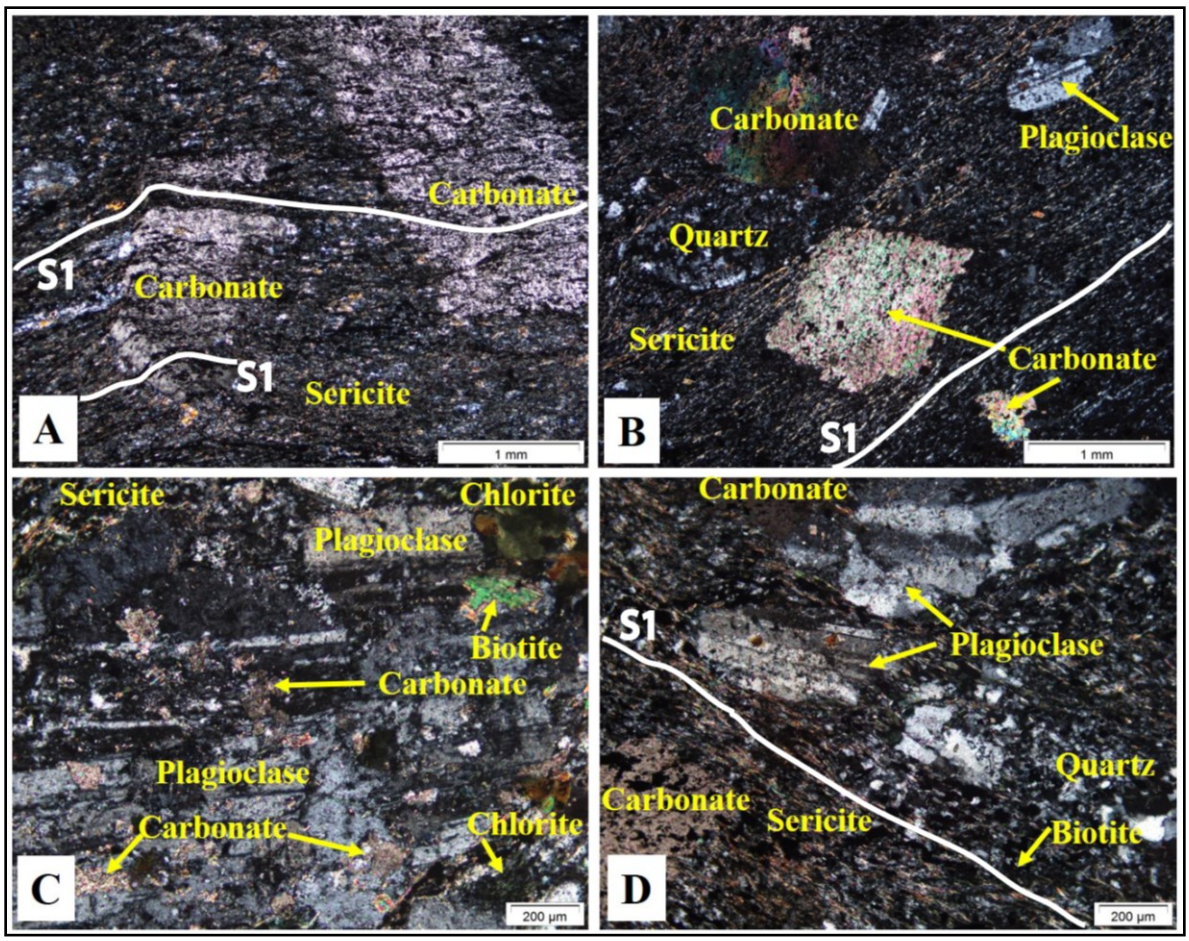


Figure 3.11 Multiple mineral overgrowths in the tuff. A) Calcite grains are cut through by the foliation. While calcite grains exhibit undulose extinction, the micas display kinked microfolds (XPL). DBDD0003: 47.28 m – 47.48 m – DB3S13-D18a. B) Coarse-grained calcite overgrowth over the foliation (sericite). This is the opposite of what is in 'image A' (XPL). DBDD0003: 85.60 m – 85.80 m – DB3S18-D19c. C) Medium-grained plagioclase replaced by fine-grained calcite, biotite and chlorite (XPL). DBDD0003: 76.24 m – 76.44 m - DB3S16-D27c. D) Plagioclase overgrown by calcite and sericite. Sericite, in contrast, is overgrown by calcite (XPL). DBDD0003: 85.60 m- 85.80 m – DB3S18-D19d. The white line defines S_1 foliation. (XPL= crossed-polarized light; PPL= plane-polarized light).

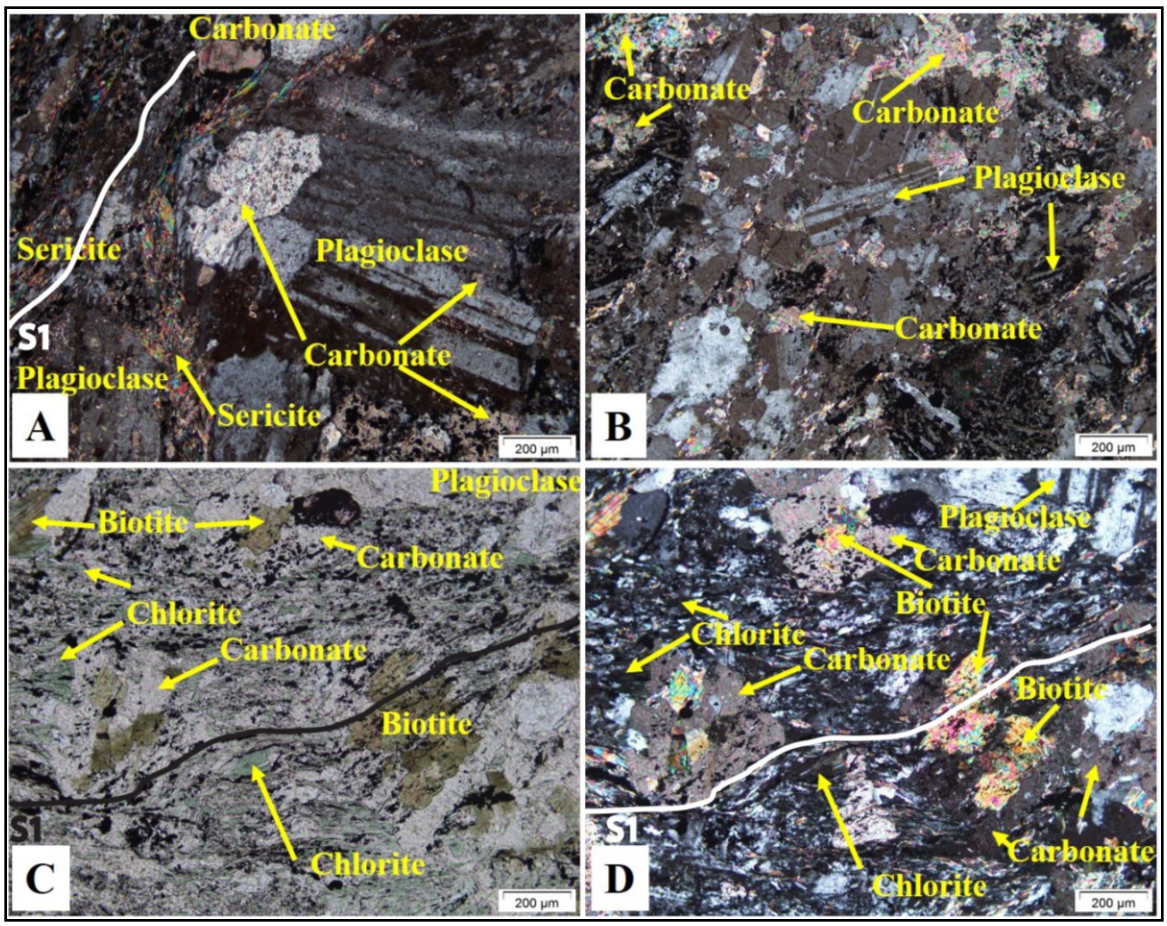


Figure 3.12 More observations of calcite overgrowths over other mineral phases. A) Plagioclase overgrown by calcite and sericite (XPL). DBDD0003: 58.00 m – 58.20 m – DB3S20-D139a. B) Ubiquitous plagioclase replacement by calcite (XPL). DBDD0003: 34.20 m – 34.40 m – DB3S9-D130b. C) Chlorite overgrowth over the foliation, whereas biotite enclosed in a calcite grain is not altered (PPL) and D) same image in crossed-nicols (XPL) DBDD0003: 75.04 m – 75.24 m – DB3S15-D142c. The white and black lines defines S_1. (XPL= crossed-polarized light; PPL= plane-polarized light).

Chlorite Schist

The chlorite schist is one of the poorly exposed rocks in the northwestern part of the study area. The chlorite schist is fine-to medium-grained and consists of mainly chlorite, sericite, biotite, plagioclase, quartz and calcite. In both outcrop and drill core (close to the surface), the chlorite schist is moderately-weathered (Figure 3.13a) and highly carbonatized. The unit has frequent quartz-calcite veins and significant malachite mineralization in both the veins and the rock matrix (hand specimen) (Figure 3.13b). While the chlorite schist is highly carbonatized close to its contact with the grey limestone in outcrop, the unit is strongly chloritized and slightly sericitized in other

parts. The foliation planes of this unit are well exposed in a trench that was dug during previous exploration programs (Figure 3.13a). In drill core, the unit occurs at various different intervals in drill core DBDD0003 (Figure 3.5). These intervals are at the following depths: (i) 0.00 m to 34.12 m, (ii) 40.80 m to 44.15 m and (iii) 76.45 m to 82.75 m depths in drill core DBDD0003 (Figure 3.5). This unit alternates with the tuff in the drill core and their contacts appear to be gradational. In the first interval (from 0.00 m to 34.12 m depth), the unit has minor amounts of malachite occurrences.

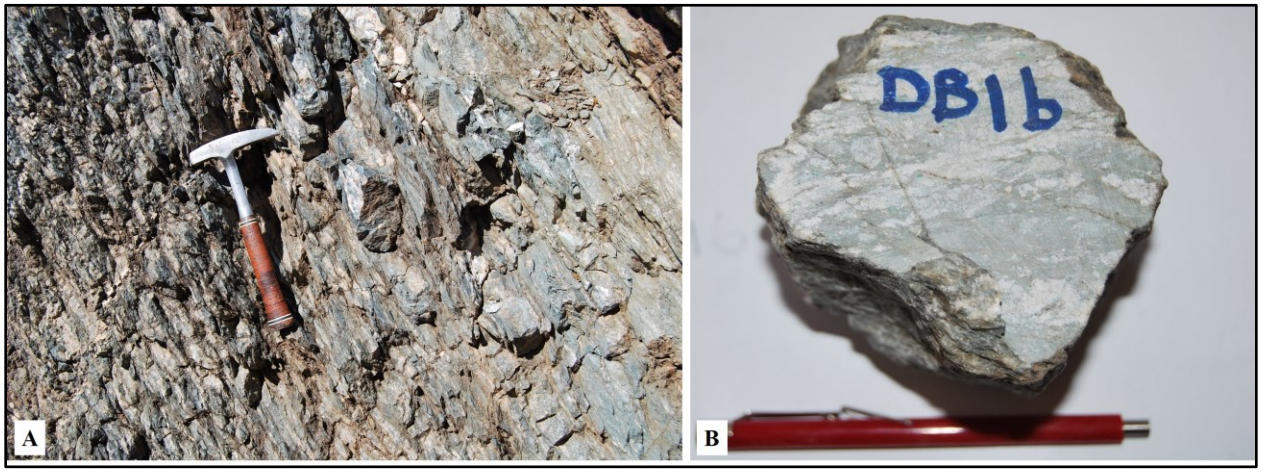


Figure 3.13 Photographs of the chlorite schist. Grid reference: 758343 mE; 781477 mN. A) Chlorite schist exposed in the exploration trench. Geological hammer for scale in the photograph. B) Hand specimen of the chlorite schist with flecks of malachite and ubiquitous quartz-calcite veins, DB1b. Magnetic pen for scale in the photograph.

Based on thin section observations, the mineralogy of the chlorite schist is made up of ~35% chlorite, 25-30% sericite, 20% calcite, ~15% quartz and ~5% plagioclase. Chlorite is very fine-to fine-grained while quartz and carbonates are fine- to medium- grained. Quartz and carbonate grains vary from 0.088 to 0.175 mm and from 0.117 to 0.194 mm, respectively. The unit is dominated by chlorite and has ubiquitous quartz-calcite veins. Chlorite grains have an anhedral form. The micas are fine-grained (0.125-0.168 mm) and make up the cleavage domains (M domain), whereas quartz and carbonate minerals comprise the microlithons (Q domain) of the disjunctive foliation (spaced foliation) (Figure 3.14). The foliation for this rock is made up of about 60% M-domains. The spatial relation between the M domains is anastomosing, whereas the transition between M domains and Q domains is gradational. Carbonate and quartz grains display

ubiquitous undulose extinction. The unit is strongly chloritized. Excessive chlorite obliterated the appearance of other mineral phases and has given the rock a conspicuous green colour. In some places, the foliation is overgrown by carbonate grains (Figure 3.14a-c) and the carbonates, in turn, are overgrown by chlorite (Figure 3.14d).

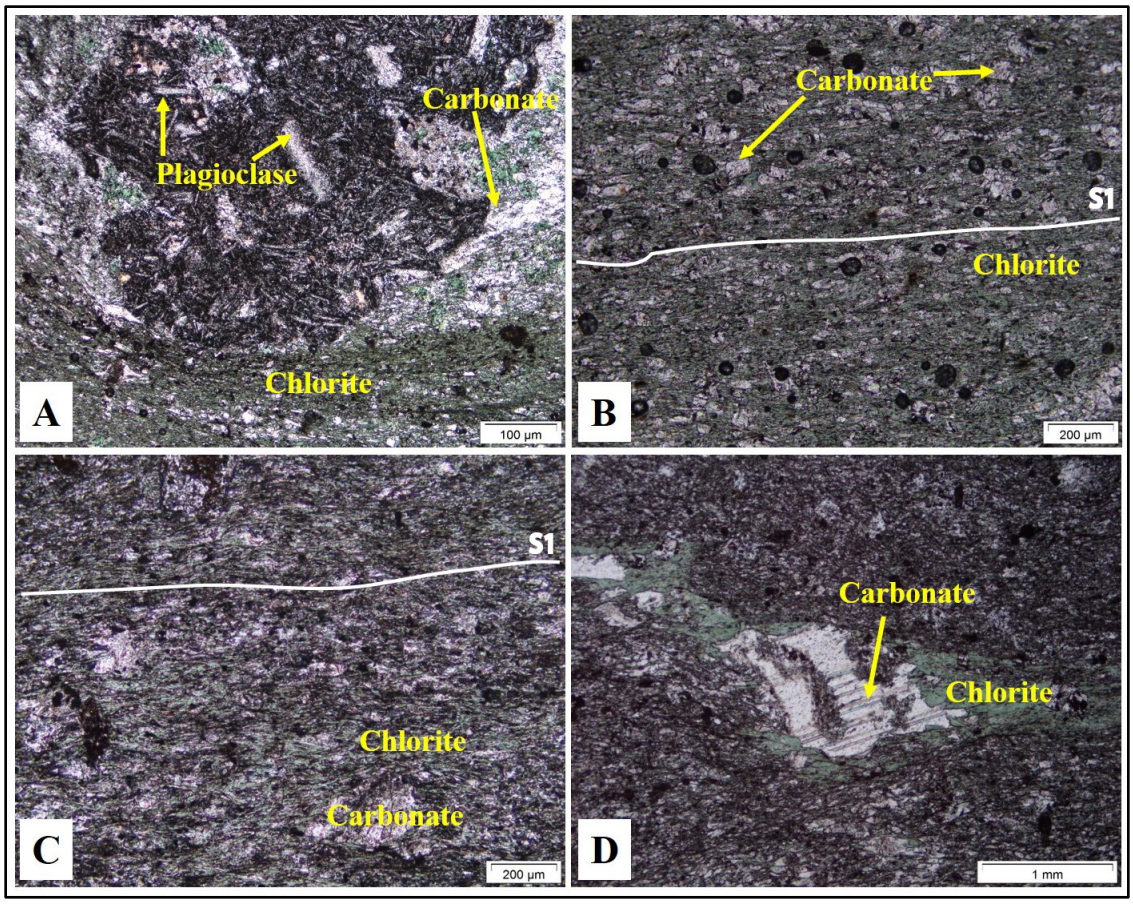


Figure 3.14 Mineral assemblage of the chlorite schist. A) Plagioclase rich pocket surrounded by carbonates and chlorite. Chlorite overgrows the primary minerals (micas) (PPL). DBDD0003: 3.73 m – 3.93 m - DB3S1-D124a. B) Micaceous spaced foliation overgrown by chlorite and fine-grained calcite (PPL). DBDD0003: 4.15 m – 4.35 m - DB3S2-D126a. C) Chlorite overgrowths. Also, the foliation is overgrown by carbonates. (PPL). Grid reference: 758268 mE; 7814999 mN: DB7a-D31a. D) Calcite overgrown by chlorite (PPL). 758268 mE, 7814999 mN: DB7a-D32b. The white line defines S_1. (XPL= crossed-polarized light; PPL= plane-polarized light).

Mafic Metavolcanic Rock

The mafic metavolcanic rock occurs in the eastern part of the study area and it was a basalt that was metamorphosed into a sericite-chlorite schist. This rock is highly deformed, foliated and folded, with kink asymmetrical folds (Figure 3.15). The kink folds deformed the pre-existing foliation, S_1 and thus they suggest a presence of S_2 in this unit. In outcrop, the unit has a dark grey weathered colour with distinct carbonate bands (Figure 3.15). In drill core, the unit appears fresh. This rock occurs as a thin layer within the agglomerate between 138.71 m and 139.3 m depth in drill core DBDD0001 (Figure 3.5). The mafic volcanic is greenish, fine-grained and, enriched in micas and chlorite with a significant amount of calcite.



Figure 3.15 Calcareous, moderately-weathered mafic metavolcanic outcrop with kink folds. Grid reference: 759554 mE, 7814668 mN. Geological hammer for scale to the right of the photograph.

Based on microscopic observations, the mineralogy of the mafic metavolcanic comprises very fine-grained sericite (~30%), fine grained-chlorite (~25%), very fine-to coarse-grained (0.088-0.583 mm) quartz (~20%) and very fine-to fine-grained (0.117-0.194 mm) carbonates that are mainly calcite (~ 20%) (Figure 3.16a). In addition, the mafic metavolcanic rock has very fine- to fine-grained (0.0292-0.146 mm) subhedral disseminated pyrite (~5%) (Figure 3.16b). The unit

displays a disjunctive foliation defined by M and Q domains (Figure 3.16c-d). The volume percentage of cleavage domains is about 70% and thus, it has a zonal spaced cleavage. The spatial relation between cleavage domains is anastomosing, whereas the transition between the cleavage domains and microlithons is gradational. The foliation is overgrown by conspicuous carbonate and chlorite grains (Figure 3.16c-d), and they indicate carbonatization and chloritization, respectively.

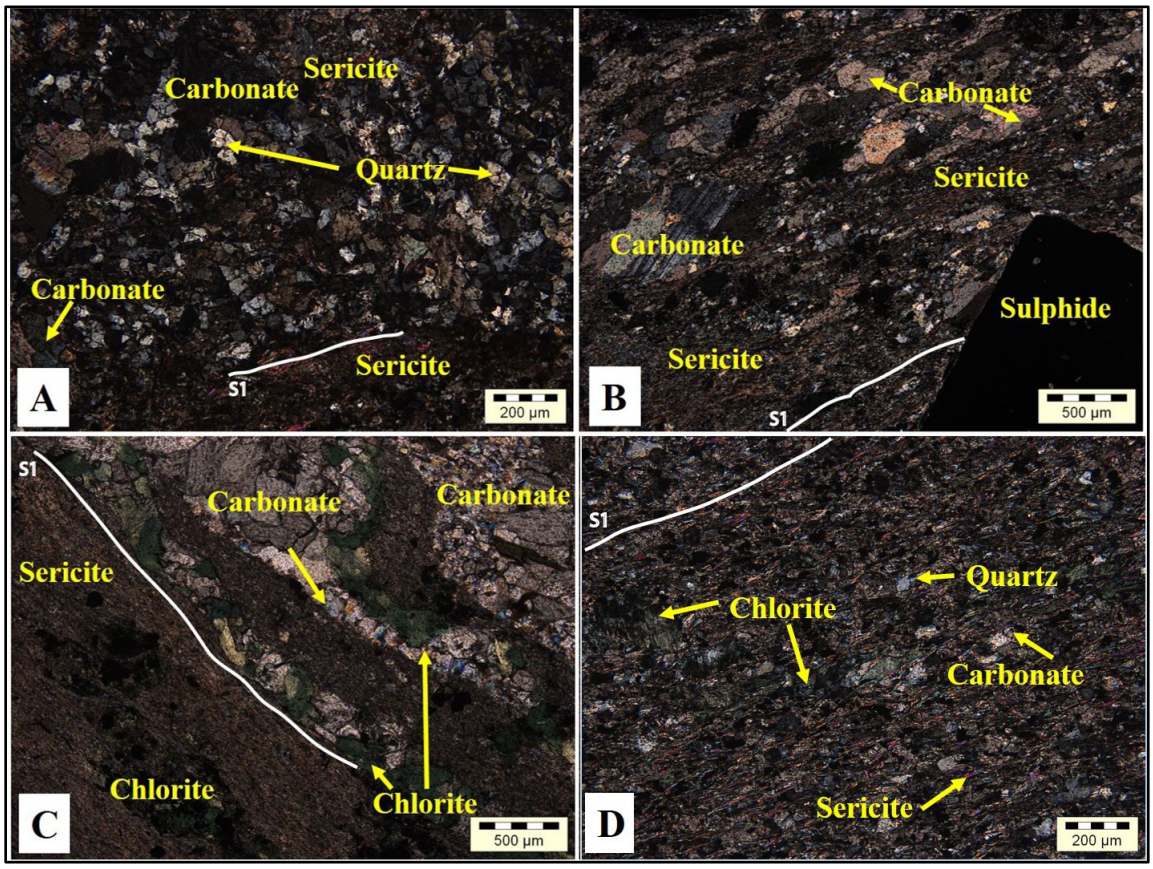


Figure 3.16 Mineral assemblage of the mafic metavolcanic rock. A) Fine-grained carbonate and quartz grains constitute the microlithon, whereas sericite makes up the cleavage domain of the foliation observed in this sample (XPL). Grid reference: 759552 mE; 7814663 mN – DB8a-D33b. B) Carbonate overgrowth on sericite in the cleavage domain (XPL). DBDD0001: 138.10 m – 138.30 m - DB1S20-D30a. C) Chlorite overgrows both the disjunctive foliation (sericite) and quartz-calcite veins (XPL). DBDD0001: 138.10 m – 138.30 m - DB1S20-D80a. D) Chlorite overprinting the foliation (S_1) and other mineral phases (XPL). DB10a-40a. The white line defines S_1. (XPL= crossed-polarized light; PPL= plane-polarized light).

Agglomerate

In outcrop, the agglomerate occurs primarily in the northwestern part of the study area. The agglomerate is poorly exposed (Figure 3.17), moderately-weathered and chloritized, whereas in drill core, the unit appears fresh although it is chloritized. Based on drill core observations this unit is unconformably overlain by the younger silicified dolomite of the Abenab Subgroup. In drill core DBDD0001 the agglomerate is in contact with thin layers of the mafic metavolcanic rock (Figure 3.5). The agglomerate is located between 137.73 m and 138.71 m depth, and between 139.30 m and 170.50 m depth (end of hole) in DBDD0001 (Figure 3.5a). In drill core DBDD0002, the agglomerate occurs from 96.71 m to 120 m depth (end of hole) (Figure 3.5b). In drill core DBDD0002, the agglomerate has a copper sulphide mineralized zone between 157.50 m and 157.62 m depth, marked by minor disseminated chalcopyrite and pyrite in quartz-calcite veins. The agglomerate is greenish grey, characterized by a moderately foliated, mica-rich matrix and fine grained mafic lava clasts that vary in size from 1-5 cm (Figure 3.17b-3.16). The rock is deformed, foliated and cross-cut by conspicuous quartz-calcite veins (Figure 3.17b-3.16) of more than one hydrothermal generation as signaled by multiple cross-cutting veins. Vein widths range from < 1 cm to 1.5 cm and are concentrated in areas with fewer clasts. The clasts are deformed, elongated, and aligned sub-parallel to parallel to the foliation (Figure 3.17b-3.16). The matrix is highly chloritized giving the entire rock a greenish appearance (Figure 3.18).

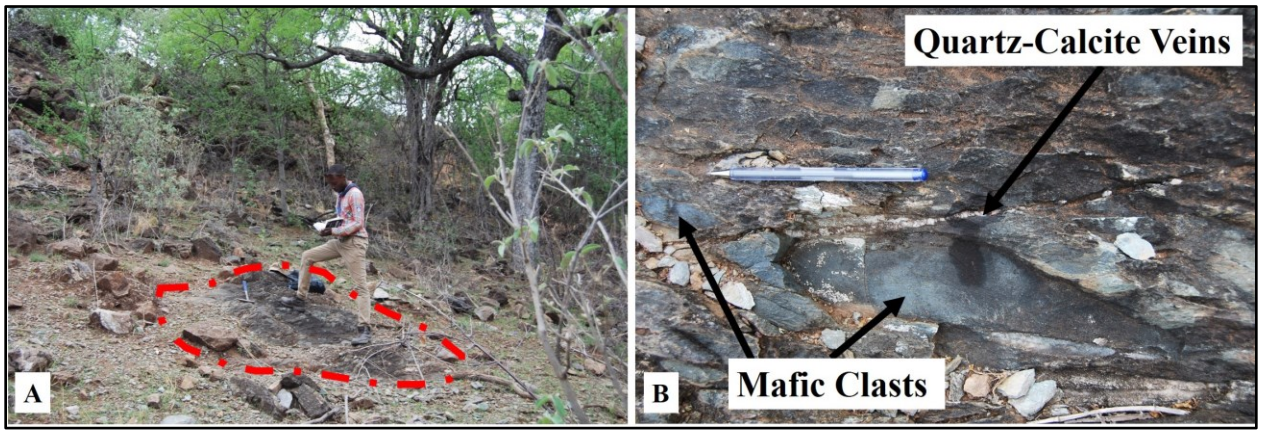


Figure 3.17 Field photographs of the agglomerate outcrop (5 x 4 m). Grid reference: 758747 mE, 7814817 mN. A) Poorly exposed agglomerate outlined in red. This unit is concealed by younger sediments. B) Deformed mafic clasts of the agglomerate that are elongated along strike. The pen for scale in the centre of the photograph.

In thin section, the rock matrix is composed of ~25% biotite, , ~25% chlorite, ~15% sericite, ~15% calcite, 15% quartz and 5% sulphides. Quartz and calcite are fine-to medium-grained (0.088-0.292 mm) and fine-to coarse-grained (0.175-0.583 mm), respectively. The agglomerate has a well-developed spaced foliation made up of biotite, sericite and calcite (Figure 3.19a). Calcite is ubiquitous and replacive in nature, occurring as calcite veins, as well as grain overgrowths (Figure 3.19a-d). Locally, calcite is replaced by chlorite (Figure 3.19a). The elongated calcite grains are overgrown by late biotite grains (Figure 3.19b).

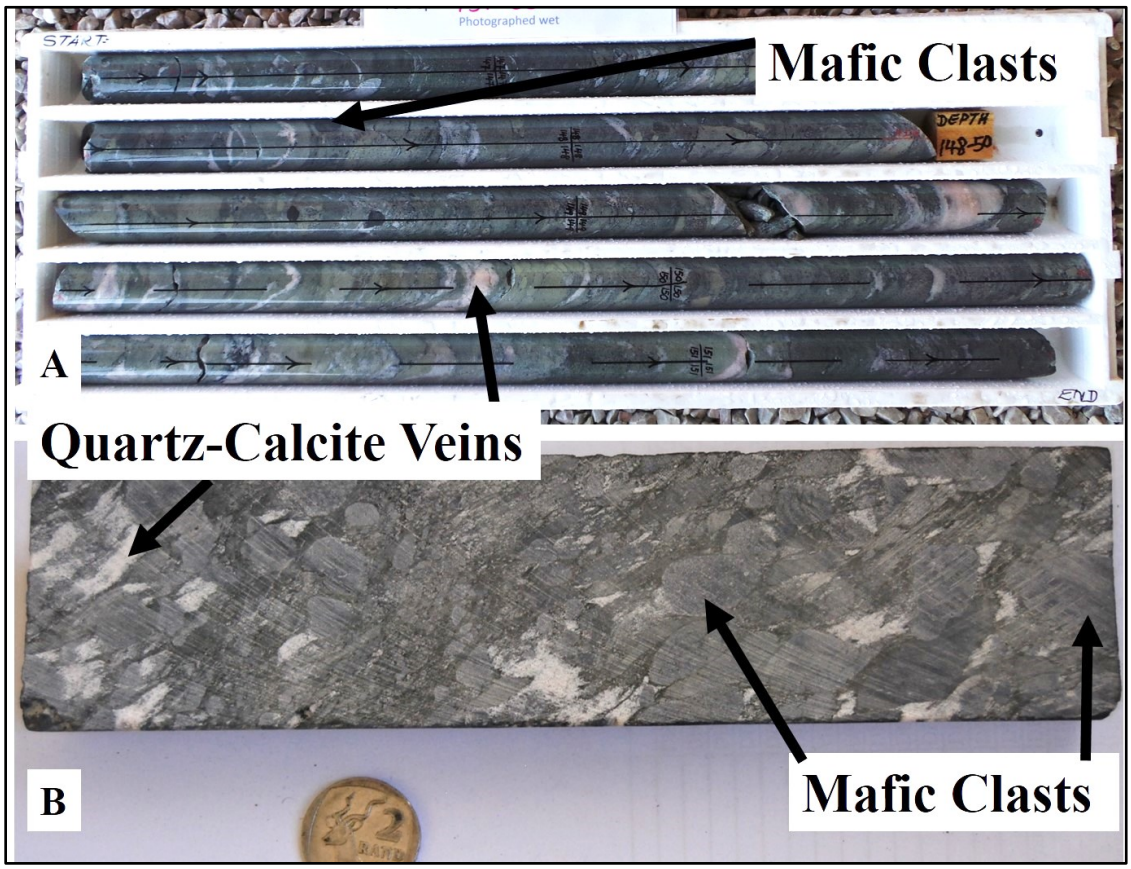


Figure 3.18 Photographs of the agglomerate in drill cores. A) The drill cores exhibit fresh, though chloritized agglomerate with a foliated matrix and fine grained mafic clasts of the agglomerate. The unit is cross-cut by abundant quartz-calcite veins. DBDD0001: 146.60 m – 151.33 m depth. B) Frequent sub-rounded mafic clasts and quartz-calcite veins in the agglomerate. DBDD001: 161.30 m – 161.50 m - DB1S23. The coin for scale in the photograph.

Based on textural relationships, the edges of the mafic clasts are surrounded by predominantly fine-grained calcite grains (Figure 3.19b). The calcite grains are fine-grained near the clasts and coarser-grained with increasing distance from the clasts. The calcite grain margins are elongated

in the same direction as the micas, and thus form a foliation plane (Figure 3.19b). This pattern implies that the calcite grains are deformed. In addition, this rock records microstructures. The quartz-calcite veins have a mosaic texture and are characterized by a lens-shape comparable to a mica fish morphology (Figure 3.19c). Quartz porphyroclast with undulose extinction are present in the micaceous matrix (Figure 3.19d). The observations of these microstructures together with the foliation curvature are evidence of the development of S-C fabric in the rock (Figure 3.19) during shearing. These microstructures which are sense of shear indicators are poorly developed in this rock.

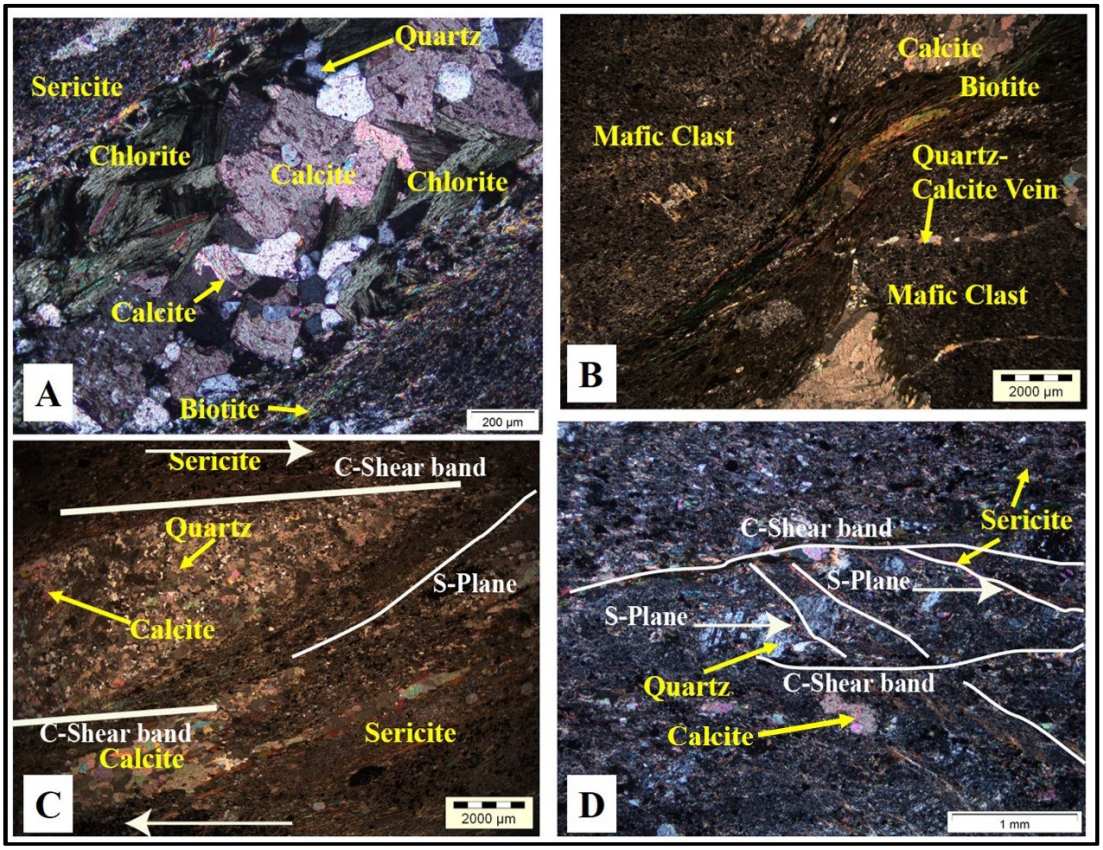


Figure 3.19 Mineral assemblage and textural relationships in the agglomerate unit. A) Chlorite overgrowth on calcite grains (PPL). DBDD0002: 109.70 m – 109.90 m - DB2S19-D26. B) Mafic clasts separated by biotite-rich cleavage domain and cross-cut by quartz-calcite veins (XPL). DBDD0001: 161.30 m – 161.50 m - DB1S23-D9h. C) Lens-shaped quartz-calcite veins with a mica-fish morphology as a result of shearing (XPL). DBDD0001: 145.00 m – 145.20 m – DB1S21-D83a. D) S-C fabric in the agglomerate with the C-plane transecting the main foliation (S-plane). DBDD0001: 161.30 m – 161.50 m - DB1S23-D9e. (XPL= crossed-polarized light; PPL= plane-polarized light). The white line defines the C-shear band and S-plane.

Felsic Volcanic Breccia

This rock occurs as an isolated outcrop, located about 400 m northwest of the study area and its exposure is very limited. The felsic volcanic breccia is pink, fine-grained with angular fragments from pebble to boulder size (<1 cm-~1 m) and with a very fine-grained matrix. The mineralogy is characterized by feldspars (~45%), quartz (~35%), plagioclase (15%) and <5% calcite. This unit is fractured and highly weathered to grey (Figure 3.20). The volcanic breccia is a metarhyolite breccia, and contains quartz (Figure 3.20a) and quartz-calcite veins (Figure 3.20b). This breccia is clast-supported with dark grey, very fine-grained silica-rich cement (Figure 3.20b). The thickness of the veins ranges from 2 cm to 15 cm. The quartz-veins contain malachite and exhibit cross-cutting relationships, which are indicative of multiple hydrothermal events (Figure 3.20a). The presence of outcropping malachite mineralization in this unit was interpreted by local exploration geologists to be the surface expression of an easterly plunging mineralized system of Deblin Copper Mine area (Golden Deeps Limited, 2012). In addition, some local exploration geologists referred to this unit as a gossan.

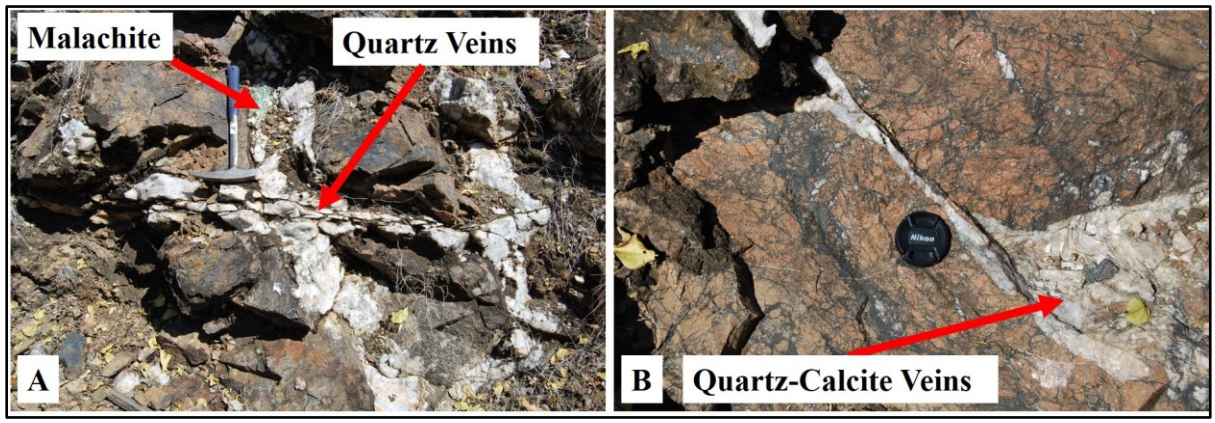


Figure 3.20 Photographs of the felsic volcanic breccia. Grid reference: 758342 mE, 7815085 mN. A) Cross-cutting quartz veins with malachite stains. B) Fine-grained pink fragments held together by a dark grey fine-grained silica cement. Geological hammer and magnetic pen for scale in the photographs.

Otavi Group

In the study area, the Otavi Group succession is dominated by carbonate rocks, which are highly variable in composition, texture and intensity of silicification over relatively small distances. These carbonate rocks include both dolomite and limestone. As a result of the variation in these carbonates, three major types of dolomite were identified and are referred to as (a) the silicified

dolomite, (b) the dolomite breccia and (c) the pyritic dolomite. Although the textures, the preserved primary structures and the alteration types are different, the mineralogy of all the dolomite types is similar. Additionally, the dolomite breccia has more clay minerals represented by the mud within the matrix. The limestone occurs in the eastern and northwestern parts of the study area, but it is poorly-exposed. However, the limestone can be divided into two units based on colour, texture and composition. The descriptions of the limestones are based only on outcrop descriptions, as they were not intersected in drill core.

Abenab Subgroup: Chuos Formation

Pyritic Dolomite

The pyritic dolomite occurs in the northwestern and eastern parts of the study area. In outcrop, this unit alternates with the grey limestone in the eastern part of the Deblin Copper Mine area. In addition, the pyritic dolomite occurs in association with a thin layer of diamictite (60 cm). The contact between this unit and the silicified dolomite lacks depositional evidence and thus it was inferred to be a tectonic contact defined by faults as indicated on the new detailed geological map (Figure 3.4). The pyritic dolomite is light grey, thinly laminated (in some places) and comprises deformed stromatolites. The pyritic dolomite is chloritized in places, weathers to brown and exhibits an elephant skin weathering texture.

This dolomite is often distinguished by conspicuous coarse-grained (0.5 mm) pyrite grains commonly pseudomorphed by goethite and accompanied by rare fine-grained (<0.1 mm) chalcopyrite hosted in thin quartz-calcite veins. Where the pyrite/goethite have been removed by weathering, there are open cubic spaces surrounded by thick layers of quartz, which are highly resistant to weathering. This carbonate consists of various quartz-calcite veins, cross-cutting quartz veins and calcite veins with malachite and numerous chert bands (Figure 3.21a). Thin section (Figure 3.21b) observations show that the pyritic dolomite consists of carbonate minerals (~55% dolomite; ~20% calcite), ~15% pyrite, <8% quartz and ~2% chlorite. Grain size ranges from very fine- to fine-grained with equigranular grains of quartz and carbonate minerals (dolomite and calcite) (<0.088 mm).

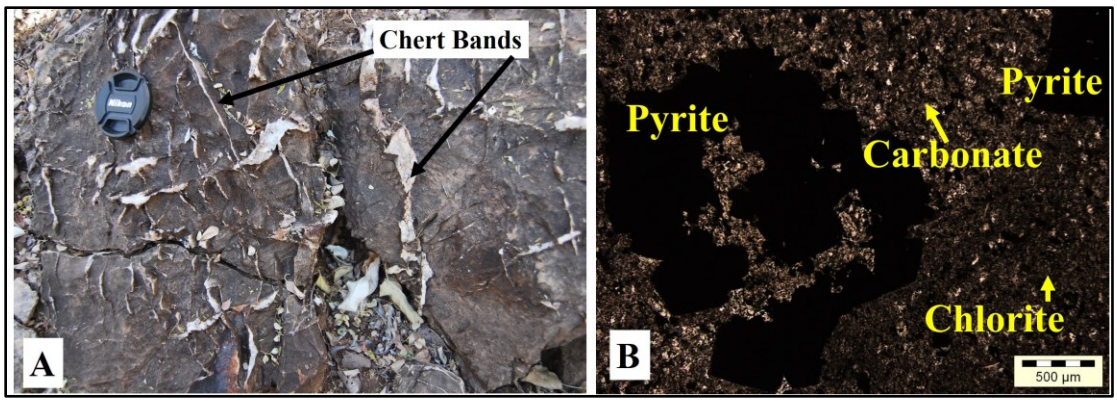


Figure 3.21 Field image and photomicrograph of the pyritic dolomite. A) Pyritic dolomite outcrop with frequent chert bands oriented in different directions. Grid reference: 759899 mE; 7814741 mN. B) Photomicrograph of the chloritized pyritic dolomite with an anhedral pyrite grain (XPL). Grid reference: 758497 mE, 7814882 mN: DB2b-D36e. (XPL=crossed-polarized light). Geological hammer and camera lens cover for scale in the photographs.

Grey Limestone

The grey limestone is poorly exposed and occurs in contact with both the mafic metavolcanic rock and the pyritic dolomite. Close to the contact with the pyritic dolomite, the unit exhibits dolomite banding (Figure 3.22a) although in some places the contact is obscured by sand cover. Where the limestone is in direct contact with the metavolcanic rocks, the carbonate is chloritized and contains admixtures of volcanically produced material. In outcrop, the grey limestone displays cross-bedding (Figure 3.22b) and contains both silica-rich and carbonate pebbles that are sub-rounded. The grey limestone is light in colour, fine- to coarse-grained and has thin laminations. The unit consists of ~80% calcite, 10% dolomite and 10% quartz. The limestone is fine to medium-grained (< 0.055 mm) and dominated by malachite-bearing quartz-calcite veins with oxidized pyrite grains.

Banded Limestone

The banded limestone occurs in the eastern part of the study area and overlies the grey limestone. The contact between the two limestone units is gradational. This limestone is poorly-exposed but the observed outcrop reaches a surface width of at least 40 m. The banded limestone displays a brown weathering colour. The unit is deformed (sheared) and exhibits microfolds that are cross cut by common quartz-calcite veins (Figure 3.23). Folding in this unit suggests the presence of the primary foliation (S_1) in addition to bedding (S_0). The composition of the banded limestone is

made up of calcite (70%), quartz (~20%) and dolomite (10%). The banded limestone is medium-grained, banded and has stromatolites in places.

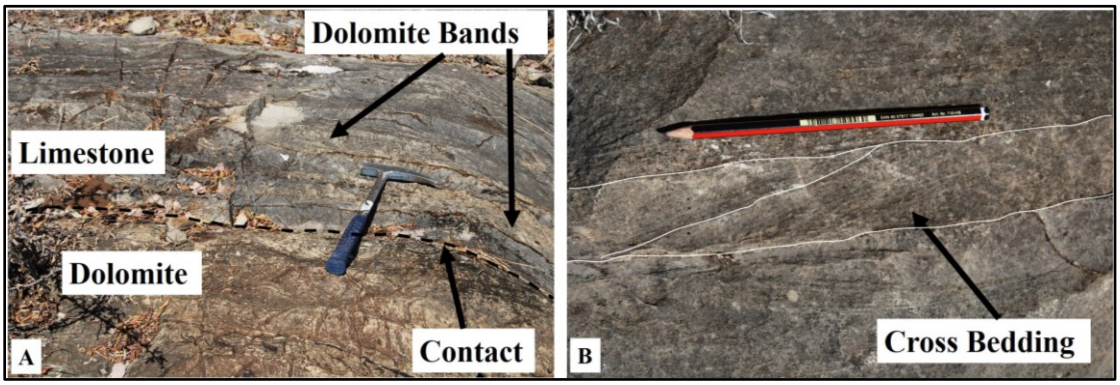


Figure 3.22 Photographs of the grey limestone. A) Contact between the limestone and the underlying pyritic dolomite. The grey limestone has dolomite bands close to its contact with the pyritic dolomite. Grid reference: 760059 mE, 7814656 mN. B) Cross-bedding in the grey limestone. Grid reference: 759832 mE, 7814629 mN. Geological hammer and pencil for scale in the photographs.

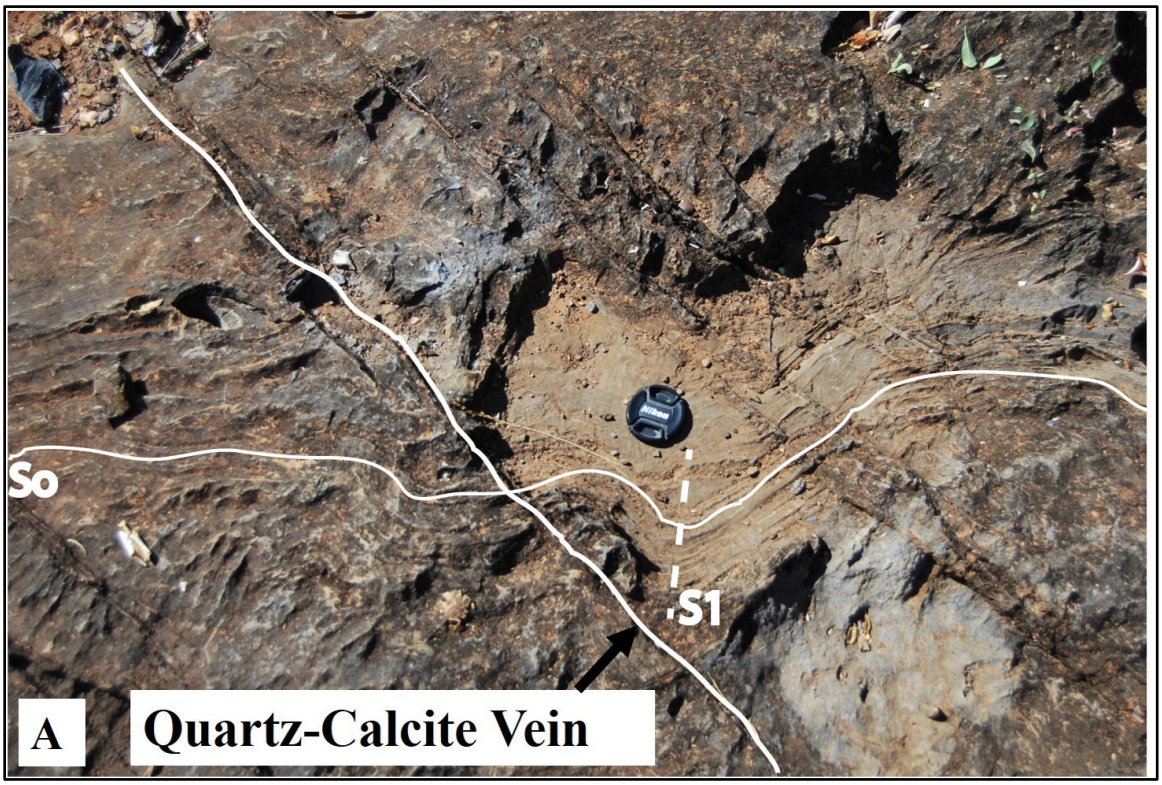


Figure 3.23 Banded limestone outcrop showing microfolds cross-cut by quartz-calcite veins. Grid reference: 759548 mE; 7814447 mN. Camera lens cover used for scale in the photograph.

Phyllite

The phyllite occurs as the minor rock type in the study area. The unit occurs in the eastern part of the study area as a thin outcrop with a width of about 10 m. The phyllite occurs directly above the banded limestone and below the overlying silicified dolomite. The unit is highly-weathered to light brown, but when fresh is dark brown and lustrous with well-developed schistosity (Figure 3.24). The phyllite is fine grained (< 0.1 mm), calcareous and consists of clay minerals (~50%), quartz (~35%), carbonates (mainly calcite) (10%) and muscovite (~5%). In addition, this unit has frequent pyrite grains that are partially or completely altered to goethite.



Figure 3.24 Intensely-weathered calcareous phyllite with brown oxidized idiomorphic cubic pyrite grains. Grid reference: 759985mE; 7814520mN. Geological hammer for scale in the photograph.

Silicified dolomite

The silicified dolomite covers a large portion of the study area, mainly in the northwestern part. Besides the main outcrops of the silicified dolomite, this carbonate has numerous discrete outcrops of less than 10 m thickness in the central part of the study area. Where the unit is in contact with the metavolcanic rocks, it exhibits thin green, deformed mafic layers. The silicified dolomite is interbedded with the dolomite breccia in both drill core DBDD0001 and DBDD0002. The silicified

dolomite is light to dark grey, very fine-grained with a massive appearance, thin laminations in places and frequent quartz-calcite veins of varying thicknesses (Figure 3.25a). This dolomite is distinguished by intense silicification, various fractures and joints, and frequent stromatolites, some of which are deformed in places (Figure 3.25b-c).

Based on microscopic observations, the mineralogy of the silicified dolomite comprises 60% carbonates (dolomite and calcite), 25% quartz, 10% sulphides and ~2% sericite. The grain sizes of the carbonate minerals show a wide range, from very fine-to coarse-grained (0.088 to 1.167 mm), whereas quartz grains span from very fine-to medium-grained (0.058 to 0.175 mm) (Figure 3.26a-b). Fine-grained pyrite and chalcopyrite occur in both the silicified dolomite matrix and in quartz-calcite veins, some of which show cross-cutting relationships (Figure 3.26c-d). While both carbonate and quartz grains exhibit undulose extinction, sericite is very fine-grained (<0.050 mm) (Figure 3.27a-b). The silicified dolomite displays carbonate overgrowths on other mineral phases such as the early carbonates and quartz, as well as sericite in the weakly developed foliation (Figure 3.27a-b).

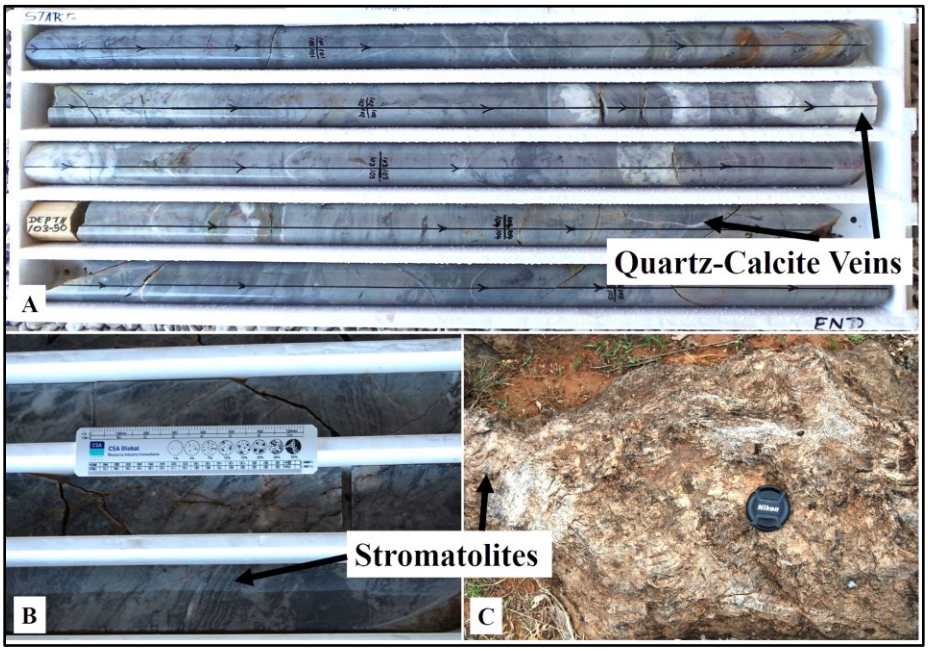


Figure 3.25 Images of the silicified dolomite in drill cores and outcrop. A) Silicified dolomite with outstanding thin and thick quartz-calcite veins. DBDD0001: 100.65 m – 105.31 m depth. B) Stromatolites in the silicified dolomite drill cores. DBDD0001: 117.00 m – 119.00 m depth. C) Silicified dolomite outcrop with deformed stromatolites and brown weathering colour. Grid reference: 759363 mE, 7814342 mN. Camera lens cover and ruler for scale in the photograph.

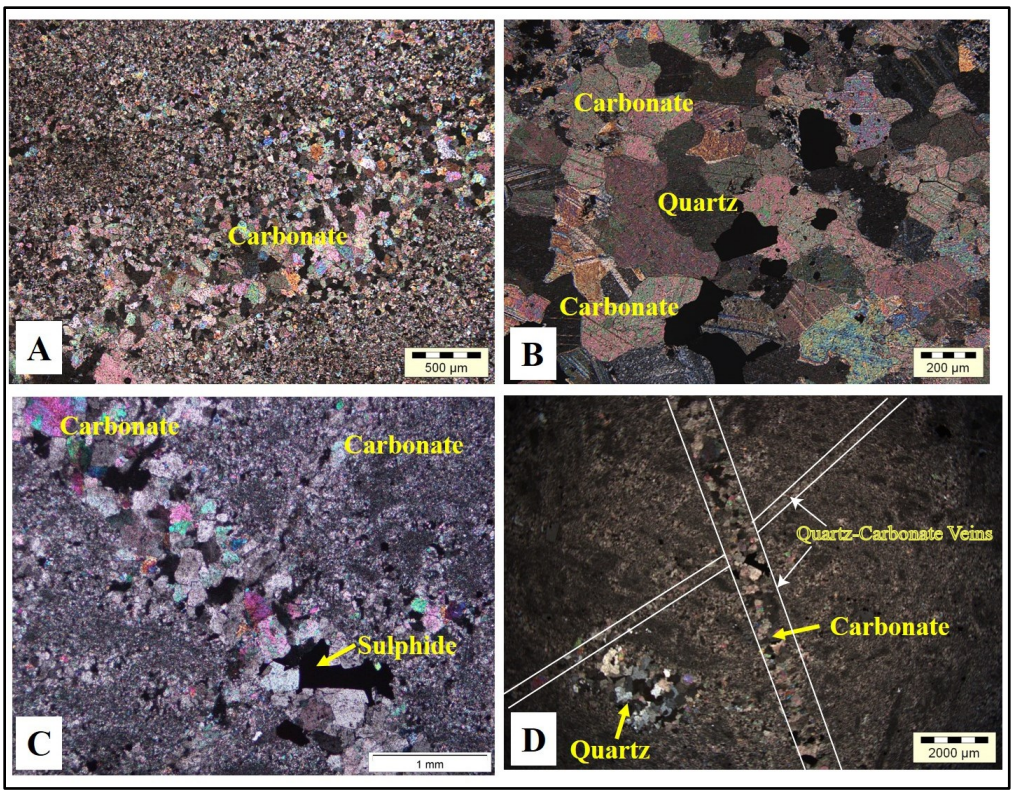


Figure 3.26 Silicified dolomite mineralogy and textures. A) Mosaic texture defined by both fine- and coarse-grained quartz and carbonate minerals (XPL). DBDD0002: 35.27 m – 35.47 m - DB2S4-D11a. B) Carbonate and quartz grains (XPL). DBDD0002: 73.40 m – 73.60 m – DB2S12-D14d. C) Coarse grained quartz-calcite veins with sulphides (XPL). DBDD0001: 3.75 m – 3.95 m – DB1S1-D1b. D) Cross-cutting relation of two quartz-calcite veins. The north-northeast trending vein is displaced by the north-northwest trending vein, which also host sulphides (XPL). DBDD0001: 3.75 m – 3.95 m – DB1S1-D1a. (XPL= crossed-polarized light).

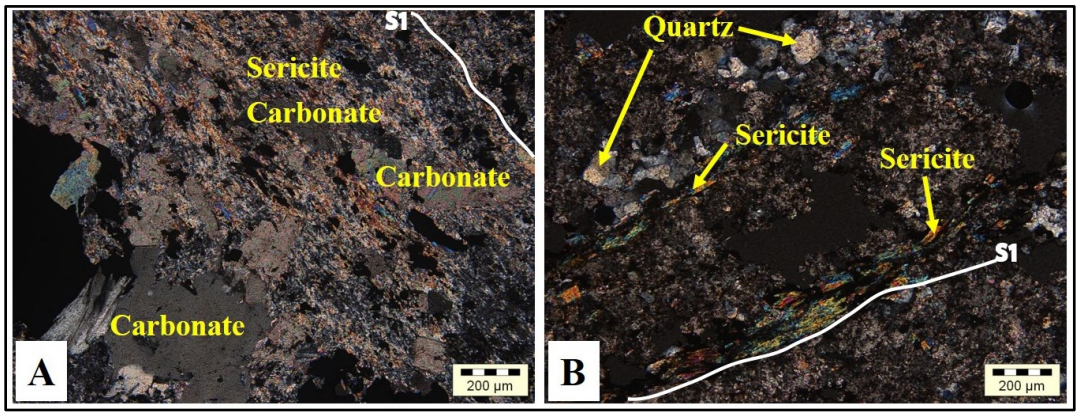


Figure 3.27 Sericite in the silicified dolomite and mineral overgrowths. A) Foliation, S_1 made up of largely sericite (XPL). Additional observations show carbonate overgrowth over sericite in the cleavage domain. DBDD0002: 73.40 m – 73.60 m – DB2S12-D14c. B) Fine-grained quartz in the quartz-calcite vein and minor distinct sericite cleavage domains (XPL). DBDD0001: 82.59 m – 82.59 m - DB1S11-D4b.

Dolomite Breccia

The dolomite breccia occurs in the northwestern part of the study area, close to the mine shaft. The dolomite breccia contains deformed stromatolites (Figure 3.28a), a fine-grained dolomitic matrix (although locally it has coarse-grained calcite cement) and coarse-grained dolomite clasts, 1-10 cm in diameter, some of which are commonly silicified (Figure 3.28b). The dolomite breccia is clast-supported and has frequent quartz-calcite veins. Although the outcrops of the dolomite breccia are mappable at the scale of 1:2500, they are nevertheless less than 20 m in width. The dolomite breccia mineral composition consists of ~70% carbonates, ~15% quartz, ~10% sulphides and ~5% clay minerals (micrite) (Figure 2.29a-b). In addition, the dolomite breccia has dark grey organic matter. This unit exhibits a mosaic texture defined by very fine- to coarse-grained (0.088-1.167 mm) carbonate minerals (dolomite and calcite) and very fine- to fine-grained (0.097-0.175 mm) quartz, recrystallized in some places.

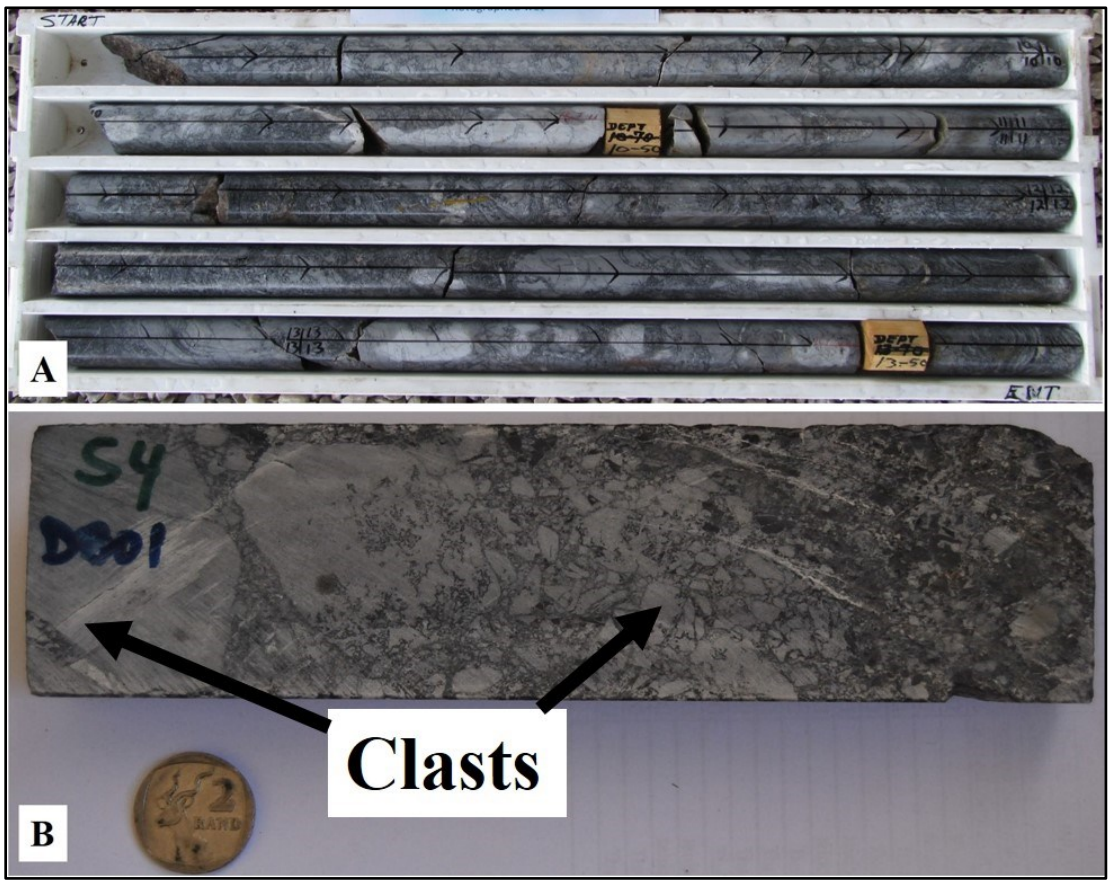


Figure 3.28 Dolomite breccia. A) Dolomite breccia with deformed stromatolites. DBDD0001: 9.14 m – 13.15 m depth. B) Clast-supported dolomite breccia. The clasts are silicified. DBDD0001: 15.84 m – 16.04 m – DB1S4. Coin for scale in the photograph.

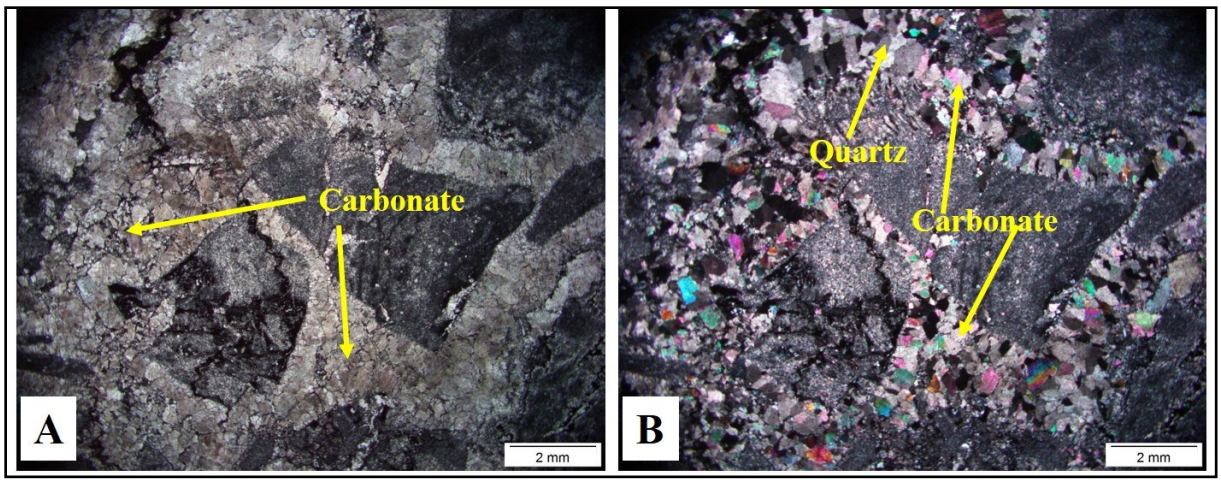


Figure 3.29 Textural characteristics of the dolomite breccia. A) Dilation in the dolomite breccia as a result of the deformation of the quartz and carbonates (PPL) and B) same image shown in crossed-nicols (XPL). DBDD0002: 13.70 m – 13.90 m – DB2S2-D10a.

Diamictite

The diamictite is distributed in the northwestern, eastern (not shown on the local 1:2, 500 geological map) and southern parts of the study area. The diamictite is composed of largely limestone and dolostone clasts, and minor mafic chlorite-rich clasts in an abundant and fine-grained, calcareous and dolomitic matrix. Dolomite clasts dominate over limestone clasts. These carbonate clasts are massive and range from <1cm-~70 cm in diameter (Figure 3.30a). The clasts are poorly sorted and typically sub-angular to sub-rounded. The mafic chlorite-rich clasts in the diamictite are derived from the underlying metavolcanic rocks of the Askevold Formation. The diamictite matrix is locally laminated, showing dolomitic depositional layers.

In the northwestern part of the study area the unit is well-exposed, whereas in the southern part of the study area the unit is poorly-exposed. In the northwestern part of the study area, the diamictite occurs with a thin poorly-exposed, highly-weathered, brown thin banded iron formation layer (Figure 3.30b). In the southern and eastern parts, the diamictite outcrops are limited due to the extensive sand cover (Figure 3.30c-d). In the southern part, the diamictite exhibits frequent cross-cutting quartz veins of thicknesses ranging from about 1 cm to 5 cm. In the eastern part, the diamictite occurs as a poorly exposed, thin layer (~60 cm) intercalated with the pyritic dolomite (Figure 3.30d).



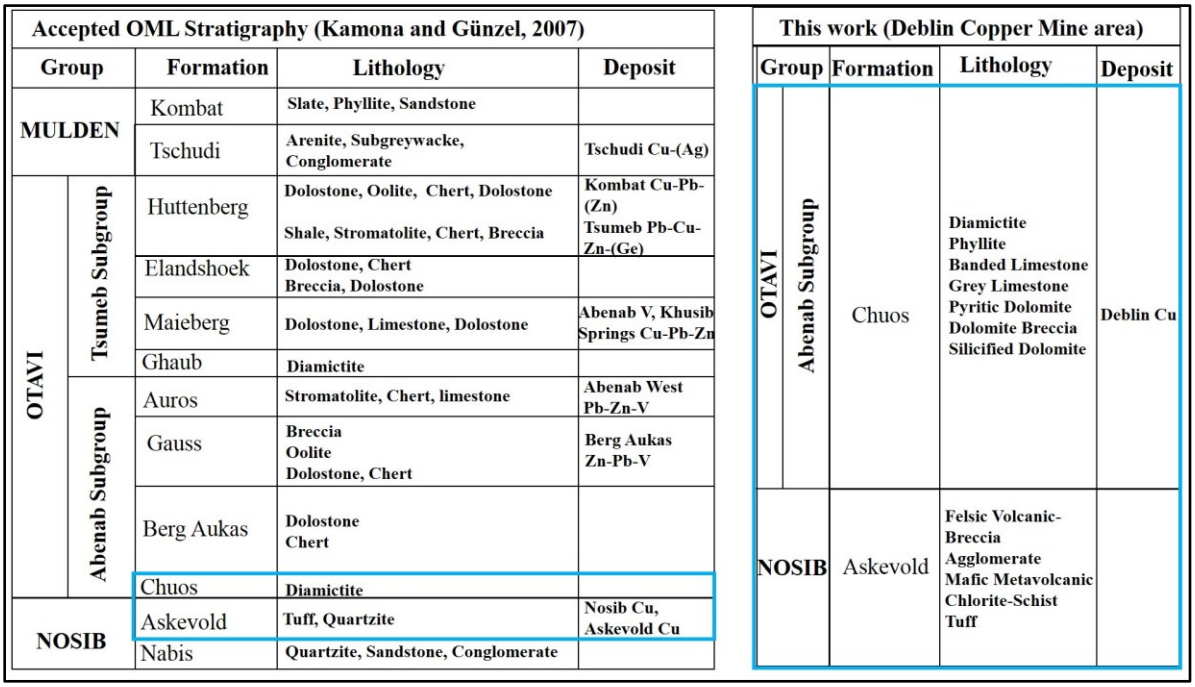
Figure 3.30 Field images of the diamictite: A) Diamictite with large angular carbonate clasts. B) A banded iron-rich layer within the diamictite. The outcrop exhibits a red colour due to ferruginous material. Both A-and B-photographs represent the outcrop in the northwestern part of the study area. Grid reference: 758810 mE, 7814791 mN. C) Diamictite with limestone and dolomite fragments in a brown calcareous matrix. The matrix of the dolomite weathers to brown. Grid reference: 759157 mE, 7814229 mN. D) Poorly exposed diamictite layer (~60 cm) with dolomitic depositional layers intercalated with the pyritic dolomite. Grid reference: 759653 mE, 7814678 mN. The photographs in C and D represent the outcrop in the southern part of the study area. Geological hammer and pen for scale in the photographs.

3.4 Discussion

The Stratigraphic Succession

Previously the stratigraphy of the Deblin Copper Mine area has not been correlated with the accepted stratigraphy of the Otavi Mountain Land. Based on the current investigations, the stratigraphy of the area around the Deblin Copper Mine consists of the Askevold Formation of the Nosib Group, unconformably overlain by lithologies of the Chuos Formation of the Otavi Group. The lithologies of the Askevold Formation are primarily metavolcanic rocks, whereas the Chuos

Formation comprises dolomite, limestone, phyllite and diamictite (Figure 3.31). In the Otavi Mountain Land, there are two glacial deposits, namely the Chuos Formation and Ghaub Formation diamictites as shown in Figure 3.31 (Hoffmann and Prave, 1996; Kamona and Günzel, 2007; Miller, 2008). The older Chuos Formation diamictite is characterized by the presence of a banded iron formation layer as well as clasts of igneous rocks in addition to the carbonate clasts. In contrast, the younger Ghaub Formation diamictite is made up of carbonate clasts only and it does not have an iron formation. Therefore, the presence of the iron formation layer and the mafic volcanic material clasts in the diamictite from the study area provides strong evidence that this diamictite belongs to the Chuos Formation of the Abenab Subgroup.



Accepted OML Stratigraphy (Kamona and Günzel, 2007)

Group		Formation	Lithology	Deposit
MULDEN		Kombat	Slate, Phyllite, Sandstone	
		Tschudi	Arenite, Subgreywacke, Conglomerate	Tschudi Cu-(Ag)
OTAVI	Tsumeb Subgroup	Huttenberg	Dolostone, Oolite, Chert, Dolostone Shale, Stromatolite, Chert, Breccia	Kombat Cu-Pb-(Zn) Tsumeb Pb-Cu-Zn-(Ge)
		Elandshoek	Dolostone, Chert Breccia, Dolostone	
		Maieberg	Dolostone, Limestone, Dolostone	Abenab V, Khusib Springs Cu-Pb-Zn
		Ghaub	Diamictite	
	Abenab Subgroup	Auros	Stromatolite, Chert, limestone	Abenab West Pb-Zn-V
		Gauss	Breccia Oolite Dolostone, Chert	Berg Aukas Zn-Pb-V
		Berg Aukas	Dolostone Chert	
		Chuos	Diamictite	
NOSIB		Askevold	Tuff, Quartzite	Nosib Cu, Askevold Cu
		Nabis	Quartzite, Sandstone, Conglomerate	

This work (Deblin Copper Mine area)

Group		Formation	Lithology	Deposit
OTAVI	Abenab Subgroup	Chuos	Diamictite Phyllite Banded Limestone Grey Limestone Pyritic Dolomite Dolomite Breccia Silicified Dolomite	Deblin Cu
NOSIB		Askevold	Felsic Volcanic-Breccia Agglomerate Mafic Metavolcanic Chlorite-Schist Tuff	

Figure 3.31 Stratigraphic column for the study area and comparison with the accepted Otavi Mountain Land stratigraphy with mineral deposits of Kamona and Günzel (2007).

In the western part of the Otavi Mountain Land the Chuos Formation is characterized by locally shallow-water carbonates with stromatolites, massive to planar-laminated carbonates, silicified dolomites and chert (Nascimento *et al.*, 2016). The current field observations show that the carbonates above the Askevold Formation are dominantly stromatolitic and locally silicified, have thin laminations to massive textures and thin chert bands in places. The diamictite is intercalated with the pyritic dolomite. All these geological features are consistent with the description of the

Chuos Formation lithologies by Nascimento *et al.* (2016) in the western part of the Otavi Mountain Land.

Current geological mapping provides evidence of the presence of the diamictite in association with the carbonates in the area previously mapped as the Askevold Formation dolomite on the regional geological map of the Geological Survey of Namibia (2008) (Figure 3.1). The indicated petrological descriptions of these carbonates suggest that they belong to the Chuos Formation. Hence, that part of the regional geological map was changed from Askevold Formation to Chuos Formation on the modified regional geological map (Figure 3.32). In addition, the interpretation of the Maieberg Formation in contact with the Chuos Formation in the southern part of the Otavi Mountain Land on the regional geological map of the Geological Survey of Namibia (2008) (Figure 3.1), is not consistent with the accepted regional stratigraphy of the Otavi Mountain Land by Kamona and Günzel (2007) (Figure 3.2). The Chuos Formation is associated with the Berg Aukas Formation which hosts the cap carbonates of the diamictite rather than the Maieberg Formation as shown on the modified regional geological map (Figure 3.32).

Previously, the base metal mineralization has been reported to occur at the contact of the Askevold Formation and the Abenab Subgroup (Adamson, 1960; Petzel, 1992; Kamona and Günzel, 2007). As there has been no subdivision of the Abenab Subgroup in the area around the Deblin Copper Mine, it was not clear as to which formation hosts the local base metal mineralization and contrasting ideas developed for the Deblin Copper Mine area. Adamson (1960), argued that the mineralized carbonates in the area around the Deblin Copper Mine belong to the Gauss Formation, whereas Kamona and Günzel (2007) suggested that the dolomites above the mineralized contact zone constitute the Chuos Formation of the Abenab Subgroup. The presented data indicate that the base metal mineralization is at the unconformable interface between the Askevold Formation metavolcanic rocks and the Chuos Formation dolomite. This study established that the Chuos Formation in the southern Otavi Mountain Land hosts the base metal mineralization and these findings are important to the identification and location of economic mineral occurrences in the stratigraphy of the Otavi Mountain Land.

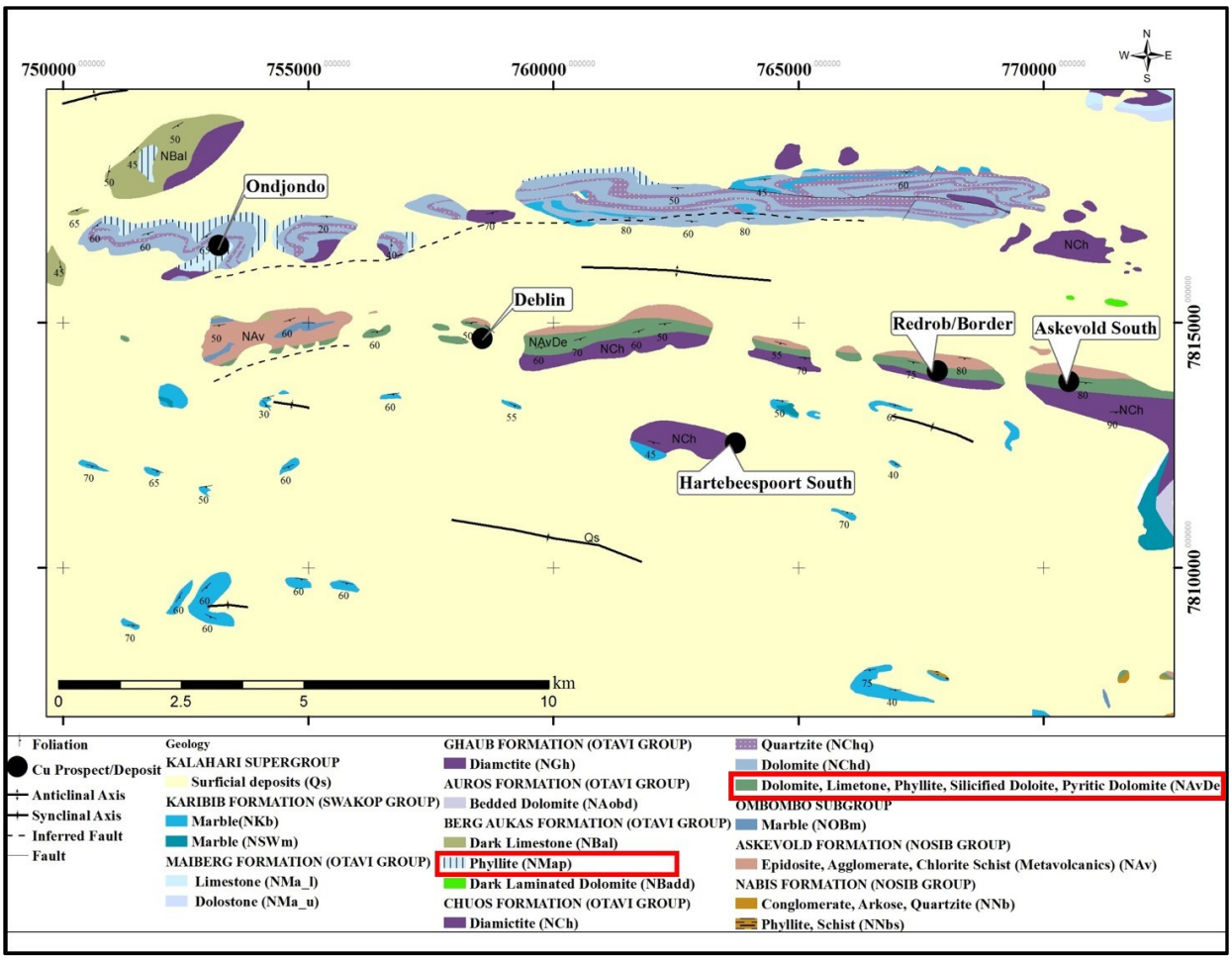


Figure 3.32 Regional geological map of the southern Otavi Mountain Land with the updated stratigraphy based on the petrological data from the Deblin Copper Mine area (Figure 3.3). The updated stratigraphy is indicated with a red rectangular box. Modified after the 1: 250,000 maps of Smit (1959) and the Geological Survey of Namibia (2008).

The Ombombo Subgroup in the Kaokoveld, west of the Otavi Mountain Land comprises largely siliciclastic sediments such as sandstone, greywacke, conglomerate and ferruginous shale (Söhnge, 1957; Miller, 2008). There is no evidence to confirm the presence of the Ombombo Subgroup rocks in the study area based on the dolomites and limestones only, which possess features such as stromatolites, that are ubiquitous in other well understood local stratigraphic units. Thus, this study supports previous studies (e.g Miller, 2008), which stated that the Ombombo Subgroup is absent in the southern Otavi Mountain Land.

Structure and Metamorphism

On a regional scale, the study area lies on an east-west southern limb of an anticline and the rocks dip at 44º-85º south. In outcrop, the most distinguishable structures include the deformed mafic clasts of the agglomerate that are elongated along strike, large scale kink folds in the mafic metavolcanic as well as brecciation in the dolomite. Other observable, though not obvious structures at the mesoscopic scale are the northeast-trending lineaments that can be inferred from the structural contacts between different rock types. At the microscopic scale, the common structural feature observed in all the metavolcanic rocks in this area is the conspicuous primary foliation (S_1), which is a very important tool to unravel the tectonic and metamorphic evolution of the study area. Both continuous and spaced foliations were observed in the metavolcanic rocks of the Askevold Formation. The dominant spaced foliation type is the disjunctive cleavage, though there are cases where poorly developed shear band cleavage C-type can be recognized, giving rise to the S-C fabric which developed during shearing. The S-C fabric suggests that the rocks are located within a regional shear zone. The presence of the shear zone is corroborated by the presence of other microscopic shear sense indicators such as the quartz porphyroclasts and lens-shape quartz-calcite veins with a mineral fish morphology, concentrated along the C surfaces in the agglomerate.

Detailed microscopic observations of the dolomite indicate two deformation types (brittle and ductile). Brittle deformation is evident by breccia textures (fractures, grain size reduction and angular fragments) in the dolomite breccia in the upper part of the stratigraphy, whereas ductile deformation is exhibited by quartz and carbonate recrystallization in the silicified dolomite. Besides the dolomite breccia and felsic volcanic (metarhyolite) breccia, other lithologies are deformed in a ductile manner. The identification of both brittle and ductile deformation within the shear zone is a result of competency difference between the carbonates and the underlying metavolcanic rocks. The presence of undulose extinction in quartz and carbonates (Figure 3.13b), and recrystallized quartz and carbonate grains are indicative of grain boundary migration. Undulose extinction is a characteristic structure in quartz that is deformed at low temperatures (below 300 °C) (Passchier and Trow, 2005), whereas in coarse-grained carbonates (e.g calcite), undulose extinction is an indication of deformation by fracturing and cataclastic flow at very low grade conditions (Kennedy and Logan, 1998).

According to Passchier and Trow (2005), the C-planes in the S-C fabric are parallel to shear zone boundaries. The deformation events in the Otavi Mountain Land are well represented by regional linear structures. The deposition of the Otavi Mountain Land stratigraphy and the associated volcanism occurred between 746 Ma and 550 Ma, and affected by three deformational events of which D_1 and D_2 occurred at about 650 Ma (Miller, 1983; Deane, 1995; Laukamp, 2006) and 512 ±7 Ma (Lehmann et al., 2016), respectively. Shearing in the rocks from the study area is probably related to D_2 deformational event which created thrust faults in the southern part of the Otavi Mountain Land.

The obvious metamorphic minerals in these rocks are biotite, sericite and chlorite and are indicative of greenschist facies metamorphism. The low grade metamorphism characterized by low temperature and pressure conditions is corroborated by low grade deformation features (e.g undulose extinction in the quartz and carbonate grains). Greenschist assemblages for these rocks are in accordance with the findings reported by previous workers (Miller, 1983; Deane, 1995; Miller, 2008), who noted low greenschist facies metamorphism in the entire Otavi Mountain Land. Although, names such as dolomite and limestone are maintained, textural petrographic observations indicate that these rocks are metamorphosed at very low grades. Besides the felsic volcanic breccia, most metavolcanic rocks exhibit schistosity and their primary volcanic textures are not preserved. The mineralogy of these units indicate that they are mafic metamorphosed volcanics. Accordingly, the following names are suggested: sericite-chlorite schist (tuff); sericite-chlorite schist (mafic metavolcanic), meta-rhyolite breccia (felsic volcanic breccia) and meta-agglomerate (agglomerate), although it has its original, but deformed mafic clasts.

Alteration

Most of the rocks of the study area have been hydrothermally altered with early sericitic alteration overprinted by chloritic then, silicic alteration with dominant carbonatization overprinting all earlier assemblages. Based on petrographic investigations it is noted that the primary mineral phases have been altered and replaced by secondary sericite, chlorite, carbonates and crystallized quartz. In addition, chlorite, carbonate and sericite occur as overgrowths on earlier minerals while all units record more than one generation of quartz-calcite veins. Carbonatization (dolomitization) alteration is dominant and occurs in all the rock types. It is commonly represented by carbonate

overgrowths on earlier mineral phases. In cases where carbonates replace other minerals it has irregular grain boundaries, however, there are also cases where calcite shows smooth grain boundaries, implying recrystallization. Where carbonates overgrow the primary foliation (S_1), it is a clear indication that these carbonate minerals postdate the deformation responsible for S_1. It should be stressed that there are cases of pre-deformation carbonates as indicated by carbonate minerals cut across by the foliation in the tuff (sericite-chlorite schist). Carbonatization alteration seems to be regionally extensive in this area and not always related to mineralization.

Chloritic alteration is the second most common type of alteration. It occurs in the contact of the mineralized zone but increases drastically downward into the agglomerate. The metavolcanic rocks are progressively more intensely chloritized. Chloritic alteration is also represented by various cases where chlorite replaces sericite. Sericitic alteration is prominent in both the tuff (sericite-chlorite schist) and silicified dolomite. Sericitic alteration is also present in the main mineralized zone (at the silicified dolomite-agglomerate contact). These observations corroborate the findings by Petzel (1991) when he reported that the mineralization at the Deblin Copper Mine is associated with chlorite–sericite alteration zones in metavolcanic schists. Silicification is represented by fine-grained recrystallized quartz with smooth grain boundaries and is dominant in the silicified dolomite. Both silicification and carbonatization occur as hydrothermal quartz-calcite veins and are in close association with vein-type sulphides. Additionally, chloritization and sericitization seem to be related to the copper sulphide mineralization. The relationship between alterations and mineralization resulted from circulation by the base metal bearing hydrothermal fluids which reacted with the host rocks. The fluid-rock interaction and alteration changed the host rocks mineralogy by introducing chlorite and sericite minerals as well as sulphides. Later sulphides precipitated within the quartz-calcite hydrothermal veins during carbonatization and sericitization alteration.

Chapter 4

Mineralization of the Deblin Copper Mine area

4.1 Introduction

In the southern Otavi Mountain Land, numerous volcanic-hosted strata-bound copper deposits have been recognized (Smit, 1959; Adamson, 1976; Petzel, 1991; Laukamp, 2006; Kamona and Günzel, 2007; Golden Deeps Limited, 2012), forming an economically important series of copper occurrences termed the "Askevold Trend" in Kombat South. Studies on the Deblin Copper Mine by many researchers have resulted in a large set of data, but also controversial interpretations. Early studies noted similarities with volcanic hosted massive sulphide deposits (Adamson, 1976; Petzel, 1991; Kamona and Günzel, 2007; Golden Deeps Limited, 2012), whereas Golden Deeps Limited (2013) proposed a shear-hosted hydrothermal Iron Oxide Copper Gold style mineral assemblage. Despite a sound theoretical understanding of the copper sulphide occurrence in the area around the Deblin Copper Mine, the mineralization style is still poorly understood. Undoubtedly, the mineralization style and deep ore prospecting in this area are still worthy of further research. This chapter describes the ore mineralogy, ore textural relationships, and the paragenetic sequence of the sulphide phases present together with, the relationship between the copper sulphide mineralization and the host rock.

4.2 Previous Work

A group of international and local researchers (Adamson, 1976; Emslie, 1979; Innes and Chaplin, 1986; Lombaard et al., 1986; Misiewicz, 1988; Petzel, 1991; Pirajno and Joubert, 1993; Kamona et al., 1999; Melcher et al., 2003; Laukamp, 2006; Kamona and Günzel, 2007; Nangolo, 2014) have conducted a lot of theoretical and applied research in the Otavi Mountain Land base metal province because it has typical MVT metallogenic characteristics and a huge amount of metal resources. The Otavi Mountain Land is characterized by largely hydrothermal carbonate rock-hosted ore systems. Furthermore, these ore systems can be subdivided into two broad types of mineralization (a) Tsumeb-type containing Cu, Pb, Zn, Ag, As, Ge, Cd and Ga and, (b) Berg Aukas-type characterized by ores containing Pb, Zn and V (Lombaard et al., 1986; Innes and

Chaplin, 1986; Hughes, 1987; Misiewicz, 1988; Pirajno and Joubert 1993; Laukamp, 2006; Kamona and Günzel, 2007). The small, low-grade volcanic-hosted copper deposits are the least common base metal deposits. These copper deposits occur with minor gold and display low grades (not more than 2.6 wt.% Cu and 0.6 g/t Au) (Petzel, 1991; Kamona and Günzel, 2007). The volcanic-hosted copper deposits are mainly distributed in the southern part of the Otavi Mountain Land, closely related to the Askevold Formation metavolcanic rocks. As a result, the southern Otavi Mountain Land is considered to be highly prospective for stratabound volcanogenic base metal sulphide ore bodies. These copper deposits were suggested to be the metal sources for the overlying Otavi Group sediment-hosted copper deposits (Miller, 1983; Pirajno and Joubert, 1993; Maiden and Hughes, 2000).

Exploration for economic-grade copper deposits in the southern Otavi Mountain Land stratigraphy has been undertaken in Kombat South historically and continues at present. This exploration has contributed greatly to stratigraphic and petrological studies of the Deblin Copper Mine area. The mineralization is observed at different intervals within the local stratigraphy, but for the most part, is located at the contact of the Askevold Formation metavolcanic rocks with the overlying Abenab Subgroup carbonates. In the Kombat South area, the most important volcanic-hosted copper deposit is at the Deblin Copper Mine (Neuwerk deposit).

The Deblin Copper Mine was discovered by Falconbridge Exploration Limited in 1970. Falconbridge Exploration Limited (as cited in Adamson, 1976) described the Deblin Copper Mine as a small body of base metal mineralization with an estimated tonnage of 260 000 t at 2.6% Cu (Adamson, 1976; Schneider and Seeger, 1992 in Kamona and Günzel, 2007; Golden Deeps Limited, 2012). Subsequently, Falconbridge Exploration Limited dug numerous exploration trenches. Thereafter, a 2 m diameter concrete-lined circular shaft (Figure 4.1) was sunk through the hanging wall dolomite (Adamson, 1976), but no mineralization was encountered (Golden Deeps Limited, 2012). In 1975, the shaft was affected by a strong flood event and hence the mine development stopped without any production records (Adamson, 1976; Golden Deeps Limited, 2012). According to Adamson (1976), Tsumeb Corporation Limited conducted geological, geochemical and geophysical surveys in the study area and other parts of the Kombat South to

investigate the extension of copper sulphide mineralization at other prospects within the Askevold Trend.



Figure 4.1 The Deblin Copper Mine concrete-lined circular shaft, grid reference 758551 mE, 7814737 mN.

Petrographic studies based on outcrop descriptions, one polished thin section of the mineralized calcite-sericite-chlorite schist and 13 thin sections of the same schist and other rock types by Adamson (1976) indicated the presence of 10-20% disseminated sulphide in a calcitic groundmass. The sulphides were dominated by pyrrhotite which enclosed anhedral grains of chalcopyrite with minor amounts of pyrite and bornite. The sulphides were unstrained and appeared to have formed with or after the present silicate and carbonate phases. Adamson (1976) observed two stratigraphically distinct zones of mineralization: (i) in the contact zone located on the Abenab Subgroup dolomite-Nosib Group schist contact and (ii) the lower zone associated with marble or dolomite lenses within the chlorite schist of the Askevold Formation. Adamson (1976) concluded

that base metal mineralization at the Deblin Copper Mine and possibly in other parts of the Askevold Formation is of a stratiform volcanic marine association. Petzel (1991) described in detail the occurrence of copper mineralization at both the Deblin Copper Mine and Askevold Copper prospect and established that both have significant copper mineralization associated with chlorite-sericite alteration zones in the Askevold Formation metavolcanic schists at the same stratigraphic position, which is the Nosib Group-Otavi Group contact zone. The mineralization is closely associated with conformable barite layers of possible volcanogenic origin (Petzel, 1991). In addition, some copper sulphides occur in fractures within the overlying dolostones.

More recently, an increase in the price of copper triggered another exploration cycle in the area around the Deblin Copper Mine. Extensive exploration programs were jointly undertaken by Golden Deeps Limited and Sabre Resources Namibia to discover copper rich VMS deposits along the Askevold Trend, similar to those at Golden Grove and Doolgunna in Western Australia. Golden Deeps Limited (2012) reported results from geological, geochemical and geophysical surveys that were conducted during the Tsumeb Corporation Limited exploration programs in the area around the Deblin Copper Mine. The surveys were aimed at confirming the grade from the drill intercepts reported by Falconbridge Exploration Limited in the 1970s, thus, getting a deep insight into the geological, structural and mineralogical aspects of the deposit as well as understanding the mineralization geometry. A four reverse circulation (RC) drilling programme revealed that the mineralization extends up dip within 80 m of surface and is open both along strike and at depth (Golden Deeps Limited (2013).

In 2013, a diamond drilling programme completed 3 holes (381.10 m in total) and the first two drill holes (DBDD0001 and DBDD0002) have successfully intersected copper sulphide-bearing mineralized zones with significant gold close to the contact between the underlying metavolcanic rocks of the Askevold Formation and the overlying carbonates of the Abenab Subgroup as shown in Figure 4.1. Golden Deeps Limited (2013) created a cross section to illustrate the morphology of the orebody and its structural controls. Golden Deeps Limited (2013) interpreted that mineralization is associated with a fault zone at the contact between the metavolcanic rocks and the carbonates (Figure 4.1).

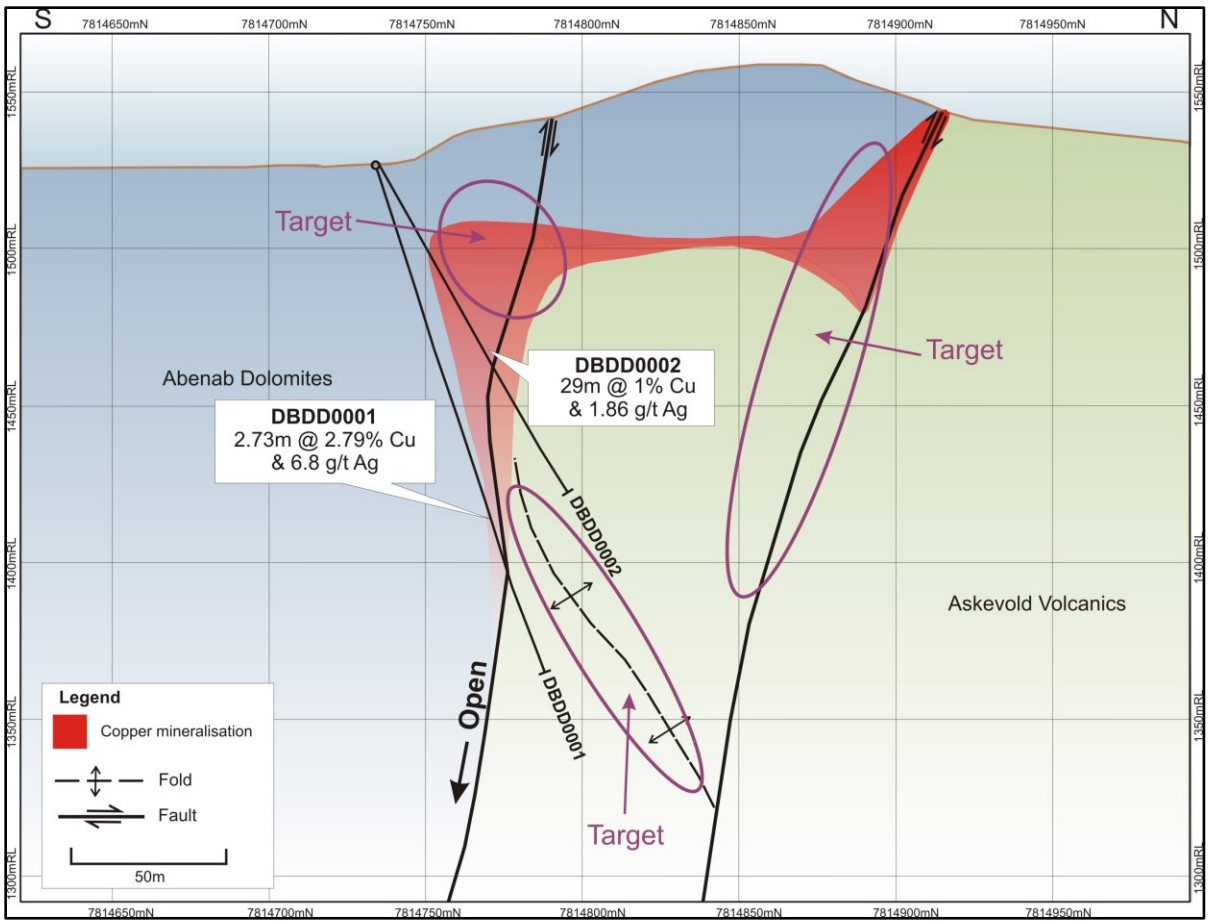


Figure 4.2 Cross section at the Deblin Copper Mine showing the modelled orebody morphology, structural interpretation, orientation of the drill holes DBDD0001 and DBDD0002 and drill targets (Golden Deeps Limited, 2013).

4.3 Current Work

4.3.1 Methodology

During fieldwork campaigns, attempts were made to identify mineralization in outcrops to propose a descriptive mineralogy of the copper mineralization in the study area. In addition, detailed drill core lithological logging enabled the identification of the mineralized intervals of the drill cores acquired from the study area, recently drilled by Sabre Resources Namibia (Appendix F). Ore bearing samples were collected from the mineralized zones of the two diamond drill cores: (i) DBDD0001 and (ii) DBDD0002. A total of 115 polished thin sections were prepared from these drill cores. Thereafter, the mineral assemblages were studied in the polished thin sections using a petrographic microscope with both transmitted and reflected illumination (Appendix G). The

microscopic study was performed in the Petrology Laboratory of the School of Geosciences, University of the Witwatersrand.

4.3.2 Hypogene Mineralization

The primary sulphide mineral assemblage of the ore consists of chalcopyrite, pyrite and sphalerite with low concentrations of bornite. Covellite is the only sulphide of secondary origin. The principal gangue minerals are carbonates and quartz with subordinate chlorite, sericite and biotite. Copper sulphide mineralization in the Deblin Copper Mine area is relatively irregularly distributed within the stratigraphy. The sulphides are somewhat irregularly distributed at different levels in the stratigraphy, but there are major occurrences in the silicified dolomite and dolomite breccia and minor occurrences observed in the agglomerate. The overall mineralized interval in drill core DBDD0001 is about 3.27 m thick and contains three discrete copper sulphide-bearing layers that are 0.12 m, 1.15 m and 2 m thick (from bottom to top). An overall interval of 1.87 m was observed in drill core DBDD0002 and the thicknesses of the individual layers are 0.53 m and 1.34 m (from bottom to top). Normally, the host rocks in the vicinity of the mineralized zones are sericitized and chloritized.

At least four mineralized zones were recognized in the drill cores from the Deblin Copper Mine area as shown in Figure 4.3. The first zone is below the agglomerate-silicified dolomite contact located between 157.5 m and 157.62 m depth in DBDD0001. Sulphides in this mineralized zone consists of chalcopyrite (~50 %) with subordinate pyrite (~40%), sphalerite (~8%) and rare bornite (~2%) hosted in the quartz-calcite vein in the highly chloritized agglomerate. The amount of copper sulphide mineralization in the agglomerate is less than that in the overlying dolomites. The second and main copper sulphide mineralized zone is located at the base of the silicified dolomite through the contact between the silicified dolomite of the Chuos Formation (Abenab Subgroup) and the underlying agglomerate of the Askevold Formation. The mineralized zone is highly sericitized and moderately chloritized, giving the host rock a greenish appearance. This mineralized zone occurs in both DBDD0001 and DBDD0002 between 136.58 m and 137.73 m depth and, 96.18 m and 96.71 m, respectively. In DBDD0001, the sulphides consist of chalcopyrite (~65%) with moderate pyrite (~20%), minor sphalerite (~10%), bornite (~4%) and

trace covellite (<1%). On the contrary, in DBDD0002, the sulphides comprises chalcopyrite (~55%) with moderate pyrite (~30%), minor sphalerite (~10%), and bornite (~5%).

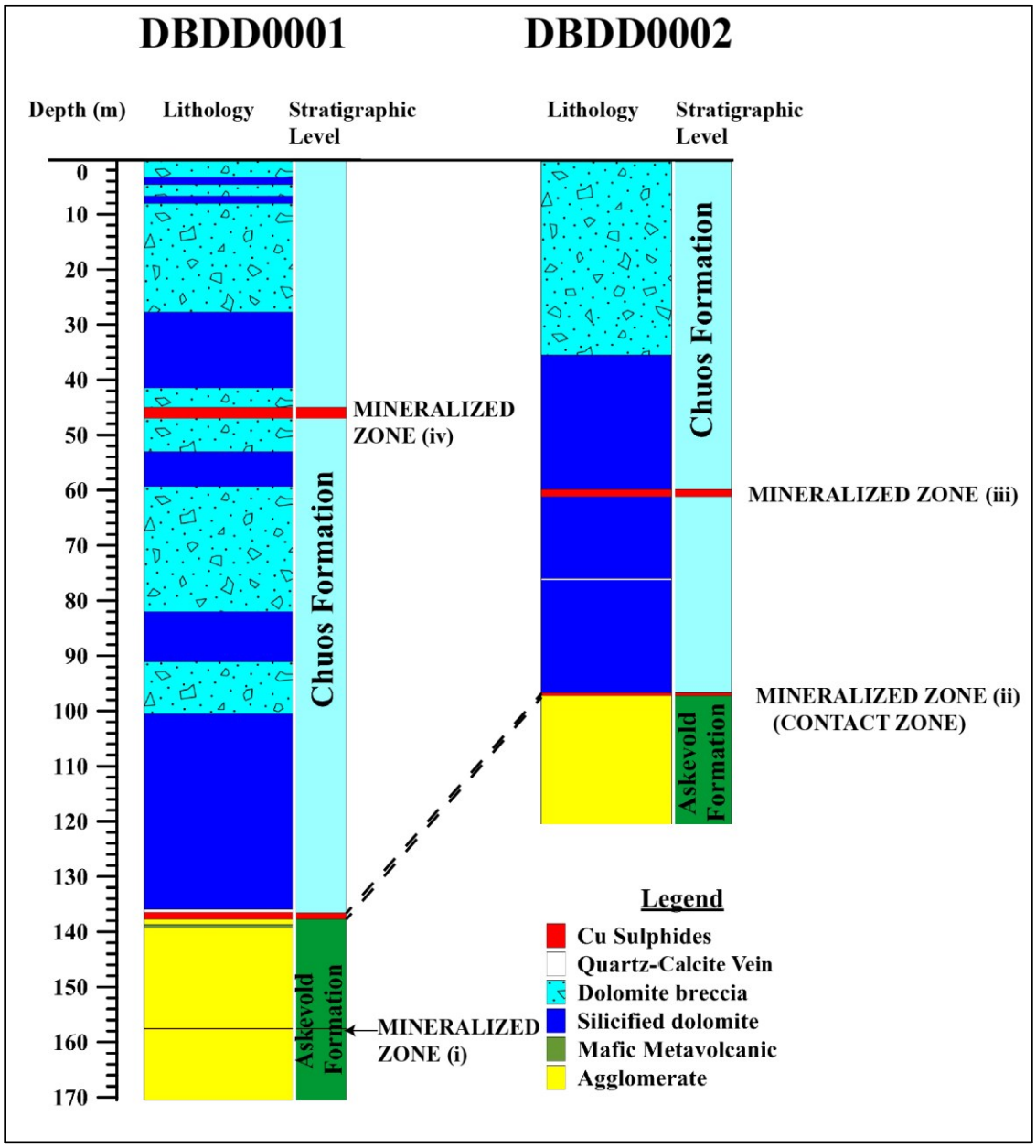


Figure 4.3 Lithostratigraphic logs from the Deblin Mine area showing the four ore-bearing horizons. DBDD0001 has a maximum depth of 170.5 m and intersected three mineralized zones in the agglomerate, silicified dolomite and dolomite breccia. DBDD0002, by contrast, has a maximum depth of 120 m and records two mineralized zones located in the silicified dolomite and dolomite breccia. Drill hole DBDD0001 is located at 758547 mE, 7814734 mN, whereas drill hole DBDD0002 is located at 758547 mE, 7814735 mN.

The third mineralized zone is the second most sulphide-rich interval in the silicified dolomite which is at a depth between 59.34 m and 60.68 m in DBDD0002. The sulphides consist of chalcopyrite (~60%) with moderate pyrite (~35%), minor sphalerite (~3%), and bornite (~2%). The fourth mineralized zone is in the uppermost part of the borehole core stratigraphy and was intersected in DBDD0001 from 45 m to 47 m depth. The sulphides consist of pyrite (~48%) with moderate chalcopyrite (~35%), minor sphalerite (~10%), bornite (~6%) and covellite (<1%).

4.3.3 Types of Mineralization

Detailed drill core logging and conventional optical petrography of the mineralized intervals of DBDD0001 and DBDD0002 drill cores (Figure 4.3), allowed the subdivision of the hypogene sulphide mineralization into two types: (a) disseminated and (b) vein.

a) Disseminated type

This mineralization type is characterized by disseminations of chalcopyrite and pyrite associated with > 90 % carbonate and silicate gangue minerals in the host rock groundmass. Both chalcopyrite and pyrite disseminations are common in the silicified dolomite and dolomite breccia (Figure 4.4). In addition, pyrite disseminations commonly occur in the agglomerate (Figure 4.5). In rare cases chalcopyrite occurs with subordinate bornite. Disseminated sulphides occur as discrete euhedral pyrite grains and weakly to strongly elongated grains of both chalcopyrite and pyrite grains in the host rock. In some cases, they are randomly distributed and lack a preferred orientation. This type of mineralization is found in all the mineralized zones within the carbonates and at the contact between the silicified dolomite and the underlying agglomerate. This mineralization type accounts for ~30% of the total sulphide observed in the drill cores.

a) Vein type

This mineralization type is the most prominent and consists of chalcopyrite and pyrite hosted in quartz and quartz-calcite veins. The veins range between <1 mm and 100 mm in thickness. Also, this mineralization type includes chalcopyrite and pyrite veinlets that range from <1 mm to ~5 mm in width. In some places, chalcopyrite rarely occurs as stringers. The sulphide veinlets occasionally exhibit cross-cutting relationships and cross-cut not only each other but also the disseminated sulphides and chalcopyrite stringers (Figure 4.6). These sulphide veinlets have an anastomosing

configuration and are generally polydirectional (Figure 4.7-4.9). The sulphide veinlets are highly ductile deformed with buckled forms and microfolds (Figure 4.9).

In some cases, the sulphide veinlets surround fragments of carbonate grains and silicate gangue minerals, usually dominated by quartz. The sulphide-bearing quartz-calcite veins constitute 5-10% of the host rock. Moreover, both pyrite and chalcopyrite veinlets contain accessory discrete euhedral to subhedral pyrite grains. Chalcopyrite veinlets, by contrast, contain rare subordinate bornite grains. This type of mineralization is common in the upper part of the carbonates and in the main mineralized zone at the contact between the silicified dolomite and the agglomerate. This mineralization type accounts for ~65% of the total sulphide mineralization observed in the Deblin Copper Mine drill cores.

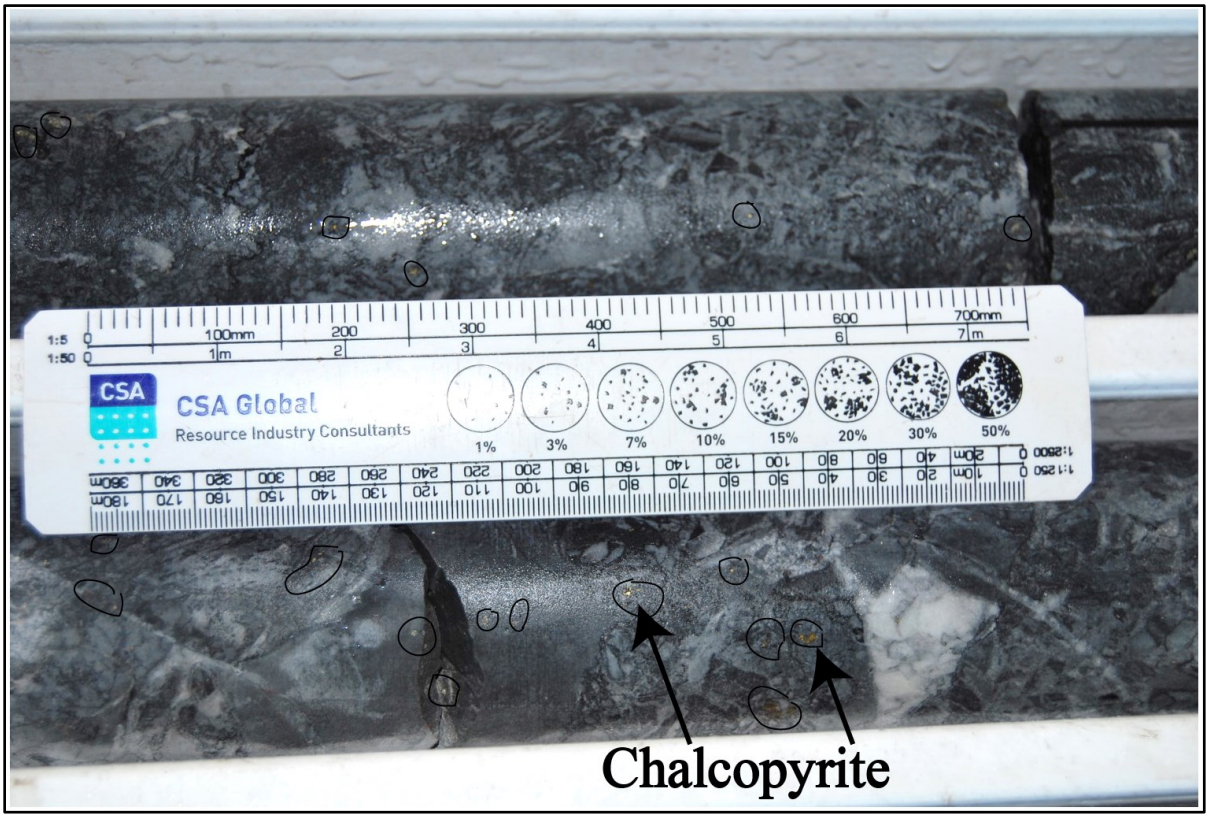


Figure 4.4 Disseminated chalcopyrite grains (enclosed in black circles) in the dolomite breccia. DBDD0001: 45.41 m – 46.20 m.

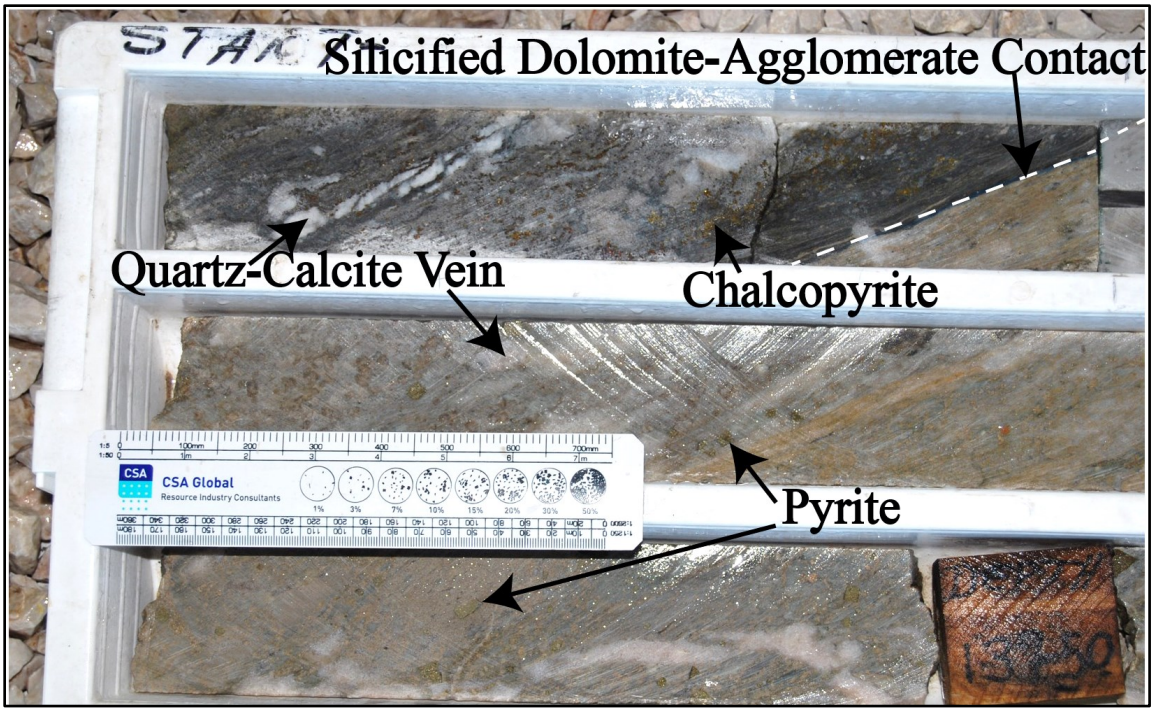


Figure 4.5 Pyrite disseminations in the agglomerate below the contact and vein type mineralization with chalcopyrite in the silicified dolomite above the contact. DBDD0001: 137.41 m – 139.50 m. The quartz-calcite veins in the agglomerate are not mineralized.

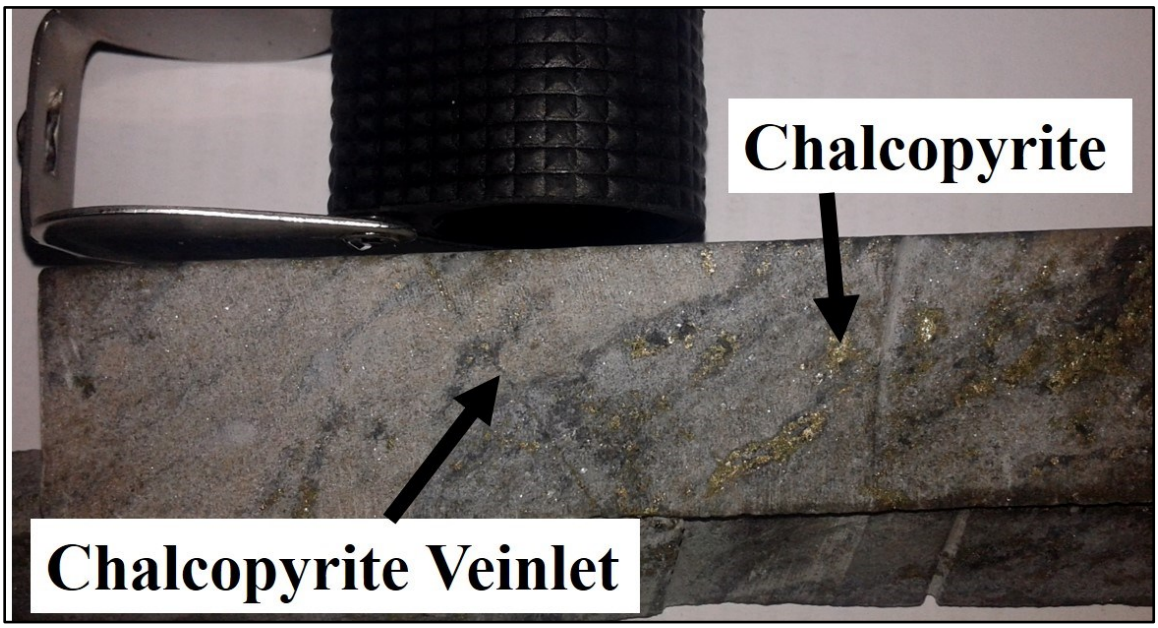


Figure 4.6 Stringer chalcopyrite cross-cut by later chalcopyrite veinlet in the silicified dolomite. DBDD0001: 82.20 m – 82. 40 m - DB1S10.

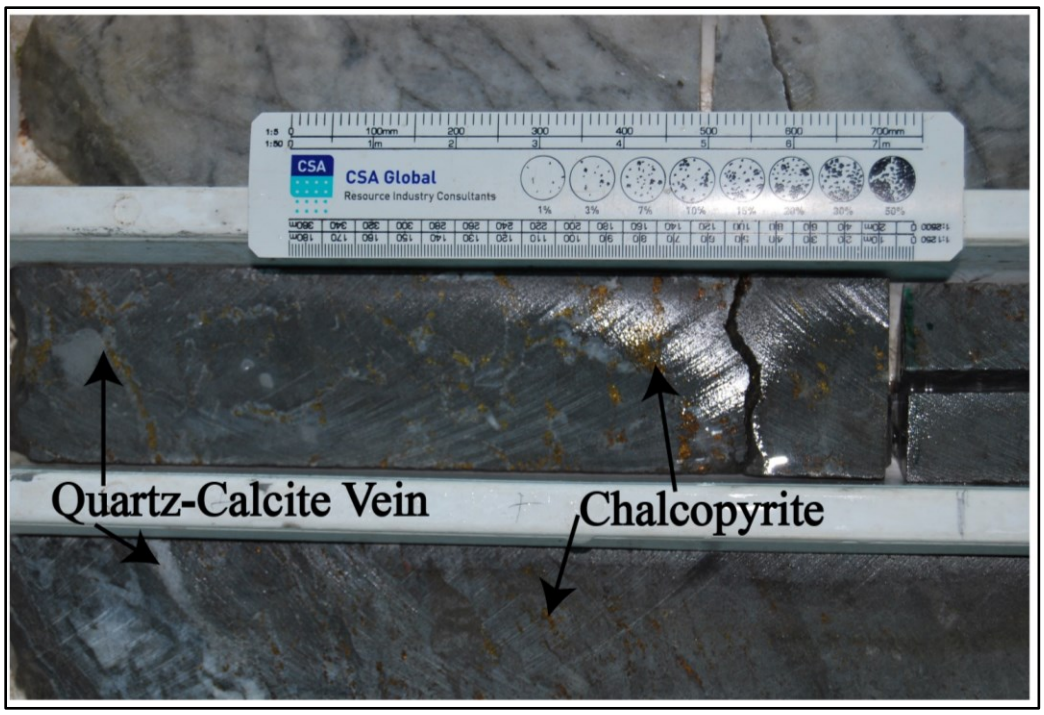


Figure 4.7 Chalcopyrite-bearing quartz-calcite veins, chalcopyrite veinlets and minor chalcopyrite disseminations in the silicified dolomite. DBDD0002: 59.15 m - 59.40 m.

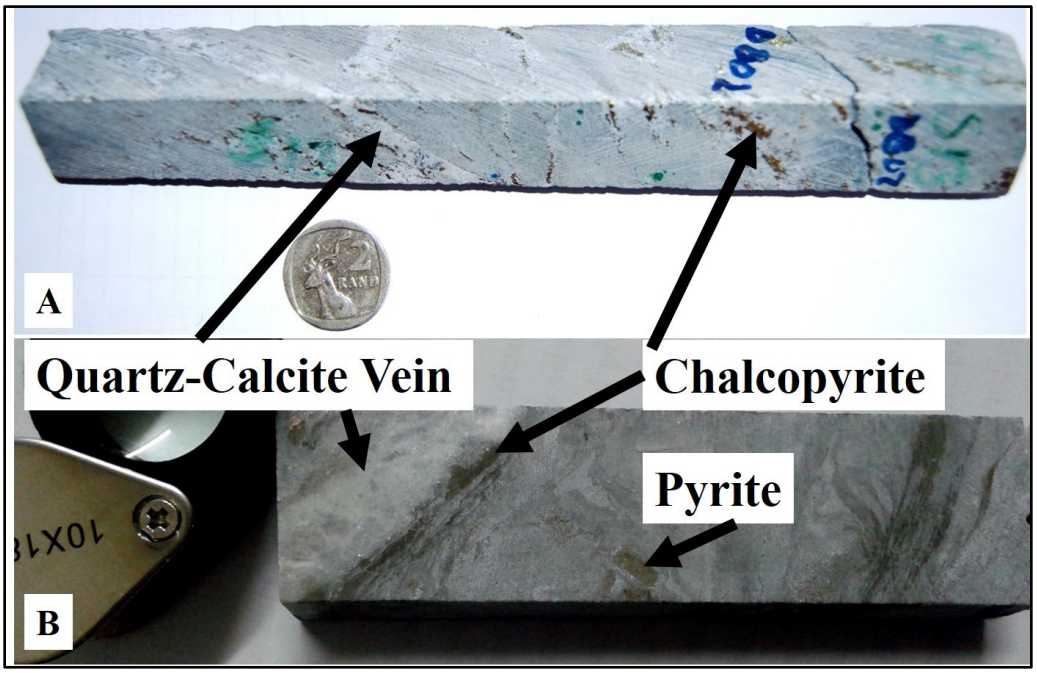


Figure 4.8 Drill core images of silicified dolomite showing vein type mineralization. A) Quartz-calcite vein-hosted chalcopyrite mineralization. DBDD0002: 84.00 m - 84.20 m - DB2S12. B) Convoluted chalcopyrite and pyrite bands, discrete euhedral pyrite grains in the matrix and a fabric-parallel quartz-calcite vein with chalcopyrite mineralization along the margin of the vein. DBDD0002: 72.62 m - 72.82 m – DB2S11.

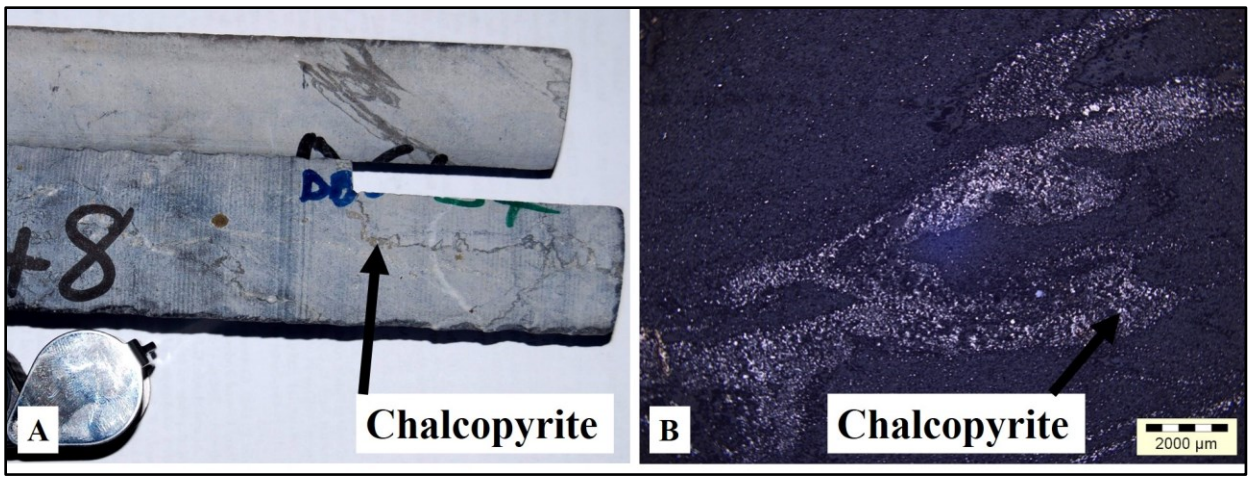


Figure 4.9 Photograph and photomicrograph of the folded sulphides in the silicified dolomite. A) Polydirectional, highly folded fine-grained chalcopyrite and pyrite veinlets. DBDD0001: 54.78 m – 54.98 m – DB1S7 (bottom sample); DBDD0001: 109.67 m – 109.87 m – DB1S15 (top sample). B) Highly folded chalcopyrite. DBDD0001 109.67 m – 109.87 m - DB1S15-D61 (Reflected Light).

4.3.4 Ore Mineralogy and Textures

a) Chalcopyrite

Chalcopyrite is a ubiquitous sulphide in all the mineralized zones of both drill cores (DBDD0001 and DBDD0002) and it is the most abundant ore mineral of the Deblin Copper Mine. Chalcopyrite ore forms veinlets and stringers, and it is hosted in quartz-calcite veins in the silicified dolomite, dolomite breccia and rarely in the underlying agglomerate. Chalcopyrite is also disseminated in the groundmass of the silicified dolomite and dolomite breccia. Chalcopyrite occurs as fine-to coarse-grained (0.12-0.44 mm) anhedral to subhedral crystals in association with commonly pyrite and sphalerite (Figure 4.10a), and rarely with bornite and covellite. The gangue minerals with the chalcopyrite ore are quartz and calcite. Chalcopyrite veinlets and matrix are normally corroded (Figure 4.10b) and display an intergrowth replacement texture. Chalcopyrite commonly replaces pyrite, mostly following the fractures in pyrite grains (Figure 4.10c-d) and, in other cases fine-grained chalcopyrite is frequently replaced by sphalerite, bornite and covellite.

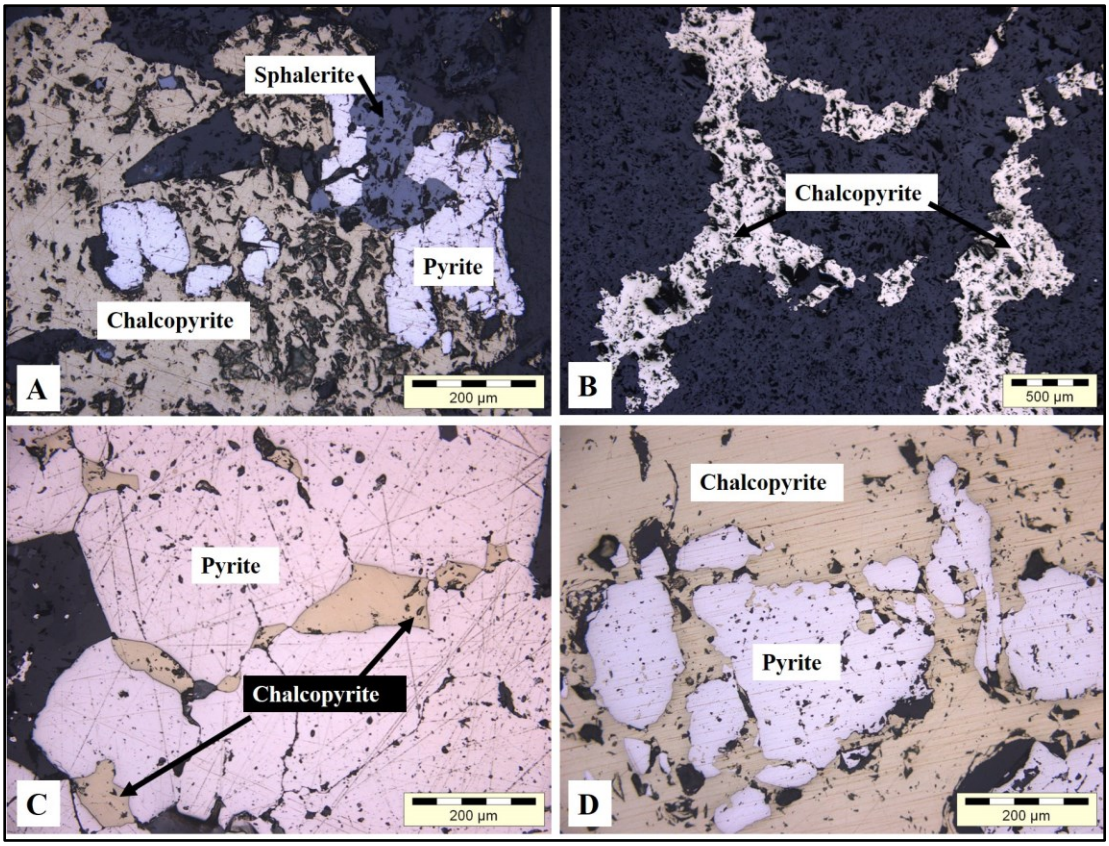


Figure 4.10 Reflected light photomicrographs showing chalcopyrite textures and replacements. A) Successive replacement of pyrite by corroded chalcopyrite. Also shown is both chalcopyrite and chalcopyrite cut by later sphalerite. DBDD0001: 137.22 m – 137.42 m – DB1S17-D69a (silicified dolomite). B) Corroded chalcopyrite veinlets. DBDD0001: 136.61 m – 136.81 m – DB1S16-D63e (silicified dolomite). C) Chalcopyrite veinlets infilling fine cracks of pyrite. DBDD0001: DBDD0002: 96.52 m – 96.71 m – DB2S17-D118c (silicified dolomite). The pinkish color in the pyrite grain is caused by the wrong field of light of the camera. D) Chalcopyrite largely replacing pyrite groundmass. DBDD0002: 59.87 m – 60.07 m – DB2S9-D104d (silicified dolomite).

Pyrite

Pyrite is subordinate to chalcopyrite in the sulphide ore-bearing quartz-calcite veins. Pyrite is also hosted as ubiquitous disseminations in the groundmass of the silicified dolomite, dolomite breccia and agglomerate, and it occurs in a variety of habits. Pyrite is widely distributed as anhedral to subhedral and euhedral grains. Deformed pyrite commonly displays brittle fractures that are filled by chalcopyrite, sphalerite (Figure 4.11a-b) and gangue minerals (Figure 4.11c). Detailed microscopic observations identified more than one stage of pyrite development. The first generation pyrite occurs as fine-grained (0.05-0.11 mm) anhedral, discrete disseminations in the

silicified dolomite and dolomite breccia. Although these pyrite microcrysts appear in all rock types, they tend to be concentrated in the silicified dolomite. Notably, in the agglomerate, pyrite is intensely altered to chlorite and highly fractured. In the agglomerate, pyrite grains are fine to coarse-grained (0.117-0.35 mm). In the second instance, pyrite commonly occurs as relatively larger subhedral to anhedral grains that are concentrated together with chalcopyrite and sphalerite in medium to coarse-grained quartz-calcite veins. Pyrite is partially to completely pseudomorphed by goethite, typically with a colloform texture (Figure 4.11d-Figure 4.12a). Where oxidation is complete, especially in the quartz-calcite veins, pyrite has been replaced by goethite, forming dark reddish brown veins.

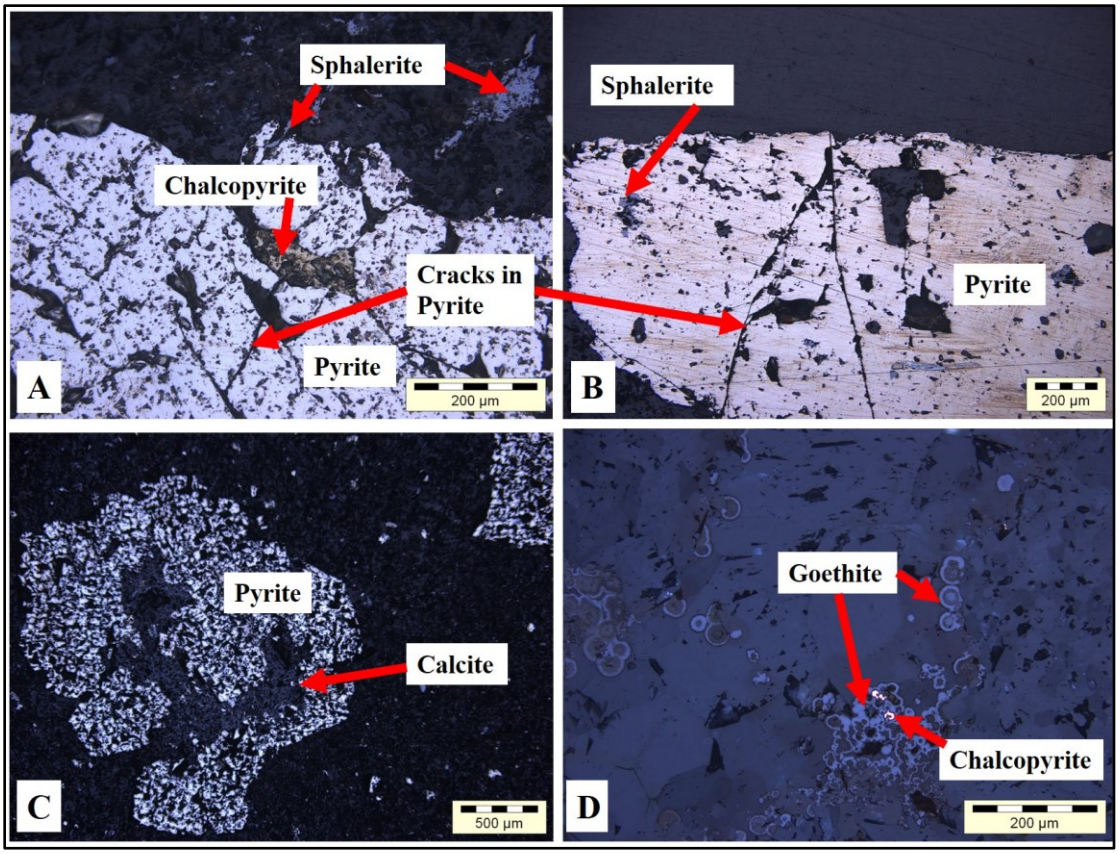


Figure 4.11 Reflected light photomicrographs showing replacement patterns of pyrite A) Fractured pyrite with minor chalcopyrite and sphalerite infills. DBDD0001: 137.73 m – 137.93 m – DB1S18-D75c (agglomerate). B) Outstanding fractures in pyrite with slivers of sphalerite and gangue minerals. DBDD0001: 139.10 m – 139.30 m – DB1S20-D80f (mafic metavolcanic). C) Highly corroded pyrite with cracks invaded by gangue minerals. Grid reference: 758497 mE, 7814882 mN – DB2b-D37 (pyritic dolomite). D) Colloform texture of goethite (formerly pyrite) and replacement of chalcopyrite by goethite. DBDD0001: 46.80 m – 47 m – DB1S6-D47g (dolomite breccia).

Sphalerite

Sphalerite is subordinate to chalcopyrite and pyrite in the sulphide ore-bearing quartz-calcite veins, where it is disseminated as anhedral grains. Sphalerite is not visible in hand specimen, however, in polished thin sections it is evident as anhedral to subhedral, very fine-grains (<0.03 mm), and commonly replaces pyrite and chalcopyrite (Figure 4.12b) or as fracture infills in pyrite. It mostly occurs as veinlets, exhibiting hydrothermal replacement of pyrite and chalcopyrite (Figure 4.12 c-d), and in places sphalerite is replaced by covellite.

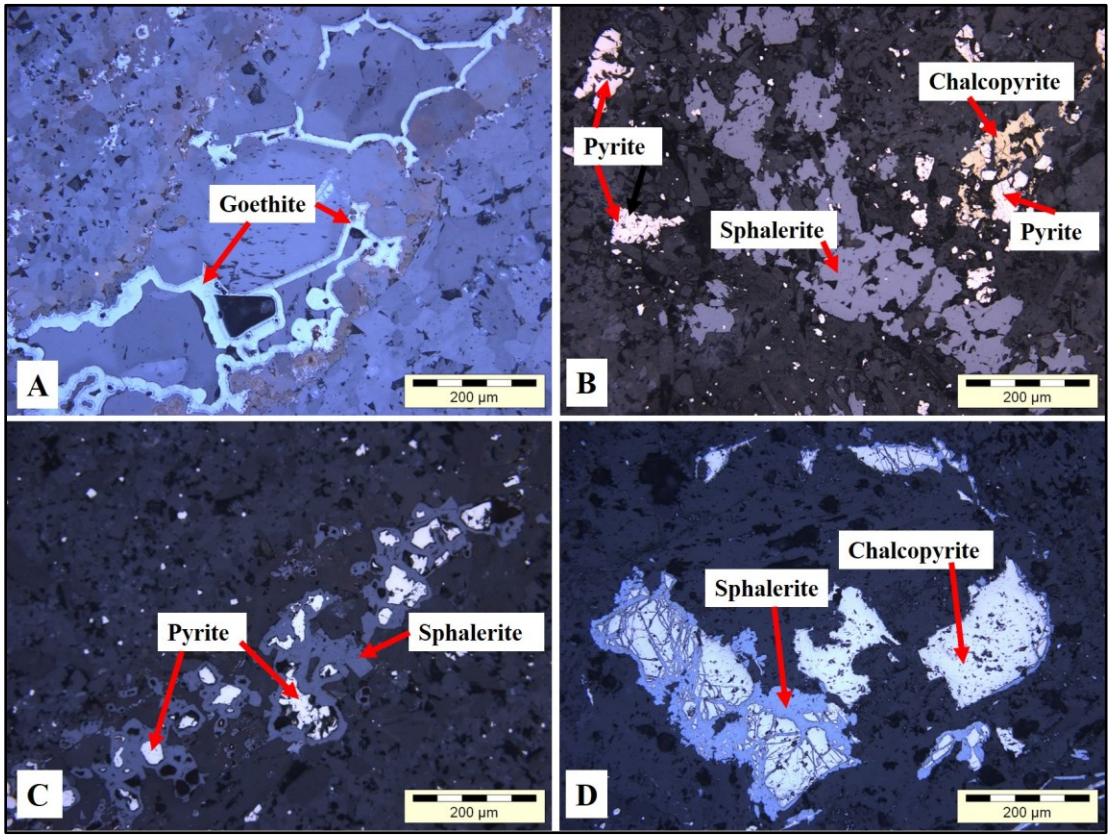


Figure 4.12 Reflected light photomicrographs showing the sphalerite texture and replacements. A) Goethite with colloform texture along the margins of quartz-calcite veins. DBDD0001: 46.80 m – 47 m – DB1S6-D47f (dolomite breccia). B) Sphalerite replacing both pyrite and chalcopyrite, whereas chalcopyrite is replacing pyrite. DBDD0001: 60.70 m – 60.88 m – DB1S9-D50c (dolomite breccia). C) Pyrite enclosed in sphalerite as a consequence of pyrite replacement by sphalerite. DBDD0001: 82.20 m – 82.40 m – DB1S10-D55e (silicified dolomite). D) Chalcopyrite groundmass transected by a network of sphalerite veinlets. Please note that sphalerite in this image appears light bluish because image was taken in the wrong field of light. DBDD0001: 46.80 m – 47 m – DB1S6-D46c (dolomite breccia).

Bornite

Bornite is a minor sulphide phase associated with sphalerite ore. Like sphalerite, bornite is only discernible in polished thin sections. Bornite is very fine-grained (<0.03 mm) and occurs as veinlets, which cross-cut chalcopyrite (Figure 4.13a). In addition, bornite displays brittle fractures filled by gangue minerals (Figure 4.13b).

Covellite

Covellite occurs in trace amounts and is of secondary origin in the main chalcopyrite ores. Like bornite, covellite is not visible in hand specimen and can only be described under the microscope and is less abundant than bornite. Covellite is very fine-grained (<0.02 mm) and replaces chalcopyrite (Figure 4.13c-d).

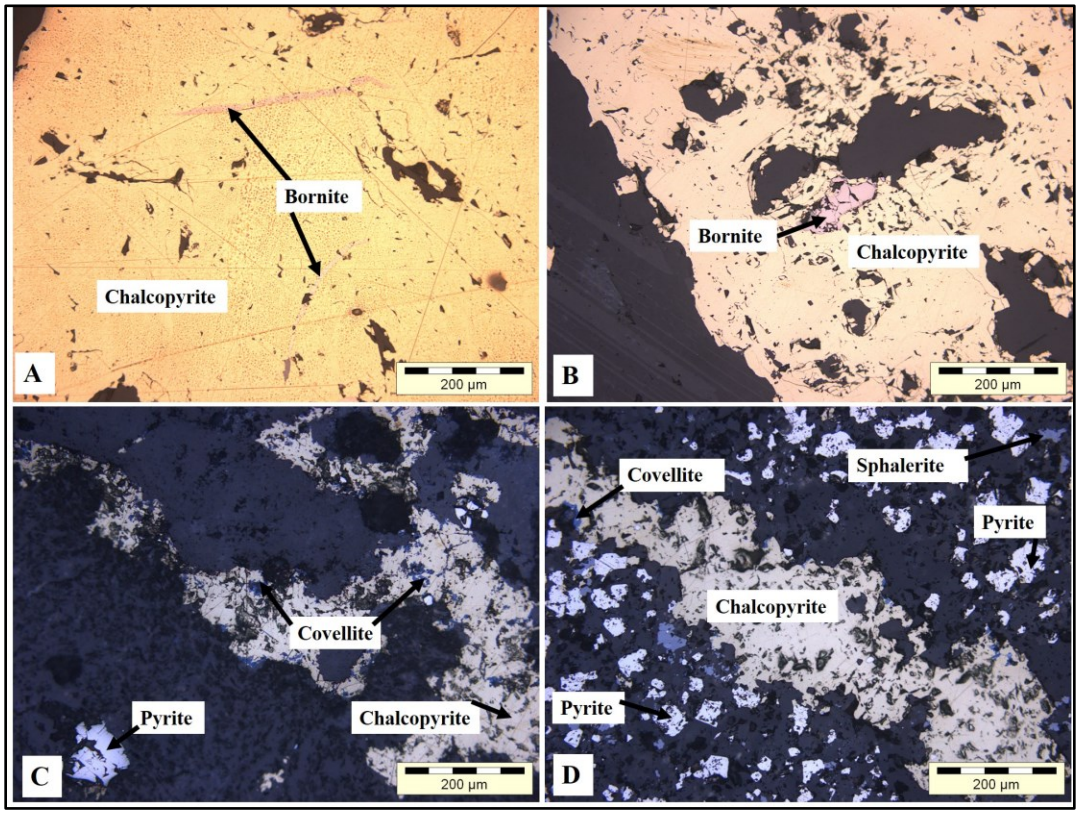


Figure 4.13 Reflected light photomicrographs showing textures and replacement patterns of bornite and covellite. A) Bornite veins cut-across chalcopyrite matrix. DBDD0002: 59.36 m – 59.56 m – DB2S7-D99d (silicified dolomite). B) Fractured bornite replacing chalcopyrite. In addition, the fractures in bornite are infiltrated by gangue minerals. DBDD0002: 59.36 m – 59.56 m – DB2S7-D100b (silicified dolomite). C) Fine-grained covellite replacing tarnished chalcopyrite. DBDD0001: 60.70 m – 60.88 m – DB1S9-D50a (breccia dolomite). D) Sporadic fine-grained covellite replacing chalcopyrite. DBDD0001: 109.67 m – 109.87 m – DB1S15-D61e (silicified dolomite).

4.3.5 Supergene Enrichment

Supergene enrichment in the Deblin Copper Mine area is poorly exposed, however, several mineral exploration trenches cutting through different rock types including the volcanic breccia (Figure 4.14a-b), silicified dolomite (Figure 4.14c-d) and chlorite schist indicate supergene malachite hosted in quartz and quartz-calcite veins. Ferric oxide minerals are abundant in the brown iron-stained rock outcrops (gossans), (Figure 4.14b&d), where they commonly occur as goethite replacing pyrite in pseudomorphs, whereas supergene sulphides are scarce and discernable only under the microscope such as covellite, which occurs as replacement of the primary sulphides.

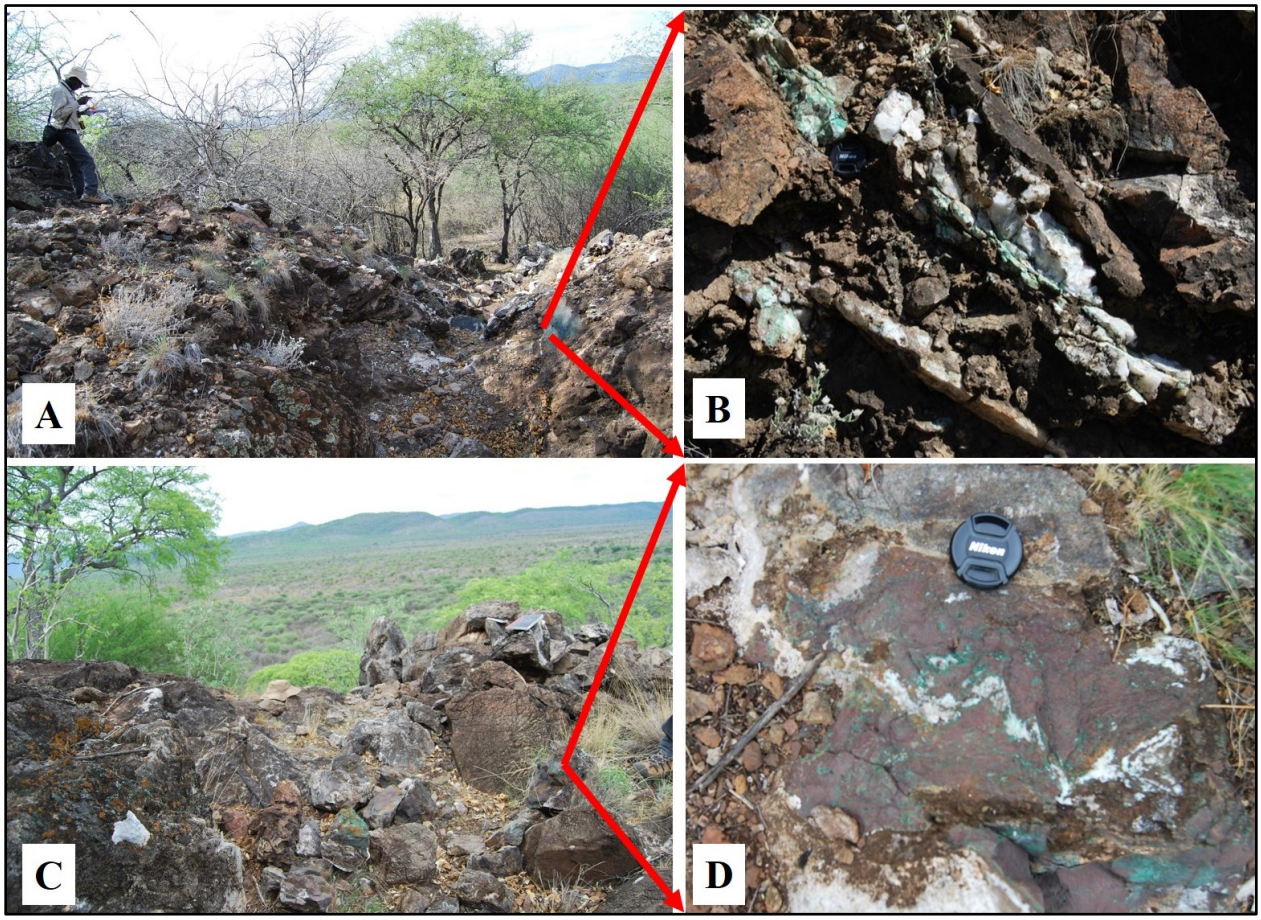


Figure 4.14 Field images of the exploration trenches showing supergene enrichment of malachite. A) A 20 m long, 4m wide and 1.5 to 2 m deep pink volcanic breccia exploration trench. B) Volcanic breccia outcrop with malachite in cross-cutting quartz veins. Grid reference: 758342 mE, 7815085 mN. C) A 12 m long, 5 m wide and ~8 m deep silicified dolomite exploration trench. D) Malachite and quartz-calcite veins hosted in a highly oxidized silicified dolomite. Grid reference 758747 mE, 7814817 mN.

4.4 Discussion

The Deblin Copper Mine ore is characterized by chalcopyrite as the main ore mineral with minor amounts of sphalerite and rare bornite. The main gangue minerals are quartz, calcite and dolomite. These sulphides occur primarily as vein and disseminated types. The vein type occurs in the agglomerate and the overlying silicified dolomite and dolomite breccia, while the disseminated type occurs in the silicified dolomite and dolomite breccia, but absent in the agglomerate. Although most of the mineralization appears to be hosted in the carbonates, these observations suggest that mineralization of the Deblin Copper Mine is hosted in both carbonates and metavolcanic rocks. The main mineralized zone, characterized by vein type mineralization is the contact zone of the agglomerate and the overlying silicified dolomite, which is in agreement with previous studies by Adamson (1976), Petzel (1991) and Kamona and Günzel (2007). Although the occurrence of the ore mineralization at this contact is in accordance with the mineralization model of the Deblin Mine orebody reported by Golden Deeps Limited (2013) as shown in Figure 4.2 in terms of the stratigraphic position, the thickness of the main zone of mineralization established by this study is not in agreement with the thickness reported by Golden Deeps Limited (2013). This is because the mineralized zones shown in the model by Golden Deeps Limited (2013) are based on geochemical assay data and include barren zones that are not yet drilled. The undrilled zones are indicated as drill targets. In contrast, this study determined the thickness of intersected mineralization based on the petrographic drill log data.

Golden Deeps Limited (2013) indicated that the mineralization is shear-hosted, which is in accordance with the findings of this study. Hence, this study confirmed that the Deblin Copper Mine lies within a shear zone, and the associated faults possibly acted as conduits for the metal-bearing hydrothermal fluids. The dominant vein type mineralization at the contact indicates that metal-bearing hydrothermal fluids migrated through fractures in the agglomerate, thereby resulting in precipitation of metals along the unconformable contact of the agglomerate and the overlying dolomite. Additional hydrothermal fluids continued to migrate upward and precipitated more metals in the overlying carbonates. Sulphide mineralization formed after the formation of the host rocks and commonly associated with hydrothermal events, which suggests that mineralization is epigenetic.

Multistage mineralization and extensive replacement as observed in the sulphide ores from the Deblin Copper Mine area are common in hypogene mineralization. Ore microscopic investigations indicate frequent replacement of all the hypogene minerals. According to Augustithis (1995), considering the formulas of bornite (Cu_2FeS_4) and chalcopyrite ($CuFeS_2$), the replacement of chalcopyrite by bornite could be accounted for by the introduction of Cu and lattice reorganization. Hence, this replacement represents relative enrichment in Cu. Progressive enrichment in Cu in the sulphides from the Deblin Copper Mine area is endorsed by patterns where: 1) Pyrite is replaced by chalcopyrite and 2) Chalcopyrite replaced by bornite. Similarly, the replacement of chalcopyrite by sphalerite depletes the amount of Cu, whilst Zn is introduced into the ore.

The paragenetic sequence of minerals from the ore veins and host rock groundmass are illustrated in Figure 4.15. Paragenetic relationships appear in three stages: early stage, main stage (ore (hypogene) and supergene. Each stage is characterized by unique mineral assemblages and textures (Figure 4.15). The early stage consists of disseminated anhedral to subhedral and euhedral pyrite and anhedral to subhedral chalcopyrite. The main hydrothermal stage has vein-hosted pyrite and chalcopyrite, which also occur as veinlets, postdated by sphalerite. Bornite precipitated at the end of the main sulphide mineralization as veinlets that cross-cut chalcopyrite groundmass. The supergene post-ore assemblage consists of covellite, malachite and goethite.

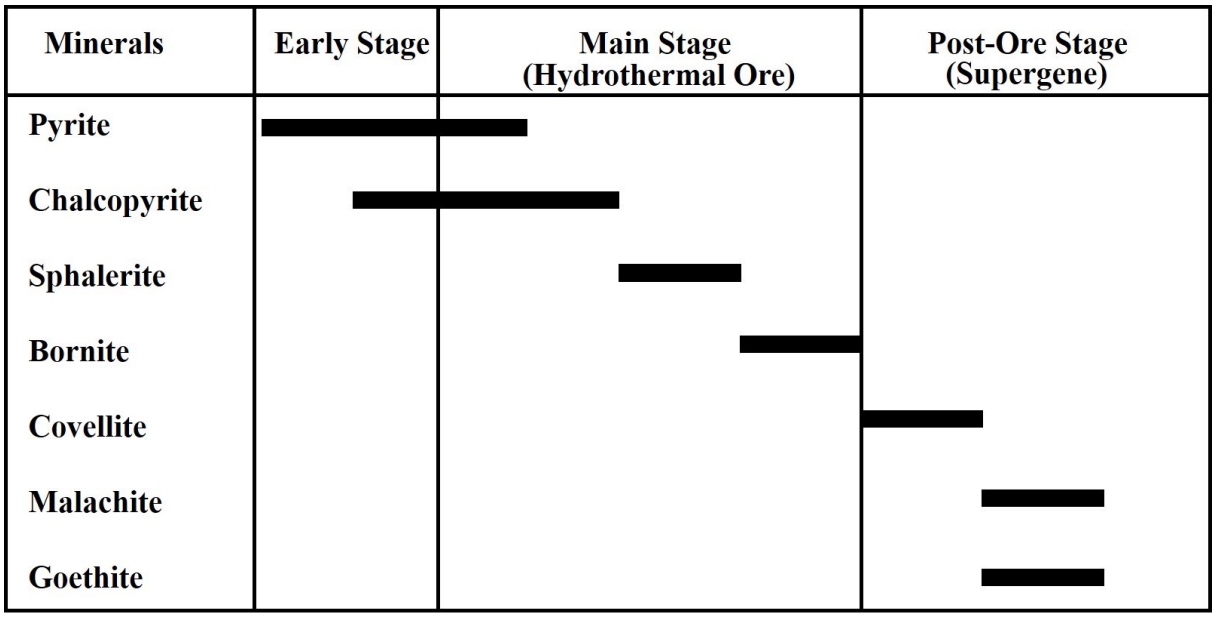


Figure 4.15 Paragenetic sequence of sulphide minerals and supergene minerals as defined by mineral assemblages and textures.

The host sedimentary succession does not include terrigenous clastic rocks such as wacke, sandstone, siltstone, argillite which are typical for a VMS sedimentary lithofacies association (Franklin *et al.*, 2005; Galley *et al.*, 2007). Although vein type mineralization occurs in the agglomerate, massive sulphide mineralization is absent, which would be expected if the mineralization is a characteristic VMS deposit. Such VMS deposits are normally synruptive and redeposited or intercalated with terrigenous sediments (Franklin *et al.*, 2005) which are absent in the Deblin Copper Mine area. Therefore, the evidence does not fully support the VMS mineralization type. These conclusions argue against the findings of the previous authors (Adamson, 1976; Petzel, 1991; Kamona and Günzel, 2007) who suggested that mineralization in the Deblin Copper Mine area is hosted in the chlorite-sericite schist of the Askevold Formation, suggesting VMS mineralization type.

According to Williams *et al.* (2005) chalcopyrite is the only economically significant hypogene copper mineral in most magnetite-dominated IOCG deposits, whereas hematite-dominated IOCG deposits have distinct chalcopyrite-bornite-chalcocite zoning in addition to chalcopyrite being the only significant hypogene copper sulphide. Although the Deblin Copper Mine mineralization is characterized by hydrothermal chalcopyrite ore, magnetite and/or haematite were not observed in the studied rocks. While the Deblin Copper Mine sulphide ores are hosted in ubiquitous quartz-calcite veins, Williams et al. (2005) argued that the limited amounts of vein quartz in IOCG deposits compared to many other hydrothermal ore deposits is one of the distinctive features that influence the interpretation of IOCG mineralization processes. Generally, typical large IOCG deposits develop in association with granitoid magmatism and the majority are hosted in strongly altered crustal rocks such as andesites, granitoids and various common sorts of metasedimentary rocks (Williams *et al.*, 2005). Thus, an IOCG mineralization style, suggested for the Deblin Copper Mine by the Golden Deeps Limited (2013) can also be excluded.

According to Paradis *et al.* (2007) MVT-associated deposits include a variety of deposits that belong to the range of sediment-hosted base metal deposits. The mineralized silicified dolomite and dolomite breccia are enriched in organic material as evidenced by the presence of deformed stromatolites which are indicative of shallow marine environments. These observations of silicified dolomite and dolomite breccia as the host rocks appear to lend support to a model of

carbonate rock-hosted MVT ore system. According to Kamona (2011) paragenesis of MVT ores are complex and variable from deposit to deposit but generally pyrite and marcasite formed early, followed by chalcopyrite, sphalerite and galena. With the exception of marcasite and galena, which are absent, the paragenetic sequence of the ore minerals from the Deblin Copper Mine area reflect that of other MVT deposits. Although the Deblin Copper Mine appears to represent an MVT carbonate-hosted Cu deposit which is comparable to the Kipushi copper type, the occurrence of sulphide mineralization in the agglomerate does not favour the MVT style of mineralization. Hence, mineralization types and host rocks cannot be used as evidence to categorically classify this deposit as an MVT or VMS-type.

Chapter 5

Sulphur Isotopic Studies of the Deblin ores

5.1 Introduction

Sulphur isotopic studies contribute much to the understanding of the processes of ore deposition. The application of stable sulphur isotope data, has improved the understanding of the ore deposition of the major MVT-type base metal deposits in the Otavi Mountain Land. Although different studies argued differently in terms of the host rock and mineralization type of the Deblin Copper Mine, sulphur isotope studies have not been applied to this deposit previously. Base metal mineralization at the Deblin Copper Mine is of an epigenetic, hydrothermal nature occurring largely in quartz-calcite veins and, also as disseminations, but the origin of the sulphur is not well constrained. This study has undertaken sulphur isotope investigations in order to answer the question of whether or not the sulphur of this deposit was of magmatic hydrothermal or biogenic sedimentary origin. The study analyzed only chalcopyrite and pyrite from the Deblin Copper Mine, and interpretations have been generally concerned with the fractionation effects of these sulphide minerals. Moreover, sulphur isotopic data from this deposit were compared to new chalcopyrite and bornite isotopic sulphur data from the Kombat deposit to assess if there are any correlations between the two deposits.

5.2 Previous Work

Sulphur isotope studies of the Otavi Mountain Land carbonate-hosted base metal sulphide deposits have been conducted by several authors (Hughes, 1987; Misiewicz, 1988; Chetty, 1998; Kamona et al., 1999; Chetty and Frimmel, 2000; Melcher, 2003; Kamona and Günzel, 2007). In the Otavi Mountain Land, sulphur isotope studies have been used to characterize most base metal deposits as Tsumeb-type or Berg Aukas type. The Tsumeb deposit is characterized by heavy and homogeneous sulphur isotope ratios of sulphides (+13.1‰ to +26.6‰) (Lombaard et al., 1986; Hughes, 1987; Kamona et al., 1999; Kamona and Günzel 2007). The Kombat deposit sulphides, by contrast, have sulphur isotope ratios which range from -11.3‰ to + 26.2‰ (Hughes, 1987). Innes and Chaplin (1986) attributed the wide range of the sulphur isotope ratios to thermochemical

sulphate reduction or the involvement of a magmatic ore fluid, which usually contains an average composition of 0±5‰ $\delta^{34}S_{CDT}$ (Ohmoto, 1986; Sharp, 2007; Allègre, 2008). Furthermore, Hughes (1987) suggested that the wide range of the Kombat deposit sulphur isotope ratios is due to the mixing of seawater with an isotopically light sulphur-bearing fluid derived from bacteriogenic reduction of seawater sulphate or variations in oxygen fugacity.

The Berg Aukas deposit sulphides have an average sulphur isotope ratio of +19.9‰ $\delta^{34}S_{CDT}$, analogous to those of the Tsumeb sulphides (Kamona and Günzel, 2007). Melcher et al., (2002) reported that the Khusib Springs deposit has heavy sulphur isotope ratios for sulphides (+22.9‰ to +27.8‰), that is relatively similar to sulphur isotope ratios from the Tsumeb and Berg Aukas deposits. Sulphates (anhydrite, barite and gypsum) from both Tsumeb and Kombat deposits have heavy sulphur isotopic signatures (average $\delta^{34}S_{CDT}$ of +28.7‰) (Hughes, 1987). The heavy sulphur isotopes of the sulphate and sulphides from the Tsumeb, Berg Aukas and Khusib Springs suggest seawater as the main source of sulphur (Kamona and Günzel, 2007). There are no previous sulphur isotope analyses conducted on the sulphides of any of the Askevold Trend base metal sulphide deposits. The isotopic data from the Tsumeb, Berg Aukas and Kombat deposits are shown in Figure 5.1.

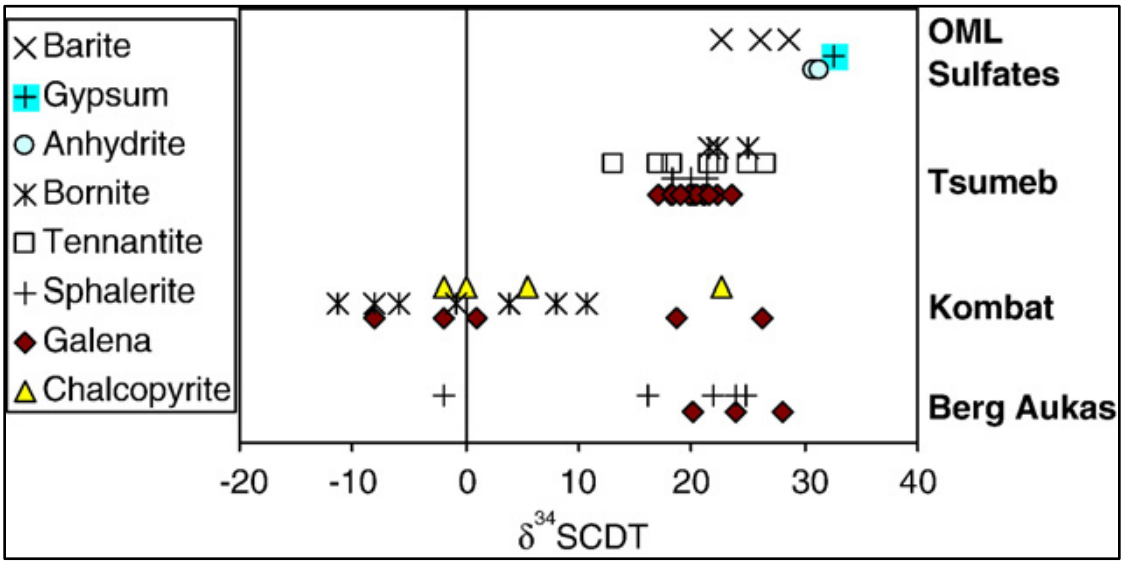


Figure 5.1 Sulphur isotope ratios ($\delta^{34}S_{CDT}$) in sulphides and sulphate of the major deposits in the Otavi Mountain Land (OML). Taken from Kamona and Günzel (2007).

5.3 Current Work

5.3.1 Methodology

Mineral fractions of chalcopyrite, bornite and pyrite for mass spectrometry analyses were separated by hand picking from sieved fractions in the sizes <63 µm under a high magnification binocular microscope. Moreover, the handpicked grains were pulverized to very fine grains (<20 µm). The sulphur isotope analyses were carried out at the Ithemba Labs, University of the Witwatersrand, South Africa. The sulphur isotopes of the sulphides were determined following the method of Robinson and Kusakabe (1975). The measurements of the isotope ratios ($\delta^{34}S$ values) are reported relative to the Cañon Diablo Troilite (CDT) standard (Ault, 1963).

5.3.2 Sulphur Isotope Geochemistry

Sulphur isotope ratios ($\delta^{34}S_{CDT}$) were determined on 13 sulphide mineral separates (Table 5.1 and Appendix B) in order to establish the source of the sulphur. The analyzed sulphides include vein and disseminated types of chalcopyrite and pyrite from the Deblin Copper Mine, and chalcopyrite and bornite from the Kombat deposit. Results are shown Figure 5.2 and Table 5.1.

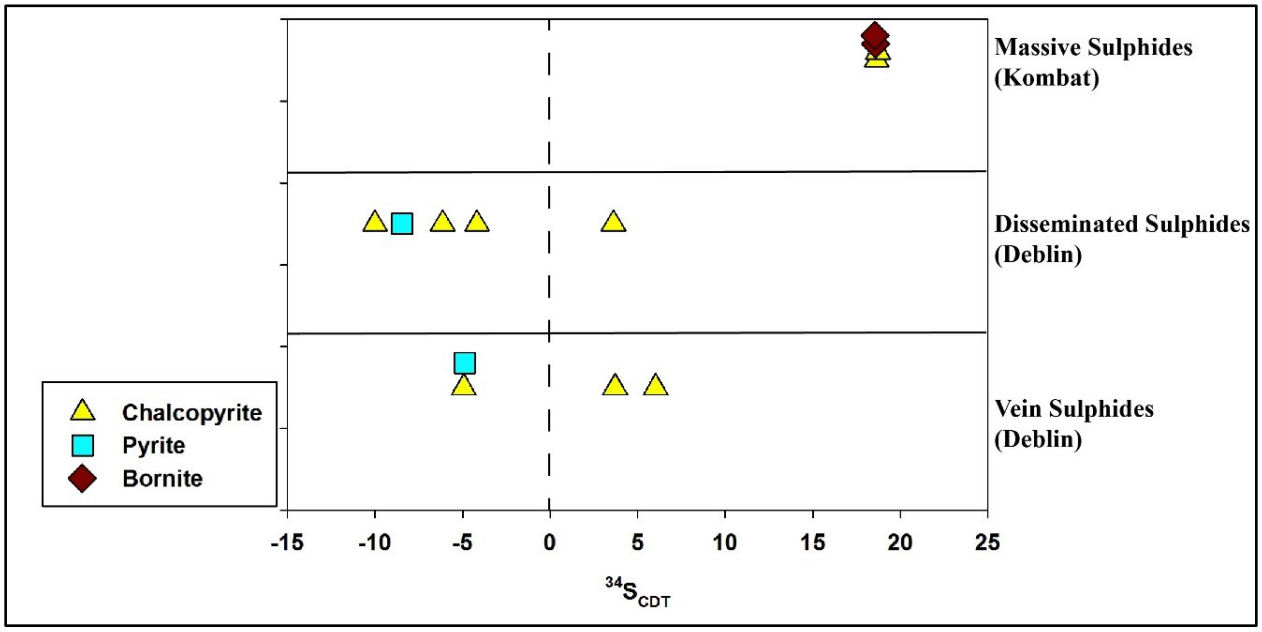


Figure 5.2 Variation of sulphur isotope ratios ($\delta^{34}S_{CDT}$) in sulphides of the Deblin Copper Mine and Kombat deposit.

Vein Sulphides

The sulphur isotope ratios of the four mineral separates of chalcopyrite and pyrite from the quartz-calcite veins hosted in the silicified dolomite and agglomerate (Table 5.1) are characterized by a heterogeneous group, which range from -4.93‰ to +6.04‰ with an average value of -0.01‰ $\delta^{34}S$ (n=4). The measured pyrite shows $\delta^{34}S$ values lower than those of chalcopyrite. Occurrences of vein chalcopyrite and pyrite mineralization are accompanied by minor amounts of fine-grained sphalerite, bornite and covellite in places. However, it was not possible to analyze these from the Deblin Copper Mine drill cores due to lack of sufficient material.

Disseminated Sulphides

Disseminated chalcopyrite and pyrite are abundant in the silicified dolomite at different depths. Disseminated pyrite is widespread in the agglomerate, although it is mostly very fine-grained. The disseminated chalcopyrite samples from the silicified dolomite have a sulphur isotopic signature characterized by values in the -9.99‰ to +3.63‰ range. The average value of these samples is -4.17‰ $\delta^{34}S$, n=4. The disseminated pyrite sample from the agglomerate has a negative isotope ratio of -8.46‰ $\delta^{34}S$, which is lighter than the average value (-2.23‰ $\delta^{34}S$) of the disseminated chalcopyrite from the silicified dolomite.

Massive sulphides (Kombat deposit)

Sulphur isotope ratios of massive chalcopyrite and bornite from the Kombat deposit are heavy and relatively homogeneous (+18.65‰ to +18.72‰ and +18.58‰ to +18.61‰) with average values of +18.69‰ (n=2) and +18.60‰ (n=2), respectively.

Table 5.1 Sulphur isotope ratios (permil δ^{34}SCDT) of sulphide minerals from the Deblin Copper Mine and Kombat deposit.

Sample No.	Borehole ID	Depth (m)	Host Rock	Mineralization Type	δ^{34}S (Chalcopyrite)	δ^{34}S (Pyrite)	δ^{34}S (Bornite)
DB1S16	DBDD0001	136.61-136.81	Silicified Dolomite	Vein	-4.93		
DB2S7	DBDD0002	59.36-59.56	Silicified Dolomite	Vein	3.73		
DB2S8	DBDD0002	59.67-59.87	Silicified Dolomite	Vein	6.04		
DB1S22	DBDD0001	157.50-157.70	Agglomerate	Vein		-4.88	
DB1S17	DBDD0001	137.22-137.42	Silicified Dolomite	Disseminated	-6.14		
DB2S9	DBDD0002	59.87-60.07	Silicified Dolomite	Disseminated	3.63		
DB2S12	DBDD0002	73.40-73.60	Silicified Dolomite	Disseminated	-4.17		
DB1S18	DBDD0001	137.73-137.93	Agglomerate	Disseminated		-8.46	
DB2S17	DBDD0002	137.22-137.42	Silicified Dolomite	Disseminated	-9.99		
Kombat1	Kombat Deposit		Limestone	Massive	18.65		
Kombat2	Kombat Deposit		Limestone	Massive	18.72		
Kombat3	Kombat Deposit		Limestone	Massive			18.61
Kombat4	Kombat Deposit		Limestone	Massive			18.58

5.4 Discussion

Ore minerals in the Deblin Copper Mine are relatively simple, and the main sulphur-bearing minerals are chalcopyrite and pyrite, and no sulphate mineral has yet been found. So, the sulphur source of this deposit can only be inferred from the present sulphides, chiefly chalcopyrite and pyrite. Sulphur isotope ratios of the vein type sulphides exhibit a narrow range of $\delta^{34}S$ values (-4.93‰ to +6.04‰) and the disseminated sulphides have a wide variation of $\delta^{34}S$ (-9.99‰ to +3.63‰). These observations indicate that sulphur isotope ratios from these mineralization types overlap, although the sulphur isotope ratios of vein sulphides (average $\delta^{34}S$= -0.01‰, n=4) are relatively heavier than the disseminated sulphides (average $\delta^{34}S$= -5.03‰, n=5). Based on this it can be suggested that the sulphur of the two sulphide mineralization types from the Deblin Copper Mine may have formed in different environments.

Sulphur within the natural environments is generally either of igneous (mantle) or seawater origin (Sharp, 2007; Allègre, 2008). The determined $\delta^{34}S$ values ($\delta^{34}S$= -4.93‰ to +6.04‰) of the vein type sulphides from the Deblin Copper Mine are within the typical magmatic sulphur values of 0±5‰ δ^{34}_{SCDT} (Ohmoto, 1986; Sharp, 2007; Allègre, 2008) and therefore, a magmatic origin can be suggested. On the contrary, the disseminated sulphides have a large variation and negative sulphur isotopic ratios ($\delta^{34}S$= -9.99‰ to +3.63‰), which are indicative of sedimentary sulphides produced through bacterial reduction of seawater sulphate in the marine sediments. Additionally, most of the sulphur isotopic ratios are within the 0±5‰ $\delta^{34}_{SCDT,}$ and therefore a magmatic origin contribution cannot be excluded.

The new sulphur isotope ratios of sulphides from Kombat deposit are heavy and homogeneous (18.58‰ to +18.72‰) with an average value of $\delta^{34}S$= 18.64‰ (n=4). Although the new sulphur isotopic data of the sulphides from the Kombat deposit are limited to 4 mineral separates, the current study lends support to the seawater origin of the sulphur. This is in full agreement with the previous interpretation by Innes and Chaplin (1986). Furthermore, when these sulphur isotopic data are compared to the Deblin Copper Mine the sulphur isotope ratios of sulphides from Kombat are positive and heavier (Figure 5.3). Hence, the presented new sulphur isotopic data do not show any direct correlations between the sulphur source of the sulphides from the Deblin Copper Mine and Kombat deposit.

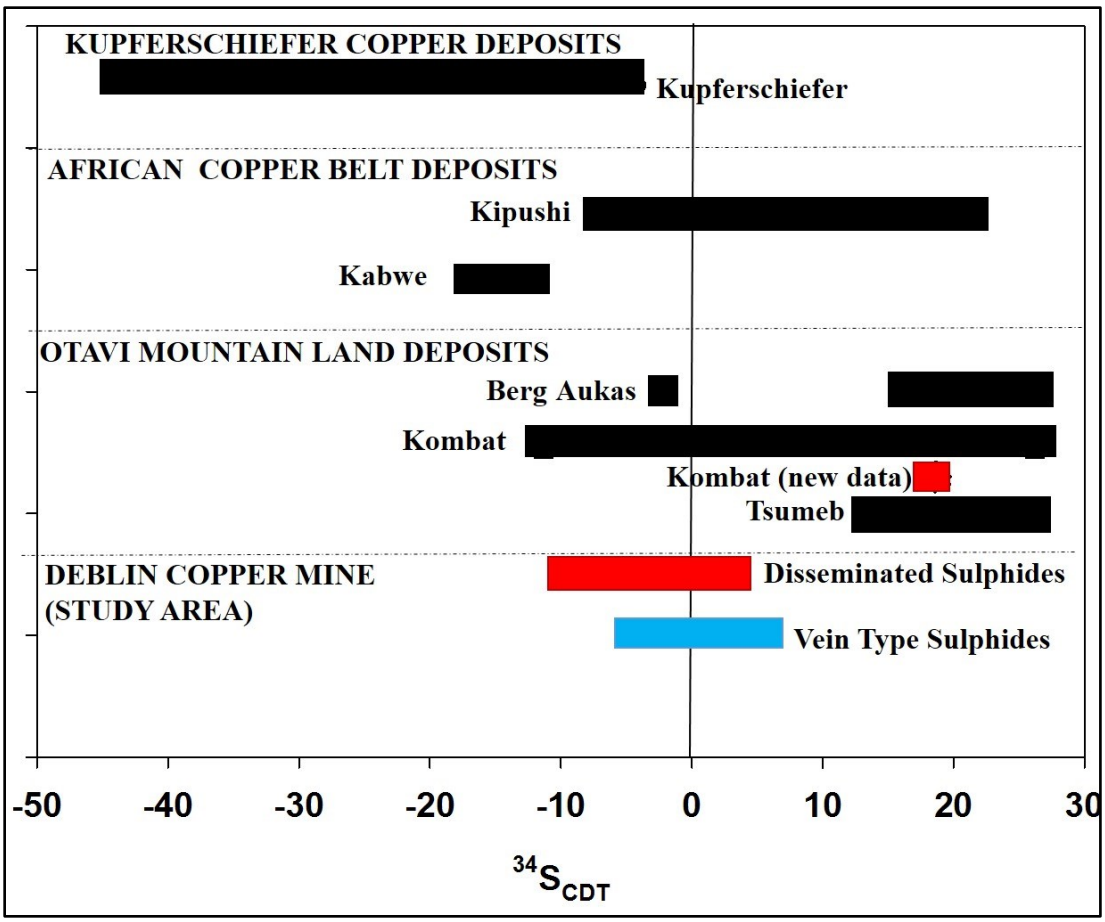


Figure 5.3 Sulphur isotope ratios ($\delta^{34}S_{CDT}$) in the major deposits in the Otavi Mountain Land (OML), central African Copper belt and Kupferschiefer. Data taken from Dechow & Jensen (1965), Sawlowicz (1989) and Kamona and Günzel (2007).

When the sulphur isotope ratios of sulphides from the Deblin Copper Mine are compared to those from other base metal deposits within the Otavi Mountain Land (Figure 5.3), they tend to be lower than those of sulphide minerals of the Tsumeb and Berg Aukas deposits. Moreover, when compared to the published $\delta^{34}S$ values of the sulphides from the Kombat deposit, which range from -11.3‰ to +26.2‰ with an average value of $\delta^{34}S$= +5.2‰ (n=19) (Hughes, 1987), the Deblin Copper Mine $\delta^{34}S$ data overlaps with the light $\delta^{34}S$ values of the Kombat deposit. In addition, the Deblin Copper Mine $\delta^{34}S$ data for both vein and disseminated sulphides overlap with the light $\delta^{34}S$ values from the Kipushi carbonate-hosted Cu-Pb-Zn deposit, which is characterized by a wide range of $\delta^{34}S$ values ($\delta^{34}S$= -7.4‰ to +21.8‰) and suggestive of a biogenic origin of the sulphur (Dechow and Jensen, 1965; Kamona, 2011). Remarkably, the Deblin Copper Mine disseminated sulphides $\delta^{34}S$ data ($\delta^{34}S$= -9.99‰ to +3.63‰) partly overlap with those of the Kupferschiefer,

which consists of $\delta^{34}S$ values in the range of -44‰ to -4‰, reflecting the production of sulphide by bacteriogenic sulphate reduction (Sawlowicz, 1989) (Figure 5.3). These observations lend strong support to the argument that the Deblin Copper Mine disseminated sulphides are produced through bacterial reduction of seawater sulphate in the marine sediments, whereas the hydrothermal vein type sulphide are of magmatic origin.

Chapter 6

Whole Rock Geochemistry

6.1 Introduction

The Askevold Formation metavolcanic rocks that occur in the base metal prospective areas of the southern Otavi Mountain Land such as the Deblin Copper Mine have been mapped and petrographically investigated previously, however, the origin and tectonic setting of emplacement of the metavolcanic rocks are not well constrained, partly because these rocks are poorly exposed. Adamson (1976) suggested that the sericite-chlorite schist of the Deblin Copper Mine area is derived from trachytic or trachyandesitic tuffs. In contrast, geochemical interpretations by Miller (2008), with data derived from unpublished literature, suggest that these rocks were derived from alkali basalts. Limited literature exists on the geochemistry of the Askevold Formation metavolcanic rocks. The tuff, mafic metavolcanic and chlorite schist are the principal metavolcanic rocks under study. These metavolcanic rocks are distributed, although poorly exposed, over much of the study area and have been distinguished by field mapping and drill core lithological logging. This chapter, reports on new major, trace and rare earth element (REE) whole rock geochemical data obtained for the Askevold Formation metavolcanic rocks from the area around the Deblin Copper Mine. The geochemical signatures are discussed in the context of the available data in order to establish the origin and tectonic setting these rocks.

6.2 Methodology

Samples

A total of 75 samples of different rock types were collected from the field for petrographic thin section studies. Out of these samples, 15 samples of the metavolcanic rocks were selected for geochemical analyses. A total of 9 samples were taken from drill cores, whereas 6 samples were taken from outcrops. The samples were selected taking into consideration the level of weathering and hydrothermal alteration based on field and thin section observations.

Analytical Methods

The samples were cleaned, jaw-crushed and ground to <63 μm in an agate disc mill in the rock crushing laboratory of the School of Geosciences, University of the Witwatersrand. The selected rock samples were analyzed for their whole rock major and, trace and REE contents by X-ray fluorescence spectrometry (XRF) and Inductively Coupled Plasma-Mass Spectrometry (ICP-MS) methods, respectively. Analysis of the major elements was conducted on fused discs using an automated X-ray fluorescence (XRF) spectrometer, Axios by Panalytical at the Earth Laboratory, University of the Witwatersrand, Johannesburg, South Africa. The XRF analyses followed the procedures of Feather and Willis (1976). In addition, trace elements and rare earth elements (REE) analyses of the selected samples were performed by fusion Inductively Coupled Plasma-Mass Spectrometry (ICP-MS) ELAN DRC made by Perkin Elmer at the Earth Laboratory of the University of the Witwatersrand. The instruments run the internal replications to determine the precision. The accuracy of the analytical procedure was determined by using Certified Reference Materials (CRMs) as the standard samples. The Certified Reference Materials used include U.S. Geological Survey DTS-1, W-2, AGV-2 and, National Institute for Metallurgy (Republic of South Africa) NIM –L, NIM-D, SARM 1, SARM 2, SARM 3, SARM 4, SARM 5 and SARM 6. Precision of XRF major and ICP-MS trace element analyses is better than ±2.5% (2σ), whereas accuracy for both methods is better than ±2.0% (2σ).

6.3 Data

The major, trace and rare earth elements for the metavolcanic samples from the study area are shown in Table 6.1-6.3 and Appendix C. New data from this study were compared to the previous geochemical data of the Askevold Formation metavolcanic rocks from published work by Miller (2008) (Table 6.4). The analytical data are plotted on a number of rock classification and tectonic discrimination diagrams.

Table 6.1 Whole-rock major element compositions of metavolcanic rocks from the area around the Deblin Copper Mine. The major element concentrations are in wt.% and were analyzed by X-ray fluorescence spectrometry.

Sample	DB3S14	DB3S19	DB3S9	DB3S20	DB3S16	DB1S19	DB1S20	DB8a	DB7a	DB3S8	DB1b	DB3S7	DB10h	DB10a	DB10b
SiO_2	48.67	43.73	40.85	41.97	44.73	44.49	42.28	37.92	45.00	31.08	37.33	33.11	35.07	44.18	41.74
Al_2O_3	11.98	12.22	12.76	12.87	14.35	14.47	16.61	10.97	14.44	11.68	6.77	9.47	7.43	9.13	9.93
Fe_2O_3	1.35	1.60	1.47	1.03	1.28	0.55	0.87	0.98	0.95	0.90	0.49	0.60	0.61	0.83	0.90
FeO	10.89	12.93	11.95	8.37	10.38	4.46	6.99	7.92	7.71	7.28	3.97	4.86	4.92	6.77	7.28
MnO	0.12	0.16	0.16	0.20	0.18	0.12	0.13	0.14	0.12	0.58	0.25	0.61	0.29	0.14	0.12
MgO	5.77	3.01	1.48	0.91	7.95	1.96	2.72	7.24	9.03	4.51	4.76	6.10	1.97	7.05	7.36
CaO	5.11	7.93	10.32	13.66	4.55	10.77	9.57	12.01	7.59	16.33	22.46	17.29	24.99	10.37	12.04
Na_2O	4.05	5.04	3.15	5.71	4.27	0.09	0.05	0.07	0.03	nd	0.04	nd	nd	0.03	0.05
K_2O	1.53	1.53	4.07	1.27	1.37	5.07	5.49	3.30	2.16	4.98	0.94	3.95	2.50	2.94	2.14
TiO_2	1.91	2.00	2.85	2.26	1.99	2.75	3.49	2.28	1.58	2.03	0.96	1.84	1.24	1.64	1.29
P_2O_5	0.28	0.21	0.40	0.29	0.21	0.35	0.60	0.24	0.33	0.26	0.16	0.25	0.17	0.20	0.19
LOI	8.48	9.77	10.11	11.86	8.98	7.90	9.48	16.84	11.07	20.22	20.36	22.10	20.75	16.56	16.94
Total	100.16	100.16	99.61	100.42	100.28	93.00	98.30	99.94	100.02	99.88	98.51	100.20	99.97	99.88	100.02

Table 6.2 Whole-rock trace element and REE compositions of metavolcanic rocks from the area around the Deblin Copper Mine. Trace element and REE concentrations are in ppm and were analyzed by Inductively Coupled Plasma-Mass Spectrometry (ICP-MS)

Sample	DB3S14	DB3S19	DB3S9	DB3S20	DB3S16	DB1S19	DB1S20	DB8a	DB7a	DB3S8	DB1b	DB3S7	DB10h	DB10a	DB10b
Li	42.23	12.25	23.81	11.44	51.72	60.23	59.44	23.89	83.17	66.88	36.41	48.73	21.22	17.50	46.20
Sc	26.84	24.57	23.16	25.69	30.31	33.96	32.97	22.65	22.71	23.12	12.85	16.58	16.80	18.41	18.57
Ti	10333	10463	15893	11411	10946	17163	20314	13127	9354	11565	5628	10112	6741	9259	7321
V	272	197	198	167	283	309	360	235	220	228	131	180	131	167	157
Cr	29.89	19.80	6.47	32.09	79.40	107	87.77	118	66.94	56.47	55.02	58.52	80.12	76.04	63.57
Co	57.99	29.46	33.55	18.80	72.72	45.90	14.72	25.33	26.41	16.85	29.80	27.76	22.83	13.81	19.61
Ni	39.98	43.16	36.51	27.51	64.28	102	59.04	55.22	42.76	59.18	50.07	34.77	37.56	31.59	63.23

Cu	10.67	7.70	8.84	8.87	8.48	79.37	11.01	8.06	33.31	33.41	5153	30.25	383	6.33	109
Zn	237	100	97.40	57.35	300	37.28	85.18	59.75	93.20	92.88	63.54	58.70	50.82	41.71	80.99
Ga	16.84	15.45	20.65	15.19	19.92	19.68	25.48	14.91	19.45	17.27	9.66	13.29	10.23	12.58	13.37
Rb	99.44	59.02	195	74.29	73.47	164	219	122	109	283	56.33	190	122	102	64.52
Sr	57.38	83.22	93.71	152	55.07	63.40	63.55	74.58	31.75	103	111	90.20	166	76.98	56.29
Y	13.55	18.06	26.96	24.97	10.12	23.38	29.17	22.48	20.49	24.37	19.04	23.34	22.75	19.00	16.47
Zr	167	145	288	180	146	230	403	173	198	158	101	140	126	133	119
Nb	22.23	23.32	42.91	28.99	22.50	35.61	48.45	29.33	31.63	26.82	15.76	22.59	15.68	21.16	18.05
Ba	358	627	1675	691	496	4058	3652	684	254	580	180	337	437	368	268
Cs	5.85	1.92	1.83	1.19	4.79	1.85	3.07	8.84	1.83	3.63	1.01	2.60	1.12	6.24	3.66
La	17.14	16.55	21.67	14.61	13.45	17.96	36.98	24.02	28.44	17.29	18.91	12.67	19.52	20.97	17.94
Ce	39.13	34.16	47.35	33.11	30.57	48.60	81.23	51.89	61.57	37.63	37.69	29.86	39.04	44.58	39.29
Pr	5.50	4.50	6.71	4.81	4.29	7.02	11.37	6.63	7.71	5.11	4.79	4.02	4.89	5.72	4.87
Nd	23.81	18.95	28.15	22.18	19.11	31.74	47.95	27.42	31.02	21.91	19.12	17.66	20.37	23.15	19.79
Sm	5.25	4.55	7.43	5.67	4.54	9.00	12.17	5.86	6.04	5.16	3.72	4.63	4.46	4.88	4.03
Eu	1.48	1.49	2.51	1.92	1.37	2.91	4.61	1.75	1.51	1.93	0.85	1.72	1.32	1.42	1.07
Gd	4.69	4.34	6.52	5.22	3.73	6.36	9.19	5.42	5.81	4.89	3.75	4.88	4.61	4.85	4.02
Tb	0.62	0.62	0.96	0.76	0.48	0.90	1.20	0.76	0.76	0.72	0.55	0.76	0.67	0.69	0.57
Dy	2.87	3.30	5.01	4.22	2.23	4.62	5.89	4.08	3.98	3.99	3.15	4.47	3.83	3.66	3.11
Ho	0.48	0.62	0.92	0.75	0.40	0.85	1.01	0.76	0.72	0.79	0.62	0.86	0.72	0.66	0.57
Er	1.31	1.64	2.44	2.03	1.11	2.24	2.78	2.07	2.11	2.19	1.78	2.26	1.97	1.89	1.59
Tm	0.20	0.24	0.37	0.31	0.18	0.33	0.41	0.31	0.33	0.32	0.26	0.33	0.29	0.28	0.24
Yb	1.47	1.63	2.54	2.19	1.28	2.12	2.78	1.98	2.08	2.08	1.70	2.00	1.75	1.80	1.53
Lu	0.24	0.25	0.39	0.34	0.22	0.33	0.45	0.29	0.32	0.31	0.26	0.29	0.27	0.28	0.23
Hf	3.69	3.49	6.40	4.18	3.72	5.49	8.77	4.42	5.02	3.79	2.48	3.43	3.02	3.47	3.04
Ta	1.24	1.35	2.77	1.64	1.30	2.12	3.14	1.70	2.03	1.52	0.94	1.31	0.88	1.28	1.13
Pb	7.35	9.84	22.84	20.28	7.08	4.00	4.09	2.15	7.12	20.34	10.35	16.06	6.31	1.95	2.21
Th	2.60	2.62	3.66	2.89	2.43	2.96	7.00	5.33	8.97	2.36	3.82	2.17	2.68	5.42	3.50
U	0.54	0.56	1.03	0.77	0.48	0.89	1.19	1.33	1.41	0.72	2.23	0.59	0.73	0.83	1.26

Table 6.3 Chondrite-normalized ratios of selected REEs of the metavolcanic rocks from the area around the Deblin Copper Mine.

REE ratio	DB3S14	DB3S19	DB3S9	DB3S20	DB3S16	DB1S19	DB1S20	DB8a	DB7a	DB3S8	DB1b	DB3S7	DB10h	DB10a	DB10b
$(La/Sm)_N$	2.11	2.35	1.88	1.66	1.91	1.29	1.96	2.64	3.04	2.16	3.28	1.77	2.82	2.77	2.87
$(Dy/Lu)_N$	1.21	1.34	1.29	1.26	1.02	1.38	1.31	1.40	1.25	1.30	1.22	1.52	1.42	1.33	1.36
Eu/Eu*	0.91	1.03	1.10	1.08	1.02	1.18	1.33	0.95	0.78	1.18	0.70	1.11	0.89	0.89	0.81

Table 6.4 Geochemical compositions of the Askevold Formation SE of Otavi in Miller's report (as cited in Miller, 2008). Major element concentrations are in wt.% whereas trace element and REE concentrations are in ppm.

Sample	A1070	A1072	A1074	A1075	A1076	A1071	A1073
SiO_2	43.42	44.02	49.26	42.43	42.81	26.71	22.47
Al_2O_3	13.93	17.81	17.63	12.78	14.10	6.60	5.38
Fe_2O_3	4.26	3.62	3.02	8.99	9.95	7.07	4.45
FeO	4.89	4.41	5.85	3.35	4.18	3.28	2.57
MnO	0.18	0.14	0.14	0.18	0.14	0.28	0.42
MgO	4.17	3.62	3.42	2.72	2.32	5.34	3.11
CaO	11.53	7.24	4.04	12.11	9.30	26.59	32.98
Na_2O	2.04	0.00	0.22	2.61	1.33	0.10	0.72
K_2O	2.83	6.32	6.71	1.86	5.25	0.64	1.00
TiO_2	2.87	3.68	3.69	3.68	2.72	1.23	0.84
P_2O_5	0.41	0.46	0.50	0.73	0.32	0.29	0.28
Cr	111	-	124	-	49	-	-
Ni	59	68	32	31	68	85	11
Cu	864	1855	294	422	564	266	1825
Zn	121	95	102	73	81	100	79
Ga	20	24	22	21	21	15	13
Rb	98	264	231	144	213	26	38
Sr	77	63	39	103	90	170	213
Ba	546	-	1110	-	2276	-	-
Y	35	27	46	5	26	22	13
Zr	248	331	332	422	218	107	82
Nb	36	44	42	50	34	17	16
Pb	nd	9	6	nd	nd	64	13
Th	nd	nd	nd	nd	7	nd	nd

6.4 Element mobility and chemical alteration assessment

The petrographic studies show that the primary textures and mineralogy of all the Deblin Copper Mine area samples have been obliterated as a result of deformation, metamorphism and hydrothermal alteration. The primary mineralogy of the rocks has been overprinted by regional metamorphic and alteration minerals notably chlorite, sericite, biotite and late calcite and dolomite. The extent of the alteration is corroborated by the high loss on ignition (Table 6.1).

Major elements such as Si, Na, K, Ca and some other trace elements, including the large ion lithophile elements (LILE) such as Cs, Rb, Ba and Sr are easily mobilized during metamorphism and by hydrothermal fluids (Rollinson, 1993; Dampare *et al.*, 2008; Senyah *et al.*, 2015). In addition, according to Pearce and Cann (1973) Sr is generally fairly stable in uncarbonated rocks below greenschist facies, although it can be affected by greenschist facies metamorphism. However, all the rock samples under consideration record high CaO contents (Table 6.1), have carbonate overgrowths and have undergone greenschist facies metamorphism as shown by petrographic studies. These conditions are unfavourable for Sr and therefore Sr characterization in this study is inapplicable. In contrast, the high field strength elements (HFSE) (e.g. Ti, Zr, Hf, P, Ta, Y and Nb), transitional elements (e.g. Ni, Cr, Co, Sc and V) and REE tend to be very immobile during alteration, weathering and low-grade metamorphism (Cann, 1970; Pearce and Cann, 1973; Floyd and Winchester, 1975; Winchester and Floyd, 1977; Shervais, 1982; Rollinson, 1993; Pearce, 1996; White, 2013). Consequently, it is important to evaluate the chemical effects of alteration on the samples before any attempts are made to interpret the petrogenesis and tectonic setting.

The loss on ignition values range from 7.90 wt.% to 22.10 wt.% (Table 6.1), in samples which shows intense alteration. In addition, all samples display high CaO and low SiO_2 contents (Table 6.1), suggestive of a remobilization of CaO, represented by carbonate metasomatism as observed in the petrographic studies. The positive relationship observed between LOI and CaO (Figure 6.1a), the negative correlation observed between LOI and SiO_2 (Figure 6.1b), the weak negative correlation between LOI and total alkali content (Figure 6.1c) and lack of trends between the LOI and LILE plots (Figure 6.1d-f) indicate the mobilization of the major elements and LILE in the analyzed metavolcanic rocks. The plot of LOI vs total alkali content shows that the samples have

lost most of the total alkali content. These observations suggest that the major and mobile elements (LILE) are greatly affected by alteration and thus the measured compositions may not indicate the original unaltered values. As a consequence, the discussion below will use only the HFSE and other immobile elements compositions.

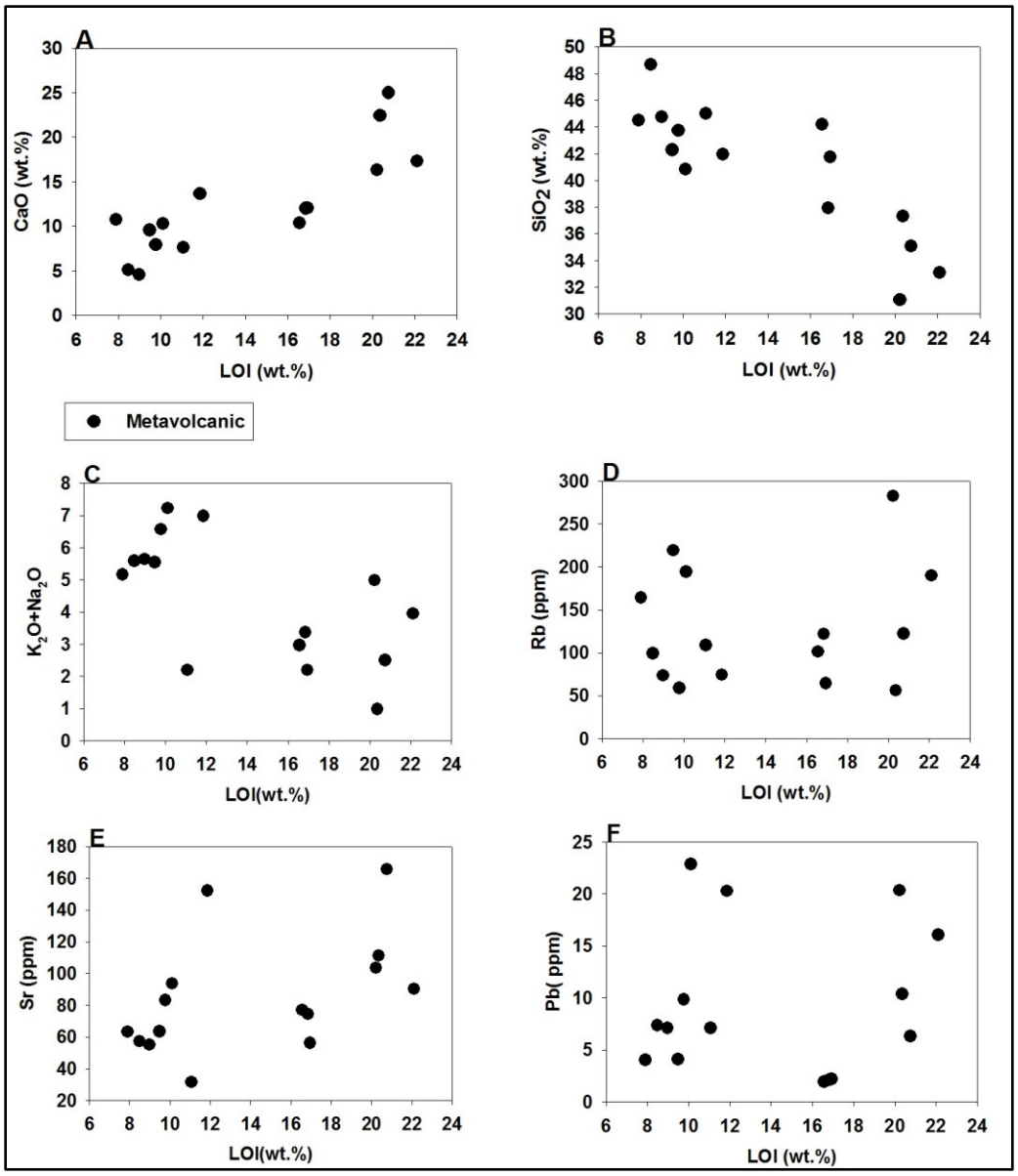


Figure 6.1 Bivariate plots of Loss on Ignition (LOI) versus selected major elements and Large Ion Lithophile Elements (LILE). The Rb, Sr and Pb plots do not show any correlations. A) The plot of the Loss on Ignition with CaO displays a positive trend. B) The Loss on Ignition vs SiO_2 exhibits a negative trend. C) The LOI vs total alkali content (K_2O+Na_2O) plot. D) The LOI vs Rb plot. E) The LOI vs Sr plot. F) The LOI vs Pb plot.

6.5 Trace element geochemistry

In this section, efforts to determine the geochemical affinities and tectonic significance of these metavolcanic samples, are focused on the immobile elements, predominantly the HFSE and REE. Diagrams using incompatible elements such as the Nb/Y-Zr/Ti diagram of Pearce (1996) (Figure 6.2) were proposed for the classification of the analyzed metavolcanic rocks. All the samples fall within the alkali basalt field and hence show values of Nb/Y close to 1. These observations suggest that these metavolcanic rocks represent altered alkali basaltic lavas. Based on these observations all the metavolcanic samples formed from the same alkali basalt, although now they have different metamorphic names based on the alteration assemblage as described in the petrographic section.

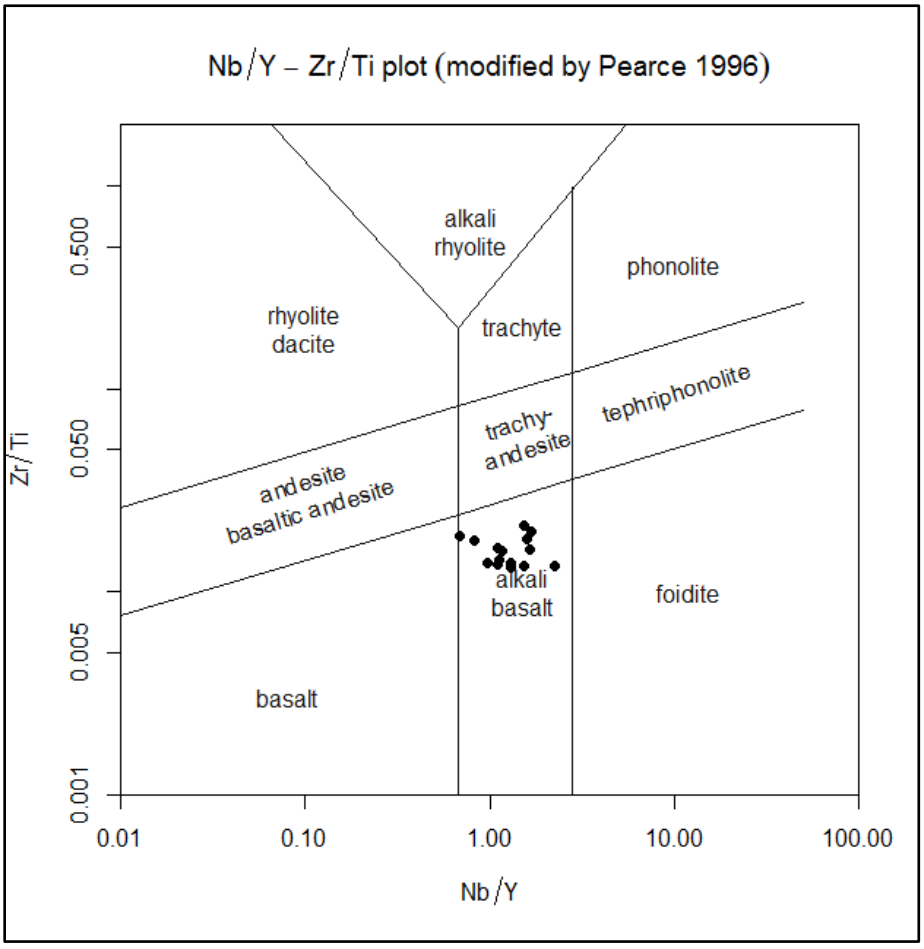


Figure 6.2 Geochemical classification of the metavolcanic rocks of the Askevold Formation using the Nb/Y-Zr/Ti diagram of Pearce (1996). The samples plot within the alkali basalt field, although one sample plots close to the basalt field.

The metavolcanic rocks show high contents of Zn, Cu and Ni. The high content of Ni implies that these rocks were originally of a mafic composition. Since Zr is considered immobile under greenschist facies conditions (Cann, 1970; Pearce and Cann, 1973; Floyd and Winchester, 1975; Pearce, 1996), selected trace elements were plotted against Zr (Figure 6.3). The plots of Zr against HFSE (e.g Ti, Nb) and REE (e.g Ce, Sm) display strong positive correlations (Figure 6.3) which suggest that these rocks are genetically related.

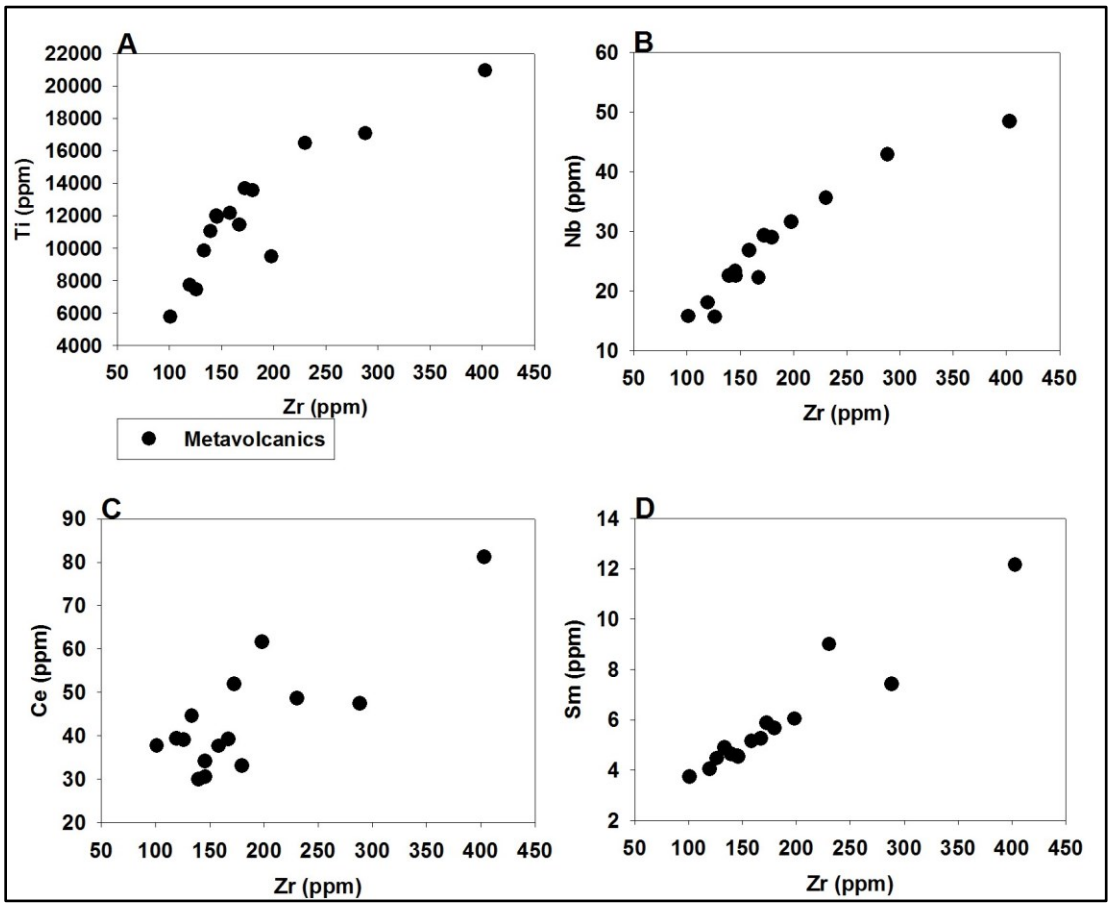


Figure 6.3 Bivariate graphs of Zr versus selected HFSE and REE showing positive correlations. A) The Zr vs Ti plot. B) The Zr vs Nb plot. C) The Zr vs Ce plot. D) The Zr vs Sm plot.

The REE are usually normalized to a common reference standard, which generally comprises the values for meteorites (Sun and McDonough, 1989; Rollinson, 1993). In this study, the REE concentrations are normalized using chondritic meteorites, primitive mantle, N-MORB and Oceanic Island Basalts (OIB**)** values of Sun and McDonough (1989). The chondrite-normalized REE patterns for the analyzed samples from the study area show that these metavolcanic rocks are

characterized by simple linear patterns with enrichment in LREE relative to the HREE (Figure 6.4), with La_N/Sm_N values from 1.28 to 3.27 (average is 2.30), where $_N$ refers to chondrite-normalized values. The samples show a slightly enriched to flat HREE pattern. The Dy_N/Lu_N ratios vary between 1.01 and 1.51 (average is 1.30), where $_N$ refers to chondrite-normalized values.

The Eu (Eu/Eu*) anomaly was calculated from: $Eu/Eu^* = Eu_N/(Sm_N x Gd_N)^{1/2}$ (Taylor and McLennan, 1985). The Eu anomalies vary between 0.69 and 1.33 (average is 0.99), representing both negative and positive Eu anomalies for the studied metavolcanic samples. As shown in the chondrite-normalized diagram, the samples show both positive and negative Eu anomalies (Figure 6.4), which suggest that plagioclase played a role in fractionation as supported by strong positive correlations of TiO_2 vs Eu/Eu* and Nb vs Eu/Eu* (Figure 6.5).

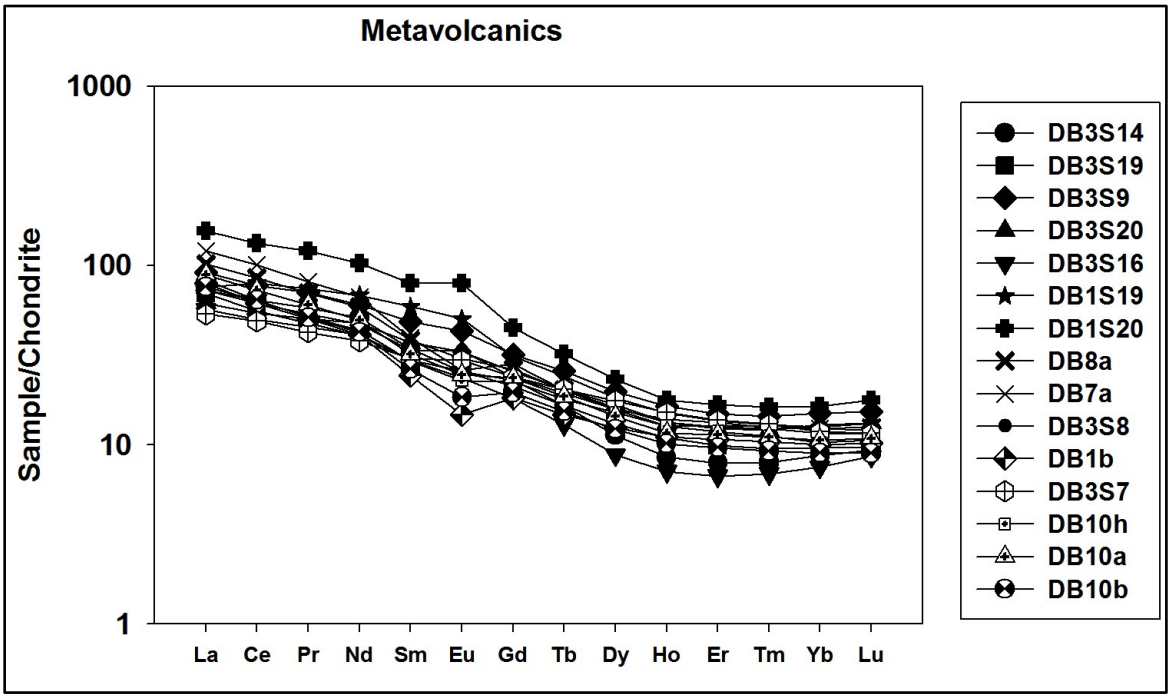


Figure 6.4 Chondrite-normalized REE patterns of the metavolcanic samples from the area around the Deblin Copper Mine, with subtle positive and negative Eu anomalies. Normalization values and the order of the elements are taken from Sun and McDonough (1989).

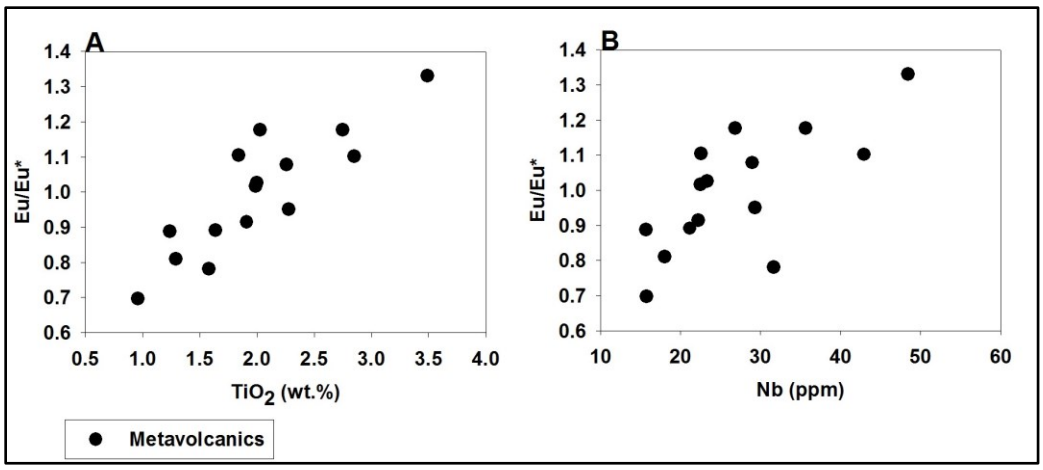


Figure 6.5 Plots of Eu/Eu* vs A) TiO_2 and B) Nb showing positive trends.

Furthermore, the metavolcanic samples were plotted on the primitive mantle-normalized spider diagram (Figure 6.6) to compare the metavolcanic rocks chemistry with the mantle source. The primitive mantle-normalized multi-element plots (Figure 6.6a) show variable patterns defined by trace element concentrations with both depletions and enrichments relative to the primitive mantle values of Sun and McDonough (1989). Primitive mantle-normalized spider diagrams of the metavolcanic rocks (Figure 6) do not exhibit the typical depleted pattern of Mid-Ocean Ridge basalts (MORB) nor do they show the depletion in HFSE like subduction-related basalts. They rather exhibit a pattern similar to that of within plate basalts (Figure 6.6b). Also, when plotted on the OIB-normalized spider diagram, samples show a typical flat pattern (Figure 6.7), except the enrichment in Cs, Rb, Ba, K and Pb which is due to alteration and depletion in Sr that can be due to alteration and/or plagioclase fractionation.

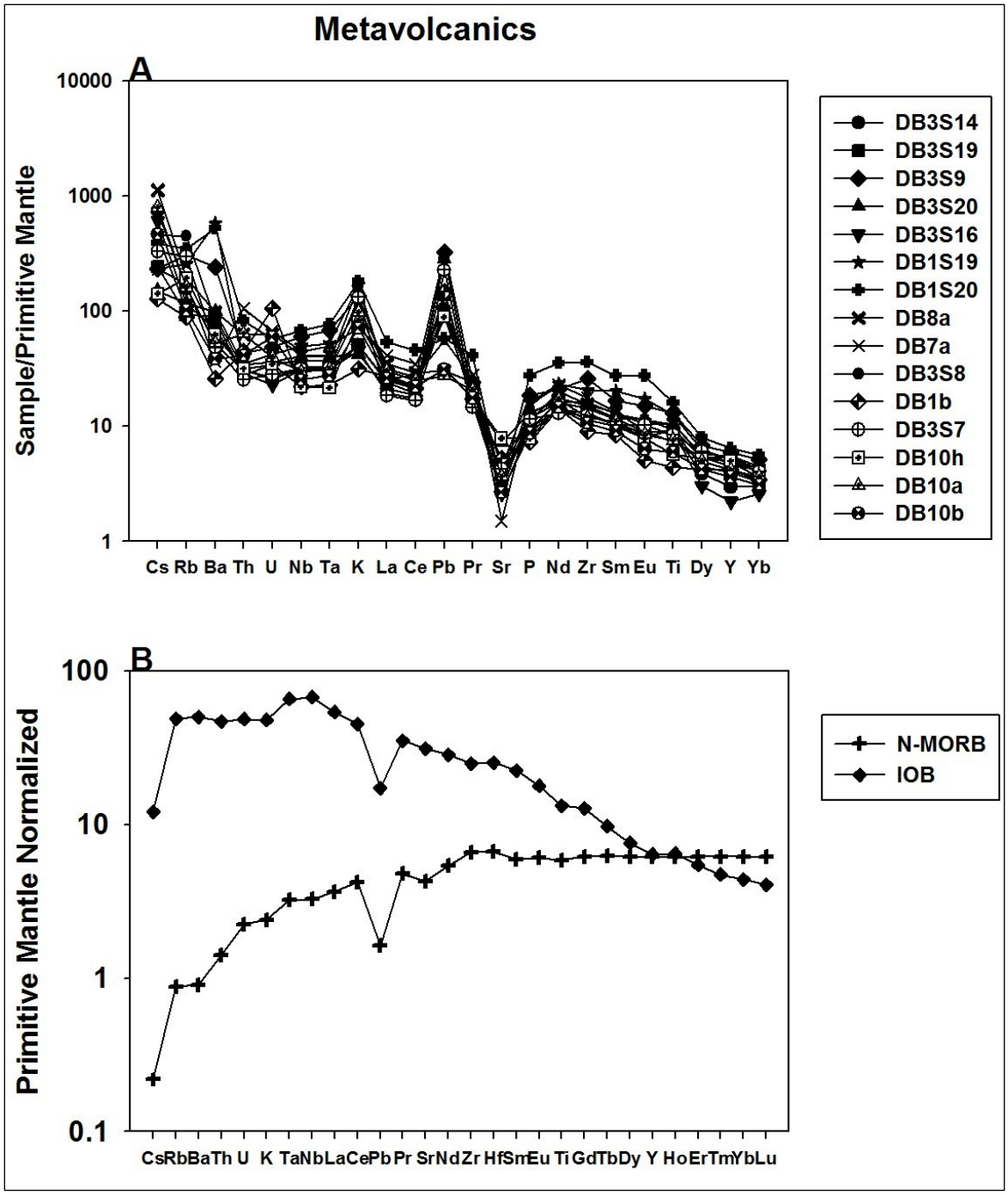


Figure 6.6 Primitive mantle-normalized spider diagrams. A) Primitive mantle-normalized multi-element patterns of the metavolcanic samples from the area around the Deblin Copper Mine. B) A comparison of the primitive mantle-normalized spider diagrams of the N-MORB and Oceanic Island Basalts (OIB) average values. All normalization values and the order of the elements are taken from Sun and McDonough (1989).

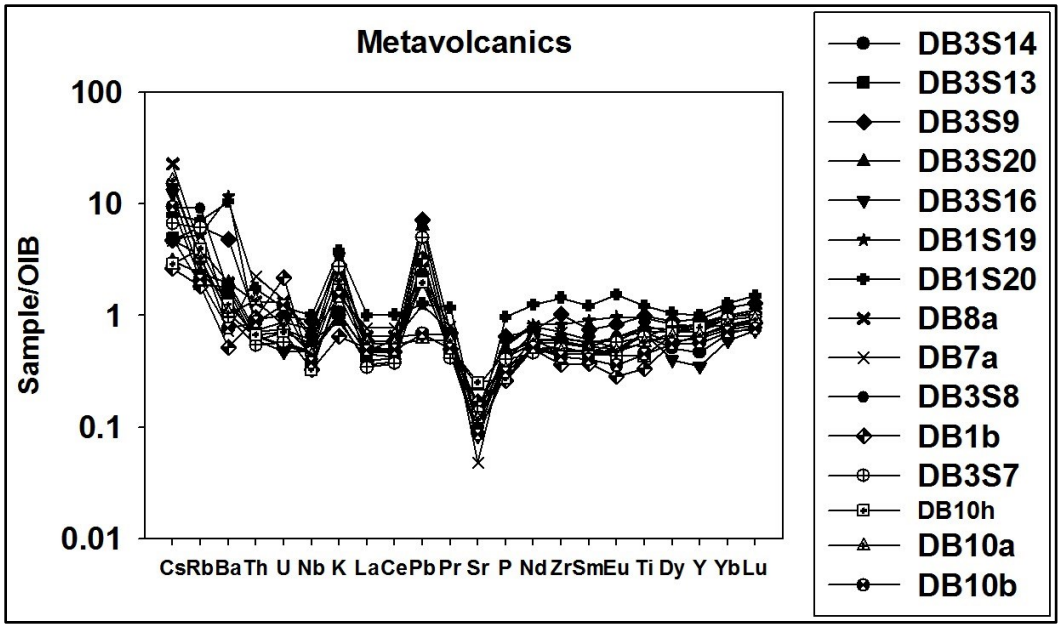


Figure 6.7 Oceanic Island Basalt (OIB)-normalized multi-element patterns of the metavolcanic samples from the area around the Deblin Copper Mine. Normalization values and the order of the elements are taken from Sun and McDonough (1989).

6.6 Tectonic implications

Differences in the geochemical features of modern volcanic rocks, primarily HFSEs, LILEs, and REEs from different tectonic settings have been used to establish tectonic settings (Pearce and Cann, 1973; Pearce and Norry, 1979; Floyd *et al.*, 1989; Sun and McDonough, 1989). As stressed earlier, the rocks of the Askevold Formation have experienced greenschist facies metamorphism and hydrothermal alteration. Consequently, the tectonic setting of the rocks have been inferred using discriminating diagrams which use alteration resistant elements, predominantly Nb, Zr, Ti, Y, V, La, and Yb (Pearce and Cann, 1973; Floyd and Winchester, 1975; Wood, 1980; Shervais, 1982; Sun and McDonough, 1989).

Since the samples from the study area appear to have originally been alkali basalts (Figure 6.2), then the basalt geotectonic diagrams are appropriate to determine the tectonic setting. According to Pearce and Cann (1973), the concentrations of trace elements such as Ti, Zr, Y, Nb and Sr are effective in characterizing basic volcanic rocks from different tectonic settings. Pearce and Cann (1973) used these trace elements to construct diagrams in which tectonic settings of unknown volcanic rocks can be identified. However, the methods require extreme caution such as the

possibility of the content of the elements in the rock being affected by weathering or metamorphism. For instance, Sr should not be used when the rock is altered and when it signals features such as albitization and calcium-depletion in greenschist facies metamorphism. Therefore, this study does not use any Sr-bearing basalt geotectonic diagram because the samples are metamorphosed to greenschist facies and hydrothermally altered. The four elements, Ti, Zr, Y and Nb are stable under greenschist facies conditions, and insensitive to alteration processes (Pearce and Cann, 1973; Pearce and Norry, 1979; Shervais, 1982; Pearce, 1996). Pearce and Cann (1973) established a Ti-Zr-Y diagram to identify basalts erupted within plates (ocean island and continental basalts). Furthermore, Pearce and Cann (1973) suggested that the Y/Nb ratio can be used to classify whether the basalt is tholeiitic or alkalic.

Samples from the area around the Deblin Copper Mine dominantly plot in the within-plate field of the Zr-Ti basalt tectonic discrimination diagram of Pearce (1982) (Figure 6.8a). In addition, on the La/Yb-Nb-La basalt tectonic discrimination diagram of Hollocher et al. (2012) all samples plot within the oceanic islands field (Figure 6.8b). These observations propose a within oceanic plate palaeotectonic setting.

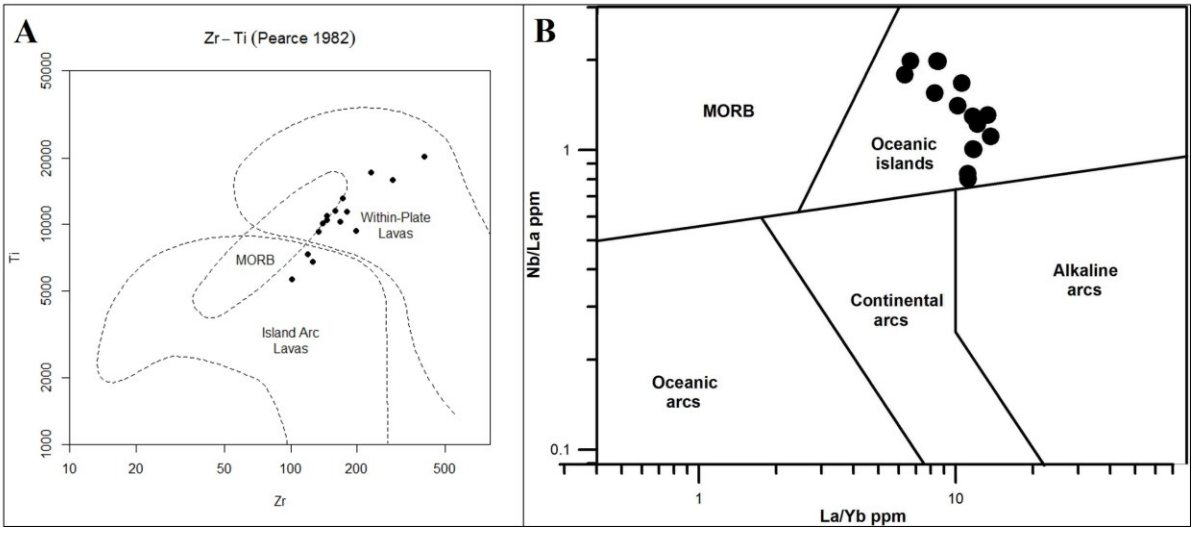


Figure 6.8 Basalt tectonic discrimination diagrams. A) The majority of the metavolcanic samples plot in the within-plate lavas field. B) Metavolcanic samples plot within the oceanic islands field on the La/Yb-Nb/La diagram of Hollocher et al. (2012).

6.7 Discussion

The major and trace element geochemistry of the metavolcanic rocks provided a new insight into the Neoproterozoic volcanism of the Askevold Formation in the southern Otavi Mountain Land. The rocks from the area around the Deblin Copper Mine are metamorphosed to greenschist facies and hydrothermally altered. This may have affected the distribution of the LILE. The application of most major elements and LILE to determine the geochemical characteristics and infer the possible tectonic setting of emplacement of these rocks proved not to be reliable. As a result, immobile trace elements including the REE compositions were used instead because they are alteration resistant.

Based on the immobile trace element volcanic classification diagrams of Floyd and Winchester (1977) and Pearce (1996), the Nosib Group Askevold Formation metavolcanic rocks of the area around the Deblin Copper Mine were originally alkali basalts. These observations are consistent with the findings by Miller (2008), when he reported that based on Nb/Y ratios the mafic volcanics of the Askevold Formation represent alkali basalts. In contrast, Adamson (1976) suggested that the sericite-chlorite schist of the area around the Deblin Copper Mine is derived from trachytic or trachyandesitic tuffs. The current study, contradicts the findings of Adamson (1976). The good linear positive trends on the plots of Zr against HFSE (e.g Ti, Nb) and REE (e.g Ce, Sm) suggest that the volcanic rocks are genetically related. The positive and negative Eu anomalies of the metavolcanic rocks on the chondrite-normalized diagram, suggest that the metavolcanic rocks are related to each other by the fractionation of plagioclase.

In order to determine the palaeotectonic setting of the metavolcanic rocks, their geochemical character is compared with those of modern volcanic rocks from mid-ocean ridge, subduction-related and within plate. The samples do not support the MORB tectonic setting because they do not show depletion patterns and their composition is alkalic (Figure 6.2) but not tholeiitic. Similarly, the samples are not arc-related (subduction-related) but rather represent within-plate volcanism as shown on both the Zr-Ti basalt tectonic discrimination diagram by Pearce (1982) and La/Yb-Nb/La diagram of Hollocher et al. (2012) (Figure 6.8).

To explain whether the metavolcanic samples are within-plate ocean island or continental basalts, rock association and field observations were considered in this study to supplement the available geochemical data. Field mapping revealed the presence of a felsic metavolcanic breccia which is suggestive of bimodal volcanism. Furthermore, the study considered the sedimentary rocks present in the area around the Deblin Copper Mine that are associated with the metavolcanic rocks. The mapped sedimentary rocks are carbonates (dolomite and limestone) and phyllite (metamorphosed shale), which are shallow marine sediments. Thus, the associated sedimentary rocks support the oceanic geotectonic environment. The absence of typical continental rift-related sedimentary rocks such as the conglomerate and sandstone (quartzite) in the study area argues against continental rift environment. However, previous researchers (e.g Kamona and Günzel, 2007; Miller, 2008) stressed that the metavolcanic rocks in this area formed as a result of rift related volcanism that produced bimodal volcanic rocks in the Northern Rift of the Damara Orogen about 746 Ma ago (Kamona and Günzel, 2007; Miller, 2008). Based on the presented geochemical and petrological data, this study argues that the metavolcanic rocks of the Askevold Formation around the Deblin Copper Mine area formed as alkali basalts in an oceanic island geotectonic setting at the rift margin of the Damara Orogen. This interpretation is in agreement with the location of the study area, which is located at the transition from the Swakop Basin to the carbonate platform of the Otavi Mountain Land fold and thrust belt.

With respect to the concentrations of the base metals in the metavolcanic rocks, the samples have higher Ni concentrations (27.51 to 102 ppm) than the Co concentrations (13.81 to 72.71 ppm), whereas Zn concentrations (37.28 to 300 ppm) are higher than Pb concentrations (91.995 to 22.84 ppm). The Cu concentrations show a wide variation (6.33 to 5153 ppm). The metal contents in the metavolcanic rocks are associated with the hydrothermal fluids and they are important for assessing the economic resources. The Cu concentrations (266 to 1855 ppm) of the samples collected from other parts of the Askevold Formation by Miller (2008) (Table 6.4) are higher than those from the Deblin Copper Mine. The Zn concentrations (79.00 to 121 ppm) are somewhat similar.

Chapter 7

Geophysical Study of the Deblin Copper Mine area

7.1 Introduction

The Deblin Copper Mine area has poor rock outcrop due to extensive Kalahari Supergroup sand cover, which leads to difficulties in understanding the local structural framework and developing links between the local and regional architecture. The concealed structures in the entire southern Otavi Mountain Land including the Deblin Copper Mine area, are thought to have major influences on the distribution of base metal mineralization (Smit, 1959; Golden Deeps Limited, 2013). New approaches that can map and identify the geometry of the structures in this area are essential to help understand the distribution of lithologies, stratigraphy, and the structural development that may have controlled copper mineralization in the area around the Deblin Copper Mine.

The study area provides a framework that allows the integration of stratigraphic and structural geological analysis with geophysical methods because its geological history is well understood, although poorly exposed, and the units are not deeply buried, which means the geological component of the magnetic signal is not strongly attenuated. This model has not been applied anywhere in the Otavi Mountain Land and it could be used as an exploration tool in similar terrains. Potential field datasets are predominantly effective at giving insights into the subsurface geology beneath sedimentary cover, as the magnetic sources within the cover succession are often weaker than metamorphic rocks underlying the sedimentary stratigraphy (Milligan and Gunn, 1997; Betts et al., 2003). Magnetic datasets have frequently been used for imaging the subsurface as they can provide a link between rock outcrop and the subsurface (Betts et al, 2003). According to Hinze and Kane (1985), interpretation of aeromagnetic data has been used to infer the regional-scale architecture of poorly exposed regions. The level of constraint depends on the aeromagnetic data resolution, the extent of rock outcrop, the level of detail in geological mapping and the availability of rock physical property data (Aitken and Betts, 2009).

This chapter reports the investigation of a study on the structural framework of the area around the Deblin Copper Mine using magnetic susceptibility data, high resolution aeromagnetic and ground magnetic data. The chapter presents the regional interpretation of the aeromagnetic data of the southern Otavi Mountain Land as well as the local interpretation of the ground magnetic data of the Deblin Copper Mine area. Furthermore, the study integrates ground magnetic data interpretations with stratigraphic and structural data such as foliations and bedding measurements presented on the regional geological maps of the Geological Survey of Namibia (2008) and Smit (1959).

The specific objectives of this chapter are: (i) to develop links between local and regional architecture from available aeromagnetic data and published geological data to delineate the boundary between the Swakop Basin and the carbonate platform of the Otavi Mountain Land; (ii) to establish and classify magnetic signatures of various rock formations in the study area; (iii) to identify faults and lineaments below and within the Otavi Group carbonates which may have important inferences for focusing mineralizing hydrothermal fluids in the Deblin Copper Mine area; (iv) to integrate regional aeromagnetic data with the published regional geology and high resolution ground magnetic data from the Deblin Copper Mine area to identify prime areas of exploration interest for copper.

7.2 Previous Geophysical Work

7.2.1 Southern Otavi Mountain Land

Generally, areas covered by predominantly igneous and metamorphic rocks show complex magnetic variations, whereas in sedimentary regions, magnetic anomalies are small, mainly reflecting the basement lithologies (Jaques *et al.*, 1997). The Otavi Mountain Land is a sedimentary-dominated region with prominent metamorphic formations, such as the Askevold Formation with an east-west orientation located in the southern part. Regional geophysical surveys which are primarily used in mineral and groundwater exploration in Namibia have been undertaken by the Geological Survey of Namibia. In addition to mineral exploration, regional airborne magnetic and radiometric data were collected to give an insight into the field of crustal evolution research (Eberle *et al.*, 1995; Hutchins *et al.*, 1997).

The first regional airborne magnetic and radiometric survey in Namibia funded by the government of Namibia was conducted in 1968 (Hutchins and Wackerle, 2007). Subsequently, several regional airborne magnetic surveys of high resolution covering Namibia were conducted between 1968 and 1990 by the Geological Survey of Namibia in collaboration with the German Federal Institute of Geoscience and Natural Resources (BGR) (Eberle et al., 1995; Hutchins et al., 1997). The total magnetic data were collected from 41 different survey blocks across Namibia using different magnetomters, principally fluxgate, proton precession and cesium vapour magnetometers (Eberle et al., 1995; Hutchins et al., 1997). The data were acquired with varying survey parameters such as line spacing of 0.5 km to 1 km, tie-line spacing of 10 km and flight height of 70 m to 150 m with various flight directions perpendicular to the strike of the lithologies (Eberle et al., 1995; Hutchins et al., 1997). Some surveys undertaken in sedimentary basins for petroleum exploration assumed a wider line spacing of up to 10 km. Successively, the data from individual survey blocks were then merged to form a single compatible data base (Eberle et al., 1995) (Figure 7.1). The resultant regional magnetic compilations provided a new insight into the crustal evolution of Namibia and delineated areas for future mineral exploration potential (Eberle et al., 1995; Hutchins et al., 1997; Hutchins and Wackerle, 2007).

Despite this commendable effort, high resolution data collected with the latest technological advancements, including increased sampling rate, closely spaced survey line and improved computer processing became crucial (Hutchins and Wackerle, 2007). As a consequence, according to Hutchins and Wackerle (2007), Namibia implemented high resolution magnetic and radiometric surveys. The parameters of these high resolution surveys consist of 200 m line spacing, 2500 m tie-line spacing and a nominal terrain clearance of 80 m.

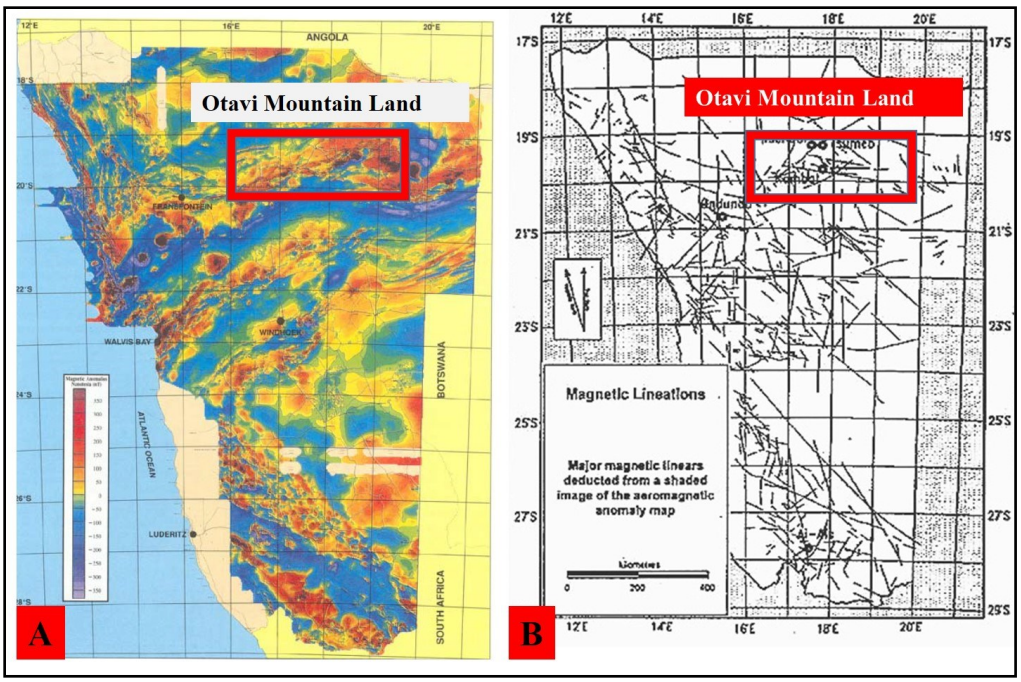


Figure 7.1 Regional aeromagnetic map of Namibia, 1: 1 000 000 scale. A) The airborne magnetic anomaly map (nT) of Namibia, with the International Geomagnetic Reference Field at the time of acquisition removed. B) Pattern of magnetic lineaments representing regional geological features, derived from (A). The red open boxes in both maps show the location of the Otavi Mountain Land. Both maps are modified after Eberle et al., (1995).

Previous geophysical studies in the Otavi Mountain Land attempted to discover sediment-hosted base metal deposits. A systematic analysis of the structural signature of known mineral occurrences such as the Deblin Copper Mine area reveal previously unknown mineral occurrences, mostly of an epigenetic nature, of which about two thirds are located close to intersections of magnetic lineaments (Eberle et al., 1995).

Different parts of the Otavi Mountain Land have been extensively explored for ore bodies similar to the Tsumeb type. The first regional airborne magnetic surveys covering the Otavi Mountain Land were conducted between 1968 and 1990 (Eberle *et al.*, 1995; Hutchins *et al.*, 1997) (Figure 7.1a). With technological advancements, new high-resolution aeromagnetic data were collected over the Otavi Mountain Land region between 2007 and 2008 by the Geological Survey of Namibia (Geological Survey of Namibia, 2008). Eberle *et al.* (1995), suggested that the magnetic lineations mapped in the Otavi Mountain Land using the aeromagnetic data (Figure 7.1b) reflect geological faults, shear zones, and magnetic and non-magnetic dykes. Eberle *et al.* (1995) noted

that the magnetic lineations become weak in the central western part of the Otavi Mountain Land and are even absent in some places. This can be explained by the suppression of the magnetic signal by younger non-magnetic Otavi and Mulden Groups sedimentary cover (Eberle et al., 1995). Eberle et al., (1995) suggested that the structures linked to these magnetic lineations have controlled the epigenetic base metal mineralization in the Otavi Mountain Land and have southwest-northeast and west-northwest-east-southeast orientations.

Corner (1983; 2008) conducted studies that involved interpreting the aeromagnetic data covering the Otavi Mountain Land. According to Corner (2008) the conspicuous strong magnetic signatures in the southern Otavi Mountain Land are largely attributed to the highly magnetic diamictites of the Chuos Formation and mafic volcanic rocks of the Askevold Formation. The Chuos Formation consists of a banded iron formation, which has positive magnetic response (Corner, 2008; Miller; 2008). Miller (2008) argued that the conspicuous east-west trending anticlinal structures visible in the magnetic data from the southern Otavi Mountain Land separate spacious magnetically quiet areas of the higher stratigraphic levels such as the Mulden Group strata situated in the synclines. In contrast, the high magnetic signatures in the antiforms are largely attributed to the exposure or shallow sub-outcrops of the diamictites and possibly volcanics associated with the Nosib Group of the lower Damara strata.

7.2.2 Kombat South: Deblin Copper Mine Area

The area around the Deblin Copper Mine has been subjected to various geophysical methods, predominantly magnetics and electromagnetics (EM). In the Deblin Copper Mine area, Adamson (1976) observed positive magnetic anomalies in ground magnetic data and interpreted that they are attributed to the presence of pyrrhotite located at the contact zone of copper mineralization. The magnetic values were determined with an Askania torsion balance instrument on a five lines survey. The base station was located on the dolomite at the end of the first line of the survey array and readings were taken at the completion of each traverse. The current study uses ground magnetic data collected with a cesium vapour magnetometer along the survey lines, across the study area and a proton precession magnetometer at the base station to record the diurnal variation.

The interpretations of the high resolution aeromagnetic data collected by the Geological Survey of Namibia indicated cross-cutting northeast-trending lineaments (Golden Deeps Limited, 2013). It was suggested that the Deblin Copper Mine appears to be located close to an intersection of the east-west trending Askevold Trend and the northeast trending structures, of which one lineament appears to intersect the Kombat deposit (Golden Deeps Limited, 2013), located northeast of the study area, in the central Otavi Mountain Land. As a result, this has raised speculations as whether these structures possibly represent regional controls on the copper mineralization in the southern Otavi Mountain Land (Golden Deeps Limited, 2013).

Recently, it was anticipated that successful EM surveys would allow the EM method to be used as a tool to discover copper mineralization along the whole Askevold Trend. Subsequently, Golden Deeps Limited (2013) conducted an EM survey primarily the downhole EM and the fixed loop surface EM surveys, to test a 1.6 km strike extent copper in soil anomaly. Results were not known at the time of writing this thesis. This study uses recently collected high resolution ground magnetic data to establish the structural framework of the study area and its relationship with the local base metal mineralization.

7.3 Structural geological analysis

The geological cross-sections were constructed in order to understand the structural geology of the study area before interpreting the available aeromagnetic and ground magnetic data. The cross-sections of the southern Otavi Mountain Land (Figure 7.2) are presented in Figure 7.3. The cross-sections are based on extrapolating surface information to provide vital assessments of the geological record and interpretation of the structure at depth. The cross-section interpretations are based on the data collected by the present study, orientation of faults and folds, and dip and strike measurements (Appendix D) taken from the regional geological maps and reports by Smit (1959) and the Geological Survey of Namibia (2008) as well as the stratigraphic sequence taken from Hoffman and Prave (1996), Kamona and Günzel (2007) and Miller, (2008).

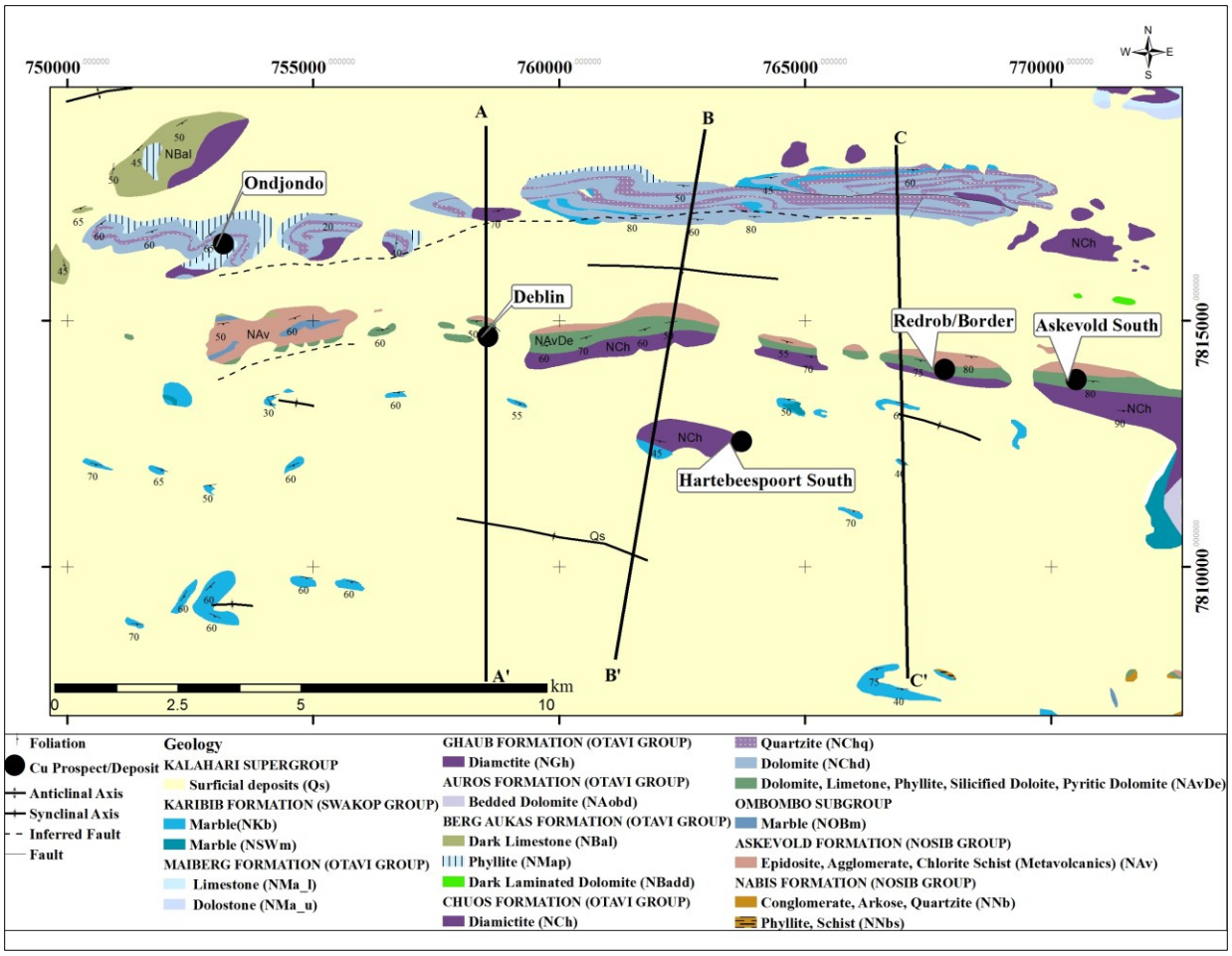


Figure 7.2 Regional geological map of the southern Otavi Mountain Land showing the AA'-CC' lines of the cross-sections shown on Figure 7.3. Modified after Smit (1959) and the Geological Survey of Namibia (2008).

The cross-sections (Figure 7.3) show the Askevold Formation metavolcanic rocks overlain by the Chuos Formation carbonates and diamictite. The Chuos Formation, in turn, is overlain by the Karibib Formation of the Swakop Group in the central and southern parts of the study area. The Askevold Formation outcrops occur in the central part of the map and consists of the agglomerate, epidosite and chlorite schist The Karibib Formation schist is inferred from the geological map of the southern Otavi Mountain Land by Smit (1959). The cross-sections AA'-CC' (Figure 7.3) show the presence of several thrust faults and anticline and syncline folds. The cross-sections exhibit that the rocks in the south are thrust northward along the thrust faults. This resulted in overturned folds as shown in Figure 7.3.

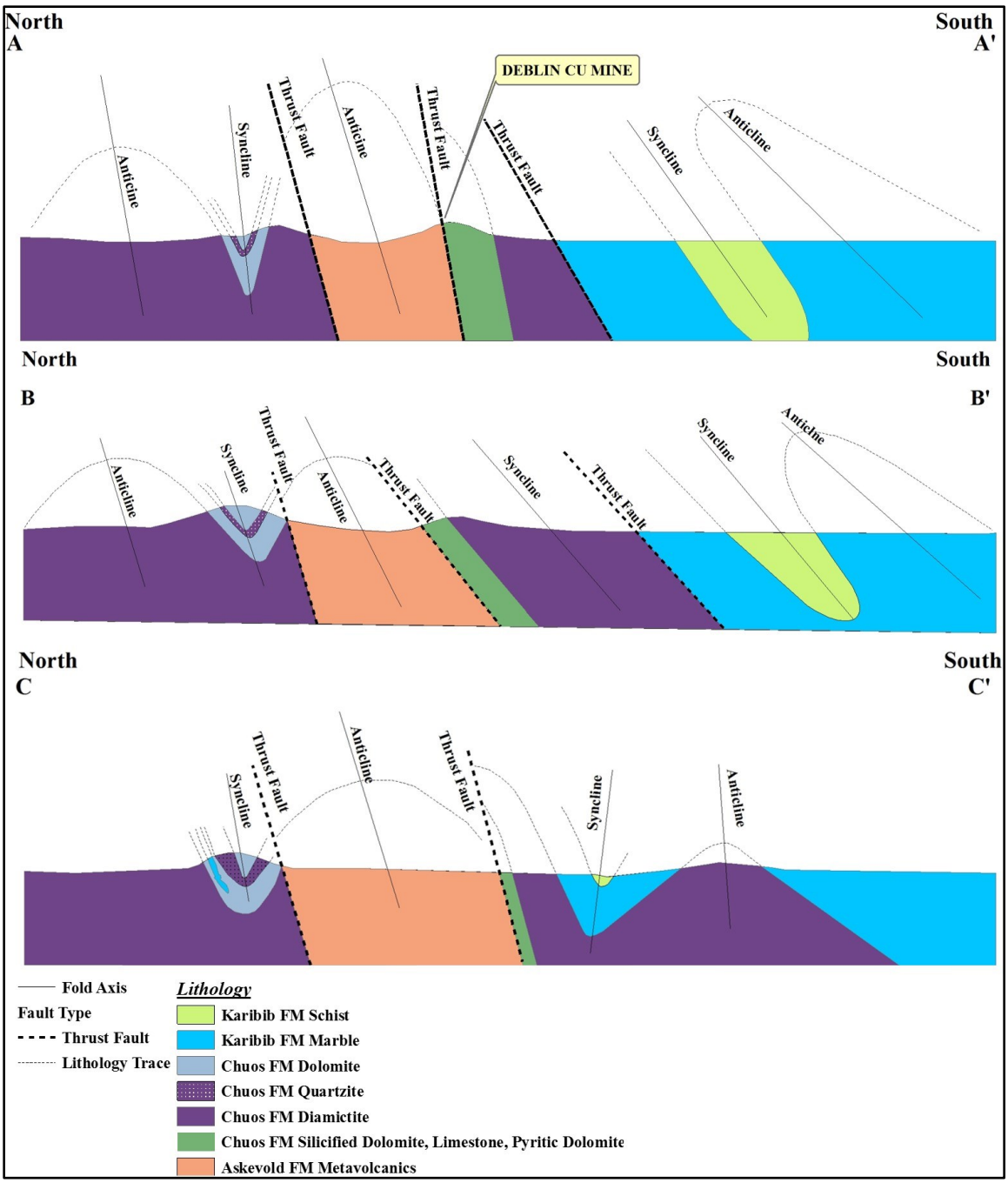


Figure 7.3 Regional geological cross-sections showing interpreted structural architecture of the southern Otavi Mountain Land.

These observations suggest the presence of a regional overturned antiformal structure in the central and southern parts of the area, which contains the Askevold Formation in the core. The southern limb of the antiform is partially covered by sand and thus occurs as discontinuous outcrops with

east-west strike, whilst the northern limb appears to have been eroded and fully concealed by sand cover. The truncations of the quartzite, massive dolomite and marble in the northern part suggest the possibility of a shear zone or a thrust fault. Additionally, the presence of thin units of marble within the quartzite and massive dolomite in the northern part (cross-section CC') appear to indicate that the units are overturned forming a northward-vergent fold-and-thrust belt.

In addition, local structural data based on structural analysis (Appendix D) were undertaken at several localities on the outcrops and in three drill cores in the study area. The cross-sections of the local study area are drawn from the detailed geological map of the Deblin Copper Mine area (Figure 7.4). The cross-sections from the local geological map represent the detailed geology of the southern limb of the antiform on the regional geological map.

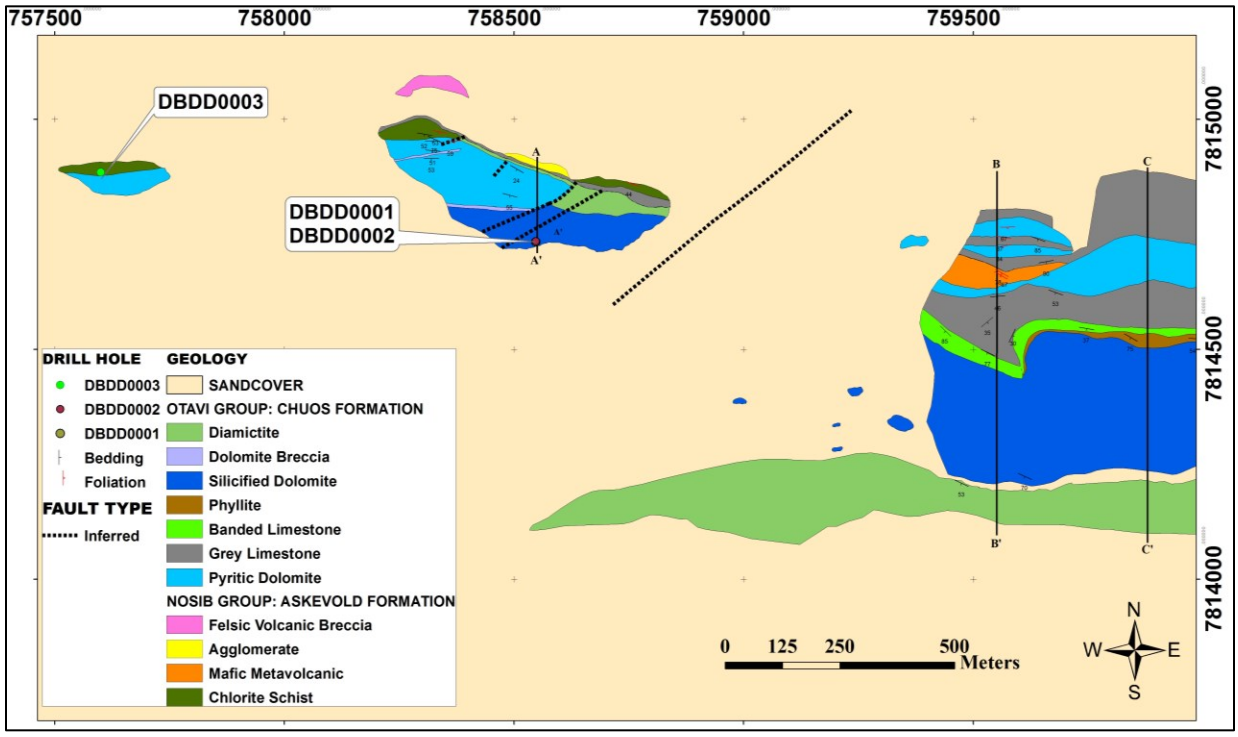


Figure 7.4 Geological map of the Deblin Copper Mine are showing the AA'-CC' lines for the cross-sections shown on Figure 7.5.

The cross-sections (Figure 7.5) show the Askevold Formation metavolcanic rocks overlain by the Chuos Formation carbonate successions. Cross-section AA' shows the agglomerate overlain by the grey limestone, diamictite and the silicified dolomite. The contact between the agglomerate and

the carbonate is interpreted to coincide with a thrust fault. DBDD0001 and DBDD0002 did not intersect both the grey limestone and diamictite for they appear to represent a pinchout structure or a tight synform. Cross-sections BB' and CC' are dominated by the Chuos Formation carbonates and show tight folding. The lack of continuity of the pyritic dolomite and grey limestone in relation to the mafic metavolcanic rock suggest the possibility of structural contacts between the carbonates and the mafic metavolcanic. Cross-section BB' consist of a mafic metavolcanic, whereas cross-section CC' does not have any metavolcanic rocks. While the diamictite appears to occur only at shallow depths in cross-section AA', it appears to be more extensive in the cross-section CC' as it overlies the silicified dolomite. All the cross-sections show different rock configurations and thus they cannot be correlated laterally. These conclusions indicate the presence of concealed local faults.

The style and complexity of deformation in the study area is poorly understood due to limited exposure. The general strike of the lithological units is east-west with a dip ranging between 44º and 85º to the south. Evidence for faulting is provided by unit truncation and local tectonic brecciation textures. The faults trend in northeast and northwest directions and range between 50 m and 260 m in length. Lineations such as slickensides were not observed and thus neither the throw nor the displacement of the mapped faults could be established.

It is clear from the cross-sections above that in this study the geological cross-section method is limited by the insufficient amount and position of outcrops, reducing the ability to extract meaningful geological and structural information. Thus, insufficient information about the deformation history restricts any accurate regional and local interpretations. Consequently, methods that provide some continuity between discrete outcrops to help interpret the structural framework of the study area are required. Several recent studies (Aitken and Betts, 2009; Stewart *et al.*, 2009; Crawford *et al.*, 2010; Stewart and Betts, 2010; Gaafar, 2015) have demonstrated that potential field interpretations are of importance in determining the geological constraints in areas of poor outcrop. Therefore, the structural framework of the study area can be constrained via the integration of qualitative aeromagnetic and ground magnetic data interpretation with quantitative two-dimensional (2D) forward modeling. The interpretation of magnetic data permits the

identification and interpretation of continuous concealed magnetic bodies where there is no outcrop.

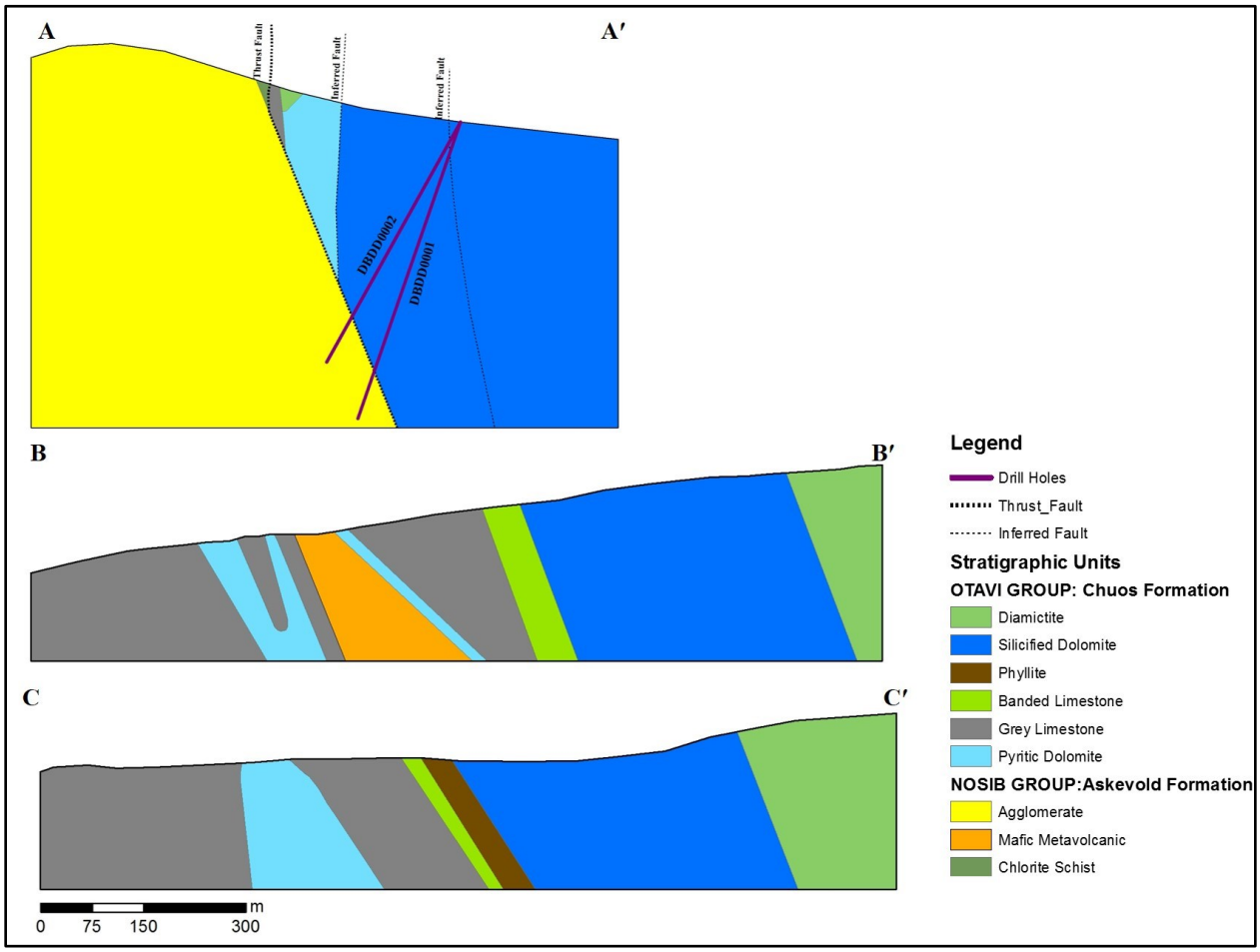


Figure 7.5 Geological cross-sections showing interpreted structural architecture of the Deblin Copper Mine area.

7.4 Magnetic Susceptibility Data

Rock magnetism is controlled by the iron content in the rock type (Dentith and Mudge, 2014). The magnetic properties of the rocks are controlled by their mineral assemblages, whereas the magnetic properties of the minerals are deeply linked to their mineralogical characteristics (Lanza and Meloni, 2006). To investigate rock magnetism in the study area, the magnetic responsiveness of the lithologies were tested by determining their magnetic susceptibility prior to conducting the ground magnetic survey. Magnetic susceptibility gives an indication of the amount of

ferromagnetic minerals, primarily magnetite present in a lithology. Therefore, magnetic susceptibility data were collected to determine where magnetic minerals such as magnetite and pyrrhotite occur in the local stratigraphy. Moreover, magnetic susceptibility influences the anomalies caused by lithologies to the Earth's magnetic field, and thus the data were essential in interpreting the magnetic sources in both the aeromagnetic and ground magnetic data.

7.4.1 Equipment and Data Collection

The magnetic susceptibility data were collected using a hand held SM 20 magnetic susceptibility meter (Figure 7.6) during fieldwork between 30 November 2015 and 17 December 2015. The SM 20 magnetic susceptibility meter belongs to the Geology Department, University of Namibia. In the field, magnetic susceptibility data were collected on the outcrop (in situ) of different rock types present in the study area (Figure 7.7). Also see Appendix D for details. In addition, magnetic susceptibility readings were taken on drill cores (DBDD0001, DBDD0002 and DBDD0003), approximately every 60 cm. Magnetic susceptibility readings from rock outcrops and drill cores were recorded in the notebook and lithological log sheets, respectively, and subsequently entered into digital files.



Figure 7.6 A photograph of the handheld SM 20 magnetic susceptibility meter.

7.4.2 Magnetic Susceptibility Data Analysis

The different rock types from the study area have different compositions and textures and, hence their magnetic susceptibility values are extremely variable. Rock outcrop and drill core magnetic susceptibility measurements are presented in Figures 7.7-7.12. The distribution of the magnetic susceptibility values of the rocks exposed in the study area is shown in Figure 7.7. Amongst the outcropping lithologies, it is evident that the agglomerate has the highest magnetic susceptibility values, whereas the carbonates record the lowest magnetic susceptibility values.

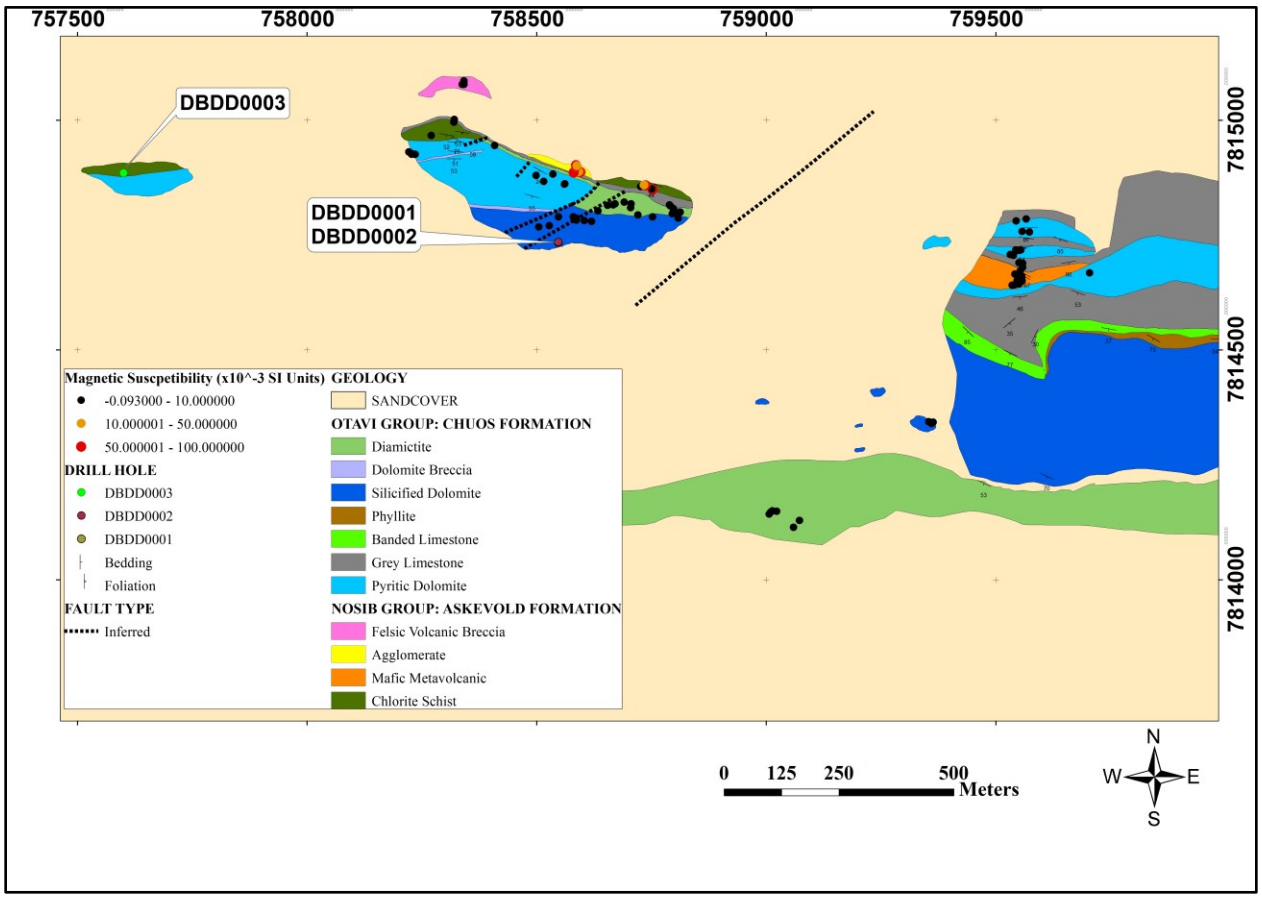


Figure 7.7 Detailed geological map of the Deblin Copper Mine area showing the distribution of the magnetic susceptibility values of different rock types.

a) Askevold Formation

In the Deblin Copper Mine area, agglomerate is the most magnetic rock type characterized by high magnetic susceptibility with values in the range of 50 to 181 $x10^{-3}$ SI units (Figure 7.8-7.10). However, magnetic susceptibility in the agglomerate is not uniformly distributed and thus some

parts of the unit has low magnetic susceptibility values as low as 0.002 x10^{-3} SI units (Figure 7.9-7.10). The high magnetic susceptibility values occur in areas that are mafic clast-dominated, whereas the low magnetic susceptibility values occur in the rock groundmass, which has frequent quartz-calcite veins. The chlorite schist is weakly magnetic with magnetic susceptibilities in the range of 0.005 to 86.4 x10^{-3} SI units from outcrop measurements (Figure 7.8) and -1.65 to 1.81 x10^{-3} SI units in drill core (Figure 7.11). These observations indicate that the agglomerate and chlorite schist have significant amounts of fine-grained ferromagnetic minerals such as magnetite in places. The mafic metavolcanic has magnetic susceptibility values in the range of 0.244 to 0.646 x10^{-3} SI units, while the felsic volcanic breccia has lower low magnetic susceptibility readings in the range of 0.057 to 0.256 x10^{-3} SI unit (Figure 7.8). The tuff is characterized by a wide range of magnetic susceptibility values in the range of -2.5 to 2 x10^{-3} SI units, which prove that this unit is non-magnetic (Figure 7.11).

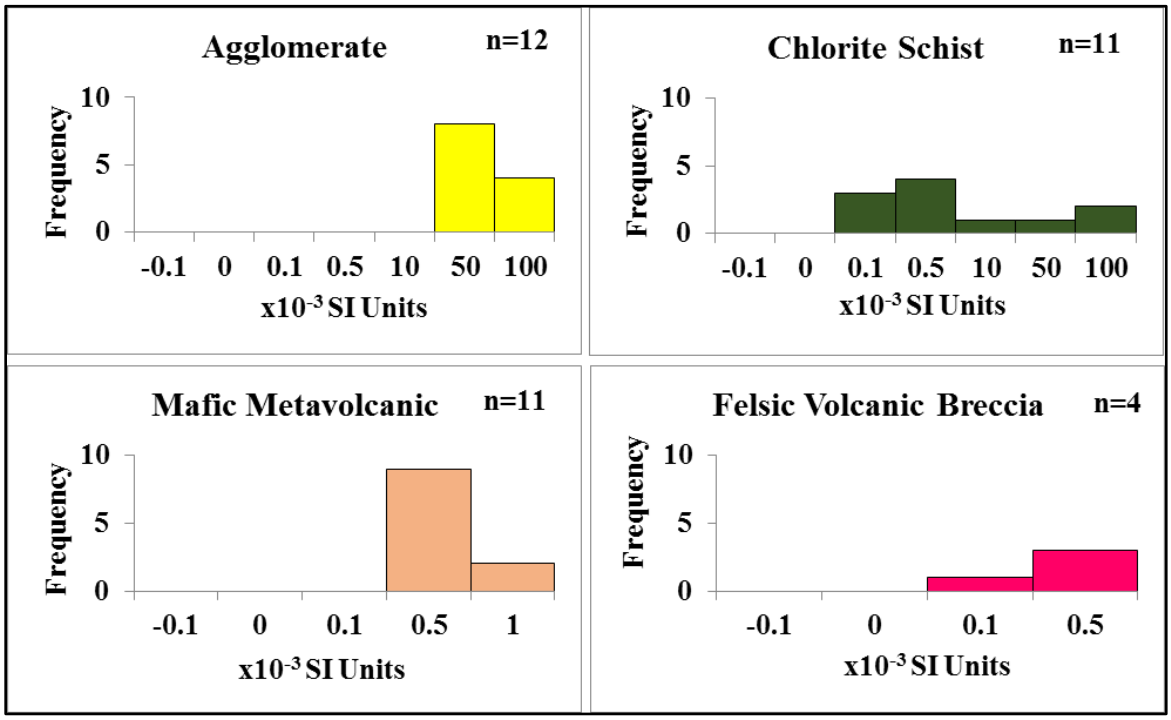


Figure 7.8 Histograms of in situ measured magnetic susceptibility data of the Askevold Formation lithologies.

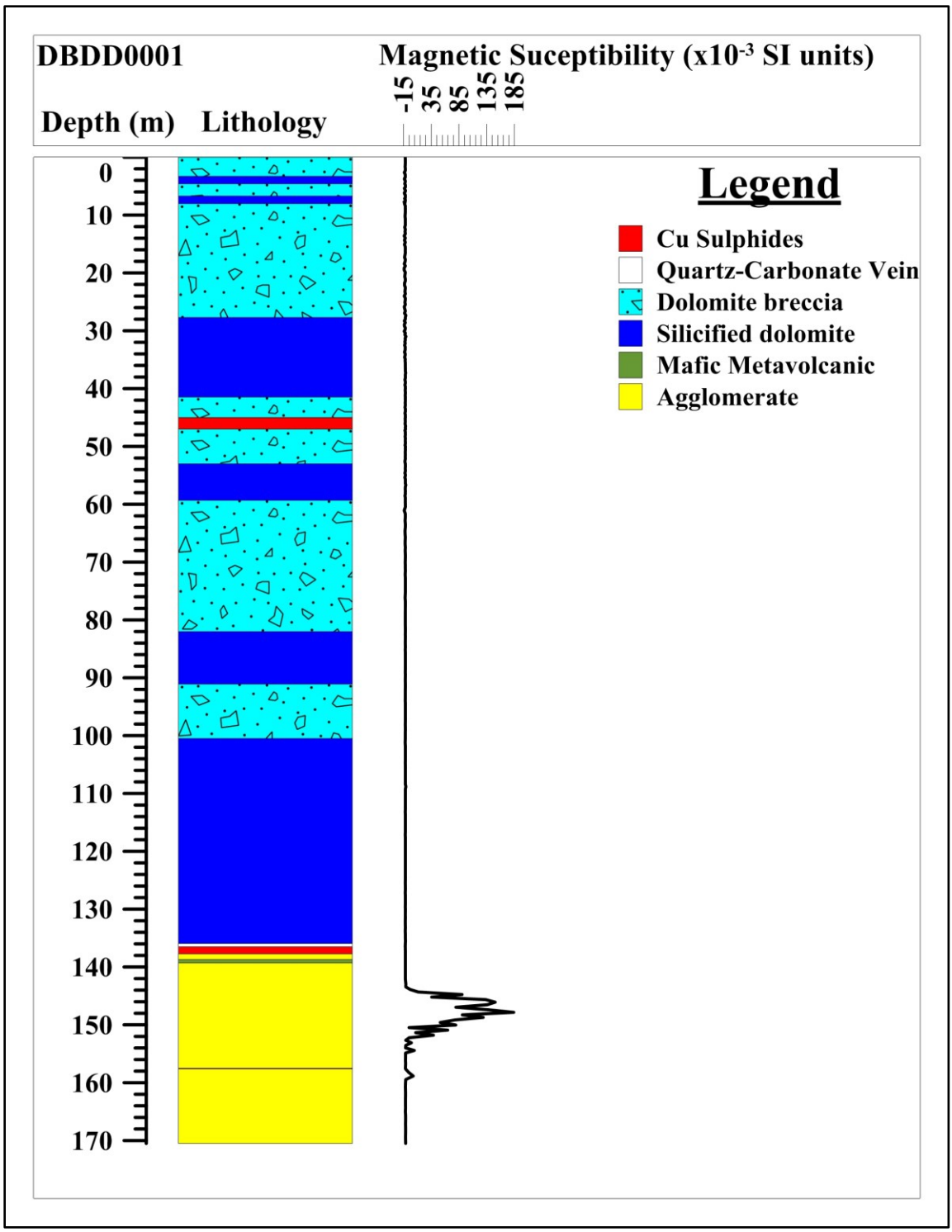


Figure 7.9 Magnetic susceptibility log for drill hole DBDD0001. The high values of the agglomerate suppress the variations in the overlying carbonates.

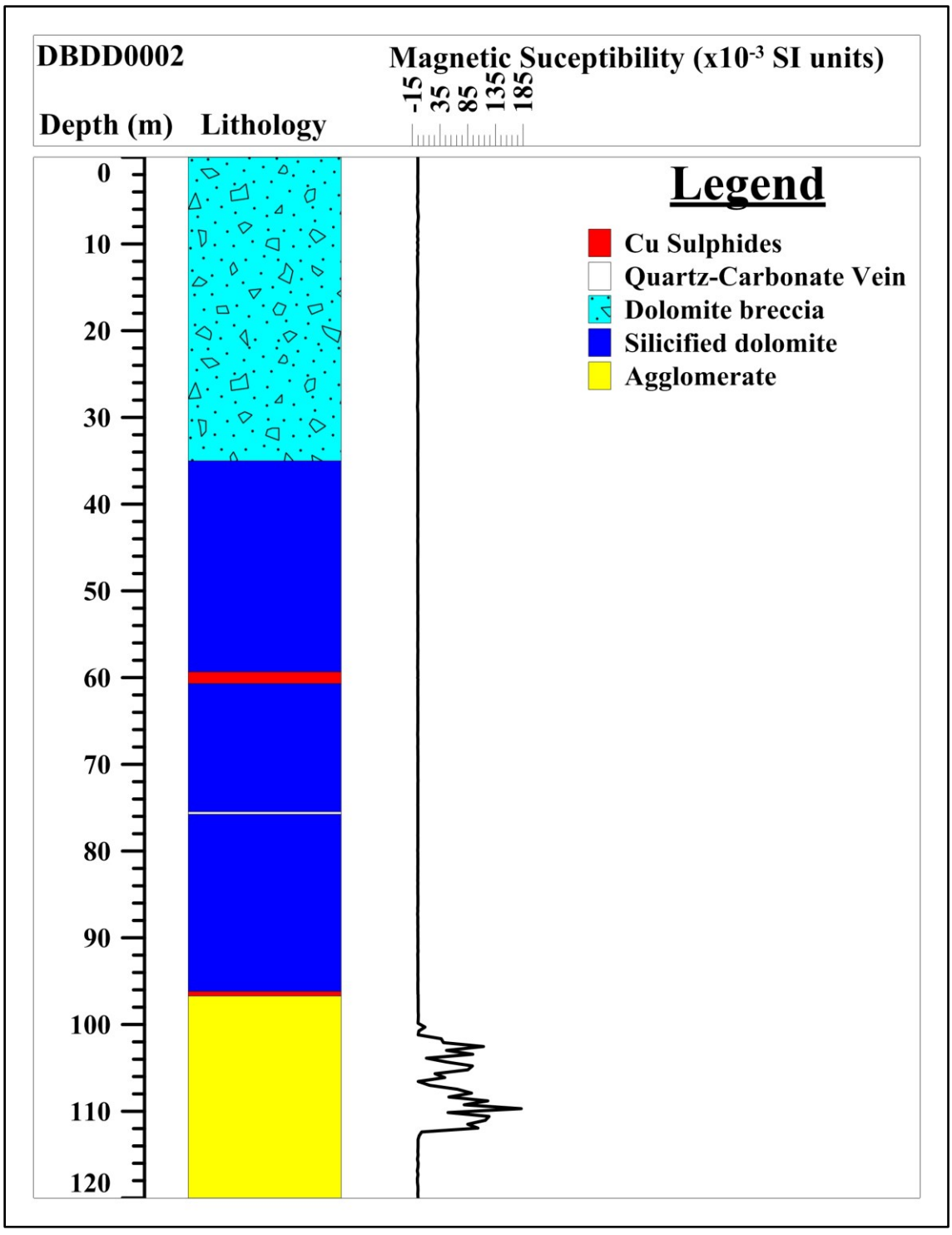


Figure 7.10 Magnetic susceptibility log for drill hole DBDD0002. The high values of the agglomerate suppress the variations in the overlying carbonates.

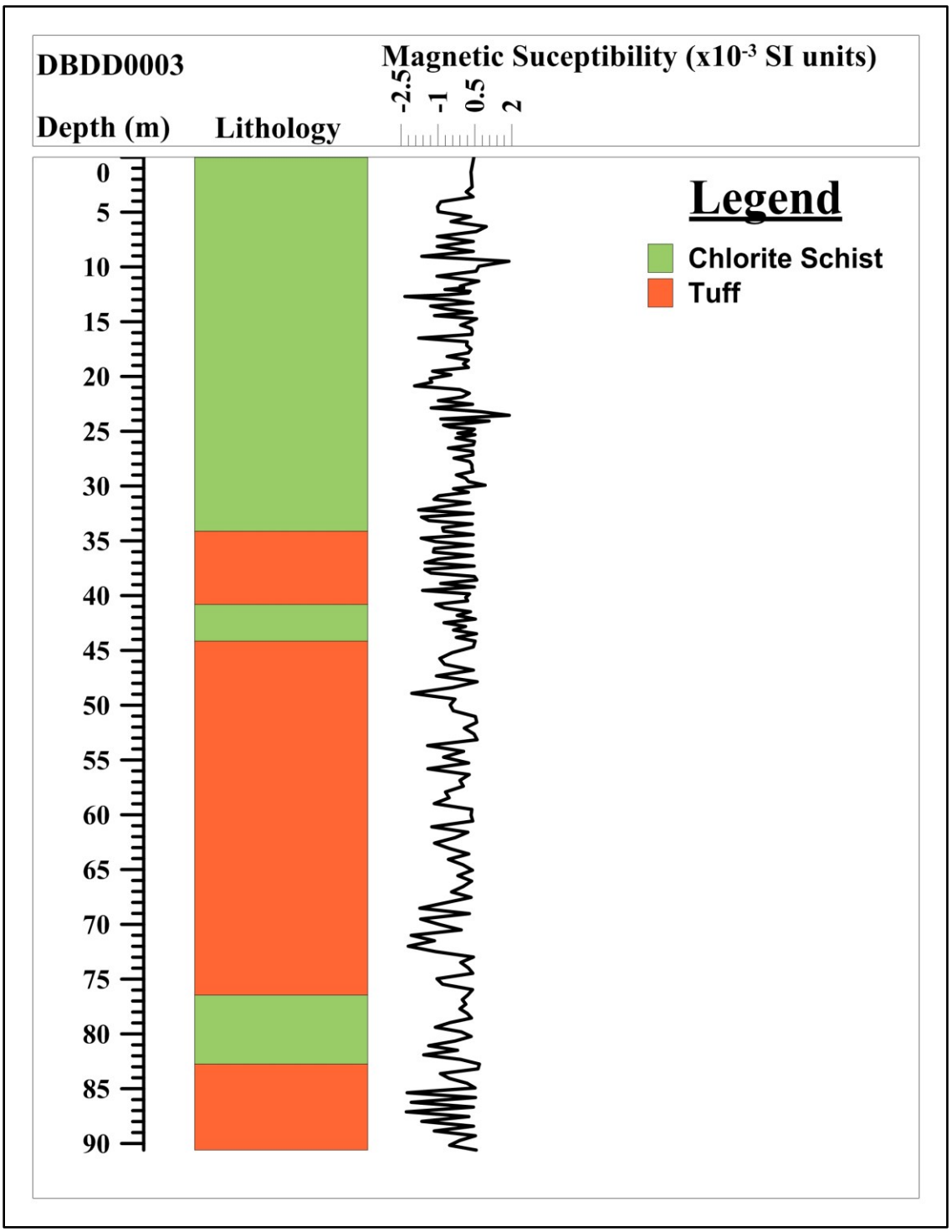


Figure 7.11 Magnetic susceptibility log for drill hole DBDD0003 showing low values.

b) Chuos Formation

The overlying carbonates of the Chuos Formation are not magnetic and have very low magnetic susceptibility values as shown in Figure 7.12. These carbonates are iron-deficient as they do not contain appreciable magnetite or pyrrhotite. It is noteworthy that locally the diamictite outcrops have low magnetic susceptibility values (Figure 7.7) and this is because the readings were taken on the surface of the carbonate clasts and matrix. On the regional scale, this diamictite is commonly associated with a strongly magnetic banded iron formation (Kamona and Günzel, 2007; Corner, 2008; Miller, 2008). In the study area, the banded iron formation is poorly exposed, and where it is present as a small outcrop, it is highly weathered to reddish brown attesting to the dominance of haematite. This banded iron formation outcrop is rarely significantly magnetized with very low magnetic susceptibility values in the range of 0.013 to 1.032 $x10^{-3}$ SI units. The mineralized intervals on the drill cores are characterized by very low magnetic susceptibility values, similar to the readings taken from the unmineralized zones.

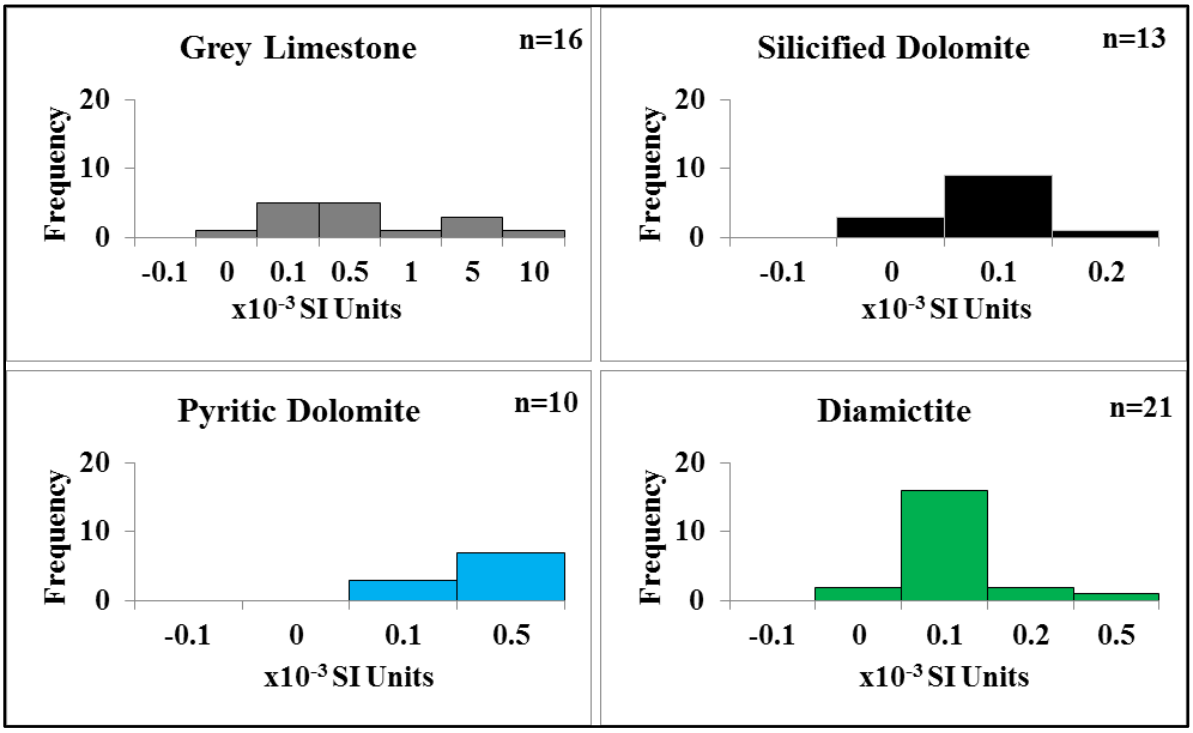


Figure 7.12 Histograms of in situ measured magnetic susceptibility data of the Chuos Formation lithologies.

7.4.3 Interpretation of the magnetic susceptibility data

The rocks with high magnetic susceptibilities, primarily the agglomerate and chlorite schist in places, consist of ferromagnetic minerals such as fine-grained magnetite. These units belong to the Askevold Formation and it is expected that they show positive magnetic anomalies in the aeromagnetic or ground magnetic data. The contrast in magnetic susceptibility of a single unit such as the agglomerate may have effects on the continuity of the positive magnetic anomalies in the area. The tuff and mafic metavolcanic rocks from this area, which also belong to the Askevold Formation, are non-magnetic, in spite of their mafic compositions. Although these units are of mafic composition, they are highly altered as shown in the petrography and geochemistry sections and thus their original compositions have changed. Therefore, the possible explanation for their low magnetic susceptibility values could be the effects of metamorphism or hydrothermal alteration.

The presence of these Askevold Formation non-magnetic units in this area suggest that the Askevold Formation is not magnetic everywhere, just like the Chuos Formation diamictite, which is non-magnetic where the banded iron formation is absent and this is well established in the Otavi Mountain Land. Thus, the Askevold Formation is expected to have both negative and positive magnetic responses in the study area depending on the present rock magnetism. The low negative magnetic susceptibility values in the carbonates owes to the presence of diamagnetic minerals such as quartz, calcite and dolomite.

In addition, the sulphide mineralized zones are dominated by chalcopyrite and pyrite which are paramagnetic and characterized by weak positive magnetic susceptibility values. Pyrrhotite is paramagnetic and in most cases it occurs in association with pyrite in ore environments. However, the collected magnetic susceptibility do not reflect the presence of pyrrhotite. Although, magnetite is often found in direct, or in close association with metallic sulphide ores, the magnetic susceptibility data collected on the three drill cores are not suggestive of the presence of magnetite. Based on the presented magnetic susceptibility data, a geophysical stratigraphic column can be constructed (Figure 7.13) and used to help interpret the aeromagnetic or ground magnetic data.

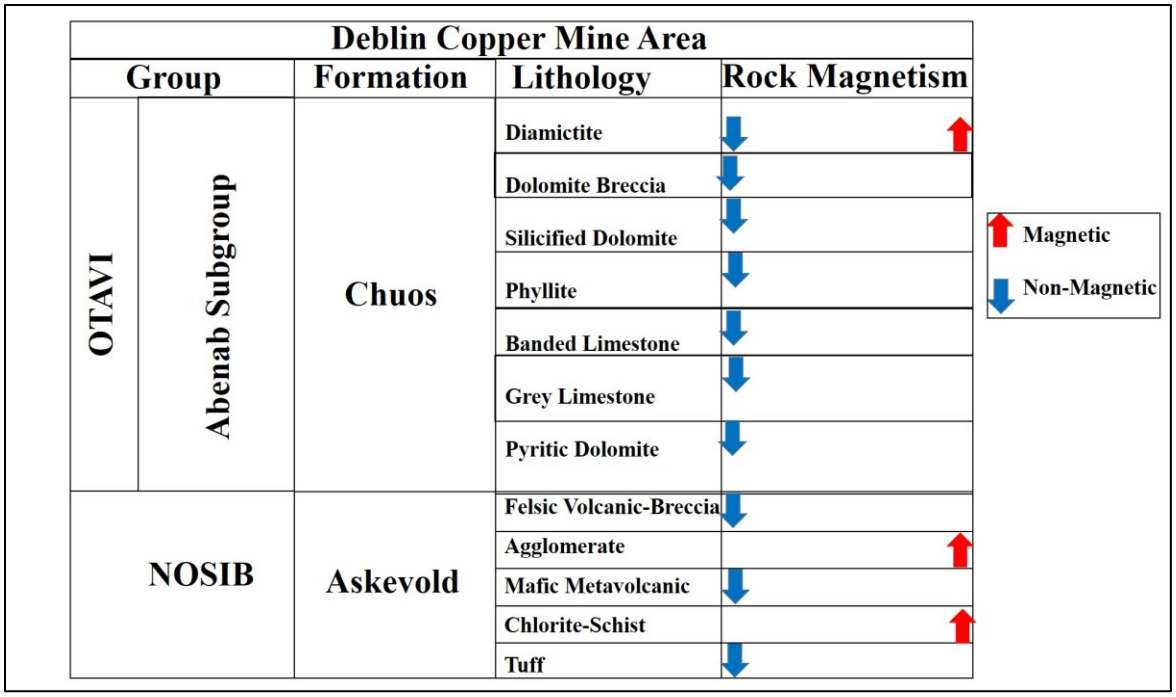


Figure 7.13 Magnetic stratigraphic column of the Deblin Copper Mine area. The diamictite is magnetic where it is associated with a banded iron formation and non-magnetic where the banded iron formation is absent.

7.5 Regional aeromagnetic data analysis of the Southern Otavi Mountain Land

Regional aeromagnetic datasets provide a link between outcropping rock and the subsurface. Aeromagnetic data are used to map and identify basement and shallow level structures (Dentith and Mudge, 2014). According to Hinze and Kane (1985) interpretation of aeromagnetic data has been used to infer the regional-scale architecture of poorly exposed regions; however, these interpretations suffer from lack of confidence in connecting the geophysical observations with geological constraints, particularly in polydeformed areas. High-resolution aeromagnetic data collected over the Otavi Mountain Land in 2008 by the Geological Survey of Namibia are used in this study as a basis for the mapping and interpretation of shallow and deep fault architecture and lithology distribution in the study area. These regional data were also used to glean geological information at different structural levels in the study area. Furthermore, these data are used to help align ground magnetic survey lines and locate the ideal base station in the survey area.

7.5.1 Aeromagnetic data

The aeromagnetic data of the Otavi Mountain Land were supplied by the Geological Survey of Namibia as a regional grid with 50 m cell size. The aeromagnetic data were collected in 2008 by GPX Surveys contracted by the Geological Survey of Namibia. The aeromagnetic data were collected along north-south flight lines at a nominal terrain clearance of 80 m, with 200 m line spacing and 2000 m tie line spacing in the east-west direction. The data collection sampling interval was 0.05 seconds. All surveys were flown using a fixed wing aircraft with cesium vapour magnetometers. The aeromagnetic data has had the diurnal variations and International Geomagnetic Reference Field (IGRF) removed.

7.5.2 Image processing and enhancement of aeromagnetic data

The gridded datasets were processed and imaged using Oasis Montaj, Geosoft software. Filtering in Oasis Montaj, Geosoft software is carried out in the frequency domain using a method for decomposing an image into a series of sine and cosine functions of difference frequencies or wavelengths known as Fourier transform. Fourier transform is explained in detail by Bracewell and Bracewell (1986) and Blakely (1996). The processed images were loaded into ArcMap 10.2.2 to overlay them with the geological mapping to facilitate interpretation. All the processed images used histogram equalization as the colour method. A histogram equalization colour method was

used to process images in order to adjust the contrast via the modification of the intensity distribution of the image's histogram.

Generally, magnetic data in areas with limited exposure, are characterized by their low contrast and poor signal-to-noise ratio and hence it is usually a serious challenge to extract subtle geological features from these data. To interpret the subsurface geology, optimum geological and structural information is extracted from magnetic data by applying a number of filters to these data. The aeromagnetic dataset has been reduced to the pole (RTP). High pass filters such as vertical, horizontal and tilt derivatives, and analytical signal are used to enhance shallow geological and structural features as well as to determine the contacts of these features. Low pass filters such as upward continuation and band-pass filtering are used to enhance deep-seated and intermediate depth-seated geological and structural features, respectively. Directional filters such as directional cosine filters, and butterworth directional filters are applied to the data to decorrugate the high amplitude magnetic signal caused by the flight line direction. Spectral analysis and filtering are applied to the aeromagnetic data to selectively remove or suppress unwanted frequency ranges (Reeves, 2005). Spectral analysis is achieved by applying Gaussian filters such as regional and residual filters. It is evident that the provided aeromagnetic grid consists of small residual errors and new errors (Figure 7.14) introduced by the gridding process and thus this data need to be microlevelled.

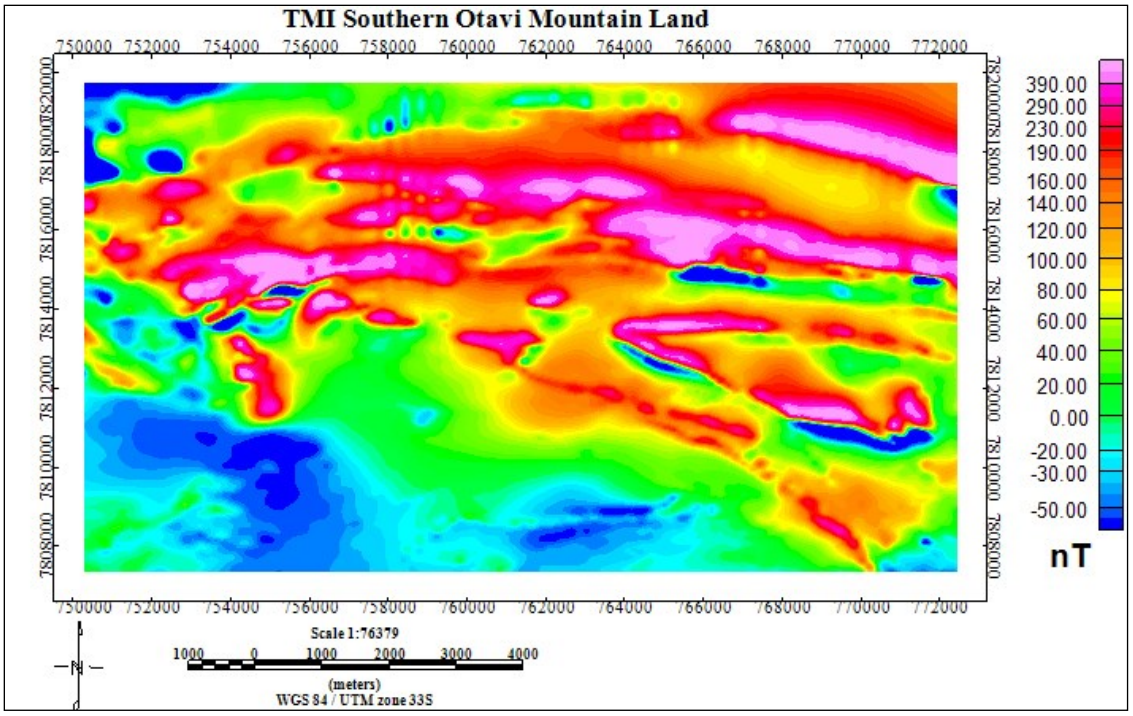


Figure 7.14 TMI map of the aeromagnetic data of the southern Otavi Mountain Land (OML).

7.5.2.1 Sun shading

Sun shading, also called shaded relief considers the magnetic data values as if they were a topographic surface that is illuminated by a light source (e.g "sun") which has a specified elevation and azimuth (Cooper, 2003). Sun shading is a directional filter which enhances linear features lying orthogonal to the illumination azimuth and attenuates features that are parallel to it (Dentith and Mudge, 2014). The particular elevation and azimuth, chosen by the interpreter are very important parameters in the application of sun shading because they determine the reflectance from topography simulated from the magnetic data values, whereby high values represent the hills, while low values represent the valleys. The reflectance from the surface is determined by several algorithms based on various physical models. According to Cooper (2003) the Lambertian reflector, which reflects light equally in all directions is the commonly used reflectance model and is defined by:

$$R = \frac{1 + p_o p + q_o q}{\sqrt{1 + p^2 + q^2} + \sqrt{1 + {p_o}^2 + {q_o}^2}}$$

Where p_o = -cos Ø tan θ; q_o= -sin Ø tan θ; θ is the sun elevation measured from the vertical, whereas Ø is the azimuth measured anticlockwise from east (Cooper, 2003).

The sun shading filter is used to enhance lineaments in the aeromagnetic data images by making them more apparent (Figure 7.15), which is helpful in the geological interpretation process.

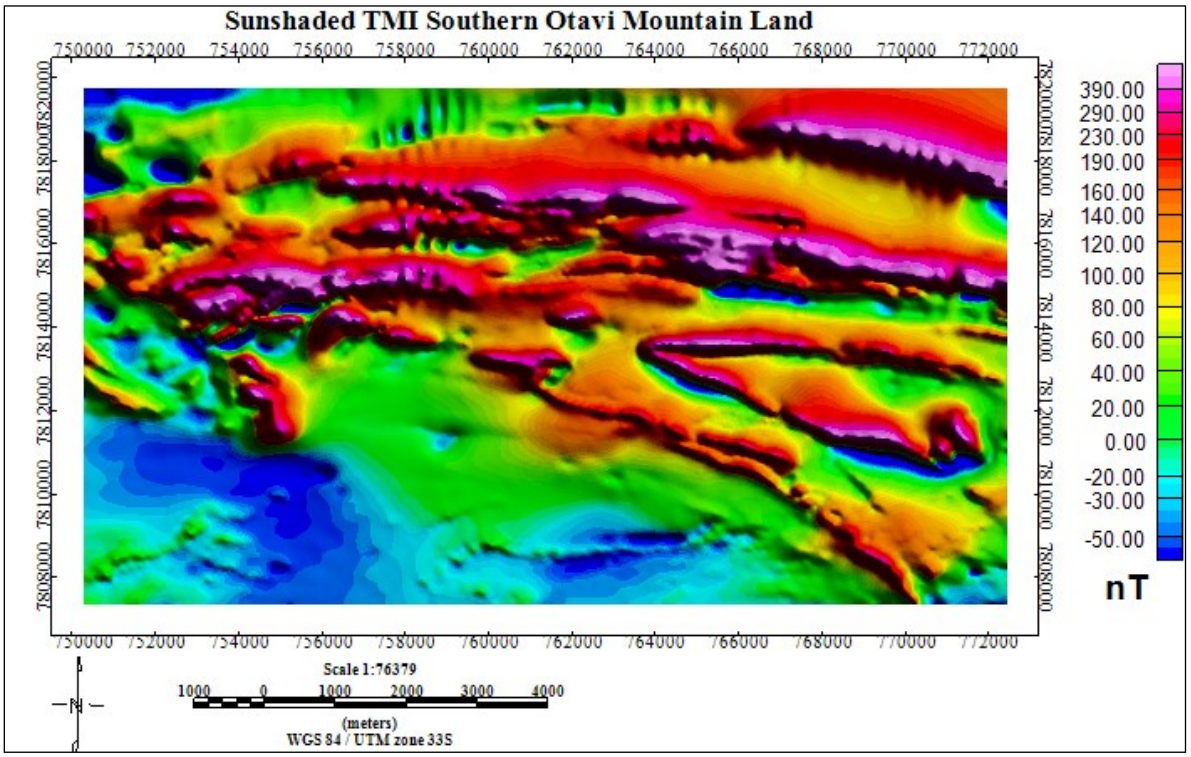


Figure 7.15 Sunshaded TMI map of the aeromagnetic data of the southern Otavi Mountain Land.

7.5.2.2 Upward Continuation

Upward continuation is a low-pass filter and it decreases the amplitude and increases the wavelength of the magnetic data (Dentith and Mudge, 2014). Also upward continuation emphasizes anomalies caused by deep magnetic sources at the expense of anomalies caused by shallow magnetic sources (Isles and Rankin, 2013). The Total Magnetic Intensity (TMI) data (Figure 7.16a) shows various small but high amplitude magnetic anomalies, which are attributed to the change in the magnetic susceptibility of the near-surface geological features and cultural features. These anomalies caused by near-surface sources obscure the anomalies of deeper geological features.

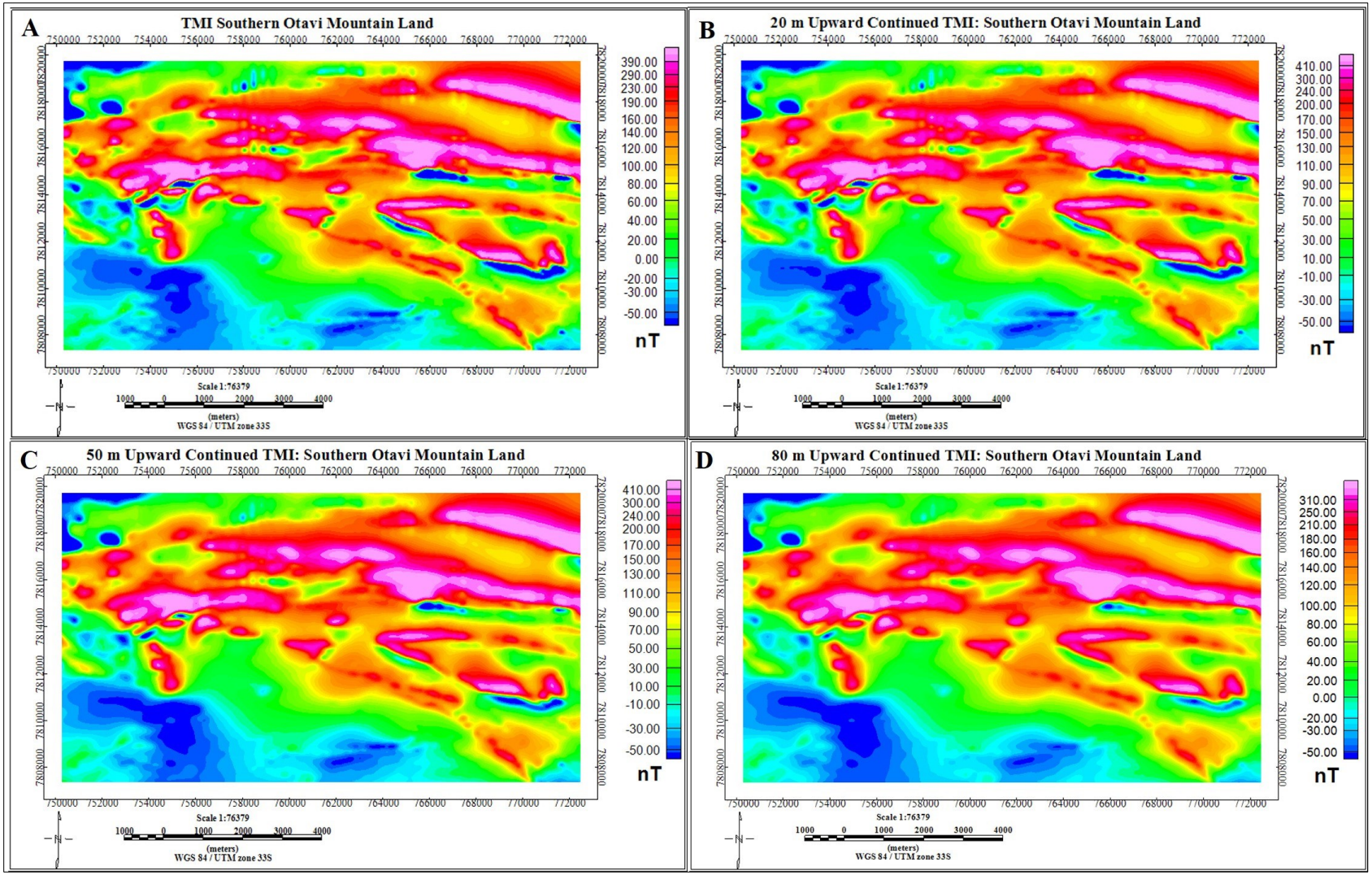


Figure 7.16 The application of upward continuation of the total magnetic intensity (TMI) aeromagnetic data of the southern Otavi Mountain Land by various heights. A) The TMI data shows details of the surface and near surface magnetic sources. B) The TMI data upward continued by 20 m. C) The TMI data upward continued by 50 m. D) The TMI data upward continued by 80 m. Notably, the higher the amount of upward continuation, the smoother the TMI data become.

The upward continuation filter was applied on the TMI data at 20m, 50m, and 80m, to illustrate the change in anomaly with increasing observation to magnetic source distance at various levels as shown in Figure 7.16b-d. These upward continued maps show anomalies due to deeper geological features by suppressing the near-surface magnetic features. The 80 m upward continuation removed most of the noise attributed to the shallow sources in the TMI data (Figure 7.16d).

7.5.2.3 Reduction to Pole

The first operator applied to the magnetic data is the reduction to magnetic pole (RTP). According to Isles and Rankin (2013) RTP is a transformation, which is a numerical process that produces new versions of the measured total magnetic intensity. Thus, it is a fundamental process which transforms Total Magnetic Intensity (TMI) data measured at any Earth's field inclination to that which would be observed if the data were collected at the magnetic poles (inclination=90º) (Baranov and Naudy, 1964; Isles and Rankin, 2013). The magnetic inclination and declination values used to calculate the RTP for the aeromagnetic data collected over the Otavi Mountain Land in 2008 are -60.13° and -9.44°, respectively. The magnetic inclination and declination values are calculated in Oasis Montaj, Geosoft using the IGRF model for the specific year of data acquisition. Accordingly, the RTP centers anomalies above their causative bodies, and largely removes the dipolar nature of magnetic anomalies and hence largely enables the interpreter to clearly decipher the geometry of the subsurface geological features. It should be noted that the application of RTP assumes induced magnetization, and is not applicable to remanence unless, specified (B. Corner, personal communication, December 21, 2016). The application of the RTP operator to the 80 m upward continued TMI aeromagnetic data of the southern Otavi Mountain Land is shown in Figure 7.17. The TMI maps show asymmetric anomalies with dipolar effects (Figure 7.14-7.16), whereas RTP map (Figure 7.17) shows symmetric anomalies that are directly on top of the sources and the anomalies have moved southward because the dipolar effect has been removed.

7.5.2.4 Decorrugation

Corrugation in the aeromagnetic data grids occurs as flight line noise that is visible as linear anomalies parallel to the survey flight lines. This flight noise remains in the aeromagnetic data after tie line levelling. Line noise is mostly due to line to line differences in flying heights,

inadequate compensation for the magnetic field resulting from the aircraft and if diurnal variations are not accurately measured at the base station, hence affecting part of the measurements along a survey line (Mogren *et al.*, 2009). Also, corrugation can occur when adjacent flight lines are in opposite flight directions. Although the contractor that acquired the aeromagnetic data performed standard compensation and diurnal corrections and levelling, the mountainous terrain of the Otavi Mountain Land precluded full removal of severe flight line noise in the gridded aeromagnetic data as seen in Figure 7.17. Notably, if the flight line noise is uncorrected then the computation of derivatives becomes dominated by these corrugations. In this study, decorrugation filtering was applied to correct for the north-south flight line noise, which is evident, though subtle in the RTP aeromagnetic data (Figure 7.17), albeit the 80 upward continuation.

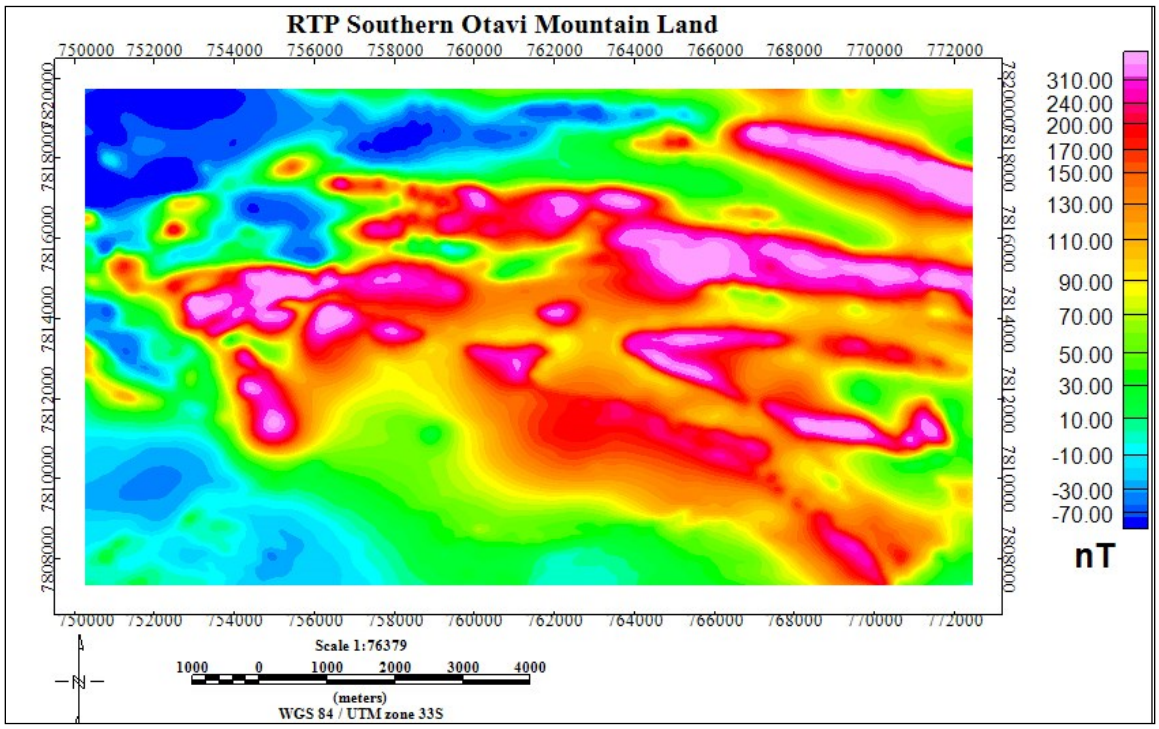


Figure 7.17 Application of the RTP operator to the TMI aeromagnetic data of the southern Otavi Mountain Land. Note that the RTP image has subtle north-south flight line noise (very clear in the sunshaded image). The flight line noise is evident in the northern part of the map.

Decorrugation was achieved by applying a combination of a high-pass Butterworth filter and a directional cosine filter. However, care must be taken when applying these filters because true geological anomalies parallel to the flight lines with similar wavelength as the leveling errors or

corrugated noise can also be obliterated. Hence, the data was decorrugated by setting the Butterworth filter cut-off wavelength to four times the line spacing and thus 800 nT; filter order = 5 and high pass filter, whereas the parameters of the directional cosine filter are: cut off azimuth = 0° (flight line direction) and degree of cosine function = 2.5. The severe line noise is largely removed in the resultant image (Figure 7.18) and the geological features can be easily determined.

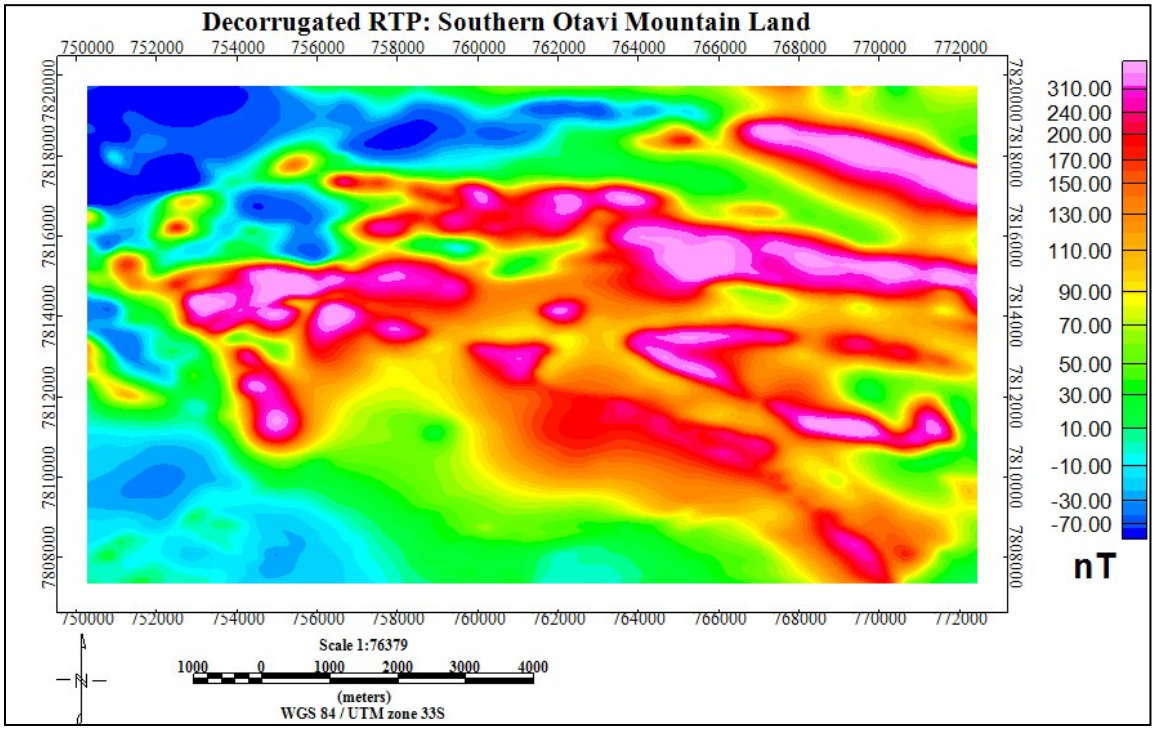


Figure 7.18 Decorrugated RTP map. The flight line noise observed in Figure 7.17 is completely removed and the image appears smooth.

7.5.2.5 Vertical Derivatives

Generally, the first vertical derivative (1st VD) is the most commonly used high-pass filter for magnetic data because it is robust in computing and readily interpretable in the context of rock bodies and their contacts (Isles and Rankin, 2013). The 1st VD, like any other high-pass filters, enhances responses from shallower geological features and suppresses responses from deeper features (Milligan and Gunn, 1997). In addition, the 1st VD has no directional bias and thus it is crucial in improving the spatial and structural resolution in the magnetic data images (Isles and Rankin, 2013). Consequently, the keystone high-pass filter in the structural analysis of the aeromagnetic data for the study area is the 1st VD because it provides a very reliable starting point

for the process of depicting structural detail from the magnetic data as well as mapping geological contacts. The response of the 1st VD is more localized than the broader response of the original TMI or RTP data (Dentith and Mudge, 2014).

The 1st VD was used to identify shallow structures and detect edges of the magnetic sources in the aeromagnetic data of the study area (Figure 7.19). The peak positions from the RTP map (Figure 7.18) are retained in the 1st VD (Figure 7.19), however, the 1st VD anomaly is considerably narrower and more closely reflects the width of their causative bodies. On the contrary, vertical derivatives also amplify high frequency noise (Cooper and Cowan, 2004; Nabighian *et al.*, 2005). Although before the digital age, the 2nd VD was used for delineating and estimating depths to magnetic sources in aeromagnetic interpretation (Vacquier *et al.*, 1951), in this study, the highest derivative order used in this study for meaningful geological interpretation is the first order (1VD).

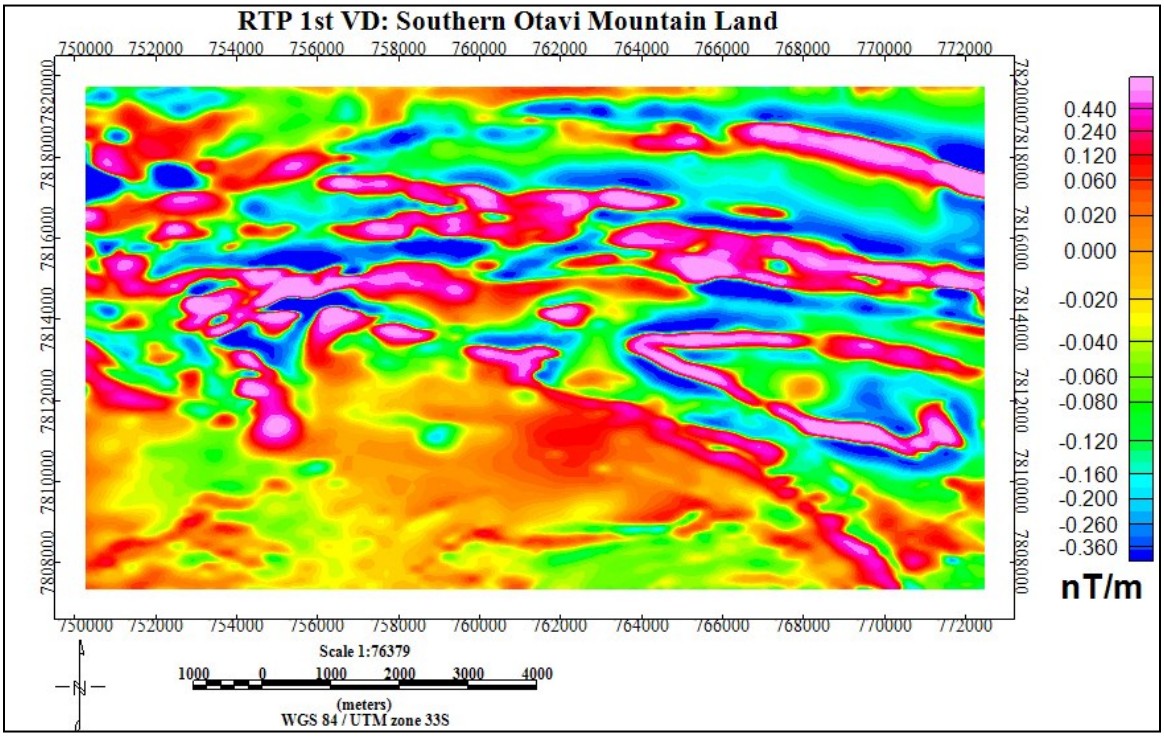


Figure 7.19 1st VD map with enhanced shallow structures. Note the presence of high frequency noise.

7.5.2.6 Tilt Derivatives (TDR)

Closely spaced shallow magnetic sources produce large amplitudes in the vertical and horizontal derivatives, which present a problem in displaying the data and mapping the geological structures. In order to resolve this problem, a high pass filter, the tilt derivative (TDR) is applied (Figure 7.20). The potential field tilt angle is the ratio of the 1st VD and absolute value of the total horizontal derivative and when the arctan function is applied to attenuate high amplitudes, it is known as the tilt derivative (Miller and Singh, 1994; Isles and Rankin, 2013) as shown in the mathematical expression below:

$$TDR\ (x,y) = tan^{-1}\left[\frac{\frac{\partial f}{\partial z}}{\sqrt{\left(\frac{\partial f}{\partial x}\right)^2 + \left(\frac{\partial f}{\partial y}\right)^2}}\right]$$

Where TDR (x,y) is the amplitude of $\frac{\partial f}{\partial z}$ is the vertical derivative; $\left(\frac{\partial f}{\partial x}\right)^2 + \left(\frac{\partial f}{\partial y}\right)^2$ is the total horizontal derivative; *f* is the observed magnetic field. The tilt derivative is effective at portraying the edges of deeper and shallower magnetic sources in similar ways.

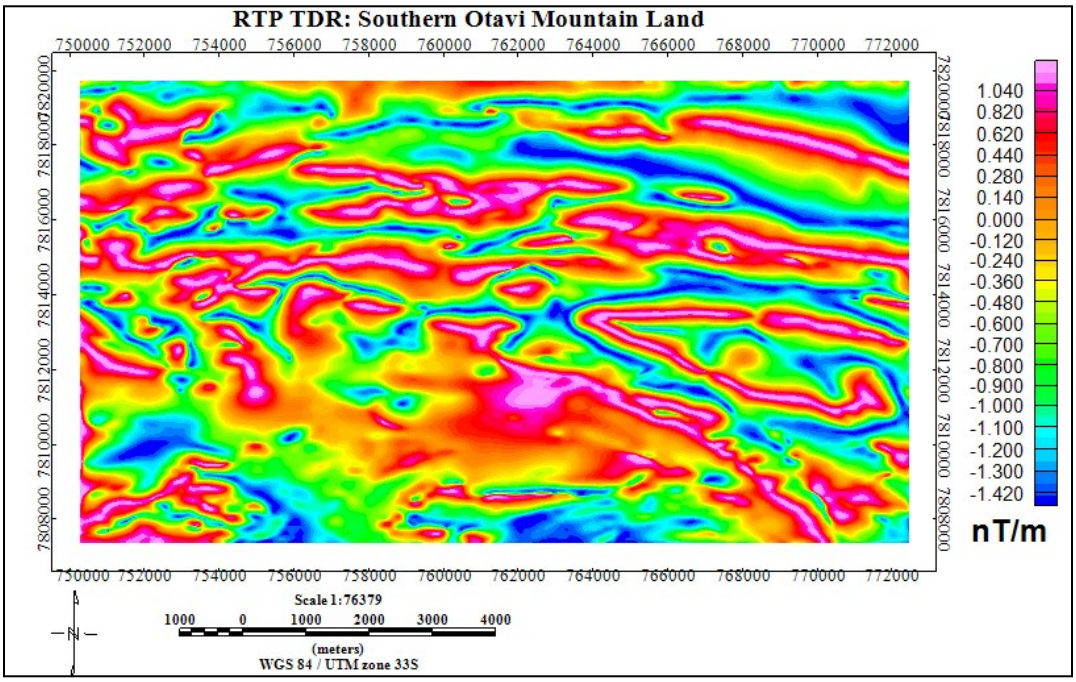


Figure 7.20 Processed TDR map showing shallow crustal features.

7.5.2.7 Total Horizontal Derivatives (THDR)

Delineating edges of the magnetic structures is crucial in geological interpretation of magnetic data and the frequently used edge detection filter is the total horizontal derivative (THDR) (Cordell and Grauch, 1985; Verduzco *et al.*, 2004; Cooper and Cowan, 2006; Arisoy and Dickmen, 2013) and is defined by Cordell and Grauch (1985) as:

$$THDR = \sqrt{\left(\frac{\partial f}{\partial x}\right)^2 + \left(\frac{\partial f}{\partial y}\right)^2}$$

Where $\frac{\partial f}{\partial x}$ and $\frac{\partial f}{\partial y}$ are the two orthogonal horizontal derivatives of the magnetic field; f is the magnetic field.

The THDR maps the anomaly inflection points which lie close to the contacts and is good for contact mapping (B. Corner, personal communication, December 21, 2016) as shown in Figure 7.21. Moreover, THDR is more effective in imaging shallow magnetic bodies (Arisoy and Dickmen, 2013).

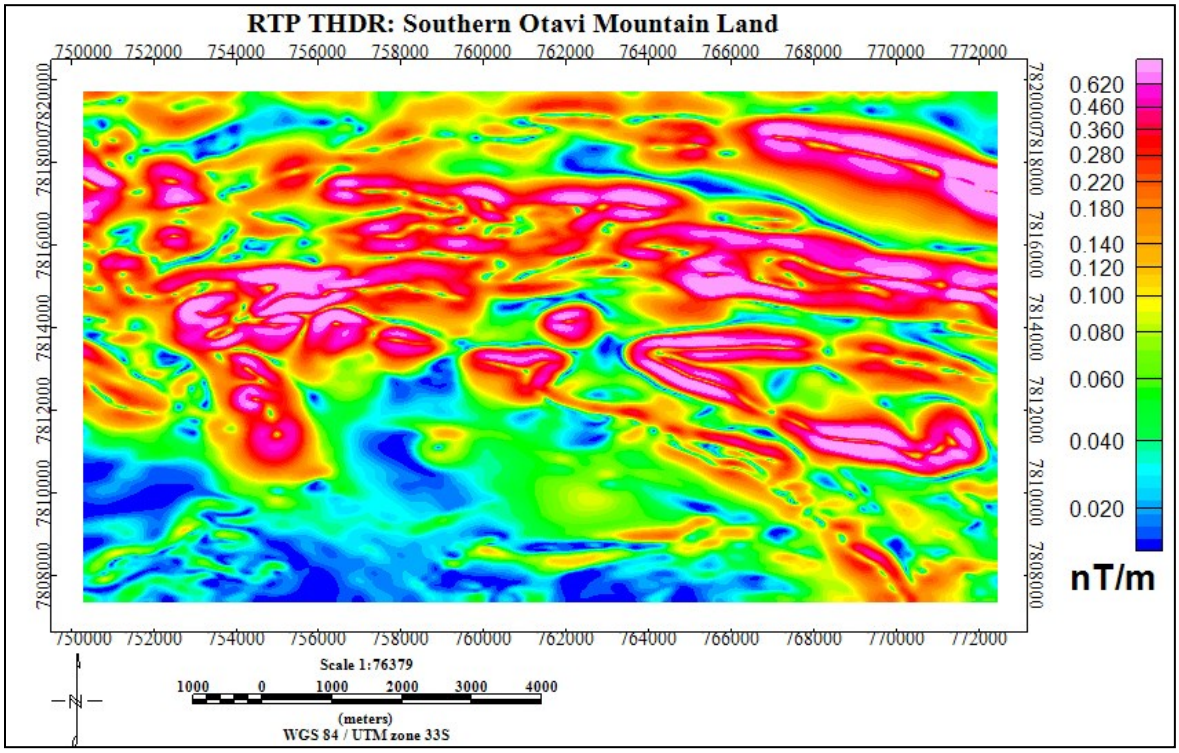


Figure 7.21 Processed THDR showing the edges of the magnetic bodies.

7.5.2.8 Analytic Signal

Analytic signal (AS) is achieved by combining the three directional gradients of the magnetic field to obtain the total gradient (Dentith and Mudge, 2014). Thus, AS is the absolute value of the total gradient calculated by taking the square root of the sum of square derivatives in all three directions; horizontal *(X, Y)* and vertical (*Z*). AS reduces deeper features with long wavelengths allowing for well-resolved anomalies which sit either directly over the body or, if the body is wider than its depth, over the contacts. AS is essential in situations where the interpreter suspects the presence of bodies with non-induced magnetization, especially where the RTP operator cannot resolve remanent magnetization (Isles and Rankin, 2013). When AS is applied to the TMI or RTP data, the anomalies commonly loose the dipolar form and like the derivatives, AS enhances noise in the magnetic data. However, unlike the 1st VD, AS loses continuity of the geological units (Figure 7.22). In addition to the THDR, AS is also an effective filter that is used to detect the edges of magnetic bodies (Pilkington and Keating, 2004; Cooper and Cowan, 2008). In this study, AS is used to detect magnetic body edges (Figure 7.22b) and to assess the presence of remanence and self-demagnetization. The 3D AS is defined by the formula (Roest *et al.*, 1992) below:

$$|AS(x,y)| = \sqrt{\left(\frac{\partial f}{\partial x}\right)^2 + \left(\frac{\partial f}{\partial y}\right)^2 + \left(\frac{\partial f}{\partial z}\right)^2} \quad ,$$

Where AS (*x, y*) is the amplitude of the analytic signal at (*x, y*); *f* is the observed magnetic field at (*x, y*).

7.5.2.9 Gaussian regional-residual separation

Regional and residual filters are derived from spectral analysis of the magnetic data (Reeves, 2005). This method is used to separate regional and residual components of magnetic data (Figure 7.23). The magnetic data observed in the aeromagnetic surveys are the total magnetic fields produced by all underground magnetic sources both shallow and deep as shown in the TMI and RTP maps and hence magnetic responses of geological features such as structures buried at shallow depths are embedded in a regional field caused by magnetic sources that are usually larger or deeper such as the basement. The magnetic response of the deeper bodies can be removed by removing the regional field from the initial field magnetic data to yield residual field (Figure 7.23) that is caused by shallow features (Li and Oldenburg, 1998).

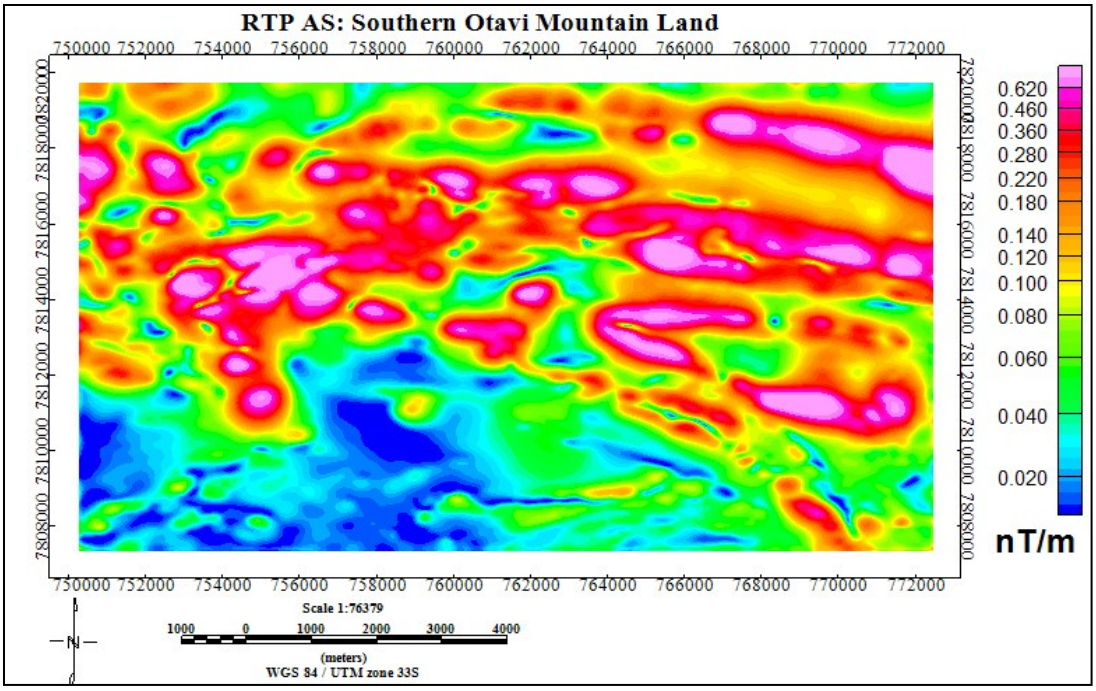


Figure 7.22 Processed AS map showing the edges of the magnetic bodies. Please note that the geological continuity is destroyed.

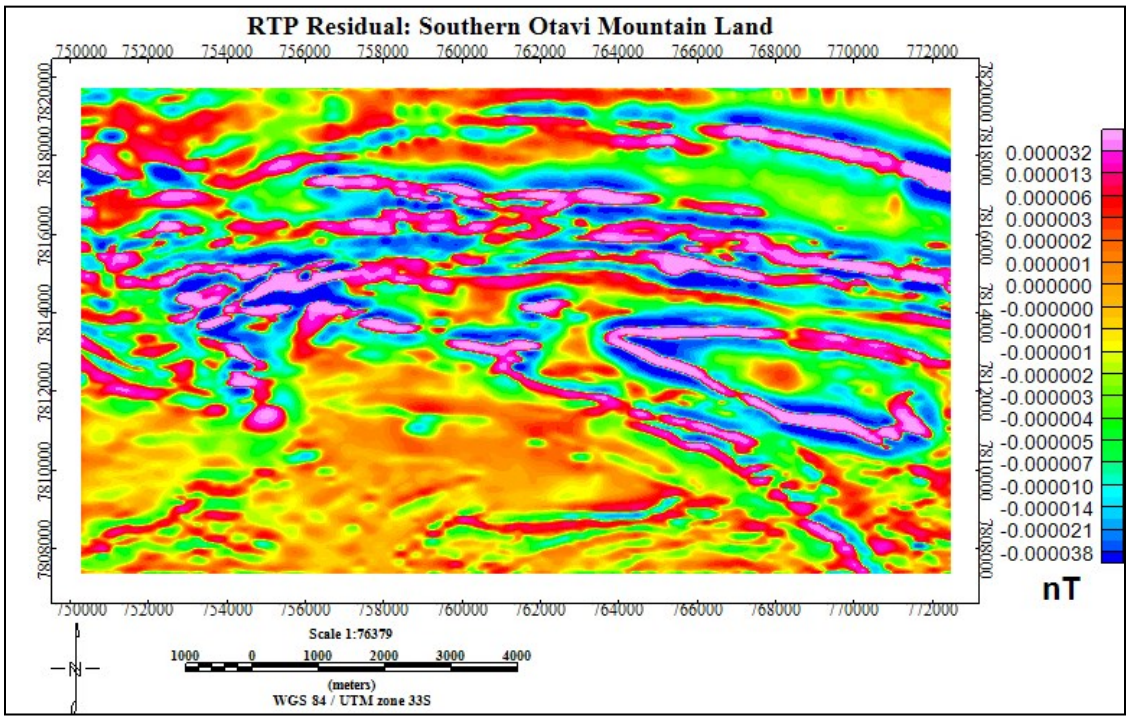


Figure 7.23 Residual filtering are applied to the aeromagnetic data to selectively remove the regional magnetic field. The residual magnetic field map shows magnetic response of the shallower bodies.

7.5.3 Interpretation of geophysical aeromagnetic data

The integrated geological picture of the study area was achieved by first defining the distribution of lithological packages over the entire study area on both the regional geological map. Subsequently, faults, folds and other structural information were introduced with the assistance of processed geophysical aeromagnetic images. The regional geological map of the southern Otavi Mountain Land captures most of what can be seen in the aeromagnetic images. Further integration of the geology with the aeromagnetic data highlighted several features of particular interest.

The aeromagnetic image selected for the interpretation follows the descriptions outlined previously in section 7.5.2 on image processing and enhancement of aeromagnetic data. The images chosen to emphasize the structural detail, in this case, are the TDR and 1st VD. Other selected images such as the AS, were used to present the lithological and structural contacts. As always, the TMI is selected as the basic record of the measured data but, as discussed earlier in section 7.5.2, the RTP is more reliable than the TMI because it centres anomalies above their causative bodies, and largely removes the dipolar nature of magnetic anomalies. Therefore, all the proposed images are derived from the RTP. In most cases the geophysical images are overlain on the regional geological map to enhance the comparison of the aeromagnetic data with the geological data.

The regional geological map of the southern Otavi Mountain Land (Figure 7.24) highlights the extensive cover over the Neoproterozoic rocks of interest. This cover includes both transported sediments and a thick weathering profile. The cover thickness in this region is not well constrained but where drilled it is rarely greater than 20 m. On the published regional geological map (Figure 7.24) of this region, the broader stratigraphic packages are visible, however the detail on individual units and contacts in some areas is hard to decipher. Despite this, the regional geological map (Figure 7.24) is useful to mainly show the location of outcrops. Briefly comparing the geology (Figure 7.24) and the aeromagnetic imagery (Figure 7.25) confirms that the extensive area of limited rock exposure have concealed magnetic units with various intensities. The aeromagnetic data of the southern Otavi Mountain Land is characterized by a prominent east-west structural grain defined by apparent folding of moderate to high-amplitude magnetic anomalies. Published mapping and stratigraphy indicates that the fold structures in the north and south are dominated by anticlines and synclines, respectively.

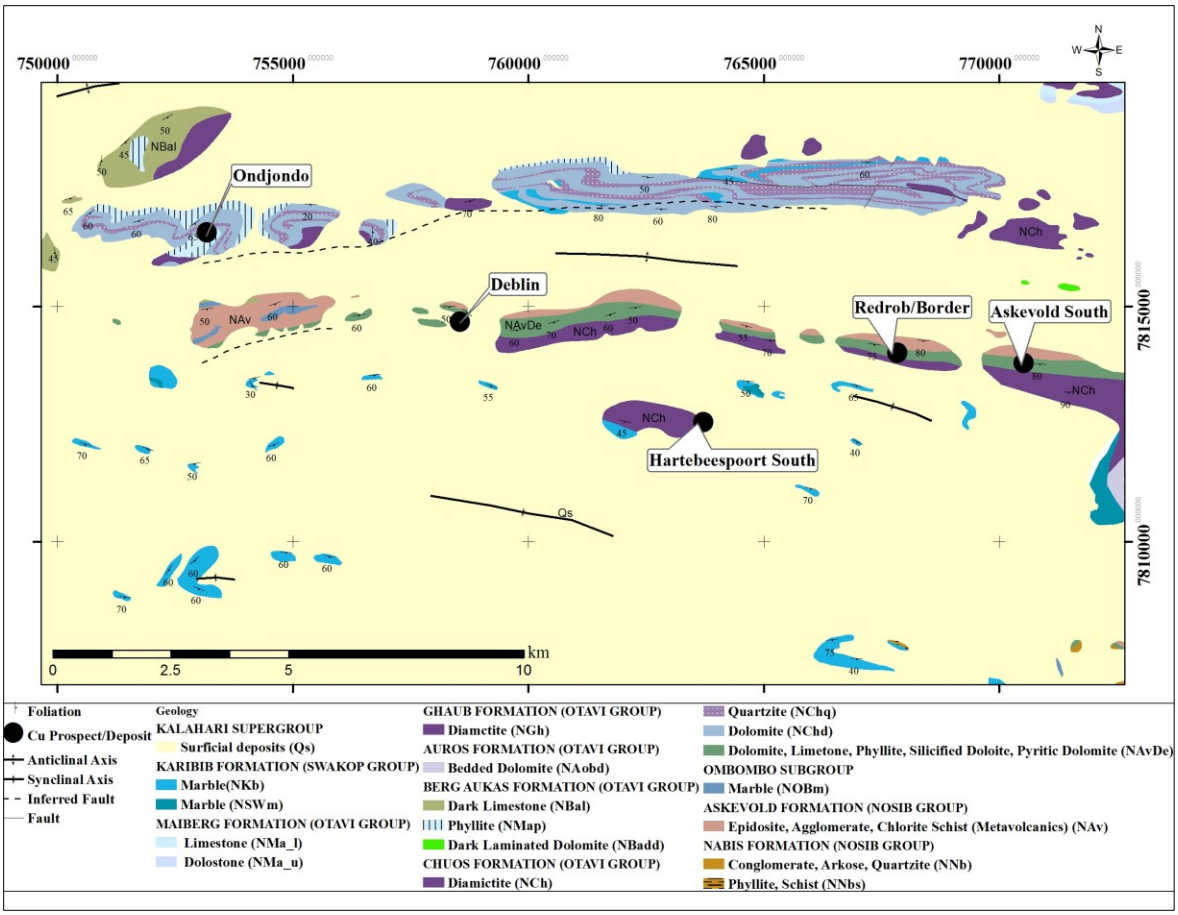


Figure 7.24 Regional geological map of the southern Otavi Mountain Land showing the extensive sand cover and limited rock exposure as well as mappable structural features. Modified after Smit (1959) and the Geological Survey of Namibia (2008).

The positive magnetic anomalies in the regional magnetic data (Figure 7.25) are correlated with the known magnetic units on the regional geological map (Figure 7.24) such as the mafic metavolcanic rocks, chiefly the agglomerate of the Askevold Formation and the banded iron formation-bearing diamictites of the Chuos Formation. Mafic metavolcanic rocks are situated in the lower part of the stratigraphy, whereas the diamictite occurs in the upper part of the stratigraphy. The magnetically quiet areas in the northern part of (Figure 7.25), correlate with the carbonate succession (Figure 7.24) in the upper part of the stratigraphy. Clearly, the Deblin Copper Mine lies on a regional positive anomaly (Figure 7.25).

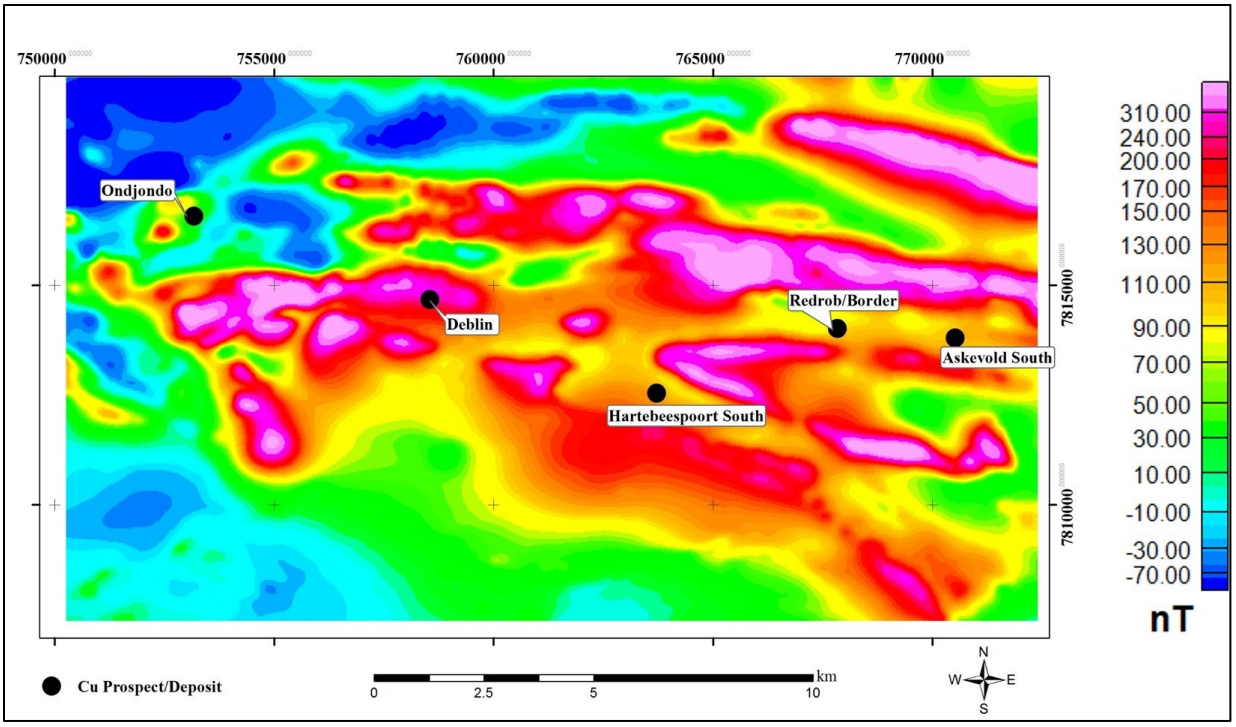


Figure 7.25 RTP map of the southern Otavi Mountain Land showing the magnetic anomalies in relation to copper deposits in the region.

Limited exposure on the regional geological map (Figure 7.24) is testimony to the sparse and discontinuous nature of the Neoproterozoic rocks in this region. In contrast, the aeromagnetic imagery (Figure 7.26) presents a wealth of structural information that will add significantly to the integrated geological picture of the area. Structural interpretations are made based on three main assumptions: 1) aeromagnetic anomalies are the product of lithological contrasts within the shallow crust; 2) linear aeromagnetic fabrics represent deformation (e.g folding and faulting); 3) truncations or offsets of magnetic anomalies indicate the location of faults.

The TDR image (Figure 7.26) of the aeromagnetic data was used to delineate the structural characteristics of the shallow crustal features that are lacking in the gross geological picture. In this image, the strongly magnetic units associated with the mafic metavolcanics and banded iron formation-bearing diamictites are apparent and can be used to define the structures. Two major east-west linear magnetic lows (thrust fault zones), labelled thrust fault 1 and thrust fault 2, characterized by low magnetic anomalies are recognizable in the TDR image (Figure 7.26). These

thrust faults have a linear control on the geometry of the metavolcanic rocks in this area. The thrust faults dissected the aeromagnetic map of this area into three magnetic domains (A-C), each with different magnetic character (Figure 7.26).

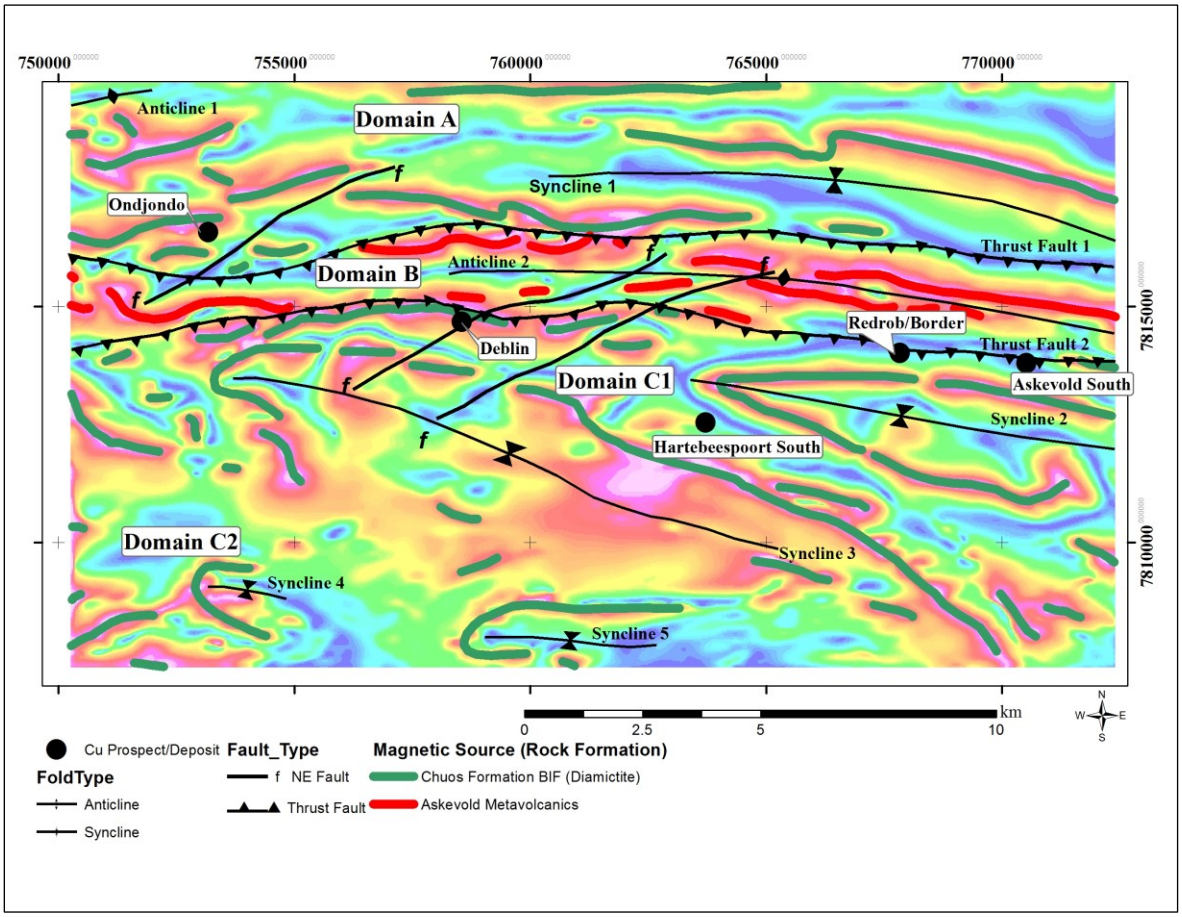


Figure 7.26 TDR map showing the response of different magnetic rock types, shallow regional crustal structures and the three different domains in the southern Otavi Mountain Land.

The Domain A is characterized by magnetic lows in the north and moderate to high magnetic anomalies in the central and southern parts of the domain with an east-west-trending structural grain. This domain comprises non-magnetic carbonates of the Chuos Formation and strongly magnetic diamictite with a banded iron formation of the Chuos Formation. This domain has an anticline and a tight syncline. The Domain A is separated from Domain B by the thrust fault 1. Immediately south of the thrust fault 1, the Domain B is characterized by a high magnetic intensity and an overall east-west-trending magnetic grain. The anomalies of this domain are caused by the mafic metavolcanics of the Askevold Formation and they form an anticline. In the north, the

Domain C is characterized by strong magnetic intensity with commonly deformed structural grain, whereas in the south the domain is characterized by low to moderate magnetic signature and a weak but discernible magnetic signature. The strong magnetic intensity is attributed to the strongly magnetic banded iron formation in the diamictites of the Chuos Formation, which have sporadic outcrops. In contrast, the low to moderate magnetic intensity in some places is caused by the Chuos Formation and Karibib Formation carbonates as well as the Chuos Formation diamictites with a banded iron formation. These units are rarely exposed. The southern part of the Domain C has an extensive area of limited rock exposure and abundant sand cover, giving rise to a low to moderate magnetic intensity of the Chuos Formation diamictite. Consequently, the Domain C can be further subdivided into Subdomain C1 and C2.

The thrust fault 1 coincides with the mapped thrust fault in areas with limited outcrop on the published regional geology map. This major thrust fault appears to terminate the Askevold Formation metavolcanic rocks to the north. This thrust fault extends further to the west in areas without outcrops and traverses just south of the Ondjondo copper deposit, where it appears to be overprinted by a northeast-oriented magnetic low (probable fault zone) (Figure 7.26).

In contrast, the fault 2 coincides with the Askevold Trend copper deposits (Askevold South, Redrob, and Deblin) (Figure 7.26). This thrust fault appears to terminate the Askevold Formation metavolcanic rocks to the south, separating the domain B from the domain C. In addition, the thrust fault 2 cuts through the Deblin Copper Mine area, just north of the Deblin Mine shaft. Clearly, this east-west lineament is a feature of considerable regional tectonic significance traversing along the Askevold Trend copper deposits. Notably, thrust fault 2 is not shown on the published outcrop regional geological map, despite having a regionally significant scale. The thrust fault 2 is not only an outstanding feature of the aeromagnetic images but is a key element of the geological evolution of this area. Therefore, this thrust fault possibly represent a thrust tectonic structure which developed during the Damaran D_2 collision of the Kalahari and Congo cratons and separates the Swakop Basin from the carbonate platform of the Otavi Mountain Land. This major thrust fault appears to be overprinted by several northeast-oriented linear magnetic lows (probable fault zones) in the proximity of the Deblin Copper Mine and further to the east.

The sets of northeast-trending faults post-date the development of the major east-west thrust faults and are related to the latest deformation event in the Otavi Mountain Land which is D_3. Although these northeast-trending faults appear to have a close relationship with the copper deposits in the southern Otavi Mountain Land, they are not shown on the regional geological map due to the extensive sand cover. The two thrust faults are suggestive of a shear zone associated with copper mineralization in the southern Otavi Mountain Land. These regional thrust faults coupled with the set of regional anticlines and synclines are indicative of the presence of both brittle and ductile conditions of deformation, giving rise to a brittle-ductile shear zone. Eventually, a solid geological map (Figure 7.27) was interpreted based on the integrated geological map data and different products (e.g RTP, AS, TDR) of the aeromagnetic data.

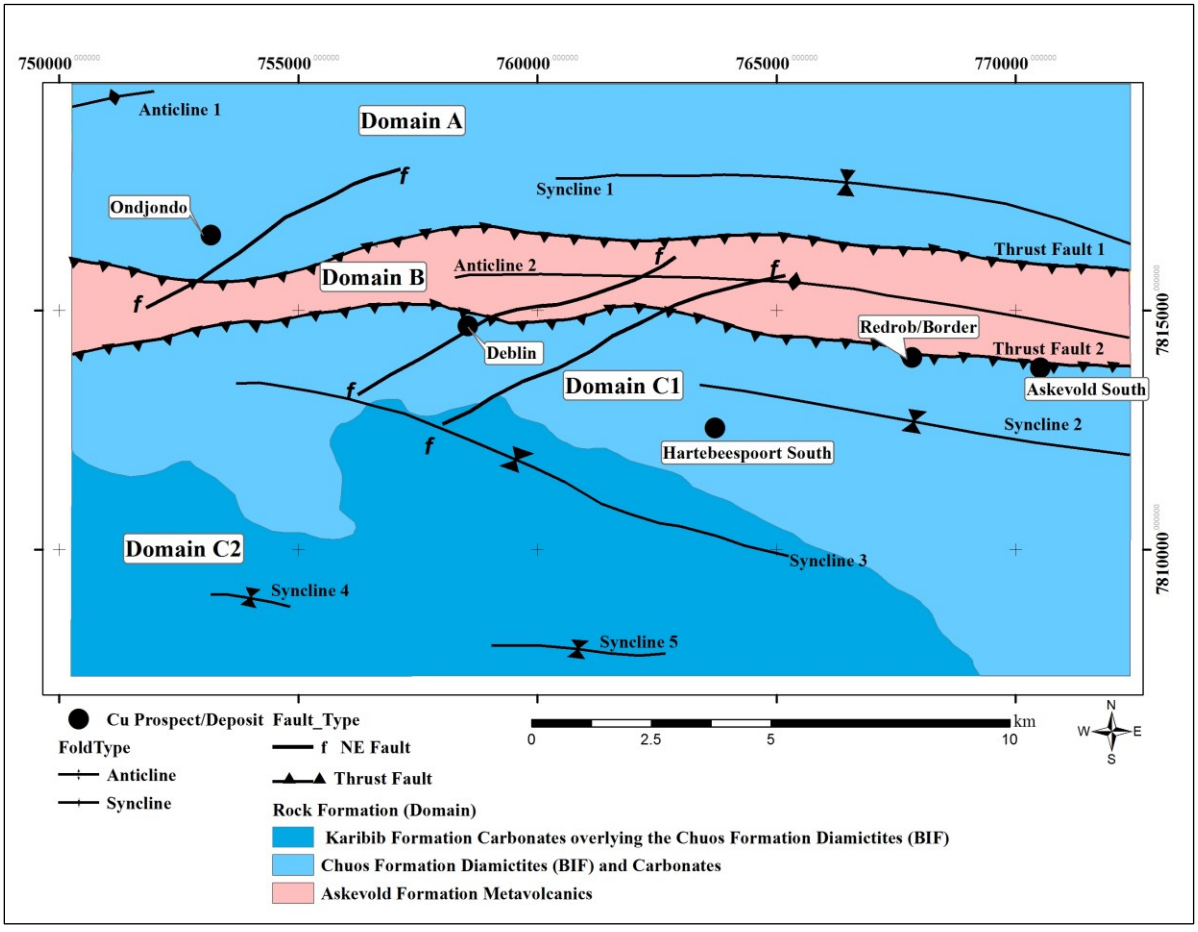


Figure 7.27 Interpreted solid geological map of the southern Otavi Mountain Land with the major east-west-trending thrust faults and shallow structural NE-trending faults as well as folds.

7.6 Ground Magnetic Survey of the Deblin Copper Mine Area

7.6.1 Ground magnetic survey parameters and configuration

High resolution ground magnetic data were collected over the Deblin Copper Mine area between 10 December 2015 and 17 December 2015 using two magnetometers (Geometrics 856 proton precession magnetometer and GSM-19 Overhauser magnetometer). The survey parameters are shown in Table 7.1. The survey area is covered by thick vegetation (thorn bushes) (Figure 7.28), which is the major access limitation in the area. Hence, the survey lines length range from 700 m to 1000 m and not all the survey lines covered the entire mapped area as shown in the survey configuration in Figure 7.28-7.29.

Table 7.1 Survey parameters for the ground magnetic survey.

Survey Parameters	
Survey line direction	Bidirectional (North-South)
Line spacing	25 m
Station spacing	0.5 m
Total number of lines	69
Total line length	62 line km
Height of the sensor	2 m
Base station location	(758200 mE; 7814360 mN) UTM Zone 33 S
Base station reading interval	30 seconds
Total number of days of the survey	7
Total Number of magnetometers	2

The level of constraint possible depends on the magnetic data resolution, the extent of outcrop, the level of detail in geological mapping, and the existence of magnetic susceptibility contrast between different rock types (Dentith and Mudge, 2014). When designing this ground magnetic survey the following factors were taken into consideration:

(a) The interpretation of the regional aeromagnetic data. The aeromagnetic data was also used to locate the ideal place for the base station, which is an area without magnetic gradients.

(b) The magnetic susceptibility contrast in the area pertaining to individual lithological units.

(c) The availability of the equipment to be used.

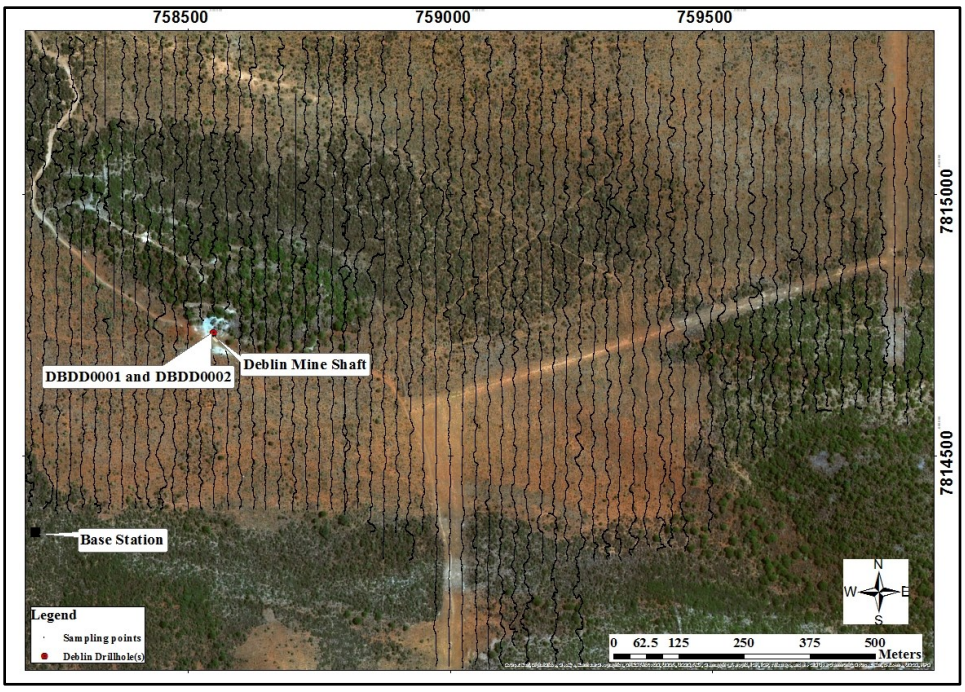


Figure 7.28 Sampling stations along the survey lines on the satellite image. The maps shows the location of the base station and drill holes. DBDD0003 does not appear on this map because it is outside the survey area.

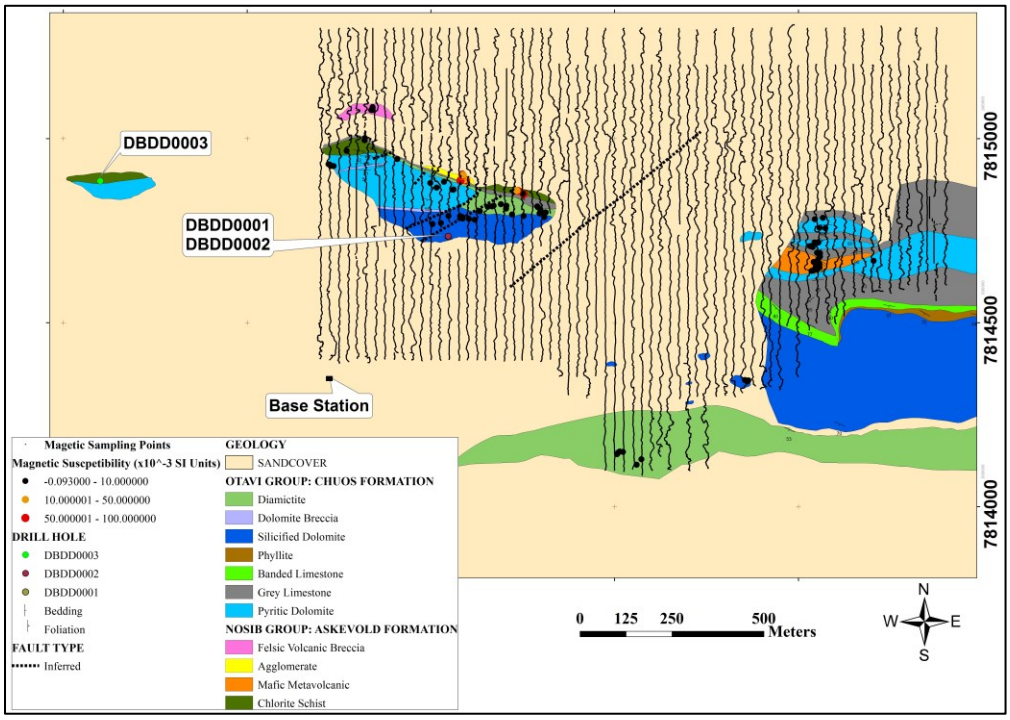


Figure 7.29 Detailed local geological map with survey lines in both areas with known geology and areas with the sand cover.

(d) The rock types present and the orientation of the mapped faults as they appear on the local geological map. The mapped faults trend in the NE and NW directions. Also the general E-W strike of the strata was taken into consideration. The data were collected along traverses oriented perpendicular to the strike of the rocks.

(e) The average minimum length of the mapped faults is 50 m. This was used to help determine the line spacing.

(f) The thickness of the soil cover. Unfortunately, there is no borehole that was drilled in the areas without outcrops and thus, the thickness of the soil cover is unknown. The depth to the highly magnetic lithological unit in the drilled areas is indicated on the borehole logs. Despite the unknown thickness of the soil cover, the survey was designed to have a station spacing of at least 0.5 m to minimize aliasing effects in the data.

(g) The location of archaeological objects (e.g Deblin Mine shaft) which are magnetic and any other cultural features that could affect the data such as the farm boundaries fence.

(h) The surface area of the survey area and the time it would take to complete the survey. The surface area is approximately 1.69 km^2.

(i) Both the topographic conditions and vegetation distribution. The area is extensively covered by tall trees and thorn bushes. This vegetation type covers more than approximately 85% of the area.

7.6.2 Equipment

The ground magnetic survey used one Geometrics 856 proton precession magnetometer (Figure 7.30a) at the base station and one GSM-19 Overhauser magnetometer (Figure 7.30b) as the rover magnetometer. Generally, both magnetometers are used in various fields such as faults and geological mapping, mineral exploration and archaeology. In this study, the rover magnetometer was used to collect TMI data along the survey lines, both in places with known geology and where there are no rock outcrops. The rover magnetometer recorded data at the interval of 1 second, whereas the base station magnetometer was put on auto cycle mode and recorded data at the interval of 30 seconds. In addition, the operation of both magnetometers is based on quantum-mechanical properties of atoms and are sensitive to the strength of the Earth's magnetic field (Dentith and Mudge, 2014).

The GSM-19 Overhauser magnetometer has a resolution of 0.01 nT, absolute accuracy of ± 0.1 nT and, has a built in Global Positioning System (GPS), and hence, it records and stores satellite-derived location information automatically. Conversely, the Geometrics 856 proton precession magnetometer measures the absolute value of total magnetic field to a resolution of 0.1 nT with 0.5 nT accuracy. The 12V lead batteries that are used by the magnetometers were charged overnight daily during the survey period.

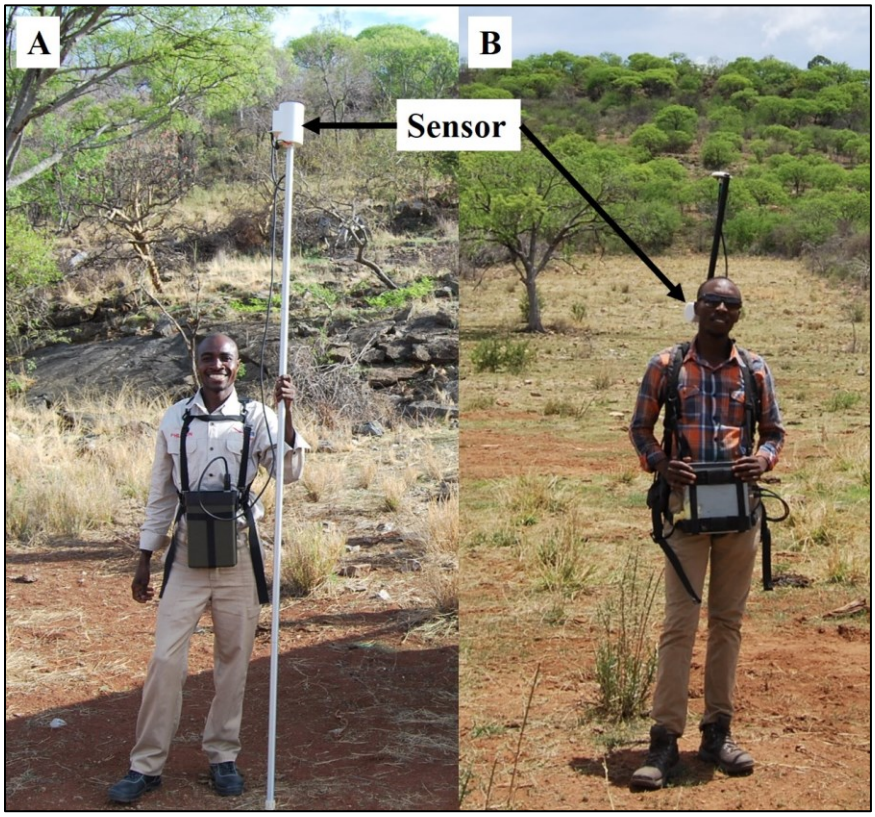


Figure 7.30 Photos of the magnetometers that were used to conduct the ground magnetic survey in the Deblin Copper Mine area. A) The Geometrics 856 proton precession magnetometer (Base station) and B) GSM-19 Overhauser magnetometer (Rover).

The GSM-19 Overhauser magnetometer is owned by Terratec Geophysical Services Namibia CC, while the Geometrics 856 proton precession magnetometer belongs to the Geology Department, University of Namibia (UNAM). Other survey equipment used are two handheld e-trex 10 Garmin Global Positioning System (GPS) from the School of Geosciences at the University of the

Witwatersrand. During the survey data collection, the time on the magnetometers was synchronized to that of the GPS devices.

7.6.3 Software

Map Source software was used to load survey waypoints into the GPS. GEMlink 5.0 and Magmap 2000 software were used to download data from the GSM-19 Overhauser magnetometer and Geometrics 856 proton precession magnetometer, respectively. The Oasis Montaj 8.3, Geosoft software was used to process the collected magnetic data. In addition, Arc Map 10.2.2, ESRI ArcGIS software was used for data and map compilations to aid in qualitative interpretation of the data. All the software packages are available at the University of the Witwatersrand.

7.6.4 Data Collection

The ground magnetic data were collected by two operators who were free of metallic objects at all times. One operator carried the navigating GPS with the survey grid walking along the designed survey lines, followed by the other operator carrying the rover magnetometer collecting data along the same survey lines. The survey lines and their dates of data collection are summarized in Table 7.2. The data were collected along 69 survey lines of different lengths (Figure 7.31). The first 35 survey lines (1 to 35) were collected between the 10th and 13th December 2015, whereas the 34 infill lines (100-3400) data were subsequently collected from 14 to 17 December 2015. The data in both sets of survey lines were collected at the line spacing of 50 m and when all the survey lines are combined (69 lines), the line spacing reduces to 25 m. On some days, for instance on the 10 December 2015, data collection was deferred from 14:22 to 15:54 due a rainfall event. Furthermore, repeat measurements on specific lines were taken on some days to account for datum shift and for line leveling purposes.

Table 7.2 Summary of the data collections dates.

Day	Date	Survey Lines	Repeated Lines	Line Spacing
1	10-Dec-15	10-13	None	50 m
2	12-Dec-15	14-30	None	50 m
3	13-Dec-15	31-35	Line 30	50 m
4	14-Dec-15	1-9	None	50 m
5	15-Dec-15	100-1000	None	50 m
6	16-Dec-15	1100-2600	Line 1000	50 m
7	17-Dec-15	2700-3400	Line 2600	50 m

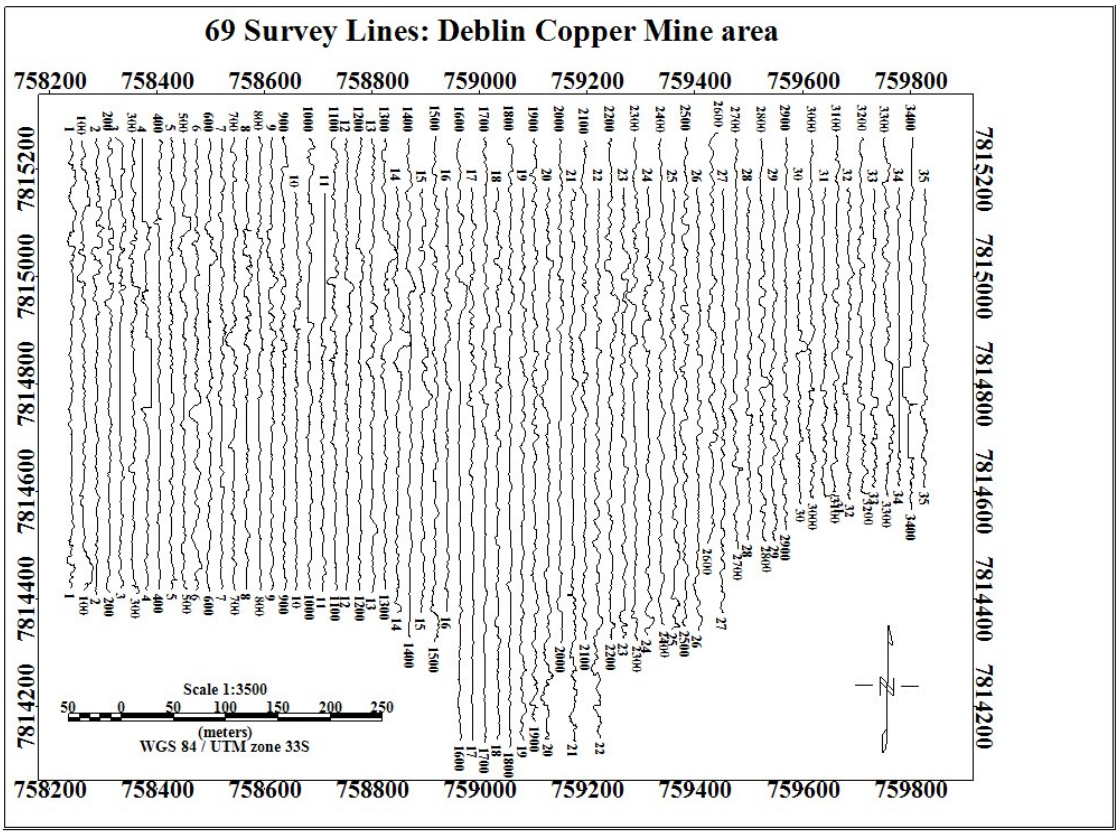


Figure 7.31 The 69 survey lines of the ground magnetic survey with the line spacing of 25 m. The survey lines have different lengths due to limited access of some parts of the survey area.

The base station (Figure 7.32) was located 800 m SW of the Deblin Mine shaft based on the preliminary interpretation of the aeromagnetic data and of a mini 2-line magnetic survey. On the first day of fieldwork, the proton precession magnetometer was then left at the proposed location for the whole day to confirm that the selected area was suitable for the base station. The results showed that the area was good for the bases station. Subsequently, a barrier made up of thorn bushes was erected around the base station (Figure 7.32a). This was done to protect the base station magnetometer from the cattle which constantly roam the survey area during daytime. Magnetic data were collected with a proton precession magnetometer set on auto cycle mode and to a sampling interval of 30 seconds (Figure 7.32b). The time on both magnetometers and GPS devices were synchronized.

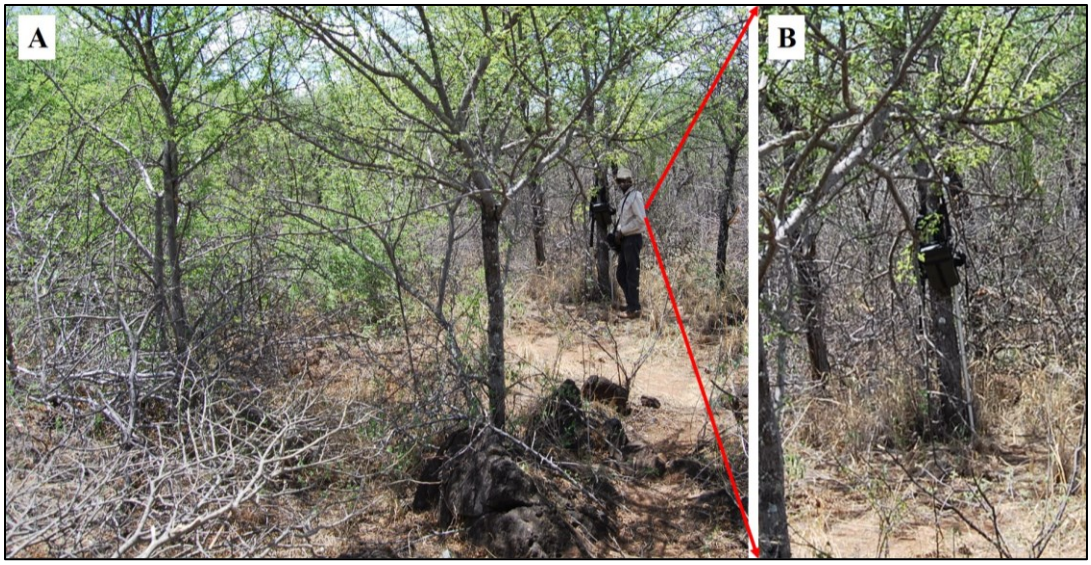


Figure 7.32 Base station. A) The field survey operator setting the base station. B) The base station magnetometer taking readings on an auto cycle mode.

7.6.5 Data Processing

Magnetic data processing includes everything done to the data between acquisition and the creation of an interpretable profile, map, or digital data set (Nabighian *et al.*, 2005). Processing of magnetic data requires care and understanding of the various strategies (Neubauer *et al.*, 1996). Data processing, herein, is considered to include data quality control, data display and data enhancement. Data quality control includes the application of a variety of corrections to the raw data obtained from the field acquisition system in order to prepare the data for enhancement and display. Data quality control is necessary to remove all contributions to the observed magnetic field that are caused by non-geological features such as cultural features (e.g fence) and environmental features (e.g diurnal variation).

7.6.5.1 Magnetic data corrections

a) De-spiking

Dentith and Mudge (2014) define spikes as sudden changes in the magnetic data which have a temporal extent, and usually as a single data point. Generally, spikes are caused by instrumental problems or they may be attributed to the natural environment. The erroneous values, such as zero values and single extreme values in the raw data are readily discernible. De-spiking involves

primarily a manual assessment of the data to remove readings that are noticeably invalid and hence spikes can be removed by using various data processing techniques or by manual editing.

The GSM-19 Overhauser magnetometer is sensitive to large magnetic field gradient and as a consequence, it records zero values in areas with large magnetic field gradients. Locations of cultural features primarily, the fence, metallic poles, metallic waste objects and concrete blocks in the vicinity of the Deblin Copper Mine shaft were noted and data collection was avoided in these areas. Erroneous values, particularly the extreme single values (spikes) were observed in the raw data. The erroneous values are attributed to cultural features such as small metallic objects and old metallic poles that are lying within the survey area. These values were removed from the data by manual editing. Moreover, the spikes in the base station data were removed with the aid of the low pass filtering with the wavelength of 40 m in Geosoft Oasis Montaj.

Besides the erraneous magnetic data, the GPS cable on the GSM-19 Overhauser magnetometer accidently disconnected several times while navigating between the thorn bushes along survey lines 11 and 34, for ~5 m long . Consquently, the equipment did not receive any sattellite data and hence did not record locations of the data in that case. The missing locations of the collected data were then interpolated from the adjacent GPS coordinate readings using the linear interpolation method.

b) Diurnal Correction

Diurnal variations are temporal variations in the geomagnetic field, which are related to sources external to the Earth attributed to mainly currents flowing in the ionosphere (Campbell, 2003; Dentith and Mudge, 2014). These are chiefly electric currents associated with radiation from the sun and they generate magnetic fields which interfere with the Earth's field causing it to vary and deviate over minutes and hours particularly during the daytime. In general, diurnal variations range up to about 30 nT and are at minimum at night (Dentith and Mudge, 2014). Diurnal variations have a big influence on magnetic survey data and hence are regularly monitored during the survey. During this survey, the diurnal variations were accounted for by setting up a base station in a place without magnetic field gradients within the survey area. The base station data for each day were

then examined to see if the variations are reasonable and within the tolerable maximum limit, which is 30nT (Figure 7.33-7.39).

Day 1: 10 December 2015

The highest and lowest recorded magnetic field on day 1 were 29,399.8 nT and 29,419.4 nT, respectively and thus the recorded daily variation is 20.4 nT. The recorded data show a noise envelope of 1.1 nT. On this day, data collection was deferred from 14:22 to 15:54 due to a rainfall event (Figure 7.33). When the survey was stopped the magnetic field was 29,417 nT and when resumed the magnetic field declined with 15 nT to 29,402 nT. This decline in the magnetic field is represented by a vertical line on the diurnal plot in Figure 7.32.

Day 2: 12 December 2015

The highest and lowest recorded magnetic field on day 2 were 29,421.6 nT and 29,393.8 nT, respectively and thus the recorded daily variation is 27.8 nT (Figure 7.34). The recorded data show a noise envelope of 2.2 nT.

Day 3: 13 December 2015

The highest and lowest recorded magnetic field on this day were 29,413.7 nT and 29,408.4 nT, respectively and thus the recorded daily variation is 5.3 nT (Figure 7.35). The recorded data show a noise envelope of 0.7 nT.

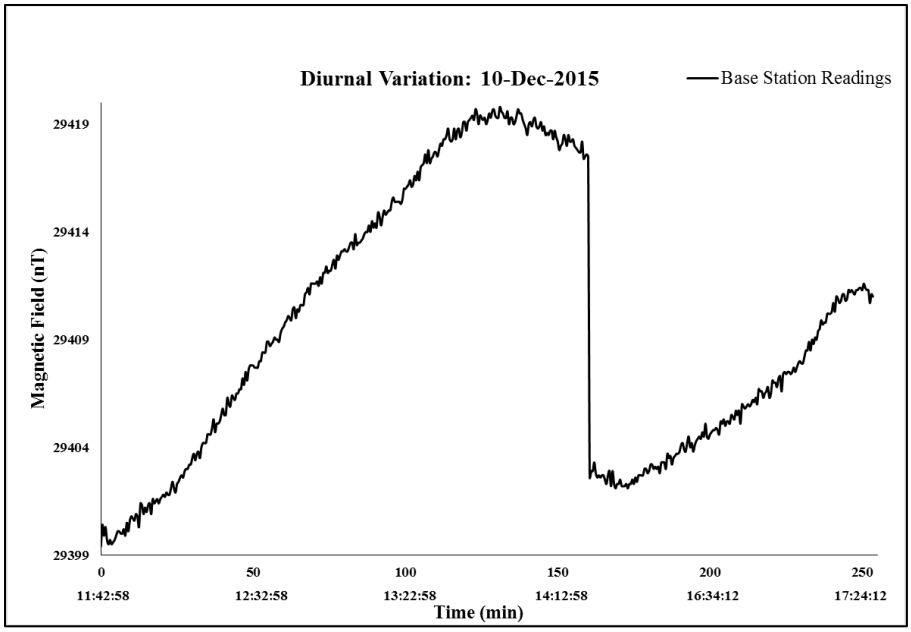


Figure 7.33 Diurnal variation plot for day 1. The Julian day is 344. The survey lasted for 253.5 minutes.

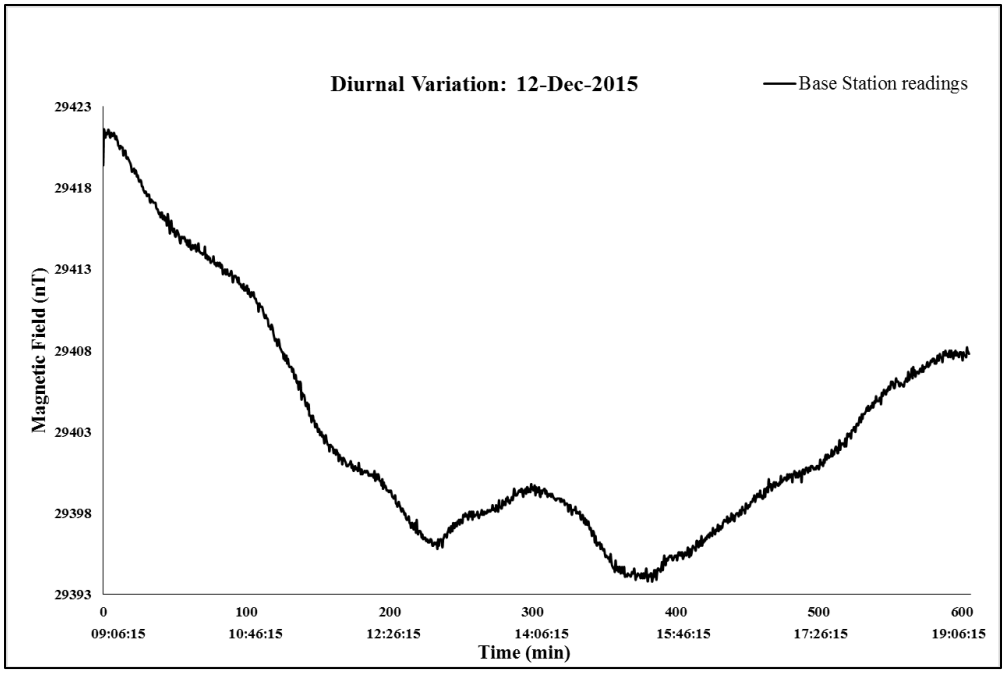


Figure 7.34 Diurnal variation plot for day 2. The Julian day is 346. The survey lasted for 605 minutes.

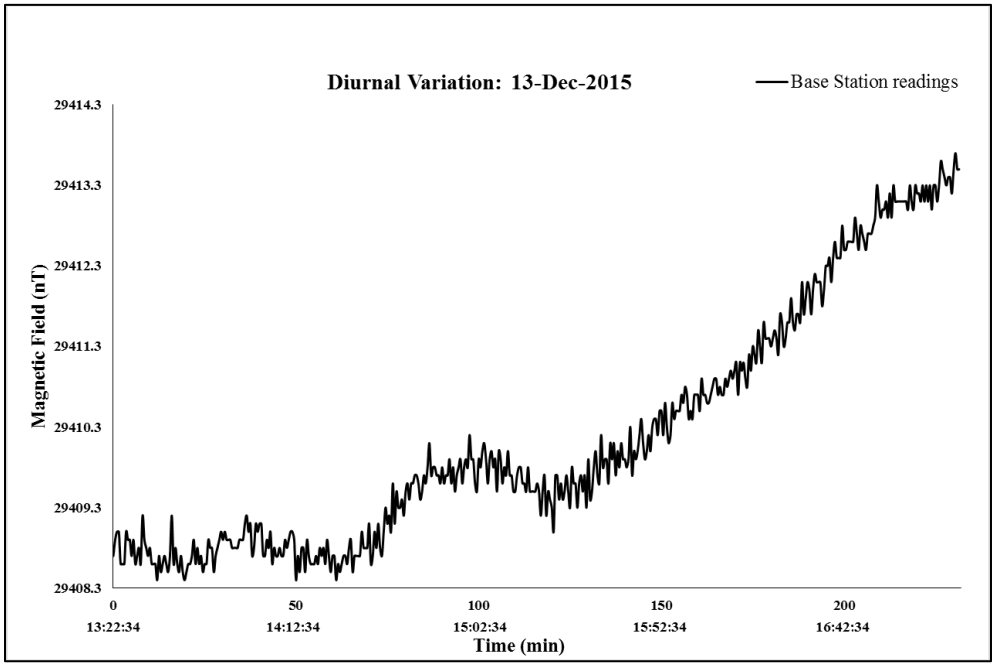


Figure 7.35 Diurnal variation plot for day 3. The Julian day is 347. The survey started after midday and lasted for 231.5 minutes.

Day 4: 14 December 2015

The highest and lowest recorded magnetic field on this day were 29,420.8 nT and 29,399.8 nT, respectively and thus the recorded daily variation is 21.0 nT (Figure 7.36). The recorded data show a noise envelope of 0.7 nT.

Day 5: 15 December 2015

The highest and lowest recorded magnetic field on this are 29,403.8 nT and 29,391.2 nT, respectively and thus the recorded daily variation is 12.6 nT (Figure 7.37). The recorded data show a noise envelope of 0.8 nT.

Day 6: 16 December 2015

The highest and lowest recorded magnetic field on this are 29,416.7 nT and 29,389.9 nT, respectively and thus the recorded daily variation is 26.8 nT (Figure 7.38). The recorded data show a noise envelope of 0.9 nT.

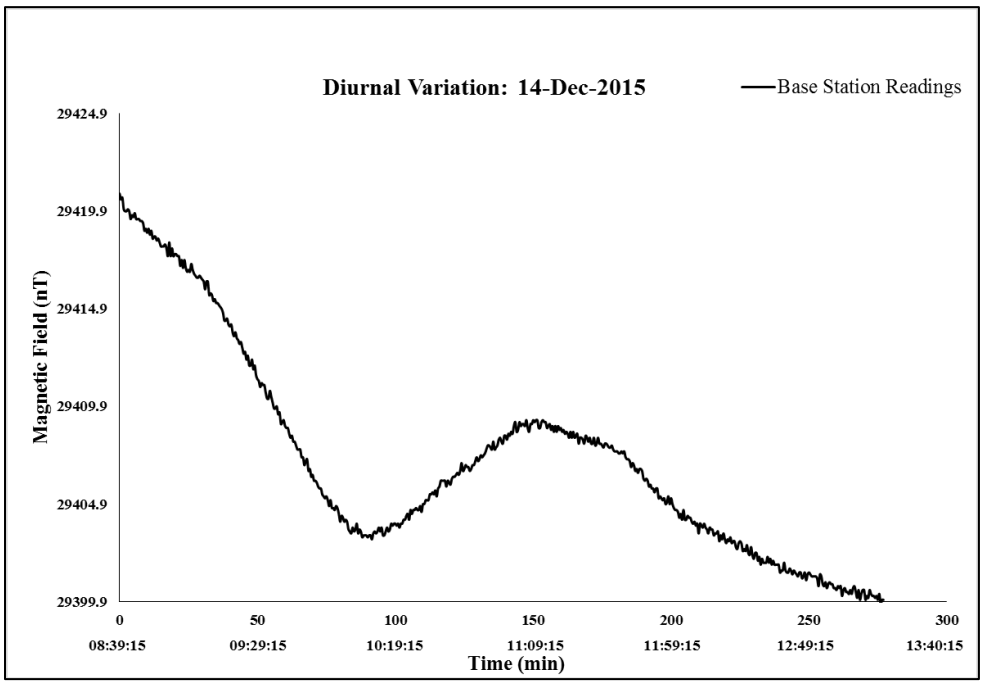


Figure 7.36 Diurnal variation plot for day 4. The Julian day is 348. The survey lasted for 277 minutes.

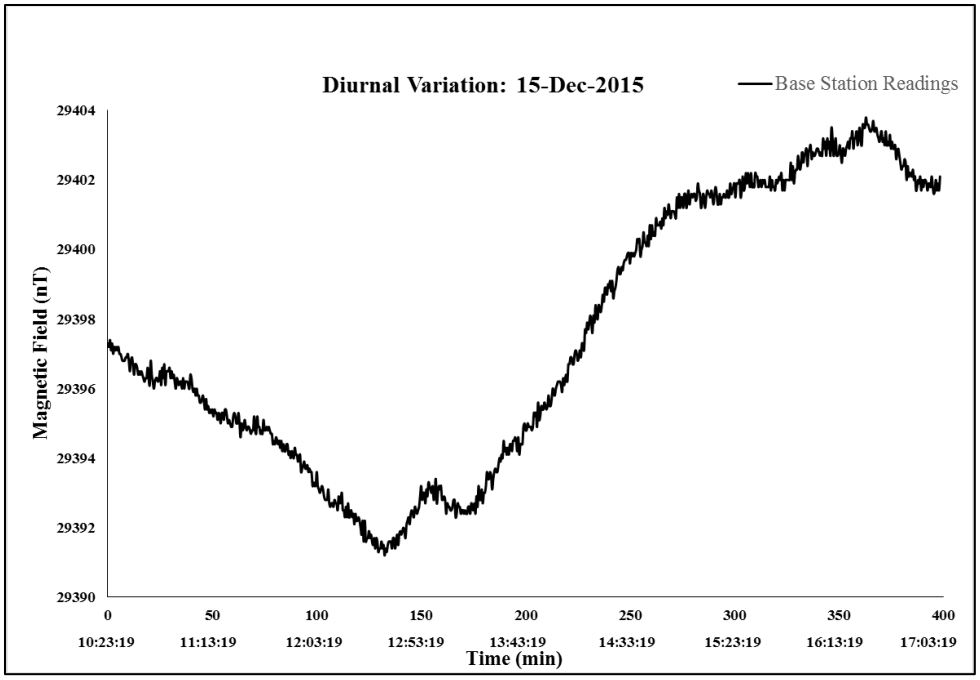


Figure 7.37 Diurnal variation plot for day 5. The Julian day is 349. The survey lasted for 398.5 minutes.

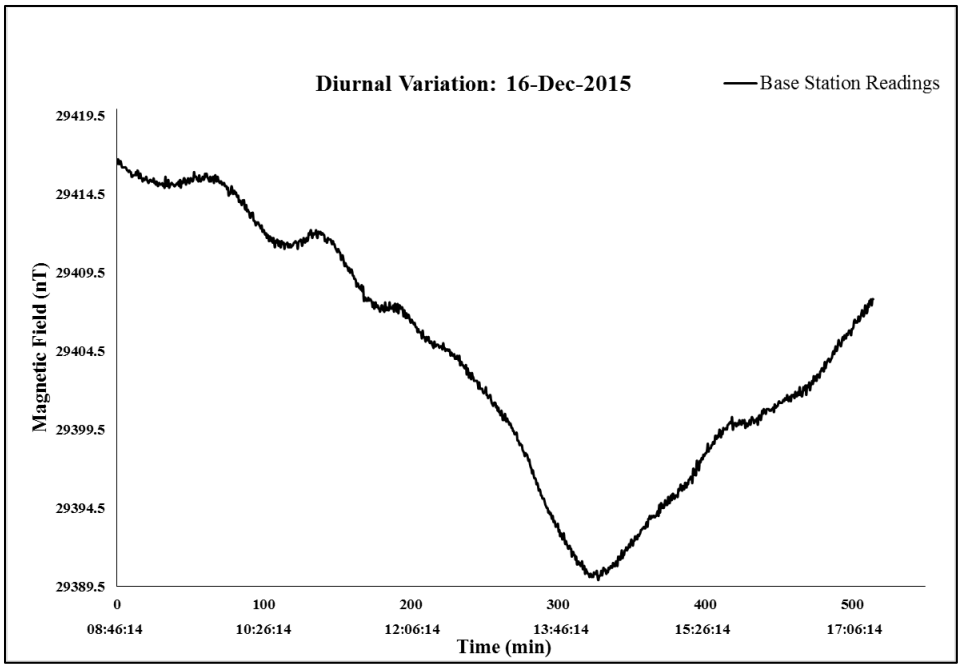


Figure 7.38 Diurnal variation plot for day 6. The Julian day is 350. The survey lasted for 514.5 minutes.

Day 7: 17 December 2015

The highest and lowest recorded magnetic field on this are 29,416.7 nT and 29,389.9 nT, respectively and thus the recorded daily variation is 26.8 nT (Figure 7.39). The recorded data show a noise envelope of 0.9 nT.

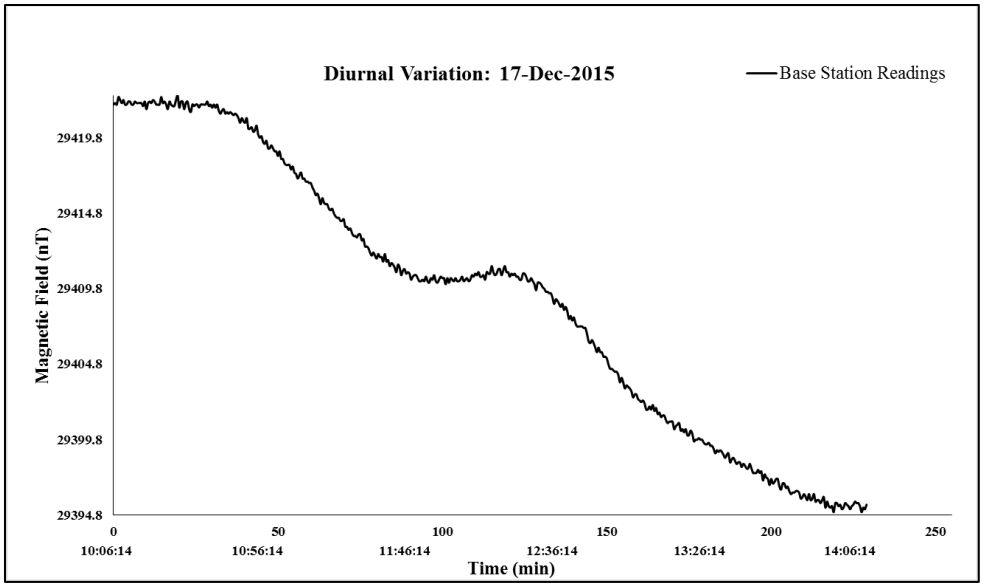


Figure 7.39 Diurnal variation plot for day 7. The Julian day is 351. The survey lasted for 229 minutes.

The highest magnetic field values (29,422.6 nT) were observed on day 7, whereas the lowest magnetic field values (29,389.9 nT) were recorded on day 6 (Figure 7.40). The micropulsations are common in the data from all the days and their amplitudes are less than 10 nT. The diurnal variations for all the survey days range from 5.3 nT to 27.8, with the highest and lowest values recorded on the day 3 and day 3, respectively. These values are less than 30 nT and thus the data are of good quality and can be used for diurnal corrections and interpretations.

The diurnal correction was performed on the ground magnetic data based on the data collected from each day. Diurnal correction was performed using the Oasis Montaj, Geosoft software. This process was divided into two steps:

Step1: Base Station Correction

The regional magnetic field intesity in the study area is 29,000 nT and a reference magnetic value of 29, 400 nT was selected. The base station magnetic field data were then subtracted

from the reference value i.e 29400 nT- magnetic field data to yield the base station correction.

Step2: Diurnal Correction

The base station correction was then applied to the rover data to yield diurnally corrected data by using the formula below.

Magnetic data from the survey lines + base station correction = diurnally corrected data.

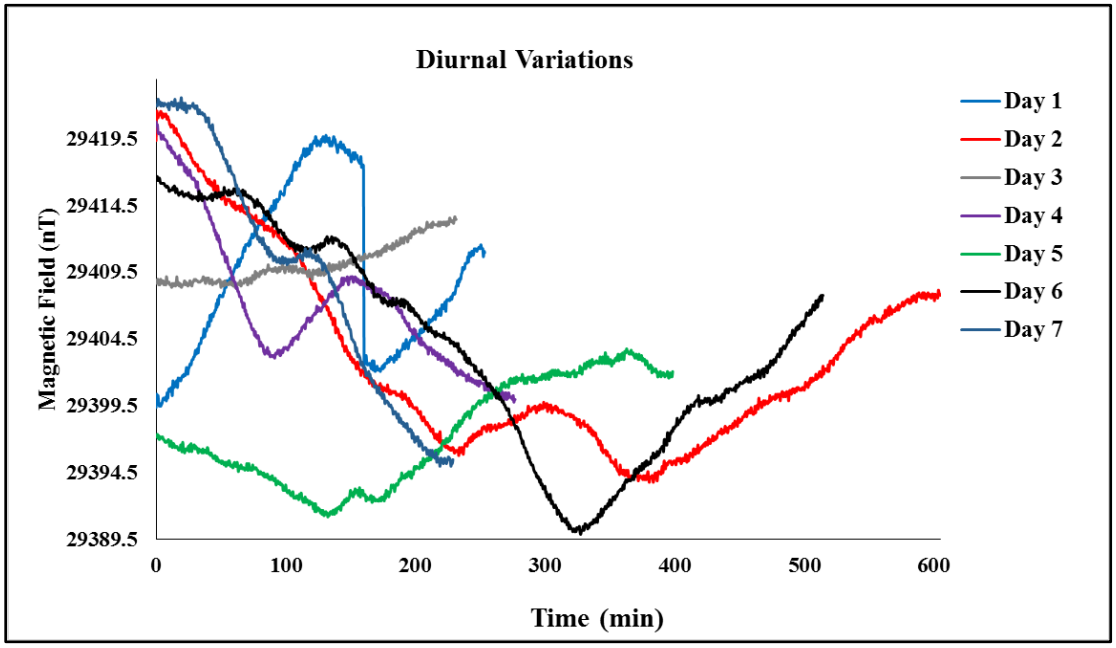


Figure 7.40 Plots for diurnal variations for all the days.

c) Removal of IGRF

Magnetic surveys measurements are a combination of the Earth's core field, known as the International Geomagnetic Reference Field (IGRF) and the field induced in crustal rocks (Reeves, 2005). The IGRF gives the magnetic data a smooth long-wavelength variation superimposed on the shorter-wavelength local geological features (Dentith and Mudge, 2014). The IGRF is published by the International Association of Geomagnetism and Aeronomy (IAGA) on a five-yearly basis (Reeves, 2005). By convention, the IGRF is removed from the magnetic data once all other corrections to the data have been made. The IGRF in the magnetic dataset is calculated at every sampling station point in a survey and subtract that value (IGRF) from the observed value to give the anomaly value, which is the magnetic field of the crustal rocks, the TMI (Blakely, 1996; Reeves, 2005). Although the presented ground magnetic data was collected from a small

survey area, the IGRF was removed from the survey data to compensate for the slower secular variations of the geomagnetic field because the data was collected over a couple of days (e.g 10-17 December 2015). The IGRF calculated for the study area at the time of the survey (2015) showed an inclination of -61.9° and a declination of – 9.4. The IGRF was calculated using the Oasis Montaj Geosoft software. There is not much difference when the IGRF removed data was compared with the original magnetic data and this is because the data was collected from a small local area. TMI is selected as the basic record of the measured data. Although, herein, the measured field is referred to as TMI, it should be noted, however, that TMI is indeed the difference between the measured magnetic field and the IGRF.

7.6.5.2 Display of the magnetic data

a) Profiles

The measured magnetic data can be presented in profile format. Although the data in profile representation are not exposed to potential artefacts caused by gridding process, profile analysis is time consuming. Nevertheless, profile analysis can resolve specific problems in places with specific and localized features with small-amplitude anomalies in the presence of higher-amplitude host rock (Isles and Rankin, 2013). Several profiles of the TMI data were generated to examine the amplitudes of the magnetic anomalies pertaining to the target geological features such as the locating the magnetic units. Line 1400 has low magnetic values at the start and end of the survey line and, both positive and negative magnetic values in the middle of the line (Figure 7.41). Both the negative and positive anomalies indicate the presence of a shallow magnetic source. Line 1800 exhibit magnetic lows in the northern part of the survey line and magnetic highs in the southern part due to regional effect (Figure 7.41). The positive magnetic values of Line 1400 are higher than those in Line 1800. The trend of positive anomalies in Figure 7.42 suggests the presence of a magnetic body.

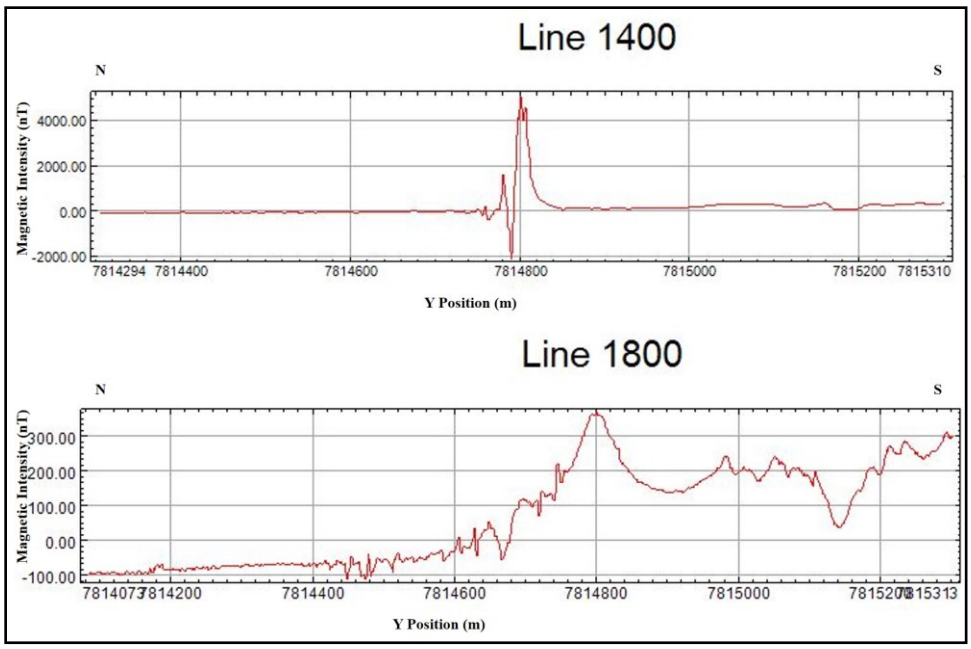


Figure 7.41 Profiles of the selected survey lines: Line 1400 and 1800.

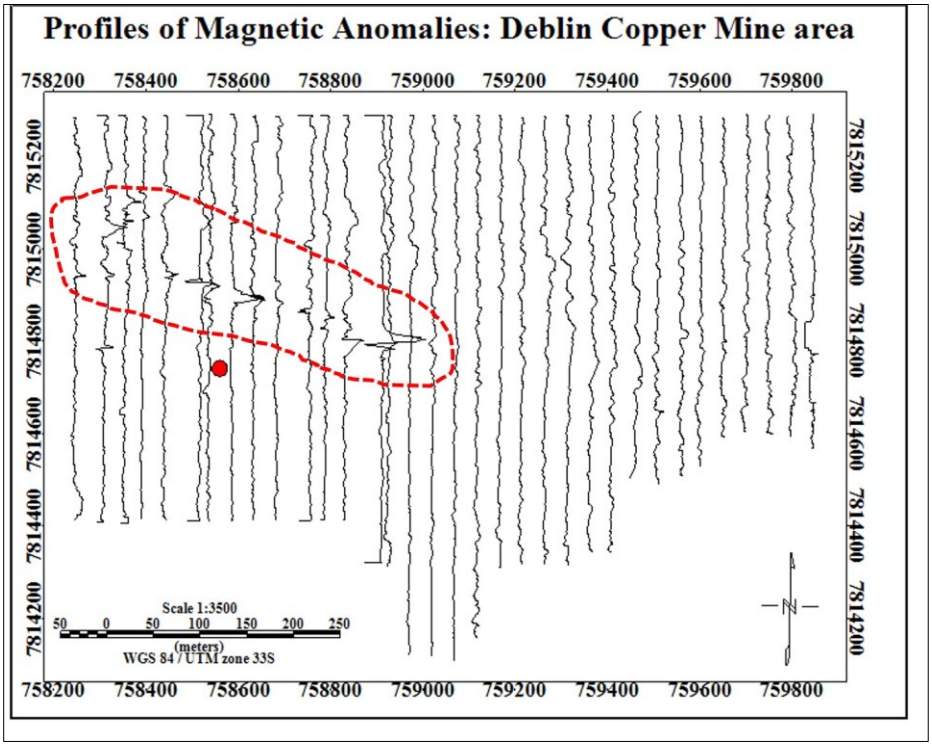


Figure 7.42 2D presentation of magnetic profiles of the 34 infill survey lines. The red dotted line represents the area with a trend of positive anomalies, whereas the red dot represents the location of the Deblin Copper Mine shaft. The trend of the anomalies indicate the strike of magnetic units.

b) Gridding

When all basic corrections have been applied to the TMI measurements, the data has to be interpolated into a grid for easy display. This is the presentation of the geophysical data in 2D, whereby the spatial coordinates are ground locations, thus forming a magnetic map. In general, the geographical distribution of the data depends on the survey type. In order to interpolate between the data points, a grid with a specified grid cell size is created. The grid cell size is preferably between 1/5 and 1/2 and thus commonly 1/4 of the line spacing. There is a wide spectrum of gridding methods and the selection of the best gridding method depends on the spatial distribution of the data. The commonly used gridding method in gridding magnetic data are minimum curvature (Briggs, 1974) and kriging (Hansen, 1993). Minimum curvature is popular for unaliased data (Nabighian *et al.*, 2005) and generates smooth surfaces, however it can create high magnitude artifacts in areas of no data (Briggs, 1974). On the contrary, kriging with an anisotropic covariance function is common in the exploration field and is also effective in almost any type of dataset (Hansen, 1993).

In this study, both the minimum curvature and kriging interpolation algorithms were applied to the 69 line ground magnetic data to evaluate any major differences in their gridded data outputs. The resultant TMI grids with 12.5 m cell size do not show any major differences (Figure 7.43) and thus either gridding method could be used to create the TMI grid. The kriging gridding method was used to create the TMI grid data.

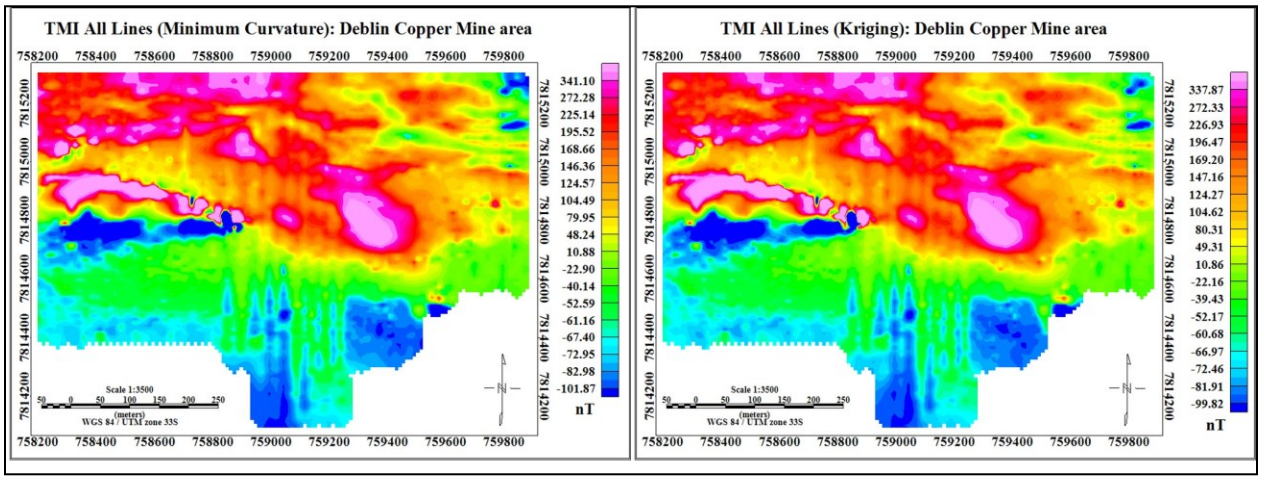


Figure 7.43 Comparison of Total Magnetic Intensity (TMI) maps gridded with A) minimum curvature and B) kriging methods.

7.6.5.3 Magnetic data enhancement and Analysis

Data enhancement includes subsequent processing of the data in order to facilitate interpretation. In addition, data enhancement techniques involve numerical algorithms operating on the survey data for specific purposes such as filtering (Dentith and Mudge, 2014). Isles and Rankin (2013) describe filters as processes which underscore desired components of the data while destroying others, particularly the unwanted part of the data or signal. The specific filters applied to the ground magnetic data are explained in section 7.5.2.

The TMI grid is a reference grid for the RTP grid, which is a reference grid for all the filtered versions of the Deblin Copper Mine area magnetic data. The resultant TMI grid of the 69 survey lines exhibit line-oriented noise which appears as linear anomalies parallel to survey lines (Figure7.44a). The data in adjacent lines were collected on different days in a bi-directional manner. This line-oriented noise in the ground magnetic data can be attributed to line to line datum shift. In addition, variation in magnetic data occurs within single lines, making it difficult to decorrugate the data manually by changing the magnetic values in the individual lines.

It is noteworthy that if the line-oriented noise is uncorrected then computation of derivatives becomes dominated by these line-oriented noise effects. Therefore, to resolve this noise in the data, the two survey data sets (first 35 lines and 34 infill lines) collected at a line spacing of 50 m are gridded separately (Figure 7.44b-c) and assessed. The grid of the first 35 lines (Figure 7.44b) has line noise in the central part of the survey area, whereas the 34 infill line grid is noise free. However, to increase the resolution in the data, the two grids are merged (Figure 7.44d). Nonetheless, the line noise is persistent in the central part of the grid and occurs as analogous to linear structures parallel to the survey line direction (N-S), evident in the RTP and 1VD images (Figure 7.45). Thus the grid of the 34 infill lines has proven to be suitable for data presentation for the study area (Figure 7.46). More data increases the resolution, however, it should be noted that the first 35 lines have noisy data.

The TMI map of the study area shows that the northern part is magnetically disturbed while the southern part is magnetically quiet. Hence, the northern part consists of magnetic lithologies, whereas the southern part lacks magnetic lithologies (Figure 7.46). The TMI values range from -94.11 nT to about 338.22 nT.

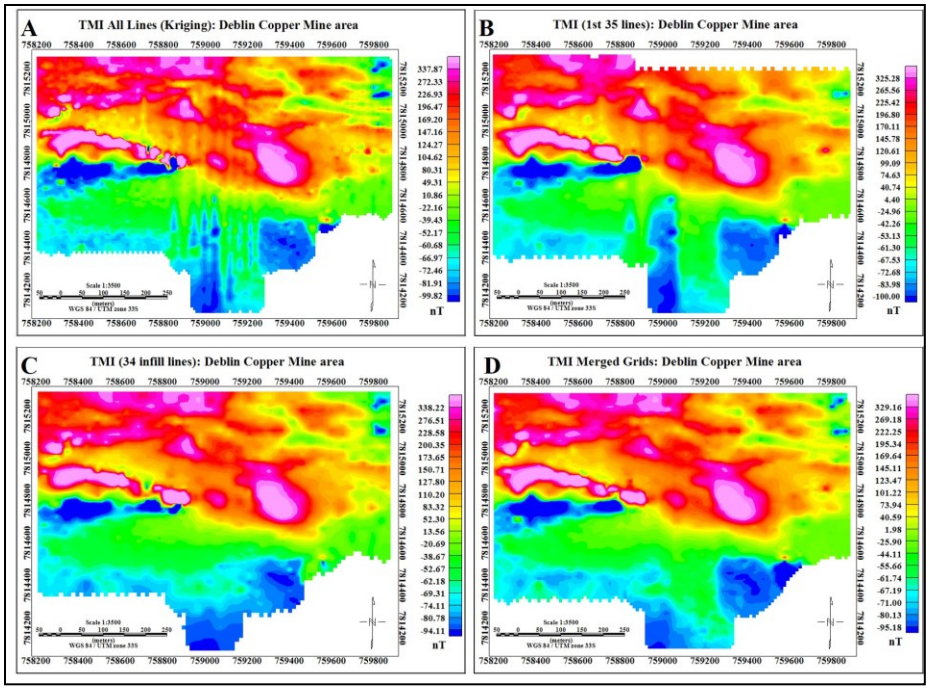


Figure 7.44 TMI maps gridded with different set of lines. A) All survey lines (69 lines). B) The first 35 lines. C) The 34 infill lines. D) A combination of two grids (B and C).

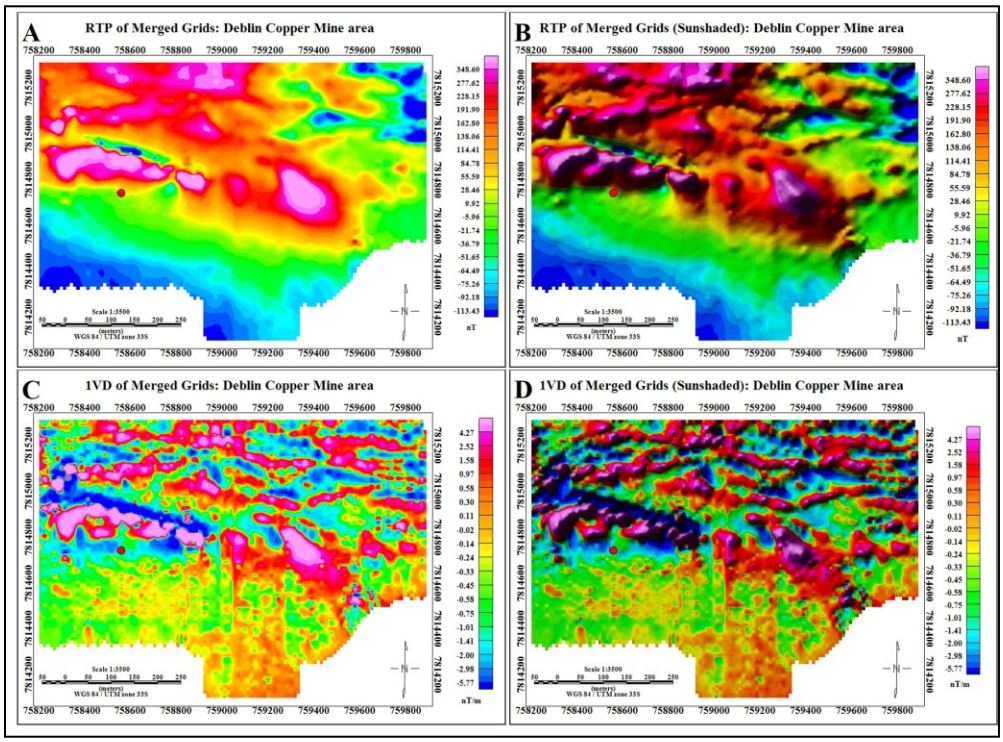


Figure 7.45 Reduced to Pole (RTP) and first vertical derivative (1st VD) maps of the merged grids with line noise, which is obvious in the sunshaded maps. The red spot in the images represent the Deblin Mine shaft. The inclination and declination for the shaded images are 45° and 45°, respectively.

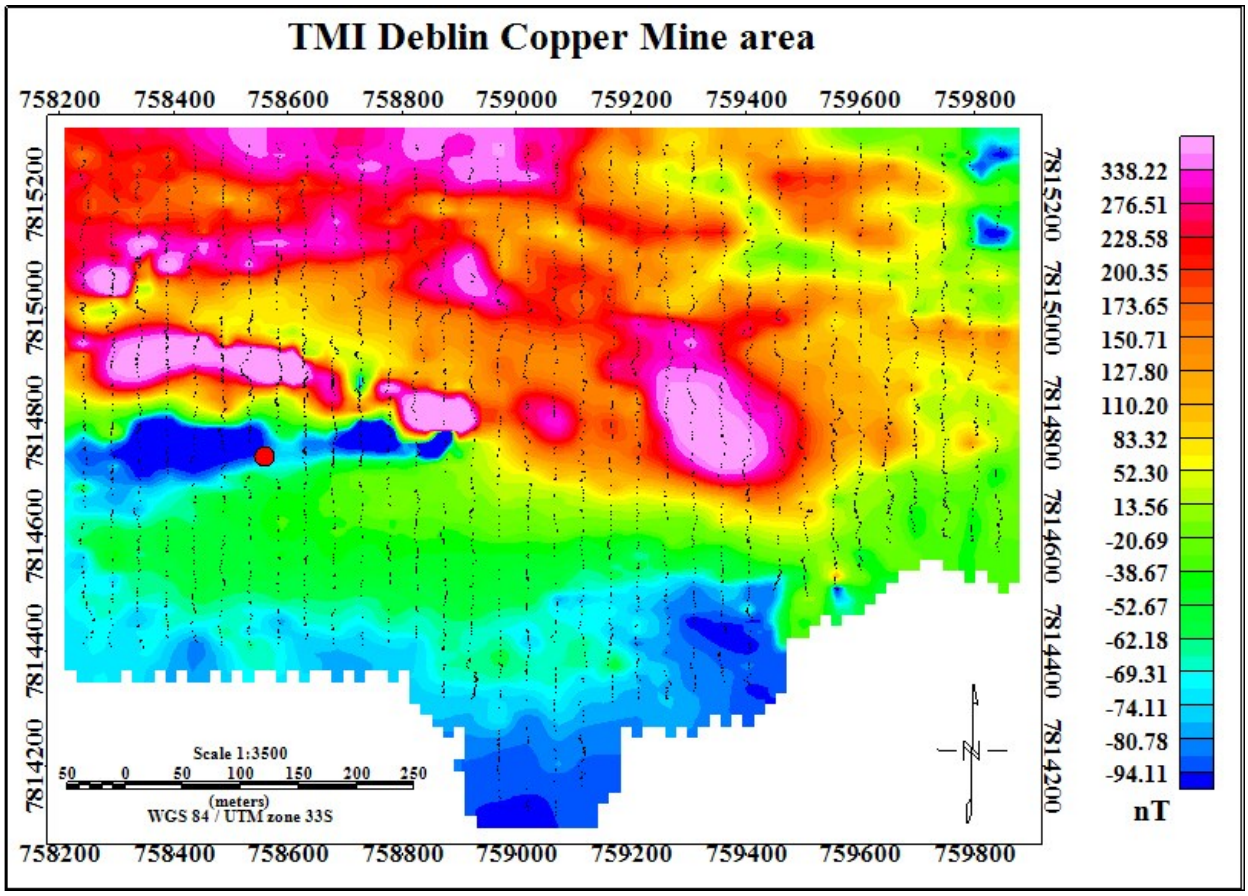


Figure 7.46 Total Magnetic Intensity (TMI) map of the Deblin Mine area with the magnetic data sampling points. The Earth's declination and inclination are -9.4 and -61.9, respectively. The red dot represents the location of the Deblin Copper Mine shaft.

a) Upward Continuation

The survey height for the presented data is 2 m, which is good for high resolution data collection and detection of small scale subsurface geological features. However, ground magnetic data collected at that height commonly exhibit high frequency noise (Figure 7.42) due to magnetic materials such as ilmenite and laterite that commonly occur in the overburden. Magnetic materials that occur in the overburden are not part of the objectives of this study and thus to remove high frequency noise effects due to these surface and near-surface sources, the ground magnetic data was upward continued by 5 m (Figure 7.47).

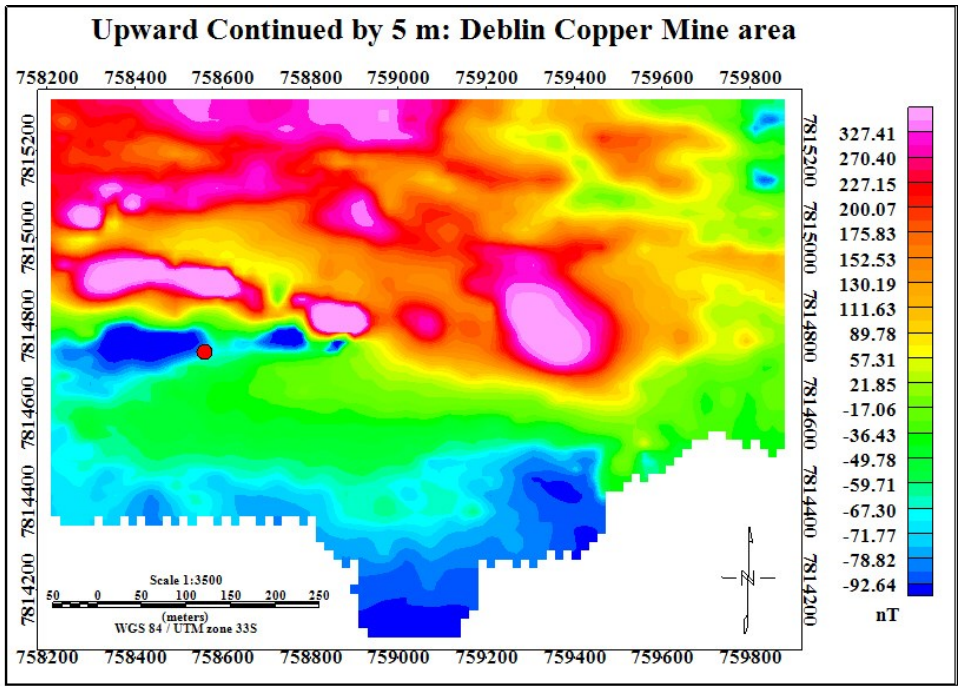


Figure 7.47 The Total Magnetic Intensity (TMI) data upward continued by 5 m. Notice how the TMI data is smoothed. The red dot represents the location of the Deblin Copper Mine shaft.

b) Reduction to Pole

The RTP operator was applied to the 5 m upward continued TMI data of the Deblin Copper Mine area to locate the measured magnetic anomalies directly on top of their sources. The dipolar effects shown by asymmetric anomalies due to dipolar effects in the TMI data (Figure 7.48a) are removed in the RTP data (Figure 7.48b) and the positive anomalies move southward.

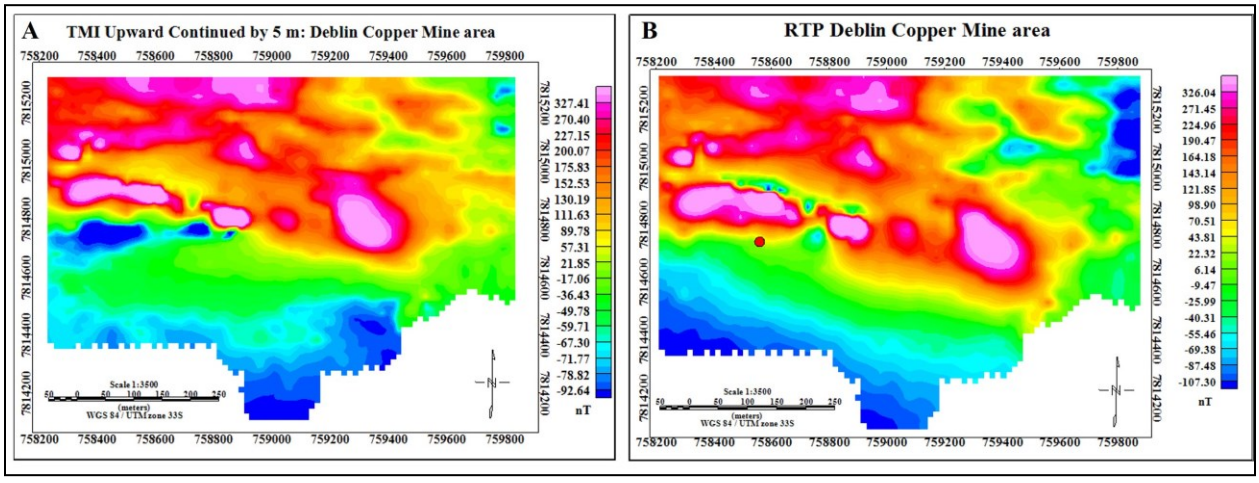


Figure 7.48 Ground magnetic data of the Deblin Copper Mine area. A) Is the Total Magnetic Intensity (TMI) image and B) is the Reduced to Pole (RTP) image of the TMI data with anomalies lying directly on top of their sources.

c) First Vertical Derivatives

The keystone high-pass filter in the structural analysis of the aeromagnetic data for the study area is the 1st VD because it provides a very reliable starting point for the process of depicting structural details from the magnetic data as well as mapping geological contacts. It is hard to depict structures in the original TMI or RTP data because of their broader magnetic response (Figure 7.49a). The application of the 1st VD filter to the RTP data of the study area enhanced shallow structural features such as lineaments as in the shown in Figure 7.49b. Although the 1st VD enhances shallow features, it also amplifies high frequency noise in the data (Figure 7.49b).

d) Tilt Derivatives

A higher order vertical derivative, such as the second order vertical derivative can be applied to aid map structural features that are closed spaced, however, the noise increases with the increasing order of derivative and thus it cannot be utilized. To resolve shallow but more closely spaced magnetic sources the tilt derivative was used (Figure 7.50). The tilt derivative filtered image exhibits the same structures as those in 1VD but with higher resolution. Similarly, noise is enhanced.

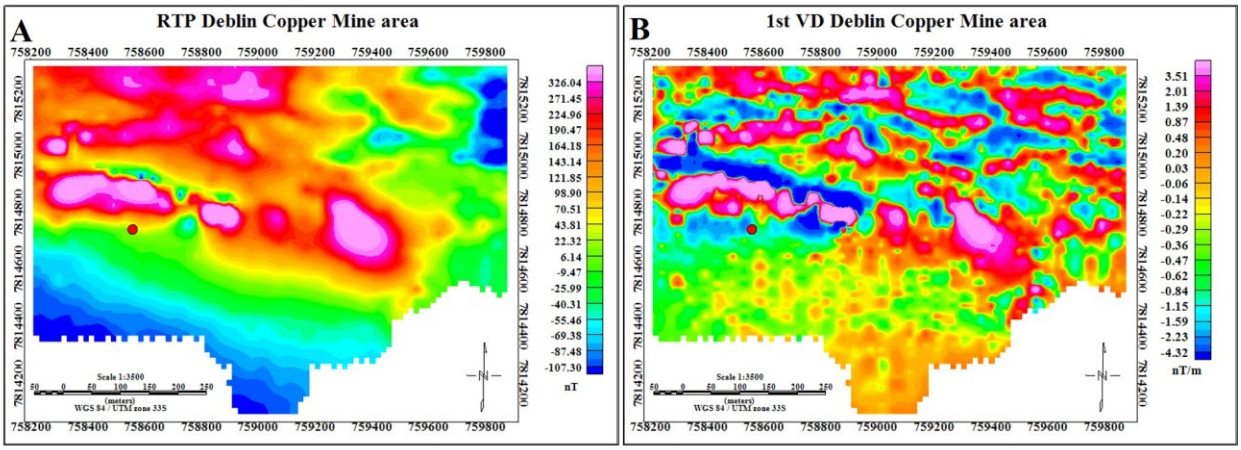


Figure 7.49 The application of the first vertical derivative (1VD) to the Deblin Copper Mine ground magnetic data. A) Reduced to Pole (RTP) map; B) 1VD map showing the shallow linear structures.

e) Total Horizontal Derivative

This study used the total horizontal derivative (THDR) to delineate edges of the shallow magnetic structures and map the contacts of the magnetic bodies (Figure 7.51a).

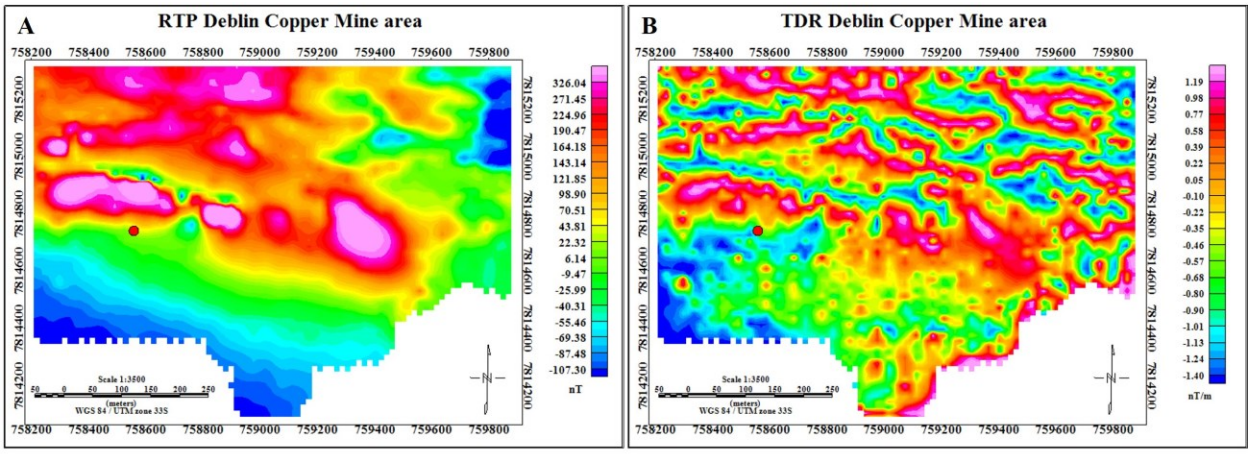


Figure 7.50 The application of the tilt derivative to the ground magnetic of the Deblin Copper Mine area. A) Reduced to Pole (RTP) map and B) the tilt horizontal derivative (TDR) which clearly maps shallow linear structures.

f) Analytic Signal

In addition to the THDR, the AS is also used for contact mapping and resolving close-spaced bodies. AS magnetic anomalies lose the dipolar form. In addition, AS was used to assess the presence of remanent magnetization in the study area. There is no evidence of remanent magnetization in the AS data. Although AS is very effective in contact mapping, like any other derivative, the AS enhances noise in the magnetic data, and breaks up the stratigraphy as it removes the continuity of the magnetic anomalies (Figure 7.51b).

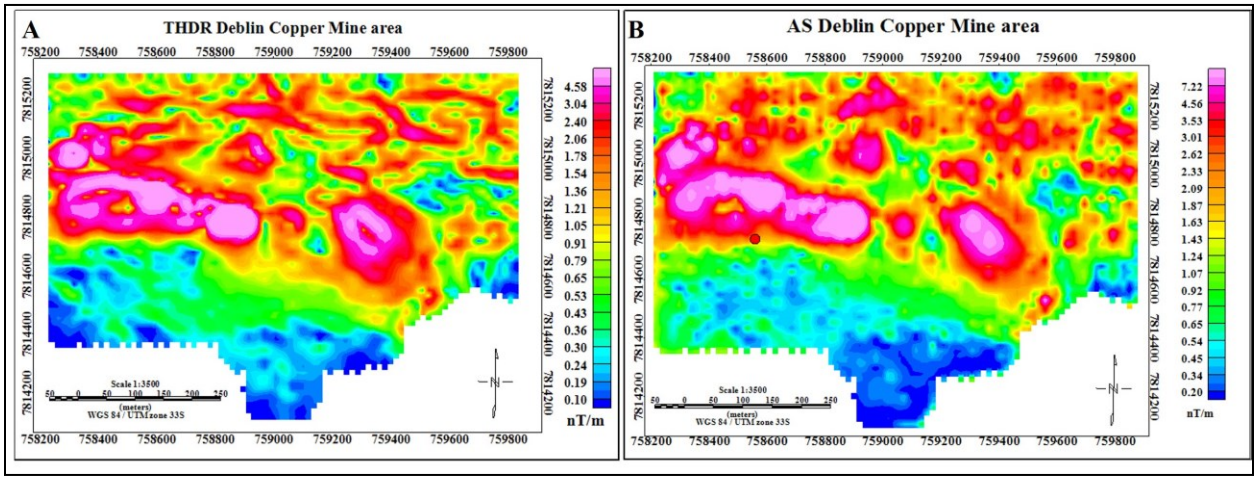


Figure 7.51 Contact mapping of the magnetic units using A) total horizontal derivatives (THDR) and B) analytic signal (AS). The maps show contacts of the magnetic maps. The continuity of the stratigraphy is preserved in the THDR map and destroyed in the AS map.

g) Spectral Filter (Gaussian regional-residual separation)

This method is commonly used to separate regional and residual components of magnetic data from the total magnetic fields produced by all underground magnetic sources located at both shallow and deep depths. This is achieved by selective removal of unwanted frequency ranges. In this study, the residual filter was applied to the ground magnetic data to remove the regional field and enhance magnetic responses of the shallow structures (Figure 7.52-7.53). The shallow structures can be clearly mapped in the residual magnetic field map (Figure 7.53a-b). Also derivatives such as 1st VD (Figure 7.53c) and TDR (Figure 7.53d) can be applied to the residual field magnetic data to enhance the structures.

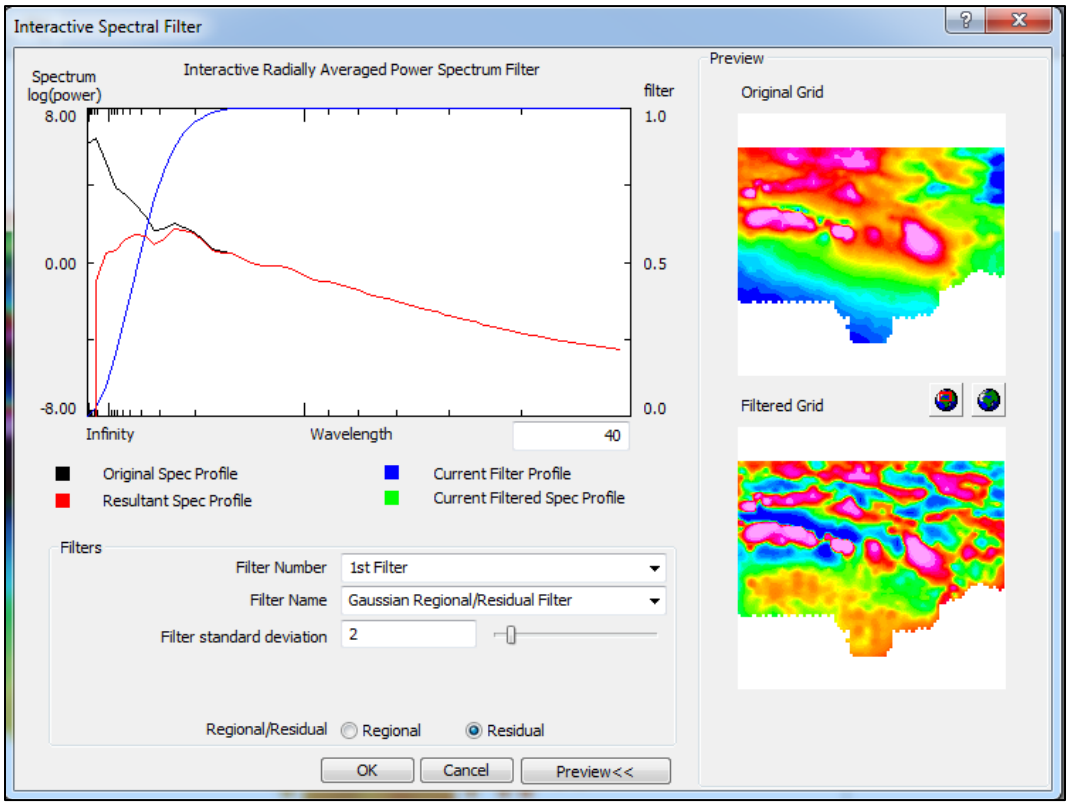


Figure 7.52 Residual filter spectral analysis of the TMI of the Deblin Copper Mine area. Cut-off frequency is 2.0.

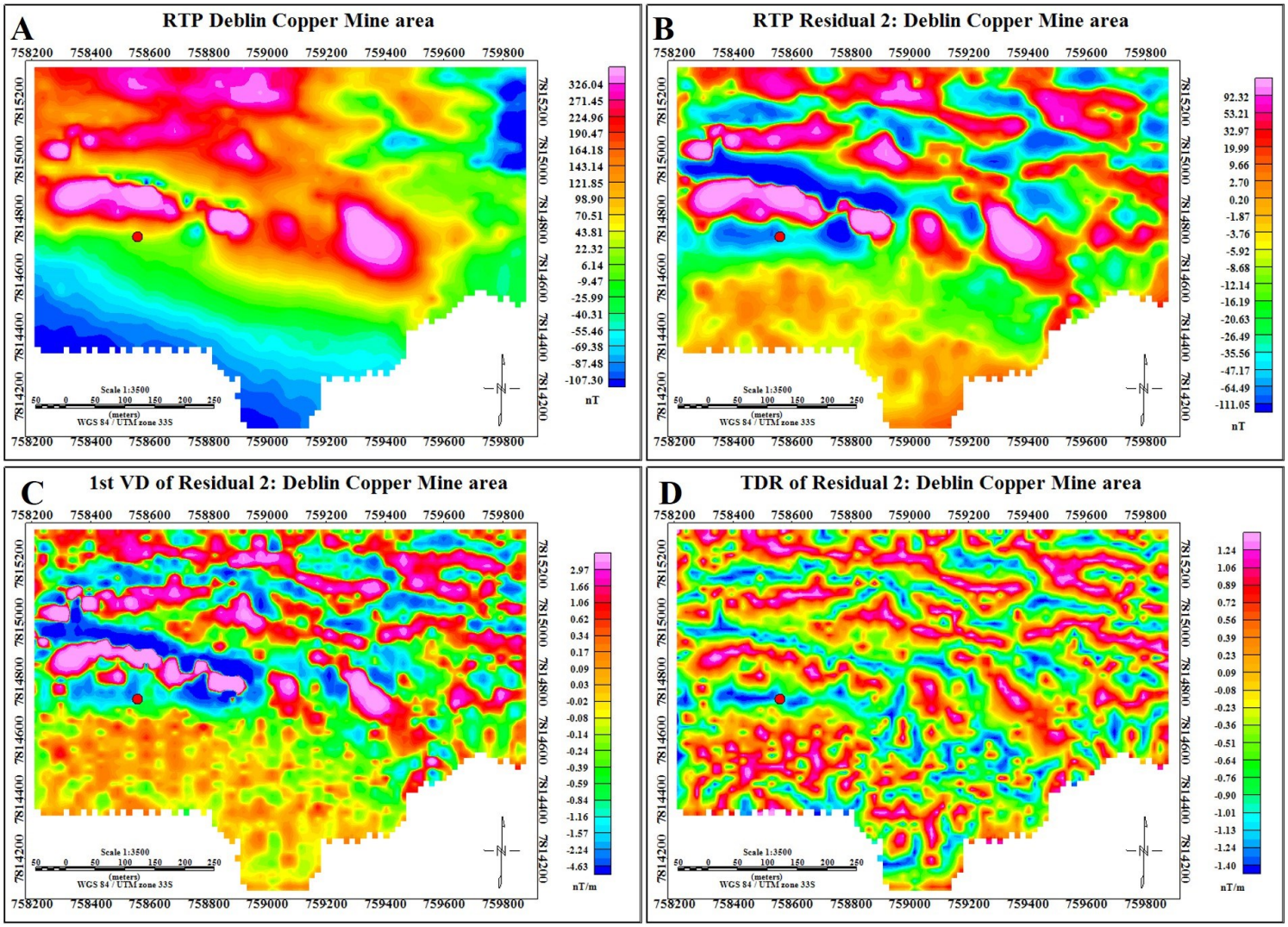


Figure 7.53 Residual filter applied to the ground magnetic data of the Deblin Copper Mine area. A) RTP map showing the total magnetic field of all the shallow and deep underground magnetic sources; B) Residual magnetic field map showing magnetic response of shallow seated sources; C) 1st VD of the residual magnetic field showing shallow linear structures; D) TDR of the residual magnetic field showing shallow linear structures with a high resolution.

7.6.6 Interpretation of the ground magnetic data

The detailed (1:2,500 scale) geological map (Figure 7.54) of the Deblin Copper Mine is characterized by outcrops of carbonates and limited metavolcanics. Most the area is highly covered by sand with a thickness that is rarely greater than 10 m. Despite the inferred faults, an almost total absence of structures on the geology map implies the presence of limited rock exposure. Consequently, the detail on continuity of individual units and contacts in some areas is hard to decipher. Nevertheless, the ground magnetic imagery provides a framework from which the magnetic signature of the major deformation events and their overprinting relationships at local-scale can be derived, before extrapolating these to the regional scale. The detailed (1:2,500 scale) geological map of the Deblin Copper Mine (Figure 7.54) makes it possible to look at specific relationships between outcrops and high resolution (50 m spaced) ground magnetic data while maintaining aspects of the big picture.

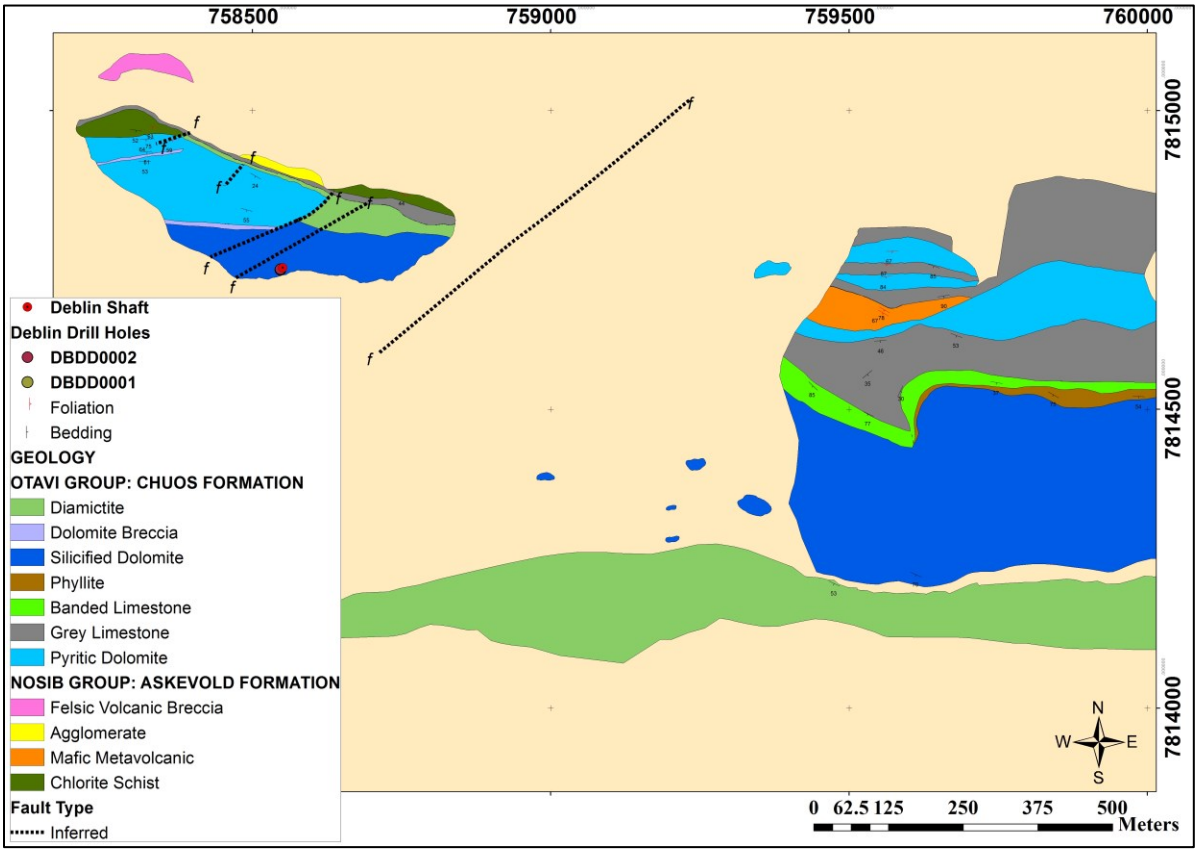


Figure 7.54 Detailed geological map of the Deblin Copper Mine showing the extensive sand cover, rock outcrops and inferred structures.

The high resolution (50 m spaced) ground magnetic data of the Deblin Copper Mine area (Figure 7.55) show that some of the lithologies can be clearly mapped under areas of sand cover due to their magnetic signatures. The high resolution ground magnetic data (e.g RTP, 1st VD, AS and TDR) clearly reveal more information on the shape of individual magnetic rock units and locate the exact positions of the east-west-oriented thrust fault, northeast-trending fault zones and lithological contacts. The ground magnetic data of the Deblin Copper Mine is characterized by east-west trending moderate to high-amplitude magnetic anomalies. The positive magnetic anomalies in ground magnetic data of the Deblin Copper Mine area are correlated with the known magnetic units such as the agglomerate on the local geological map.

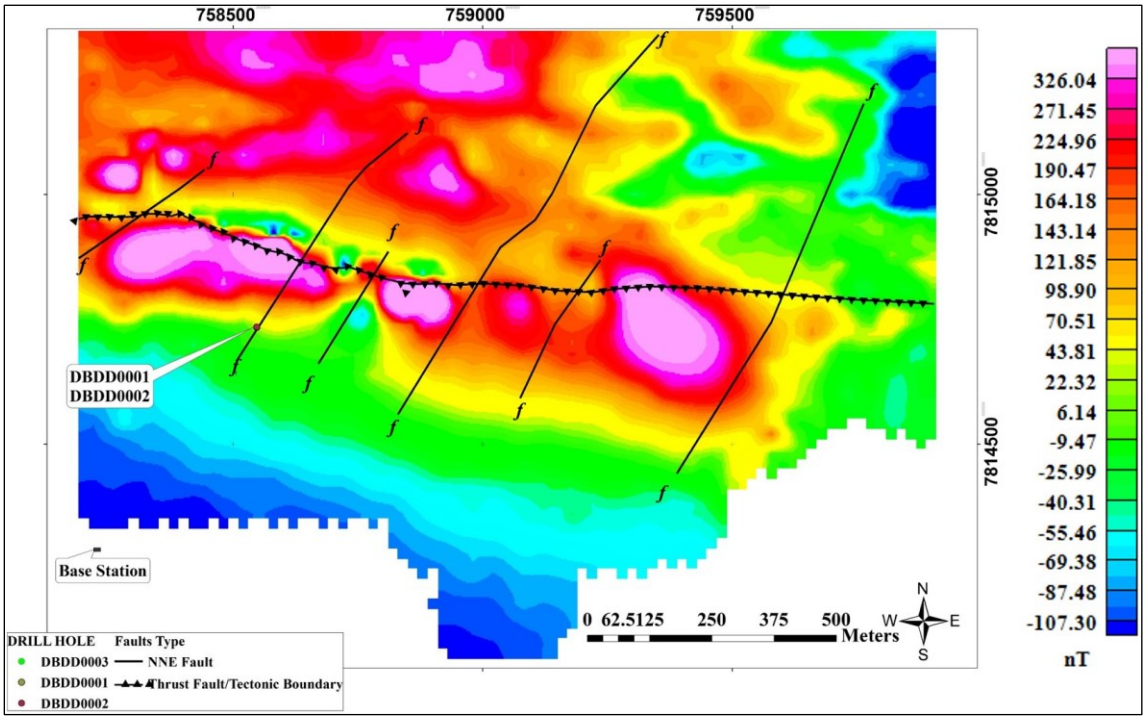


Figure 7.55 Interpreted RTP map showing the magnetic response of the rocks from the Deblin Copper Mine area and positions of the major thrust fault and northeast-oriented faults.

The ground magnetic data of the Deblin Copper Mine is characterized by conspicuous south-southeast- to east-west trending moderate to high-amplitude magnetic anomalies and a low magnetic anomaly in the south (Figure 7.55). The southernmost high amplitude magnetic anomalies lie on outcrops of different rock types including the mafic metavolcanic rocks underlying the carbonates and banded iron formation bearing diamictites. It has been established

from the magnetic susceptibility data that these carbonates are non-magnetic and thus the observed magnetic anomalies are attributed to both the underlying magnetic agglomerates and chlorite schist of the Askevold Formation or the Chuos Formation banded iron formation in the diamictites. High amplitude magnetic anomalies in the areas without outcrops to the north of the mafic metavolcanic and carbonate outcrops suggest the presence of the mafic metavolcanics, primarily agglomerate and chlorite schist.

The individual magnetic anomalies are clearly outlined on the TDR map (Figure 7.56) by the red and green lines representing different magnetic sources. The Deblin Copper Mine area magnetic data comprises both Domain B and Subdomain C1 and their dividing structural boundary, the east-west trending thrust fault 2, which were derived from the regional aeromagnetic data. In the ground magnetic data, the signature of the magnetic mafic metavolcanics can be clearly distinguished from the magnetic signatures of the banded iron formation in the diamictite based on their amplitudes.

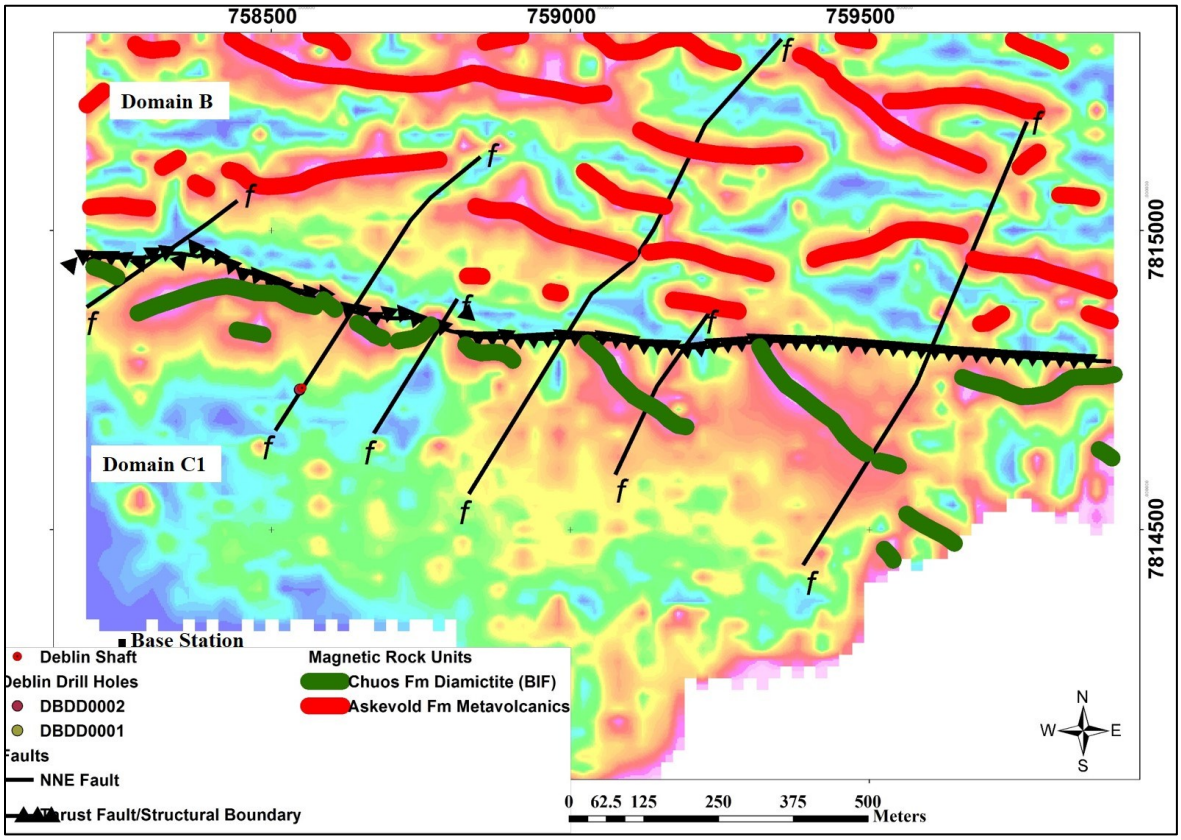


Figure 7.56 Interpreted TDR map showing the magnetic anomalies of the different magnetic units and the locations of the east-west-trending thrust fault and the shallow northeast-trending faults.

Comparing the geological map (Figure 7.54) with the ground magnetic data (Figure 7.55-7.56) confirms that the areas with linear magnetic rock signature are mainly mafic metavolcanic rocks such as the agglomerate and chlorite schist of the Askevold Formation (Domain B). The very strongly magnetic linear rock units appear to be exclusively associated with the banded iron formation-bearing diamictite of the Chuos Formation (Domain C1). The extensive areas of relatively low magnetic signature in the southern part of the area, where the sand cover extensively occurs, are due to the deeply buried Chuos Formation banded iron formation-bearing diamictite and carbonates.

Shallow crustal structures were imaged using a combination of filters including the 1st VD, TDR, residual magnetic field. All the high pass filtered maps show recognizable anomalies in areas that are smooth in the TMI/RTP data and delineate the locations and orientations of the shallow seated structures. The major east-west thrust fault terminates the highly magnetic signatures of the banded iron formation-bearing diamictites of the Chuos Formation to the north (Figure 7.56). This thrust fault forms the contact between the Askevold Formation mafic metavolcanic rocks and the Chuos Formation highly magnetic diamictites as shown in both the RTP (Figure 7.55) and TDR (Figure 7.56) maps. In addition, there are various northeast-trending linear magnetic lows (probable faults). One of these faults is located close to the DBDD0001 and DBDD0002 locations. Some of these northeast-trending lineaments mapped from the magnetic data correlate with the inferred faults on the local geological map of the Deblin Copper Mine and appear to overprint the major D_2 east-west thrust fault, which implies that these faults are of D_3 in age. These northeast-trending faults do not show in the regional aeromagnetic data. It is of note that the felsic volcanic breccia, which is described as a gossan occurs in close proximity with one of the northeast faults mapped from the ground magnetic data.

A solid geological map (Figure 7.57) of the Deblin Mine area was interpreted based on the integrated geological map data and different geophysical magnetic products (e.g RTP, AS, TDR, 1stVD) of the ground magnetic data. The overall interpretation of the ground magnetic data reiterate several key features which can be used to locate exploration targets.

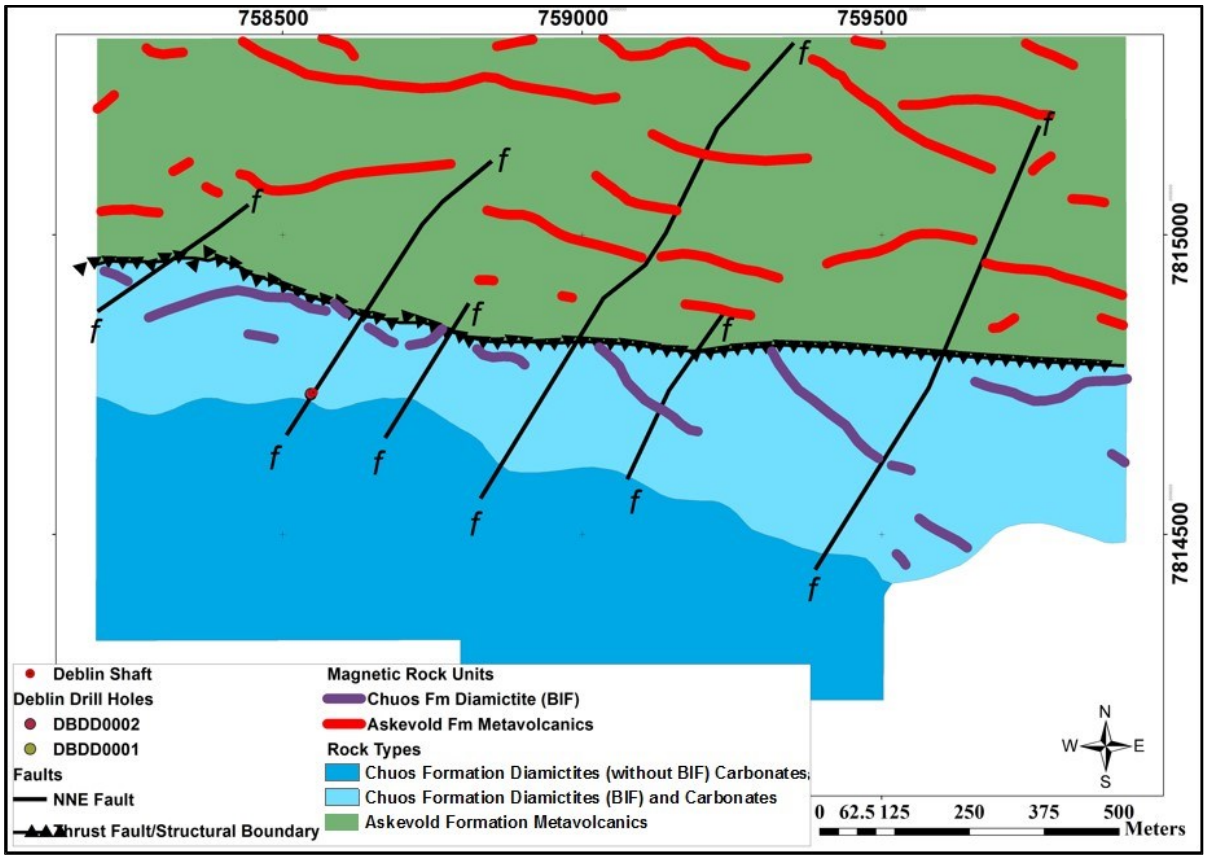


Figure 7.57 Interpreted solid geological map of the Deblin Copper Mine with the major east-west-trending thrust fault and shallow structural NE-trending faults.

7.7 Discussion

The integration of aeromagnetic and ground magnetic data with geological data successfully identified faults and lineaments below and/or within the Otavi Group carbonates which may have important inferences for focusing mineralizing hydrothermal fluids in the Askevold Trend area. The structural observations made at outcrop have been integrated with images of the aeromagnetic and ground magnetic data of the study area to correlate outcrop geology with larger scale deformation patterns. At the scales of both the aeromagnetic and ground magnetic data, several major lithological units have been distinguished and interpreted based on the location of outcropping geology and aeromagnetic and ground magnetic characteristics. Deformed outcrops in the Deblin Copper Mine area occupy a major ductile-brittle shear zone that exhibit evidence of fluid flow.

Magnetic susceptibility data collected on outcrops correlate with ground magnetic data. In addition, the ground magnetic data show zones of high magnetic intensity which are probably covered by sand on the geological map. Within the agglomerate, there are high values of magnetic susceptibility, which can be correlated with the mafic clasts which probably contain fine-grained magnetite near the top of the agglomerate layer in the stratigraphy. In contrast, the carbonates such as the silicified dolomites at the top of the drill core logs, have low magnetic susceptibility values.

On the regional aeromagnetic map, magnetic highs are present in both the Swakop Basin and carbonate platform on the mountain land. The common magnetic unit in both terrains is the Chuos Formation diamictite which has a layer of banded iron formation. The conspicuous east-west trending high-amplitude magnetic anomalies represent anticline and syncline limbs, made up of mafic metavolcanic rocks and diamictite with sporadic banded iron formation layers. The magnetically quiet zones between the magnetic highs reflect non-magnetic carbonates.

According to Miller (1983; 2008) the east-west anticlines and synclines in the Otavi Mountain Land are D_2 in age. In addition, the Swakop Group rocks were thrust over the Mulden Group rocks of the Northern Margin Zone along the Khorixas-Gaseneirob Thrust which is a structural boundary between the Northern Zone and Northern Marginal Zone during D_2. Therefore, it can be concluded that the interpreted thrust faults are of D_2 age, which is the same age as the observed F_2 fold axes and were later cross cut by the northeast D_3 faults. Since D_2, is the major Damaran deformation event in this area, the interpreted folds and thrusts that were deciphered from both ground and magnetic data confirms that this areas is a fold and thrust setting. The established major east-west-trending thrust fault 2 is located at the southern edge of the Otavi Mountain Land, which is a carbonate platform terrane and separates it from the Swakop Basin in the south. Therefore, this thrust fault is interpreted as a thrust tectonic structure which developed during the Damaran D_2 collision of the Kalahari and Congo cratons and separates the Swakop Basin from the carbonate platform of the Otavi Mountain Land.

Taking into consideration that the positive magnetic signature in the Northern Zone in the Otavi Mountain Land are attributed to the magnetic mafic metavolcanic of the Askevold Formation and the highly magnetic diamictites of the Chuos Formation (Corner, 2008), it can be suggested that

the thrust fault 2 is probably the eastern extension of the Khorixas-Gaseneirob Thrust which has not been precisely identified in this area. Shear zones are known to host ore bodies as a result of hydrothermal flow through orogenic belts. The final mineralization phases of Tsumeb ores appear to be late- to -post tectonic, after the peak of the Damara orogeny at around 530 Ma and may have been emplaced late during D_3 (Kamona and Günzel, 2007; Miller 2008). This implies that the D_3 age linear structures in this area are of mineral economic significance as the Tsumeb-type mineralization appear to have formed by copper bearing metamorphic fluids during D_2 and D_3.

Similarly, the northeast-trending faults mapped from the ground magnetic data are of D_3 age. These are analogous to the faults mapped at the Kombat deposit, located 15 km northeast of the Deblin Copper Mine and thus both local and regional lineaments could be the extensions of the Kombat deposit fault system. On both regional and local magnetic maps, these shallow structures cut across the east-west thrust faults. The intersection points of these two sets of structures are potential sites of epigenetic base metal mineralization. Therefore, they could be base metal exploration drilling targets and worth further geophysical investigations with other methods such as EM or resistivity.

A conceptual model of the ore loci can be drawn based on the interpretations made from both regional aeromagnetic and ground magnetic data (Figure 7.587). Thrusting imposed important controls on the occurrence of the hydrothermal copper mineralization observed at the contact of the Askevold Formation with the Chuos Formation carbonates and within the carbonates. The collision phase of the Damara orogeny, D_2, resulted in dewatering of the Damara basins causing evolved basinal brines to deposit copper-rich sulphides within the carbonate rocks. The D_2 thrust faults acted as conduits for the orogenic brines as they migrated from higher temperature metamorphic areas further south in the Swakop Basin into the undeformed foreland carbonate platform. When these fluids came into contact with the reducing conditions in the carbonates, they tended to precipitate the metals (e.g. Cu) forming sulphides. In addition, the late to post-tectonic Cu-ores may have been emplaced during D_3 as is the case at Tsumeb and their ore loci are probably located at the intersections of D_2 east-west oriented shear zones with D_3 northeast-trending faults.

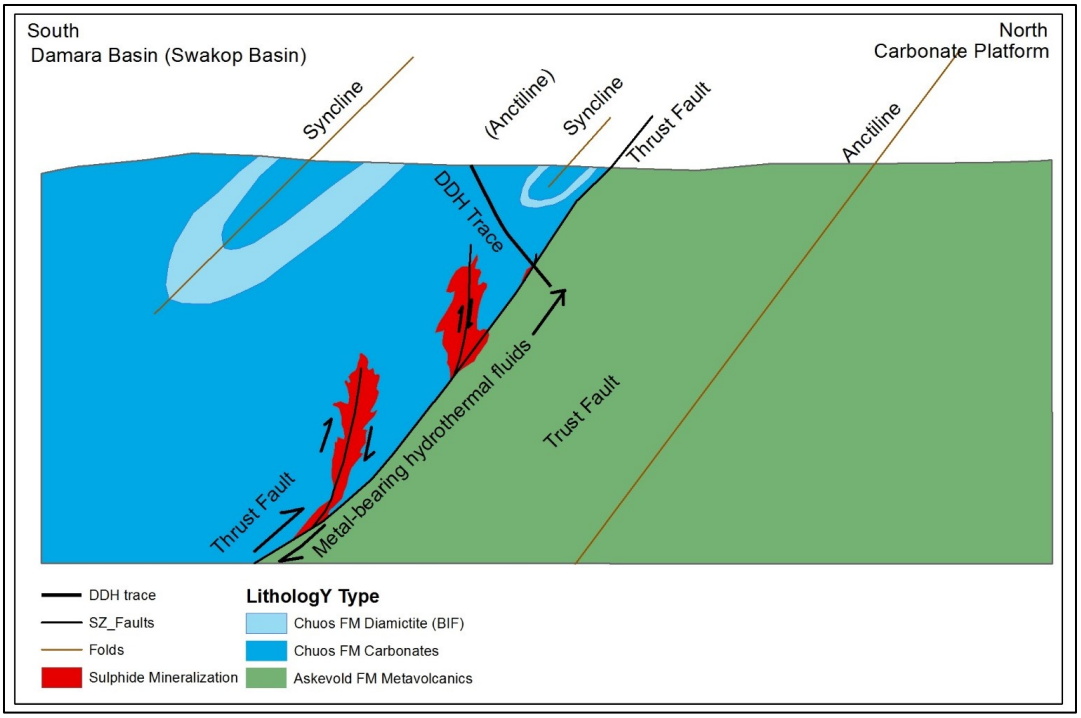


Figure 7.58. A conceptual cross-section model across the Deblin Copper Mine are showing a set of thrust faults along which metal-bearing basinal fluids were introduced into the carbonate host rocks.

Chapter 8

Discussion and Conclusion

The Deblin Copper Mine in the southern Otavi Mountain Land is located at the transition zone between the shallow water platform carbonates to the north and a deeper rift basinal area to the south. The area is characterized by poor rock exposure and consists of the metavolcanic rocks of the Nosib Group conformably overlain by the Otavi Group carbonates, which extend to the north of the study area. Although the carbonates in the study area are platform carbonates the underlying and poorly exposed metavolcanic rocks were used to determine their geochemical characteristics and the tectonic setting of the study area. The metavolcanic rocks are hydrothermally altered and show evidence of greenschist facies metamorphism. Metamorphism and alteration have resulted in the remobilization of the large ion lithophile elements (e.g Cs, Rb, Ba and Sr) as evidenced by the high values of the loss on ignition together with the lack of precise trends when different oxides are plotted on the SiO_2 bivariate diagrams. These conclusions are corroborated by the petrographic descriptions.

The whole rock trace element geochemistry indicates that these metavolcanic rocks initially formed as alkali basalts. These findings concur with the geochemical interpretation of the mafic volcanic rocks of the Askevold Formation made by Miller (2008). The geochemical characteristics of the metavolcanic rocks are comparable with the within-oceanic plate volcanic rocks. The integration of geochemical and field petrological data argue that the metavolcanic rocks of the Askevold Formation around the Deblin Copper Mine area formed in an oceanic island geotectonic setting at the rift margin of the Damara Orogen. In addition, the presence of both felsic and mafic volcanic rocks is indicative of bimodality. This interpretation of the tectonic setting is in full agreement with the location of the study area, which is the transition from the Swakop Basin to the carbonate platform of the Otavi Mountain Land fold and thrust belt. The platform carbonate is a typical tectonic setting for the Mississippi Valley Type (MVT) deposits, whereas the oceanic island geotectonic setting is typical for the volcanogenic massive sulphide (VMS) deposits. The carbonates in Otavi Mountain Land constitute a complete record for the Neoproterozoic from the

end of the Sturtian glaciation to the middle of the Ediacaran Period (Halverson et al., 2007), and they were deformed at about 650 Ma (D_1) (Miller, 1983; Deane, 1995; Laukamp, 2006) and 512 ±7 Ma (D_2) (Lehmann et al., 2016). The Neoproterozoic carbonates were deposited after rift volcanism at 746 ±2 Ma (Hoffmann and Prave, 1996).

This study presents evidence for both the VMS and MVT-type of mineralization and none for the Iron Oxide Copper and Gold (IOCG) type.

a) Evidence for VMS-type mineralization.

VMS deposits have a genetic association with coeval volcanism and mainly consists of two parts, namely a concordant massive sulphide lens and discordant vein-type sulphide mineralization (Franklin *et al.*, 2005). Formerly, it has been suggested that the Deblin Copper Mine is a VMS deposit (Adamson, 1976; Petzel, 1991; Kamona and Günzel, 2007; Golden Deeps Limited, 2012). The base metal ore of the Deblin Copper Mine is characterized by chalcopyrite, which is the main ore mineral associated with minor amounts of sphalerite and bornite. The predominance of chalcopyrite and lack of galena lend more support towards a VMS than an MVT-type. Although the metavolcanic rocks are not the major host rocks in this deposit, the minor occurrence of vein type sulphide mineralization in the agglomerate appear to suggest VMS-style of mineralization. It is noted that VMS-type deposits are characterized by massive sulphides, however, the lack of sulphide mound in this deposit does not necessarily preclude a VMS deposit. This is either because: a) the sulphide mound formed and got eroded by the seawater as it was not covered by sediments quickly enough for it to be preserved or b) the density of the hydrothermal fluid being emitted onto the seafloor was such that the ores dissipated away from the source and was not able to form a sulphide mound.

The limited number of sulphur isotope analyses of sulphides from the Deblin Copper Mine indicate two sulphur sources. The hydrothermal vein type sulphides show a narrow range of sulphur values ($\delta^{34}S$ = -4.93‰ to +6.04‰), which are within the typical magmatic sulphur values of 0±5‰ δ^{34}_{SCDT} (Ohmoto, 1986; Sharp, 2007; Allègre, 2008), and thus suggestive of magmatic origin. In contrast, the disseminated type has a wide range of sulphur values ($\delta^{34}S$ = -9.99‰ to +3.63‰) with most samples having values which are within the magmatic sulphur values of 0±5‰ δ^{34}_{SCDT}

(Ohmoto, 1986; Sharp, 2007; Allègre, 2008). The wide range of sulphur values is caused by the samples with light values, which is indicative of the involvement of ore fluids with sulphur derived from marine sediments. The magmatic source implies that the metal-bearing fluids were derived from the underlying basalts through large-scale tectonic lineaments such as rift margin faults as conduits and final precipitation of metals at the contact of the metavolcanics and carbonates, and within the overlying platform carbonates. The magmatic source of sulphur is consistent with the VMS-type deposit and inconsistent with an MVT-type deposit.

Although some of the evidence presented by this study are in support of a VMS style of mineralization, which is the existing interpretation, there is also a possible MVT-type link. This study provides new evidence that appear to support MVT-type of mineralization as discussed below.

b) Evidence for MVT-type mineralization

This study revealed that copper mineralization of this deposit is hosted mainly in platform carbonates, primarily the silicified dolomite and dolomite breccia of the Chuos Formation with minor vein type sulphide occurrences in the agglomerate of the Askevold Formation. The main mineralized zone of the Deblin Copper Mine ores is characterized by vein type mineralization at the contact zone between the agglomerate and the overlying silicified dolomite. The occurrence of the copper mineralization in the carbonates and its stratigraphic position seems to contradict the interpretation of the host rock by some previous researchers (Adamson, 1976; Petzel, 1991; Kamona and Günzel, 2007), who described that copper mineralization in this area is hosted in metavolcanic rocks of the Askevold Formation. The carbonate-hosted vein and disseminated types tend to support an MVT-style of mineralization.

Crosscutting relationships and textural characteristics of the sulphides have been used to establish a paragenetic sequence of the ore minerals: pyrite > chalcopyrite > sphalerite > bornite > covellite > malachite > goethite. Covellite, malachite and goethite constitute the supergene post-ore assemblage. With the exception of marcasite and galena, which are absent, the paragenetic sequence of the ore minerals from the Deblin Copper Mine reflect that of other MVT deposits. Based on analysis of the rock textures and alteration facies, four major alteration events are present

in the Deblin Copper Mine area. They are (in the paragenetic sequence): sericitization, chloritization, silicification and carbonatization. The distribution and intensity of the alteration types and the associated sulphide mineralization vary within the stratigraphy. Silicification is prominent in the silicified dolomite, whereas carbonatization occurs in all the rock types. Both silicification and carbonatization occur as hydrothermal quartz-calcite veins and are in close association with vein-type sulphides. These alterations introduced vein type sulphides in the host rocks and they mark the last phase of mineralization in this deposit. Additionally, chloritization is ubiquitous in the matrix of the agglomerate and seems to be related to the copper sulphide mineralization as well. Although silicification and carbonatization are the most significant alteration types that are typical for the MVT-type deposits (Paradis *et al.*, 2007; Kamona, 2011), they can also occur in any other deposit types. The sedimentary sulphur source indicated by the sulphur isotope values of the disseminated sulphides from this study is in support of the MVT-type deposit.

The structural control of mineralization of this deposit was inferred from the integration of magnetic data with geological mapping data. This technique is suitable for identifying structures in sand covered areas. The ground magnetic data suggest shallow crustal lineaments, which may correlate with structural features on the local geological map. This suggests that the lineaments from the ground magnetic data are possible extensions of those identified via surface geological mapping. The northeast-trending lineaments from the magnetic maps are analogous to the faults mapped at the Kombat deposit, located 15 km northeast of the Deblin Copper Mine and thus these lineaments could be the extensions of the Kombat deposit fault system. These shallow structures in the proximity of the Deblin Copper Mine and further to the east appear to overprint a major east-west oriented thrust fault which is probably related to the shear zone. Shear zones are known to host ore bodies as a result of hydrothermal flow through orogenic belts. The east-west thrust fault that runs through the Deblin Copper Mine coincides with all the Askevold Trend deposits. The intersection points of these two sets of structures are potential sites for epigenetic base metal mineralization. These sites are identified as base metal exploration target areas in this area and therefore, other geophysical methods such as EM or resistivity are recommended for further exploration work. On the basis of the interpreted regional aeromagnetic and ground magnetic data, a conceptual model of the ore loci in this area was established (Figure 7.58). The model suggests

that thrusting played a role in the deposition of the hydrothermal copper mineralization observed at the contact of the metavolcanic rocks of the Askevold Formation and carbonates of the Chuos Formation and within the overlying carbonates. The collision phase of the Damara orogeny, D_2, resulted in dewatering of the Damara basins, particularly the Swakop Basin causing evolved basinal brines to deposit Cu-rich sulphides within the carbonate platform. The D_2 thrust faults acted as conduits for the orogenic brines as they migrate from higher temperature metamorphic areas further south in the Swakop Basin into the less deformed foreland carbonate platform to the north. This is typical in tectonic settings of MVT-type deposits. Therefore, the conclusions from the magnetic method suggests an MVT style of mineralization.

c) Evidence for IOCG-type mineralization

The petrographic study by Golden Deeps Limited (2013) proposed a shear-hosted hydrothermal mineralization style with an Iron Oxide Copper and Gold (IOCG) style mineral assemblage hosted in the carbonates. This study has confirmed the presence of shearing as shown by the C-S fabrics in the metavolcanic rocks. However, magnetite and/or haematite are not present in the ores and thus the study does not provide any evidence to support an IOCG-type mineralization assemblage.

The Deblin Copper Mine was compared with the MVT-type carbonate-hosted deposits such as the Tsumeb, Kombat, Khusib Springs, Berg Aukas and Abenab West in the Otavi Mountain Land to establish any similarities and differences. The Deblin Copper Mine tectonic setting is the transition zone between the platform carbonates and margin of the rift basin, whereas other Otavi Mountain Land deposits (e.g Tsumeb, Kombat, Khusib Springs, Berg Aukas and Abenab West) are located in the platform carbonate tectonic setting. While carbonates of these deposits lack associations with metavolcanic rocks, the carbonates of the Deblin Copper Mine at the base of the Otavi Group are directly in contact with the Nosib Group metavolcanic rocks, which were emplaced in a within-oceanic plate island along the rift margins.

Previously, base metal mineralization in the Abenab Subgroup in the Otavi Mountain Land has been recorded only in the Gauss and Auros Formations carbonates at Berg Aukas and Abenab West deposits, respectively (Innes and Chaplin, 1986; Chadwick, 1993; Frimmel *et al.*, 1996; Kamona and Günzel, 2007). This study revealed that the Chuos Formation carbonates at the base

of the Abenab Subgroup also host base metal mineralization at the Deblin Copper Mine. The host rocks of the Otavi Mountain Land MVT-type deposits are carbonates (Kamona and Günzel, 2007). In contrast, copper mineralization at the Deblin Copper Mine is hosted in carbonates and metavolcanics. Furthermore, the distribution of carbonate-hosted hydrothermal mineralization in the Otavi Mountain Land led to the identification of two broad types, namely Berg Aukas and Tsumeb (Lombaard et al., 1986; Innes and Chaplin, 1986; Hughes, 1987; Misiewicz, 1988; Pirajno and Joubert, 1993). The Berg Aukas and Abenab West deposits, which are hosted in the Abenab Subgroup are examples of the Berg Aukas-type and are characterized by Pb-Zn and V sulphide ores and little or no Cu (Misiewicz, 1988; Pirajno and Joubert 1993; Laukamp, 2006; Kamona and Günzel, 2007). In addition, the Tsumeb-type mineralization is represented by Tsumeb, Kombat and Khusib Springs deposits, which are confined to the Tsumeb Subgroup and characterized by complex sulphide ores containing Cu, Pb, Zn, Ag, As, Ge, Cd and Ga (Lombaard et al., 1986; Innes and Chaplin, 1986; Hughes, 1987; Kamona and Günzel, 2007). The main sulphide ore mineral of the Deblin Copper Mine is chalcopyrite associated with minor amounts of sphalerite and bornite, and lacks Pb, V, As, Ga sulphides. Evidently, the Deblin Copper Mine carbonate-hosted mineralization does not seem to belong to either the Berg Aukas-type or the Tsumeb-type classification of the Otavi Mountain Land MVT-type carbonate-hosted deposits.

The sulphur isotope ratios of sulphides from Tsumeb, Kombat, Khusib Springs and Berg Aukas deposits are heavy and show wide ranges (Innes and Chaplin, 1986; Hughes, 1987; Kamona and Günzel, 2007). Sulphur isotope ratios from Berg Aukas deposit are analogous to the sulphur isotope ratios of the Tsumeb and Khusib Springs deposits (Kamona and Günzel, 2007). The heavy sulphur isotope ratios of the sulphides from Tsumeb, Berg Aukas and Khusib Springs deposits are indicative of seawater source of sulphur, which is characteristic of the MVT-type deposits. A mixed source of sulphur is suggested for Kombat deposit (Innes and Chaplin, 1986; Hughes, 1987) because the sulphides have a wide range of sulphur isotope ratios ($\delta^{34}S$=-11.3‰ to +26.2‰) (Hughes, 1987) and contain values within the typical magmatic sulphur values of 0±5‰ δ^{34}_{SCDT} (Ohmoto, 1986; Sharp, 2007). Locally, when sulphur isotope ratios of the sulphides from the Deblin Copper Mine are compared to those of the Otavi Mountain Land MVT-type carbonate-hosted deposits, they appear to be lower than the sulphur isotope ratios from Tsumeb, Berg Aukas and Khusib Springs deposits, which indicate a seawater source of sulphur. It is of interest to note

that the Deblin Copper Mine sulphur isotope ratios overlap with the light sulphur isotope ratios of the Kombat deposit, which is interpreted to have a magmatic contribution in addition to the seawater sulphur source.

Combined geological data suggests that the local tectonic setting of the Deblin Copper Mine metavolcanic rocks, ore minerals and isotopic signatures are distinctive of a VMS-type deposit, whereas the main host rock, ore mineralization types and hydrothermal alterations are similar to those of copper rich MVT-type carbonate-hosted deposits. The Deblin Copper Mine appears to have few similarities with the MVT-type deposits in the Otavi Mountain Land (Tsumeb, Kombat, Khusib Springs and Berg Aukas). Additionally, the Deblin Copper Mine mineralization appears to be inconsistent with both the Tsumeb and Berg Aukas-type. Therefore, the presented data of this deposit show ore forming processes associated with both VMS and MVT-type mineralization. Due to limited rock exposure and lack of sufficient drill cores which intersected mineralization further work is recommended to unequivocally determine the mode of occurrence of mineralization for this deposit type. The integration of geological data and magnetic data was successful in mapping the concealed faults and lineaments, which may have played a role in focusing mineralizing hydrothermal fluids in the Deblin Copper Mine area. Therefore exploration for both VMS and MVT-type mineralizations should be conducted in this area.

References

Adamson, R. G., 1976, Report on Orientation Surveys at the Deblin Mine (Farm Neuwerk, 507), Grootfontein District, South West Africa/Namibia. Unpubl.rep., Tsumeb Corporation Ltd, 7.

Aitken, A. R., and Betts, P. G., 2009, Multi-scale integrated structural and aeromagnetic analysis to guide tectonic models: an example from the eastern Musgrave Province, Central Australia: Tectonophysics, 476 (3), 418-435.

Allègre, C. J., 2008, Isotope geology, New York, Cambridge University Press Cambridge.

Arisoy, M. Ö., and Dickmen, Ü., 2013, Edge Detection of Magnetic Sources Using Enhanced Total Horizontal Derivative of the Tilt Angle: Bulletin of the Earth Sciences Application and Research Centre of Hacettepe University, 34, (1), 141-168.

Augustithis, S. S., 1995, Atlas of the Textural Patterns of Ore Minerals and Metallogenic Processes, Berlin, Walter de Gruyter & Co.

Ault, W., 1963, Summary of sulfur isotope standards, Biogeochemistry of Sulfur Isotopes, National Science Foundation Symposium Proceedings. Yale University, New Haven, 509-567.

Baranov, V., and Naudy, H., 1964, Numerical calculation of the formula of reduction to the magnetic pole: Geophysics, 29 (1), 67-79.

Betts, P.G., Valenta, R.K., Finlay, J., 2003. Evolution of the Mount Woods Inlier, northern Gawler Craton, Southern Australia: an integrated structural and aeromagnetic analysis. Tectonopshysics 366 (1-2), 83-111

Blakely, R. J., 1996, Potential theory in gravity and magnetic applications, Cambridge, Cambridge University Press.

Boni, M., Terracciano, R., Evans, N. J., Laukamp, C., Schneider, J., and Bechstädt, T., 2007, Genesis of vanadium ores in the Otavi Mountainland, Namibia: Economic Geology, 102 (3), 441-469.

Borg, G., 2000, Regional controls on sediment-hosted Pb-Zn (Ba-Cu) occurrences within the Pan-African orogenic belts of Namibia: Geological Survey of Namibia Communications, 12, 211-220.

Botha, B. J. V., 1960, The Arenaceous Rocks and the Pseudo-Aplite of the Otavi Mountain Land, South West Africa. PhD thesis, University of Pretoria.

Bracewell, R. N., and Bracewell, R. N., 1986, The Fourier transform and its applications, New York, McGraw-Hill.

Briggs, I. C., 1974, Machine contouring using minimum curvature: Geophysics, 39 (1), 39-48.

Cairncross, B., 1997, The Otavi Mountain Land Cu-Pb-Zn-V deposits: Namibia: Mineralogical Record, 28 (2), 109-157.

Campbell, W. H., 2003, Introduction to geomagnetic fields, Cambridge, Cambridge University Press.

Cann, J., 1970, Rb, Sr, Y, Zr and Nb in some ocean floor basaltic rocks: Earth and Planetary Science Letters, 10 (1), 7-11.

Chadwick, P., 1993, A study of the Berg Aukas-type Pb-Zn-V deposits in the Otavi Mountain Land, Namibia: MSc thesis, University of Cape Town.

Chetty, D., 1998, Geochemical fingerprinting of carbonate wall rock alteration at major base metal sulphide deposits in the Otavi Mountain Land, Namibia: Msc thesis. University of Cape Town.

Chetty, D., and Frimmel, H.E., 2000. The role of evaporates in the genesis of base sulphide mineralization in the Northern Platform of the Pan-African Samara Belt, Namibia: geochemical and fluid inclusion evidence from carbonate wall rock alteration. Mineralium Deposita. 35, 364–376.

Cooper, G. R., 2003, Feature detection using sun shading: Computers & Geosciences, 29 (8), 941-948.

Cooper, G. R., and Cowan, D. R., 2004, Filtering using variable order vertical derivatives: Computers & Geosciences, 30 (5), 455-459.

Cooper, G. R., and Cowan, D. R., 2006, Enhancing potential field data using filters based on the local phase: Computers & Geosciences, 32, (10), 1585-1591.

Cooper, G. R., and Cowan, D. R., 2008, Edge enhancement of potential-field data using normalized statistics: Geophysics, 73 (3), p. H1-H4.

Cordell, L., and Grauch, V., 1985, Mapping basement magnetization zones from aeromagnetic data in the San Juan basin, New Mexico. In: The Utility of Regional Gravity and Magnetic Anomaly Maps: Society of Exploration Geophysics, 181-197.

Corner, B., 1983, An interpretation of the aeromagnetic data covering the western portion of the Damara Orogenic Belt, with Special Reference to the Occurrence of Uraniferous Granite. PhD thesis, University of the Witwatersrand.

Corner, B., 2008, Crustal Framework of Namibia Derived From An Intergrated Interpretation of Geophysical and Geological Data. In: Miller, R. M., (Ed.), The Geology of Namibia, Volume 1: Windhoek, Namibia, Geological Survey of Namibia, 2-1 - 2-19.

Coward, M., 1981, The junction between Pan African mobile belts in Namibia: its structural history: Tectonophysics, 76 (1-2), 59-73.

Crawford, B. L., Betts, P. G., and Aillères, L., 2010, An aeromagnetic approach to revealing buried basement structures and their role in the Proterozoic evolution of the Wernecke Inlier, Yukon Territory, Canada: Tectonophysics, 490 (1), 28-46.

Dampare, S., Shibata, T., Asiedu, D., Osae, S., and Banoeng-Yakubo, B., 2008, Geochemistry of Paleoproterozoic metavolcanic rocks from the southern Ashanti volcanic belt, Ghana: Petrogenetic and tectonic setting implications: Precambrian Research, 162 (3), 403-423.

Deane, J., 1995, The structural evolution of the Kombat deposits, Otavi Mountainland, Namibia: Communications of the Geological Survey of Namibia, 10, 99-107.

Dechow, E., and Jensen, M., 1965, Sulfur isotopes of some central African sulfide deposits: Economic Geology, 60 (5), 894-941.

Dentith, M., and Mudge, S. T., 2014, Geophysics for the mineral exploration geoscientist, New York, Cambridge University Press.

Eberle, D., Andritzky, G., and Wackerle, R., 1995, The new magnetic data set of Namibia: its contributions to the understanding of crustal evolution and regional distribution of mineralization: Communications of the Geological Survey of Namibia, 10, 141-150.

Emslie, D., 1979, The Mineralogy and Geochemistry of the Copper, Lead and Zinc Sulphides of the Otavi Mountainland, South West Africa: PhD thesis, University of the Orange Free State.

Floyd, P., and Winchester, J., 1975, Magma type and tectonic setting discrimination using immobile elements: Earth and Planetary science letters, 27 (2), 211-218.

Floyd, P., Winchester, J., and Park, R., 1989, Geochemistry and tectonic setting of Lewisian clastic metasediments from the Early Proterozoic Loch Maree Group of Gairloch, NW Scotland: Precambrian Research, 45 (1), 203-214.

Foster, D. A., Goscombe, B. D., Newstead, B., Mapani, B., Mueller, P. A., Gregory, L. C., and Muvangua, E., 2015, U–Pb age and Lu–Hf isotopic data of detrital zircons from the Neoproterozoic Damara Sequence: implications for Congo and Kalahari before Gondwana: Gondwana Research, 28 (1),179-190.

Franklin, J., Gibson, H., Jonasson, I., and Galley, A., 2005, Volcanogenic Massive Sulfide Deposits: Society of Economic Geologists, 100, 523-560.

Frimmel, H., Deane, J., and Chadwick, P., 1996, Pan-African tectonism and the genesis of base metal sulfide deposits in the northern foreland of the Damara Orogen, Namibia: Society of Economic Geologists, Special Publication, 4, 204-217.

Frimmel, H. E., Jonasson, I. R., and Mubita, P., 2004, An Eburnean base metal source for sediment-hosted zinc-lead deposits in Neoproterozoic units of Namibia: Lead isotopic and geochemical evidence: Mineralium deposita, 39 (3), 328-343.

Frimmel, H.E., and Miller, R. McG., 2009. Mineral deposits. Neoproterozoic to Early Palaeozoic evolution of Southwestern Africa. In: Gaucher, C., Sial, A.N., Halverson, G.P., Frimmel, H.E. (Eds.): Neoproterozoic-Cambrian tectonics, global change and evolution: a focus on southwestern Gondwana. Developments in Precambrian Geology, 16, Elsevier, 227–229.

Gaafar, I., 2015, Integration of geophysical and geological data for delimitation of mineralized zones in Um Naggat area, Central Eastern Desert, Egypt: NRIAG Journal of Astronomy and Geophysics, 4 (1), 86-99.

Galley, A.G., Hannington, M., and Jonasson, I., 2007. Volcanogenic massive sulphide deposits. In: Goodfellow WD (Ed.) Mineral Deposits of Canada: A Synthesis of Major Deposit-types, District Metallogeny, the Evolution of Geological Provinces, and Exploration Methods, Special Publication, 5, 141–161.

Geological Survey of Namibia, 2008, High Resolution Aiborne Geophysics: Otavi Survey. Unpublished Report, 12.

Germs, G. J. B., Miller, R. McG., Frimmel, H. E. and Gaucher, C. 2009. Syn- to late-orogenic sedimentary basins of southwestern Africa. Neoproterozoic to Early Palaeozoic evolution of Southwestern Africa. In: Gaucher, C., Sial, A. N., Halverson, G. P. & Frimmel, H. E. (eds) Neoproterozoic–Cambrian Tectonics, Global Change and Evolution: A Focus on Southwestern Gondwana. Developments in Precambrian Geology, 16, 183– 203.

Golden Deeps Limited, 2012, Annual Report 2012. Available at: http://goldendeeps.com (Accessed: 9 February 2015).

Golden Deeps Limited, 2013, Annual Report 2013. Available at: http://goldendeeps.com (Accessed: 9 February 2015).

Gray, D., Foster, D., Meert, J., Goscombe, B., Armstrong, R., Trouw, R., and Passchier, C., 2008. A Damara orogen perspective on the assembly of southwestern Gondwana. In: Pankhurst, R., Trouw, R., Brito Neves, B., De Wit, M. (Eds.), West Gondwana Pre-Cenozoic Correlations Across the South Atlantic Region, Geological Society, London, Special Publications, 294 (1), 257–278.

Grobler, N.J., 1961, The geology of the western Otavi Mountainland, South West Africa. MSc thesis, University of the Orange Free State.

Haack, U., 1983, Reconstruction of the cooling history of the Damara Orogen by correlation of radiometric ages with geography and altitude, Intracontinental fold belts, Springer, 873-884.

Halverson, G. P., Dudás, F. Ö., Maloof, A. C., and Bowring, S. A., 2007, Evolution of the 87Sr/86Sr composition of Neoproterozoic seawater: Palaeogeography, Palaeoclimatology, Palaeoecology, 256 (3-4), 103-129.

Halverson, G. P., Hoffman, P. F., Schrag, D. P., Maloof, A. C., and Rice, A. H. N., 2005, Toward a Neoproterozoic composite carbon-isotope record: Geological Society of America Bulletin, 117 (9-10), 1181-1207.

Hansen, R., 1993, Interpretive gridding by anisotropic kriging: Geophysics, 58 (10), 1491-1497.

Hedberg, R. M., 1979, Stratigraphy of the Ovamboland Basin, South West Africa. Bulletin, 24, Precambrian Research Unit, University of Cape Town.

Hinze, W. J., and Kane, M. F., 1985, The utility of regional gravity and magnetic anomaly maps, Society of Exploration Geophysicists, 454.

Hoffman, P. F., and Li, Z.-X., 2009, A palaeogeographic context for Neoproterozoic glaciation: Palaeogeography, Palaeoclimatology, Palaeoecology, 277 (3), 158-172.

Hoffmann, K.-H., Condon, D., Bowring, S., and Crowley, J., 2004, U-Pb zircon date from the Neoproterozoic Ghaub Formation, Namibia: constraints on Marinoan glaciation: Geology, v. 32 (9) ,817-820.

Hoffmann, K., 1983, Lithostratigraphy and facies of the Swakop Group of the southern Damara Belt, SWA/Namibia: Evolution of the Damara Orogen of South West Africa/Namibia: Geological Society of South Africa, Special Publication, 11, 43-63.

Hoffmann, K., and Prave, A., 1996, A preliminary note on a revised subdivision and regional correlation of the Otavi Group based on glaciogenic diamictites and associated cap dolostones: Communications of the Geological Survey of Namibia, 11, 77-82.

Hughes, M. J., 1987, The Tsumeb ore body, Namibia, and related dolostone-hosted base metal ore deposits of Central Africa. PhD thesis, University of the Witwatersrand.

Hutchins, D., Milner, S., and Korkiakoski, E., 1997, Regional airborne geophysics and geochemistry: a Namibian perspective: in AG Gubins, (Ed), in: Proceedings of Exploration 1997, 97, 779-792.

Hutchins, D., and Wackerle, R., 2007, The High Resolution Airborne Geophysical Survey Programme of Namibia: A Success Story in Promoting Mineral Exploration, in: Proceedings of the Fifth Decennial International Conference on Mineral Exploration, Windhoek, Geological Survey of Namibia, 7, 879-883.

Innes, J., and Chaplin, R., 1986, Ore bodies of the Kombat Mine, South West Africa/Namibia. In: Anhaeusser, C.R., and Maske, S. (Eds.), Mineral Deposits of Southern Africa. Geological Society of South Africa, 2, 1789-1805.

Isles, D. J., and Rankin, L. R., 2013, Geological interpretation of aeromagnetic data. Perth, Society of Exploration Geophysicists.

Jaques, A., Wellman, P., Whitaker, A., and Wyborn, D., 1997, High-resolution geophysics in modern geological mapping: AGSO Journal of Australian Geology and Geophysics, 17 (2), 159-173.

Kamona, A.F., Leveque, J., Friedrich, G., and Haack, U., 1999, Lead isotopesof the carbonate-hosted Kabwe, Tsumeb, and Kipushi Pb-Zn-Cu sulphidedeposits in relation to Pan-African orogenesis in the Damaran-Lufilian foldbelt of central Africa: Mineralium Deposita, 34, 273–283

Kamona, A. F., and Günzel, A., 2007, Stratigraphy and base metal mineralization in the Otavi Mountain Land, Northern Namibia—a review and regional interpretation: Gondwana Research, v. 11, 396-413.

Kamona, F., 2011. Carbonate-hosted base metal deposits. In: Earth and Environmental Sciences Dar, I.A. and Dar, M.A., (Eds.), Intech Publishing, 1-31.

Kasch, K., 1983, Continental collision, suture progradation and thermal relaxation: a plate tectonic model for the Damara orogen in central Namibia: Evolution of the Damara Orogen of South West Africa/Namibia: Geological Society of South Africa, Special Publication, v. 11, p. 423-429.

Kennedy, L. A., and Logan, J. M., 1998, Microstructures of cataclasites in a limestone-on-shale thrust fault: implications for low-temperature recrystallization of calcite: Tectonophysics, 295, 167-186.

Kennedy, M. J., Runnegar, B., Prave, A. R., Hoffmann, K.-H., and Arthur, M. A., 1998, Two or four Neoproterozoic glaciations?: Geology, 26 (12), 1059-1063.

Killick, A., 2000, The Matchless Belt and associated sulphide mineral deposits, Damara Orogen, Namibia. Communications of the Geological Survey of Namibia, 12, 73-80.

Kröner, A., and Clauer, N., 1979, Isotopic dating of low-grade metamorphic shales in northern Namibia (South West Africa) and implications for the orogenic evolution of the Pan-African Damara-Belt: Precambrian Research, 10 (1-2), 59-72.

Lanza, R., and Meloni, A., 2006, The Earth's magnetism: an introduction for geologists. Berlin, Springer.

Laukamp, C., 2006, Structural and fluid system evolution in the Otavi Mountainland (Namibia) and its significance for the genesis of sulphide and nonsulphide mineralisation. PhD thesis, Ruprecht-Karls-Universität.

Lehmann, J., Master, S., Rankin, W., Milani, L., Kinnaird, J. A., Naydenov, K. V., Saalmann, K., and Kumar, M., 2015, Regional aeromagnetic and stratigraphic correlations of the Kalahari Copperbelt in Namibia and Botswana: Ore Geology Reviews, 71, 169-190.

Lehmann, J., Saalmann, K., Naydenov, K. V., Milani, L., Belyanin, G. A., Zwingmann, H., Charlesworth, G., and Kinnaird, J. A., 2016, Structural and geochronological constraints on the Pan-African tectonic evolution of the northern Damara Belt, Namibia: Tectonics, 35 (1), 103-135.

Li, Y., and Oldenburg, D. W., 1998, Separation of regional and residual magnetic field data: Geophysics, 63 (2), 431-439.

Liedtke, G., 1976, The Geology of an Area South of the Otavi Valley. Unpulished company report, Tsumeb Corporation Limited.

Lombaard, A., Günzel, A., Innes, J., and Krüger, T., 1986, The Tsumeb lead-copper-zinc-silver deposit, South West Africa/Namibia. In: Anhaeusser, C.R., and Maske, S., (Eds), Mineral Deposits of Southern Africa, Geological Society of South Africa, 2, 1761-1787.

Longridge, L., Kinnaird, J. A., Gibson, R. L., and Armstrong, R., 2014, Amphibolites of the Central Zone: new SHRIMP U-Pb ages and implications for the evolution of the Damara Orogen, Namibia: South African Journal of Geology, 117 (1), 67-86.

Martin, H., and Porada, H., 1977, The intracratonic branch of the Damara Orogen in South West Africa I. Discussion of geodynamic models: Precambrian Research, 5 (4), 311-338.

Melcher, F., 2003, The Otavi Mountain Land in Namibia: Tsumeb, Germa-nium and snowball earth: Mitteilungen Österreichische MineralogischeGesellschaft, 148, 413–435.

Melcher, F., Oberthür, T., Rammlmair, D., 2002. The carbonate-hosted, Ge- and Ag-rich Khusib Springs Cu–Zn–Pb sulphide deposit, Namibia: ore geochemistry and mineralogical variation. 11th IAGOD Quadrennial Symposium and Geocongress, Windhoek, Namibia. Geological Survey of Namibia.

Melcher, F., Oberthür, T., Vetter, U., Gross, C., Vollbrecht, A., Brauns, M.,and Haack, U., 2003, Germanium in carbonate-hosted Cu-Pb-Zn mineral-ization in the Otavi Mountain Land, Namibia. In: Eliopoulos, D., et al., (Eds.), Mineral Exploration and Sustainable Development: Proceedings 7thBien-nial SGA Meeting, Athens, Balkema, 701–704

Milani, L., Kinnaird, J. A., Lehmann, J., Naydenov, K. V., Saalmann, K., Frei, D., and Gerdes, A., 2015, Role of crustal contribution in the early stage of the Damara Orogen, Namibia: New

constraints from combined U–Pb and Lu–Hf isotopes from the Goas Magmatic Complex: Gondwana Research, 28 (3), 961-986.

Miller, H. G., and Singh, V., 1994, Potential field tilt—a new concept for location of potential field sources: Journal of Applied Geophysics, 32 (2-3), 213-217.

Miller, R. McG., 1983, The Pan-African Damara Orogen of South West Africa/Namibia. In: Miller, R. McG. (Ed.), Evolution of the Damara Orogen of South West Africa/Namibia, Special Publication, Geological Society of South Africa, 11, 431-515.

Miller, R. McG., 1997, The Owambo basin of northern Namibia: Sedimentary Basins of the World, 3, 237-268.

Miller, R. McG., 2008, Neoproterozoic and Early Palaeozoic Rocks of the Damara Orogen, *in* Miller, R. McG. (Ed), The Geology of Namibia, Volume 2: Windhoek, Geological Survey of Namibia, 13-11 - 13-403.

Milligan, P., and Gunn, P., 1997, Enhancement and presentation of airborne geophysical data: AGSO Journal of Australian Geology and Geophysics, 17 (2), 63-75.

Misiewicz, J. E., 1988, The geology and metallogeny of the Otavi mountain land, Damara orogen, SWA/Namibia, with particular reference to the Berg Aukas Zn-Pb-V deposit: a model of ore genesis. MSc thesis, Rhodes University.

Mogren, S., Fairhead, J. D., and Jassim, S. Z., 2009, Microlevelling of Aeromagnetic Data using the Naudy-Fuller Space Domain Filter. In Proceedings of the 11th International Congress of the Brazilian Geophysical Society & EXPOGEF 2009, Salvador, Bahia, Brazil, Society of Exploration Geophysicists and Brazilian Geophysical Society, 746-749.

Nabighian, M. N., Grauch, V., Hansen, R., LaFehr, T., Li, Y., Peirce, J., Phillips, J., and Ruder, M., 2005, The historical development of the magnetic method in exploration: Geophysics, 70 (6), 33ND-61ND.

Nagel, R., 1999, Eine Milliarde Jahre geologischer Entwicklung am NW-Rand des Kalahari Kratons, PhD thesis, University of Gottingen, Germany.

Nangolo, N. N. N. N., 2014, The Application of Hyperspectral Imaging for Mineralization in the Kombat South Area, BSc. Honours thesis, University of Namibia.

Nascimento, D., Ribeiro, A., Trouw, R., Schmitt, R., and Passchier, C., 2016, Stratigraphy of the Neoproterozoic Damara Sequence in northwest Namibia: Slope to basin sub-marine mass-transport deposits and olistolith fields: Precambrian Research, 278, 108-125.

Neubauer, W., Melichar, P., and Eder-Hinterleitner, A., 1996, Collection, visualization and simulation of magnetic prospection data, Analecta Praehistorica Leidensia 28, 121-129.

Ohmoto, H., 1986, Stable isotope geochemistry of ore deposits: Reviews in mineralogy, 16, 491-560.

Paradis, S., Hannigan, P., and Dewing, K., 2007, Mississippi Valley-type lead-zinc deposits: Mineral deposits of Canada: A synthesis of major deposit-types, district metallogeny, the evolution of geological provinces, and exploration methods: Geological Association of Canada, Mineral Deposits Division, Special Publication, 5, 185-203.

Passchier, C. W., and Trow, A. J. R., 2005, Microtectonics, Berlin, Springer.

Pearce, J. A., 1996, A user's guide to basalt discrimination diagrams: Trace element geochemistry of volcanic rocks: applications for massive sulphide exploration. Geological Association of Canada, Short Course Notes, 12 (79), 113.

Pearce, J. A., and Cann, J., 1973, Tectonic setting of basic volcanic rocks determined using trace element analyses: Earth and planetary science letters, 19 (2), 290-300.

Pearce, J. A., and Norry, M. J., 1979, Petrogenetic implications of Ti, Zr, Y, and Nb variations in volcanic rocks: Contributions to mineralogy and petrology, 69 (1), 33-47.

Petzel, V. W. F., 1991, Final report and assessment of the mineral potential, Neuwerk Grant Area M46/3/1654. Unpublished company report, Gold Fields Namibia Limited.

Pilkington, M., and Keating, P., 2004, Contact mapping from gridded magnetic data–a comparison of techniques: Exploration Geophysics, 35 (4), 306-311.

Pirajno, F., and Joubert, B., 1993, An overview of carbonate-hosted mineral deposits in the Otavi Mountain Land, Namibia: implications for ore genesis: Journal of African Earth Sciences, 16 (3), 265-272.

Porada, H., 1985, Stratigraphy and facies in the Upper Proterozoic Damara Orogen, Namibia, based on a geodynamic model: Precambrian Research, 29 (1), 235-264.

Rankin, W., 2014, Cross-border correlation of the Damara Belt in Namibia and equivalent lithologies in northwestern Botswana from potential field data and magnetotelluric interpretations. MSc thesis, University of the Witwatersrand.

Rapela, C. W., Fanning, C. M., Casquet, C., Pankhurst, R. J., Spalletti, L., Poiré, D., and Baldo, E. G., 2011, The Rio de la Plata craton and the adjoining Pan-African/brasiliano terranes: their origins and incorporation into south-west Gondwana: Gondwana Research, 20 (4), 673-690.

Reeves C (2005) Aeromagnetic surveys. Principles, practice and interpretation. Geosoft E-publication.www.geosoft.com/media/uploads/resources/technicalpapers/Aeromagnetic_Survey_Reeves.pdf.

Robinson, B. W., and Kusakabe, M., 1975, Quantitative preparation of sulfur dioxide, for sulfur-34/sulfur-32 analyses, from sulfides by combustion with cuprous oxide: Analytical Chemistry, 47 (7), 1179-1181.

Roest, W. R., Verhoef, J., and Pilkington, M., 1992, Magnetic interpretation using the 3-D analytic signal: Geophysics, 57 (1), 116-125.

Rollinson, H. R., 1993, Using Geochemical Data: Evuation, Presentation, Interpretation. Harlow, England, Pearson Education Limited.

Sawlowicz, Z., 1989, On the origin of copper mineralization in the Kupferschiefer: a suIphur isotope study: Terra Nova, 1 (4), 339-343.

Schaum, H. H., 1960, The Geology of the Askevold Range (Eastern Part). BSc Honours thesis, University of Cape Town.

Senyah, G. A., Dampare, S. B., and Asiedu, D. K., 2015, Geochemistry and tectonic setting of the Paleoproterozoic metavolcanic rocks from the Chirano Gold District, Sefwi belt, Ghana: Journal of African Earth Sciences, 122, 32-46.

Sharp, Z., 2007, Principles of stable isotope geochemistry, New York, Pearson Education Inc.

Shervais, J. W., 1982, Ti-V plots and the petrogenesis of modern and ophiolitic lavas: Earth and planetary science letters, 59 (1), 101-118.

Smit, J. M. v. d. M., 1959, The geology of the southern part of the Otavi Mountain Land, S.W.A. MSc thesis, University of Pretoria.

Söhnge, P., 1957, Revision of the geology of the Otavi Mountainland, South West Africa (with 1958 amended stratigraphic table). Unpublished report, Tsumeb Corporation Ltd, Tsumeb, Namibia.

Stewart, J. R., and Betts, P. G., 2010, Implications for Proterozoic plate margin evolution from geophysical analysis and crustal-scale modeling within the western Gawler Craton, Australia: Tectonophysics, 483 (1), 151-177.

Stewart, J. R., Betts, P. G., Collins, A. S., and Schaefer, B. F., 2009, Multi-scale analysis of Proterozoic shear zones: an integrated structural and geophysical study: Journal of Structural Geology, 31 (10), 1238-1254.

Sun, S. S., and McDonough, W.S., 1989, Chemical and isotopic systematics of oceanic basalts: implications for mantle composition and processes: Geological Society, London, Special Publications, 42 (1), 313-345.

Taylor, S. R., and McLennan, S. M., 1985, The continental crust: its composition and evolution, London, Blackwell.

Vacquier, V., Steenland, N., Henderson, R., and Zietz, I., 1951, Interpretation of aeromagnetic maps: Geological Society of America, Memoir 47.

Verduzco, B., Fairhead, J. D., Green, C. M., and MacKenzie, C., 2004, New insights into magnetic derivatives for structural mapping: The Leading Edge, 23 (2), 116-119.

White, W. M., 2013, Geochemistry, West Suussex, Wiley-Blackwell.

Williams, P., Barton, M., Johnson, D., Fontbote, L., Haller, A., Mark, G., Oliver, N., and Marschik, R., 2005, Iron Oxide Copper-Gold Deposits: Geology, Space-Time Distribution, and Possible Modes of Origin: Society of Economic Geologists, 100th Anniversary, 371-405.

Winchester, J., and Floyd, P., 1977, Geochemical discrimination of different magma series and their differentiation products using immobile elements: Chemical geology, 20, 325-343.

Wood, D. A., 1980, The application of a ThHfTa diagram to problems of tectonomagmatic classification and to establishing the nature of crustal contamination of basaltic lavas of the British Tertiary Volcanic Province: Earth and planetary science letters, 50 (1), 11-30.

Appendices

Appendix A

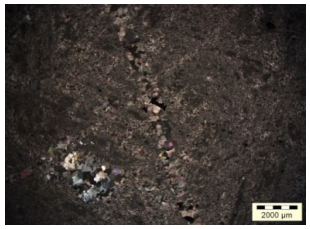
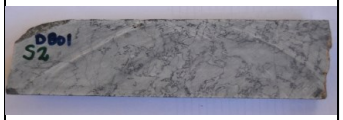
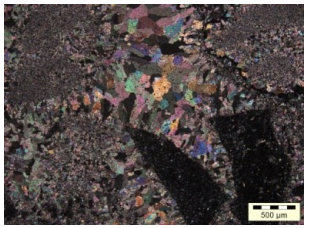
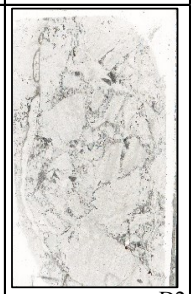
Petrographic Descriptions of the Samples.

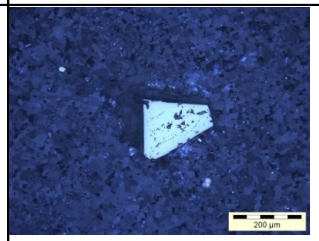
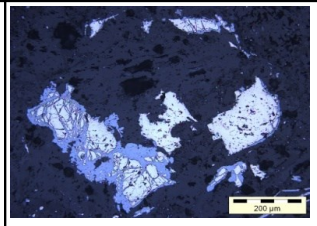
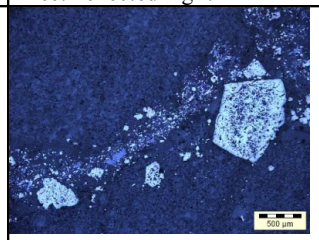
Table A-1. List of the rock samples collected from outcrops during field geological mapping.

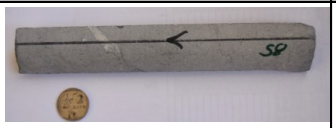
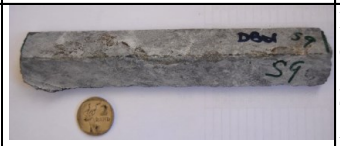
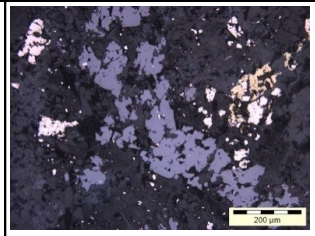
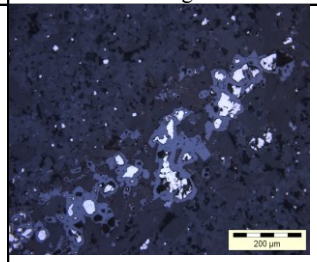
Sample ID	Easting (m)	Northing (m)	Lithology Name
DB1a	758322	7814905	Pyritic Dolomite
DB1b	758343	7814977	Chlorite Schist
DB1c	758340	7815086	Felsic Volcanic Breccia
DB2b	758497	7814882	Pyritic Dolomite
DB2a1	758482	7814805	Dolomite Breccia
DB2a2	758482	7814805	Dolomite Breccia
DB2c	758375	7814965	Banded Limestone
DB2d	758525	7814852	Silicified Dolomite
DB2e	758530	7814816	Silicified Dolomite
DB2f	758575	7814890	Agglomerate
DB3a	759641	7814738	Grey Limestone
DB3b	759659	7814688	Silicified Dolomite
DB3c	759679	7814622	Silicified Dolomite
DB3d	759679	7814622	Grey Limestone
DB3e	759746	7814543	Grey Limestone
DB3f	759747	7814524	Grey Limestone
DB3g	759747	7814524	Grey Limestone
DB3h	759702	7814347	Silicified Dolomite
DB3i	759709	7814208	Diamictite
DB3j	759628	7814158	Silicified Dolomite
DB3k	759611	7814222	Banded Limestone
DB4a	759858	7814881	Grey Limestone
DB4b	759857	7814806	Grey Limestone
DB4c	759899	7814741	Silicified Dolomite
DB4d	759961	7814638	Grey Limestone
DB4d1	759955	7814601	Grey Limestone
DB4e	759938	7814574	Grey Limestone
DB4f	759926	7814501	Grey Limestone

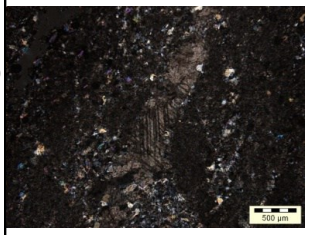
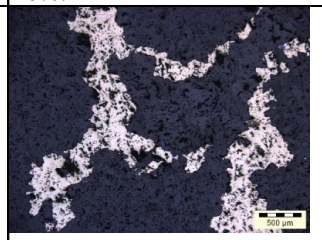
DB4i	759898	7814251	Pyritic Dolomite
DB5b1	760035	7814500	Silicified Dolomite
DB5b2	760035	7814500	Dolomite Breccia
DB6b	758666	7814811	Diamictite
DB6ba	758659	7814824	Diamictite
DB7a	758268	7814999	Chlorite Schist
DB8a	759552	7814663	Chlorite Schist
DB9a	759028	7814191	Diamictite
DB10a	759546	7814794	Mafic Metavolcanic
DB10b	759548	7814784	Mafic Metavolcanic
DB10c	759558	7814717	Mafic Metavolcanic
DB10d	759554	7814668	Mafic Metavolcanic
DB10e	758810	7814791	Banded Iron Formation
DB10f	758810	7814791	Silicified Dolomite
DB10g	758810	7814791	Diamictite
DB10h	758748	7814851	Chlorite Schist
DB10i	758769	7814818	Grey Limestone

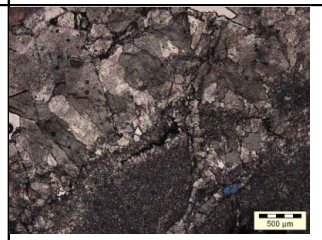
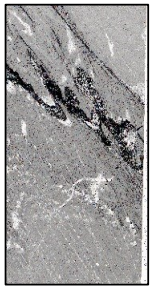
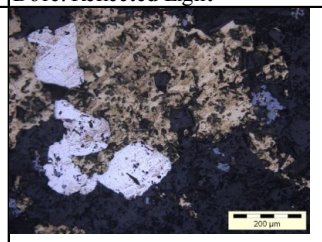
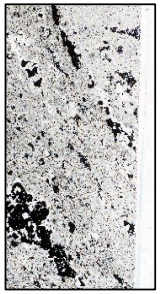
Table A-2. Description of the drill core samples from DBDD0001

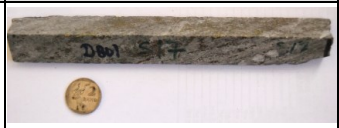
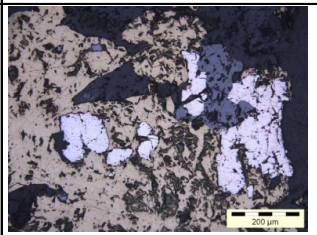
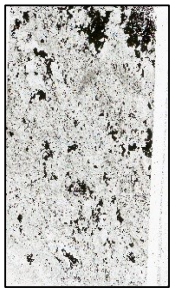
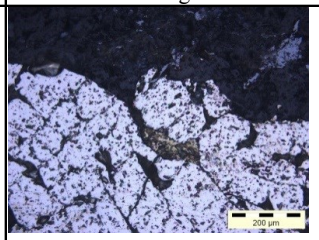
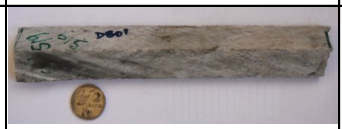
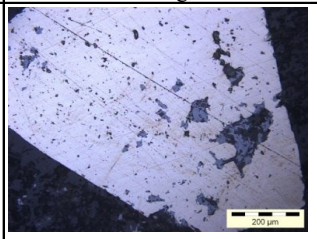
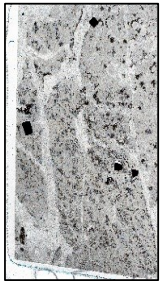
From (m)	To (m)	Spl No.	Lithology	Lithological Description	Sample Picture	Microscopic Description (Texture and Mineralogy)	Thin Section Photomicrograph	Scanned Thin Section
3.75	3.95	DB1S1	Silicified Dolomite	Silicified dolomite with moderate thin quartz and calcite veins. Rare disseminations of pyrite are present throughout the unit.		Fine-grained (0.070 mm to 0.583 mm) dolomite and calcite. Fine-to medium-graned quartz (0.097 mm to 0.292 mm). The unit is dominated by cross-cutting quartz-calcite veins. Dolomite and Calcite (70%); Quartz (28%); Pyrite 2%.	 D1a: XPL	 D1
4.30	4.50	DB1S2	Silicified Dolomite	Silicified dolomite with moderate thin quartz and calcite veins.				
13.09	13.29	DB1S3	Dolomite Breccia	Dolomite breccia with clasts size ranging from 0.5 cm to 4 cm. The unit has frequent quartz-calcite veins and stromatolites.				
15.84	16.04	DB1S4	Dolomite Breccia	Dolomite breccia with fractures filled with calcite linings. The unit records minor amounts of pyrite.		Brecciated dolomie with clay particles and a mosaic texture defined by the carbonate minerals and quartz. Dolomite and Calcite (60%); Quartz (30%); Clay (10%).	 D2a: XPL	 D2

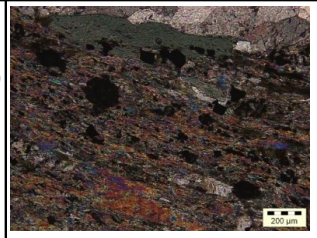
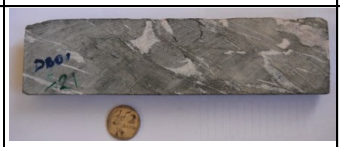
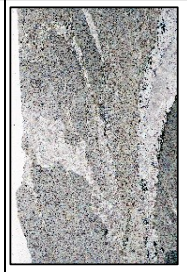
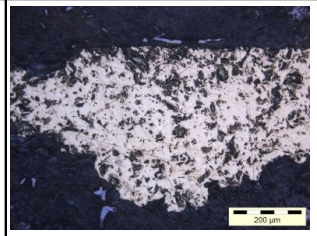
From (m)	To (m)	Spl No.	Lithology	Lithological Description	Sample Picture	Microscopic Description (Texture and Mineralogy)	Thin Section Photomicrograph	Scanned Thin Section
29.80	30.00	DB1S5	Silicified Dolomite	Silicified dolomite with various calcite veins and fractures filled with calcite. The unit consists of minor amounts of pyrite		Fine-grained dolomite and calcite (0.058 mm to 0.292 mm); Fine -grained (~0.088 mm) quartz. Dolomite and Calcite (60%); Quartz (35%); Pyrite (~5%).	 D45c: Reflected Light	 D45
46.80	47.00	DB1S6	Cu Sulphides	Frequent chalcopyrite and subordinate pyrite hosted in quartz and quartz-calcite veins.		Fine-grained (<0.03 mm) dolomite and calcite. Fine grained quartz (~0.066 mm). Dolomite and Calcite (55%); Quartz (20%); Chalcopyrite (10%), Pyrite (5%), Sphalerite (10%)	 D46c: Reflected Light	 D46
54.78	54.98	DB1S7	Silicified Dolomite	Silicified dolomite with frequent deformed chalcopyrite and pyrite veins as well as quartz-caclite veins.		Fine-grained (<0.03 mm) dolomite and calcite. Fine grained quartz (~0.066 mm). Dolomite and Calcite (~75%); Quartz (15%); Chalcopyrite (6%), Pyrite (2%), Sphalerite (2%)	 D48d: Reflected Light	 D48

From (m)	To (m)	Spl No.	Lithology	Lithological Description	Sample Picture	Microscopic Description (Texture and Mineralogy)	Thin Section Photomicrograph	Scanned Thin Section
57.55	57.75	DB1S8	Silicified Dolomite	Silicified dolomite with patches of fresh and oxidized, brown pyrite grains.				
60.70	60.88	DB1S9	Dolomite breccia	Dolomite breccia with disseminations of pyrite and vei type chalcopyrite and pyrite mineralization.		Fine-grained (<0.055 mm) dolomite and calcite. Fine grained quartz (~0.034 mm). This part of the dolomite is more carbonatized than it is silicified. Dolomite and Calcite (~76%); Quartz (~7%); Chalcopyrite (8%), Pyrite (5%), Sphalerite (<4%).	 D50c: Reflected Light	 D50
82.20	82.40	DB1S10	Silicified Dolomite	Silicified dolomite with chalcopyrite cross-cut by later chalcopyrite veinlets. The quartz-calcite veins are ubiquitous.		Coarse-grained (<0.283 mm) dolomite and calcite. Medium-grained quartz (~0.123 mm). Sphalerite is dominant in this area and occurs as replacement of pyrite. Dolomite and Calcite (~50%), Quartz (~25%); Chalcopyrite (10 %) Pyrite (5%), Sphalerite (10%).	 D55e: Reflecetd Light	 D55

From (m)	To (m)	Spl No.	Lithology	Lithological Description	Sample Picture	Microscopic Description (Texture and Mineralogy)	Thin Section Photomicrograph	Scanned Thin Section
82.59	82.67	DB1S11	Silicified Dolomite	Silicified dolomite with fine-grained quartz in the quartz-calcite vein and minor distinct sericite forming a cleavage.		Fine-to coarse-grained (0.088 to 1.167 mm) dolomite and calcite, fine-grained (0.058 mm) quartz and very fine-grained sericite (<0.050 mm). Dolomite and Calcite (60%); Quartz (25%), Sericite (~10%); Pyrite (5%)	 D57c: XPL	 D57
91.08	91.28	DB1S12	Silicified Dolomite	Silicified dolomite with greenish chloritized and sericitized thin (<cm thick) layers. Chalcopyrite and rare pyrite grains occur as disseminations		Fine-grained (0.076 mm) dolomite and calcite, fine-grained (0.04 mm) quartz. This unit is characterized by quart-calcite veins and clacopyrite and pyrite veinlets. Dolomite and Calcite= 65%; Quartz (25%), Chalcopyrite (5%), Pyrite (3%), Sphalerite (~2%).	 D59a: Reflected Light	 D59
95.70	95.90	DB1S13	Dolomite Breccia	Dolomite breccia with rare fine grained disseminations of pyrite.				

From (m)	To (m)	Spl No.	Lithology	Lithological Description	Sample Picture	Microscopic Description (Texture and Mineralogy)	Thin Section Photomicrograph	Scanned Thin Section
108.20	108.40	DB1S14	Silicified Dolomite	Silicified dolomite with frequent stromatolites and ubiquitous thick calcite veins.		Coarse grained (0.276 mm) dolomite and calcite, fine-grained (0.022 mm) quartz. Dolomite and Calcite= 70%; Quartz (30%).	 D60b: XPL	 D60
109.67	109.87	DB1S15	Silicified Dolomite	Silicified dolomite with frequent stromatolites and ubiquitous thick calcite veins. Calcite vugs occur within the fractures.		Coarse grained (0.276 mm) dolomite and calcite, fine-grained (0.022 mm) quartz. This unit has deformed chalcopyrite and pyrite veins and minor spahlerite. Dolomite and Calcite= 55%; Quartz (30%); Chalcopyrite (8%), Pyrite (5%) and Sphalerite (~2%).	 D61e: Reflected Light	 D61
136.61	136.81	DB1S16	Cu Sulphides	Chalcopyrite and subordinate pyrite hosted in quartz and quartz-calcite veins.		Coarse grained (0.12 mm) dolomite and calcite, Coarse-grained (0.212 mm) quartz. Chalcopyrite replacement of pyrite is dominant. Dolomite and Calcite= 55%; Quartz (25%); Chalcopyrite 10%), Pyrite (7%), Sphalerite (~3%).	 D63e: Reflected Light	 D63

From (m)	To (m)	Spl No.	Lithology	Lithological Description	Sample Picture	Microscopic Description (Texture and Mineralogy)	Thin Section Photomicrograph	Scanned Thin Section
137.22	137.42	DB1S17	Cu Sulphides	Chalcopyrite and subordinate pyrite hosted in quartz and quartz-calcite veins.		Coarse-grained (0.12 mm) dolomite and calcite, Coarse-grained (0.212 mm) quartz. Dolomite and Calcite= 55%; Quartz (25%); Chalcopyrite 10%), Pyrite (8%), Sphalerite (~2%).	 D69a: Reflected Light	 D69
137.73	137.93	DB1S18	Agglomerate	Deformed agglomerate rich in chlorite with weakly developed foliation, sub-rounded pebbles and patches of pyrite cubes.		Fine-grained (0.12 mm) calcite; Fine grained (0.012 mm) quartz; Fine grained (<0.04 mm) sericite and biotite; Fine-grained (<0.08 mm) chlorite. In some places chaclopyrite occurs as infills of the fractures in pyrite. Calcite (25%); Quartz (10%), Chlorite (20%), Biotite (20%), Sericite (10%); Chalcopyrite (5%), Pyrite (10%)	 D75c: Reflected Light	 D75
138.71	138.91	DB1S19	Mafic Metavolcanic	Greenish, fine grained layer of the metavolcanic enriched in micas and chlorite.		Fine-grained (0.12 mm) calcite; Fine grained (0.012 mm) quartz; Fine grained (<0.04 mm) sericite and biotite; Fine-grained (<0.08 mm) chlorite. Calcite (15%); Quartz (10%), Chlorite (25%), Biotite (15%), Sericite (15%); Chalcopyrite (5%), Pyrite (10%) and Sphalerite (5%).	 D79c: Reflected Light	 D79

From (m)	To (m)	Spl No.	Lithology	Lithological Description	Sample Picture	Microscopic Description (Texture and Mineralogy)	Thin Section Photomicrograph	Scanned Thin Section
139.10	139.30	DB1S20	Mafic Metavolcanic	Greenish, fine grained layer of the metavolcanic enriched in micas and chlorite.		Fine-grained (0.12 mm) calcite; Fine grained (0.012 mm) quartz; Fine grained (<0.09mm) sericite and biotite; Fine-grained (<0.05 mm) chlorite. Chlorite occurs as replacements of sericite and biotite in places. Calcite (20%); Quartz (10%), Chlorite (25%), Biotite (20%), Sericite (25%).	 D81a:XPL	 D81
145.00	145.20	DB1S21	Agglomerate	Deformed agglomerate rich in chlorite with weakly developed foliation, sub-rounded pebbles and patches of pyrite cubes.		Fine-grained (0.127 mm) calcite; Fine grained (0.012 mm) quartz; Fine grained (<0.0554 mm) sericite and biotite; Fine-grained (<0.098 mm) chlorite. The quartz-calcite veins have mica-fish morphoology which shows evidence of shearing. Calcite (35%); Quartz (10%), Chlorite (15%), Biotite (20%) and Sericite (20%).	 D8a: XPL	 D81
157.50	157.70	DB1S22	Cu Sulphides	Chalcopyrite and subordinate pyrite hosted in quartz and quartz-calcite veins.		Fine grained (<0.023 mm) sericite and biotite; and fine-grained (<0.016 mm) chlorite. Coarse-grained (0.114 mm) calcite. Coarse-grained (0.221 mm) quartz. Biotite (10%), Chlorite (20%), Sericite (15%), Calcite (20%), Quartz (15%); Chalcopyrite (10%), Pyrite (5%) and Sphalerite (5%).	 D86b	 D86

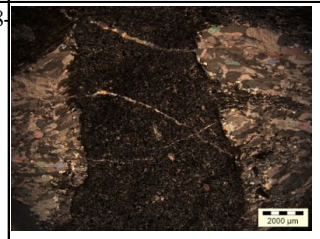
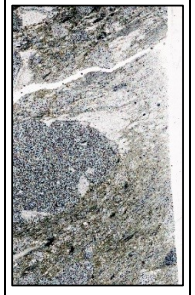
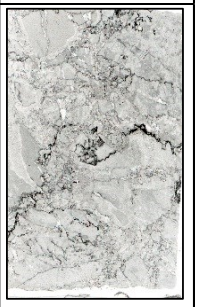
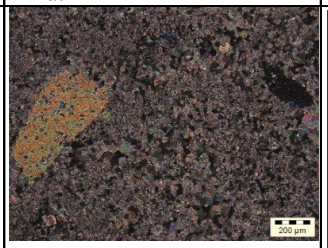
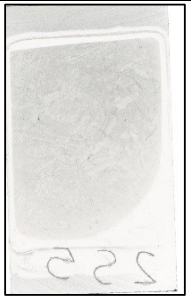
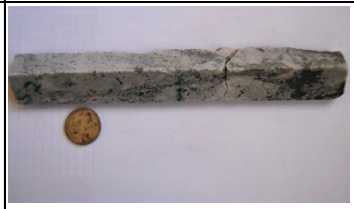
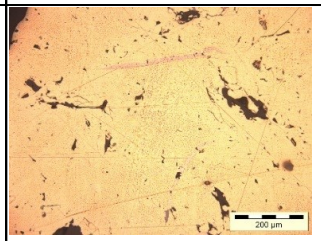
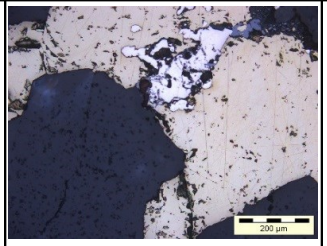
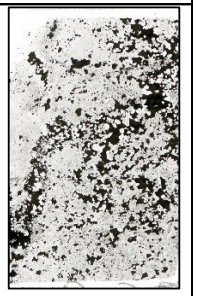
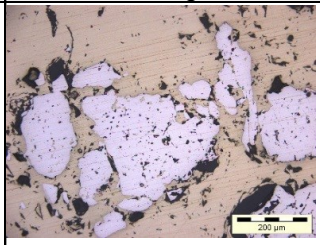
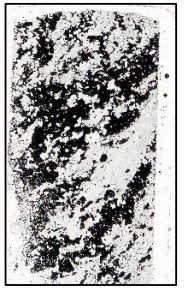
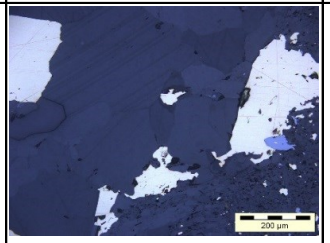
From (m)	To (m)	Spl No.	Lithology	Lithological Description	Sample Picture	Microscopic Description (Texture and Mineralogy)	Thin Section Photomicrograph	Scanned Thin Section
161.30	161.50	DB1S23	Agglomerate	Deformed agglomerate with sub to rounded elongated volcanic clasts. The unit is chlorite rich and has ubiquitous quartz-calcite veins. Pebbles range from <1 cm to 5 cm in the elongated direction.		Fine-grained (0.120 mm) calcite; Fine grained (0.012 mm) quartz; Fine grained (<0.041 mm) sericite and biotite; Fine-grained (<0.082 mm) chlorite. The quartz-calcite veins cross cut the mafic clasts. Calcite (20%); Quartz (10%), Chlorite (25%), Biotite (25%) and Sericite (20%).	 D9h	 D9
169.50	169.70	DB1S24	Agglomerate	Deformed agglomerate with sub to rounded elongated volcanic clasts. The unit in enriched in chlorite rich and have ubiquitous quartz-calcite veins. Pebbles range from <1 cm to 5 cm in the elongated direction.		Fine- to medium-grained (0.088-0.292mm) calcite; Fine-to coarse-grained grained (0.175-0583 mm) quartz; Fine grained (<0.05 mm) sericite and biotite; Fine-grained (<0.08 mm) chlorite. Biotite (~25%), Chlorite (~25%), Sericite (~15%), Calcite (~15%), Quartz (15%) and Pyrite (5%).	 84a	 84

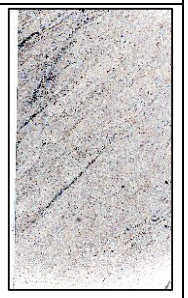
Table A-3. Description of the drill core samples from DBDD0002.

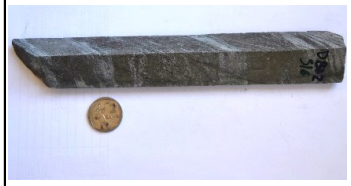
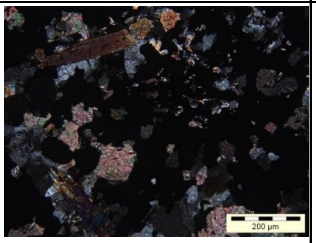
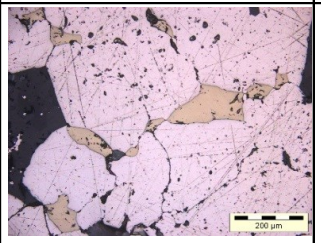
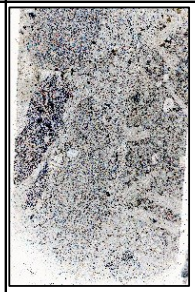
From (m)	To (m)	Spl No.	Lithology	Lithological Description	Sample Picture	Microscopic Description (Texture and Mineralogy)	Thin Section Photomicrograph	Scanned Thin Section
8.28	8.48	DB2S1	Dolomite Breccia	Dolomite Breccia with deformed stromatolites, frequent calcite and minor quartz veins consisting of minor pyrite patches.				
13.70	13.90	DB2S2	Dolomite Breccia	Dolomite Breccia with frequent deformed stromatolites. Calcite veins consists of minor pyrite and malachite.		This unit has a mosaic texture defined by very fine- to coarse-grained (0.088-1.167 mm) carbonate minerals (dolomite and calcite) and very fine- to fine-grained (0.090-0.170 mm) quartz. The mineralogy of this unit includes ~70% carbonates, ~15% quartz, ~10% sulphides and ~5% clay minerals (micrite).	 D10d: XPL	 D10
23.67	23.87	DB2S3	Dolomite Breccia	Dolomite Breccia with frequent deformed stromatolites.				

From (m)	To (m)	Spl No.	Lithology	Lithological Description	Sample Picture	Microscopic Description (Texture and Mineralogy)	Thin Section Photomicrograph	Scanned Thin Section
35.27	35.47	DB2S4	Silicified Dolomite	Silicified dolomite consisting of various calcite veins and frequent deformed stromatolites. The unit has minor zones affected by brecciation and fractured along the quartz-calcite veins.		This dolomite is highly silicified and comprises 60% carbonates (dolomite and calcite), 25% quartz, ~2% sericite, 8% pyrite and 5% chalcopyrite and The grain sizes of the carbonate minerals show a wide range, from very fine-to coarse-grained (0.088 to 1.167 mm), whereas quartz grains span from very fine-to medium-grained (0.058 to 0.175 mm)	 D11a: XPL	 D11
44.00	44.20	DB2S5	Silicified Dolomite	Silicified dolomite with various calcite veins and fractures filled with calcite. Frequent pyrite disseminations occur in the rock matrix.		This unit comprises 55% dolomite and calcite, 30% quartz, 10% sulphides and ~5% sericite. The grain sizes of the carbonate minerals show a wide range, from very fine-to coarse-grained (0.088 to 1.167 mm), whereas quartz grains span from very fine-to medium-grained (0.058 to 0.175 mm). In addition to silification and carbonatiation, sericitization is evident in this carbonate unit.	 D12: XPL	 D12
51.15	51.35	DB2S6	Silicified Dolomite	Silicified dolomite with pyrite hosted in quartz and quartz-calcite veins.				

From (m)	To (m)	Spl No.	Lithology	Lithological Description	Sample Picture	Microscopic Description (Texture and Mineralogy)	Thin Section Photomicrograph	Scanned Thin Section
59.36	59.56	DB2S7	Cu Sulphides	Frequent chalcopyrite and minor amounts of pyrite in quartz-calcite veins within the silicified dolomite.		Fine-grained (<0.055 mm) dolomite and calcite. Fine grained quartz (~0.034 mm). The sulphides occur largely as type type in quartz-calcite veins and as sulphide veinlets. Dolomite and Calcite (55%); Quartz (25%); Chalcopyrite 10%), Pyrite (5%), Sphalerite (~2%). Bornite (3%).	 D99d: Reflected Light	 D99
59.67	59.87	DB2S8	Cu Sulphides	Chalcopyrite and minor amounts of pyrite in quartz-calcite veins within the silicified dolomite.		Fine-grained (<0.038 mm) dolomite and calcite. The sulphides occur as mainly vein type with minor disseminations. Fine grained quartz (0.078 mm). Dolomite and Calcite (60%); Quartz (25%); Chalcopyrite (8%) Pyrite (5%) and Sphalerite (2%).	 D13b: Reflected Light	 D13
59.87	60.07	DB2S9	Cu Sulphides	Chalcopyrite and subordinate pyrite hosted in quartz and quartz-calcite veins.		Fine-grained (<0.075 mm) dolomite and calcite. Fine grained quartz (~0.004 mm). Dolomite and Calcite (~52%); Quartz (~28%); Chalcopyrite (10%), Pyrite (8%) and Sphalerite (<2%)	 D104d: Reflected Light	 D104

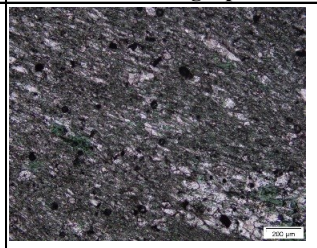
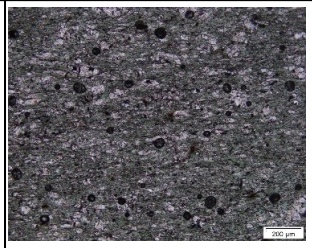
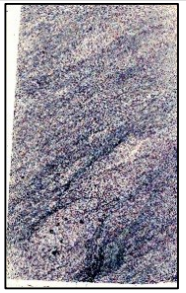
From (m)	To (m)	Spl No.	Lithology	Lithological Description	Sample Picture	Microscopic Description (Texture and Mineralogy)	Thin Section Photomicrograph	Scanned Thin Section
71.07	71.27	DB2S10	Silicified Dolomite	Deformed silicified dolomite dominated by calcite veins and disseminations of pyrite in the rock matrix.		Coarse-grained (<0.283 mm) dolomite and calcite. Medium-grained quartz (~0.123 mm). Dolomite and Calcite (~65%); Quartz (~15%). Coarse grained vein type sluphides. Chalcopyrite (10 %) Pyrite (5%) and Sphalerite (5%)		 D106
72.62	72.82	DB2S11	Silicified Dolomite	Silicified dolomite with fine-grained quartz in the quartz-calcite veins as well as sulphide veins.		Fine-to coarse-grained (0.088 to 1.167 mm) dolomite and calcite, fine-grained (0.058 mm) quartz and very fine-grained sericite (<0.050 mm). This unit is characterized by thick qaurz-calcite veins and fine grained chalcopyrite veinlets with minor pyrite. Dolomite and Calcite (65%); Quartz (28%); Chalcopyrite (5%) and Pyrite (2%).		 D110
73.40	73.60	DB2S12	Silicified Dolomite	Silicified dolomite with fine-grained quartz in the quartz-calcite veins.		Fine-to coarse-grained (0.088 to 1.167 mm) dolomite and calcite, fine-grained (0.058 mm) quartz and very fine-grained sericite (<0.050 mm). The unit has frequent quartz-calcite veins hosting chalcoyrite and pyrite. In addition, chalcopyrite, pyrite and sphalerite occur as disseminations. Dolomite and Calcite (60%); Quartz (25%); Chalcopyrite (8%); Pyrite (5%) and Spahlerite (~2%)	 D112a: Reflected Light	 D112

From (m)	To (m)	Spl No.	Lithology	Lithological Description	Sample Picture	Microscopic Description (Texture and Mineralogy)	Thin Section Photomicrograph	Scanned Thin Section
84.00	84.20	DB2S13	Silicified Dolomite	Silicified dolomite with pyrite hosted in quartz and quartz-calcite veins.		Fine-to coarse-grained (0.088 to 1.155 mm) dolomite and calcite, fine-grained (0.073 mm) quartz and very fine-grained sericite (<0.044 mm). Chalcopyrite and pyrite occur in quartz-calcite veins. Dolomite and Calcite (55%), Quartz (27%). Chalcopyrite (10%) and Pyrite (8%).		 D114
88.70	88.90	DB2S14	Silicified Dolomite	Silicified dolomite with ubiquitous thick calcite veins.		Fine-grained (<0.023 mm) dolomite and calcite. Fine grained quartz (~0.034 mm). Calcite (65%), Quartz (25%); Chalcopyrite (6%) and Pyrite (4%).		 D117
95.58	95.78	DB2S15	Silicified Dolomite	Deformed silicified dolomite with pyrite hosted in calcite veins aligned along the drill core and cut across bedding in some places.		Fine-grained (<0.030 mm) dolomite and calcite. Fine grained quartz (~0.021 mm). Calcite (55%), Quartz (25%); Chalcopyrite (10%) and Pyrite (10%).		 D116

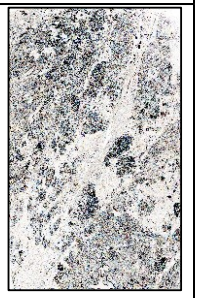
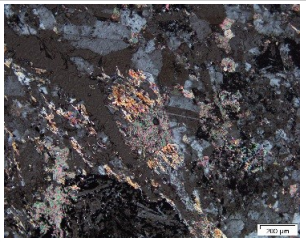
From (m)	To (m)	Spl No.	Lithology	Lithological Description	Sample Picture	Microscopic Description (Texture and Mineralogy)	Thin Section Photomicrograph	Scanned Thin Section
96.18	96.38	DB2S16	Cu Sulphides	Chalcopyrite and subordinate pyrite hosted in quartz and quartz-calcite veins.		Fine-grained (<0.011 mm) dolomite and calcite. Fine grained quartz (0.034 mm). Vein hosted chalcopyrite and pyrite are common with minor sphalerite. Dolomite and Calcite (45%), Quartz (25%); Chalcopyrite (15%), Pyrite (10%) and Sphalerite (5%).	 D15a: XPL	 D15
96.52	96.71	DB2S17	Cu Sulphides	Chalcopyrite and subordinate pyrite hosted in quartz and quartz-calcite veins.		Fine-grained (<0.067 mm) calcite. Fine grained quartz (0.012 mm). Calcite (35%), Quartz (25%); Chalcopyrite (20%), Pyrite (15%) and Sphalerite (5%).	 D118c: Reflected Light	 D118
102.00	102.20	DB2S18	Agglomerate	Deformed agglomerate with frequent quartz-calcite veins and sub-rounded mafic clasts hosted in a chlorite rich, highly foliated matrix.		Fine-grained (0.12 mm) calcite; Fine grained (0.012 mm) quartz; Fine grained (<0.04 mm) sericite and biotite; Fine-grained (<0.08 mm) chlorite. Calcite (45%); Quartz (20%), Chlorite (15%), Biotite (10%) and Sericite (10%).		 D121

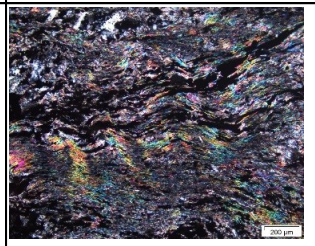
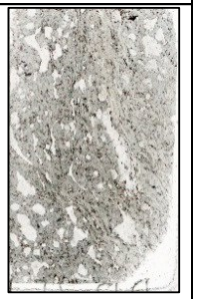
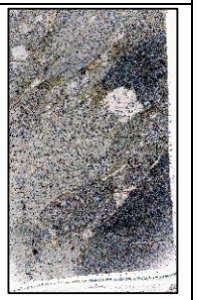
From (m)	To (m)	Spl No.	Lithology	Lithological Description	Sample Picture	Microscopic Description (Texture and Mineralogy)	Thin Section Photomicrograph	Scanned Thin Section
109.70	109.90	DB2S19	Agglomerate	Deformed agglomerate with frequent quartz-calcite veins and sub-rounded mafic clasts hosted in a chlorite rich, highly foliated matrix. Most quartz-calcite veins cross cut each other. Coarse grains of pyrite are evident in the top part of this unit.		Fine-grained (0.12 mm) calcite; Fine grained (0.012 mm) quartz; Fine grained (<0.04 mm) sericite and biotite; Fine-grained (<0.08 mm) chlorite. Calcite (20%); Quartz (15%), Chlorite (25%), Biotite (25%) and Sericite (15%).		 D123

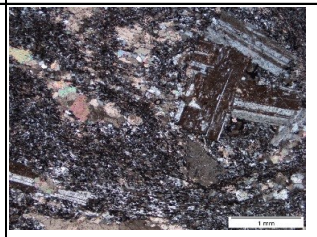
Table A-4. Description of the drill core samples from DBDD0003.

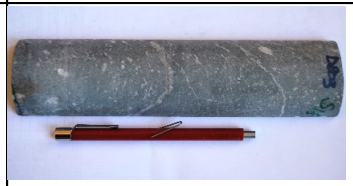
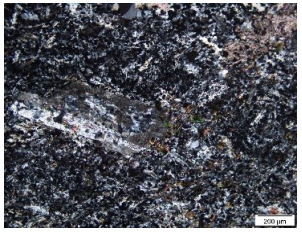
From (m)	To (m)	Spl No.	Lithology	Lithological Description	Sample Picture	Microscopic Description (Texture and Mineralogy)	Thin Section Photomicrograph	Scanned Thin Section
3.73	3.93	DB3S1	Chlorite Schist	Chlorite schist with a well-developed foliation and frequent quartz-calcite veins		Fine-to medium-grained (0.088 to 0.175 mm) quartz; Medium-grained calcite (0.117 to 0194 mm); Fine-grained (0.125-0.168 mm) chlorite and sericite, Fine-grained (0.097 to 0.002 mm) plagioclase. Chlorite is overgrowing all the other minerals. Chlorite (35%), Sericite (25%), Calcite (20%), Quartz (15%), Plagioclase (~5%)	 D124b: PPL	 D124
4.15	4.35	DB3S2	Chlorite Schist	Chlorite schist with frequent calcite veins parallel to the foliation and minor calcite veins cross-cutting the foliation.		Medium-grained (0.175 mm) quartz; Coarse-grained calcite (0.117 to 0194 mm); Fine-grained (0.125-0.168 mm) chlorite and sericite, Fine-grained (0.097 mm) plagioclase. Chlorite (35%), Sericite (25-30%), Calcite (20%), Plagioclase (<5%).	 D126a: PPL	 D126
11.75	11.95	DB3S3	Chlorite Schist	Chlorite schist with frequent quartz- calcite veins parallel to the foliation. This part is weakly weathered and affected by silicification.				

From (m)	To (m)	Spl No.	Lithology	Lithological Description	Sample Picture	Microscopic Description (Texture and Mineralogy)	Thin Section Photomicrograph	Scanned Thin Section
12.00	12.20	DB3S4	Chlorite Schist	Chlorite schist with various quartz-calcite veins of which some are cutting across foliation. In addition to silicification, it is oxidized to brown.				
13.30	13.50	DB3S5	Chlorite Schist	Chlorite schist with various quartz-calcite veins. The unit is highly silicified.				
14.20	14.40	DB3S6	Chlorite Schist	Chlorite schist dominated by frequent quartz-calcite veins and a strong foliation.				

From (m)	To (m)	Spl No.	Lithology	Lithological Description	Sample Picture	Microscopic Description (Texture and Mineralogy)	Thin Section Photomicrograph	Scanned Thin Section
19.40	19.60	DB3S7	Chlorite Schist	Chlorite schist dominated by frequent quartz-calcite veins and a strong foliation.		Coarse-grained (0.218 mm) quartz; Coarse-grained calcite (0.197 to 0194 mm); Fine-grained (0.015-0.068 mm) chlorite and sericite, Medium-grained (0.107 mm) plagioclase. Chlorite (35%), Sericite (25%), Calcite (20%), Quartz (15%), Plagioclase (~5%)		 D128
23.30	23.50	DB3S8	Chlorite Schist	Chlorite schist dominated by frequent quartz-calcite veins and a strong foliation.				
34.20	34.40	DB3S9	Tuff	The tuff with frequent quartz and calcite veins oxidized to brown and frequent calcite veins cross-cut by late quartz veins.		Medium-grained (0.35-1.167 mm) plagioclase, fine grained (0.041-0.098 mm) sericite, biotite and chlorite; Medium grained (0.117 mm) calcite and quartz. Sericite (40%) , Plagioclase (10%), Biotite (15%), Chlorite (5%), Calcite(20%), quartz (~10%).	 D130a: XPL	 D130

From (m)	To (m)	Spl No.	Lithology	Lithological Description	Sample Picture	Microscopic Description (Texture and Mineralogy)	Thin Section Photomicrograph	Scanned Thin Section
39.20	39.40	DB3S10	Tuff	The tuff with frequent quartz and calcite veins oxidized to brown and frequent calcite veins cross-cut by late quartz veins.		Fine-grained (0.088-0.25 mm) plagioclase, fine grained (0.041-0.098 mm) sericite, biotite and chlorite; Fine-grained (0.062 mm) calcite and quartz. The foliation shows evidence of C-S fabric. Sericite (35%), Plagioclase (15%), Biotite (15%), Chlorite (10%), Carbonates (mainly calcite) (16%), quartz (~9%).	 D17c: XPL	 D17
42.31	42.51	DB3S11	Chlorite Schist	Chlorite schist with weak foliation cross cut by quartz veins.		Coarse-grained (0.218 mm) quartz; Coarse-grained (0.29 to 0.194 mm) calcite; Fine-grained (0.055-0.027 mm) chlorite, biotite and sericite. Chlorite (30%), Sericite (25%), Biotite (10%) Calcite (25%), Quartz (10%).		 D133
43.60	43.80	DB3S12	Chlorite Schist	Chlorite schist with weak foliation cross cut by quartz veins.		Coarse-grained (0.218 mm) quartz; Coarse-grained (0.29 to 0.194 mm) calcite; Fine-grained (0.055-0.027 mm) chlorite, biotite and sericite. Chlorite (45%), Sericite (10%), Calcite (25%), Quartz (20%),		 D134

From (m)	To (m)	Spl No.	Lithology	Lithological Description	Sample Picture	Microscopic Description (Texture and Mineralogy)	Thin Section Photomicrograph	Scanned Thin Section
47.28	47.48	DB3S13	Tuff	Tuff with a strong foliation and frequent quartz-calcite and calcite veins.		Fine-grained (0.094mm) plagioclase, fine grained (~0.030 mm) sericite, biotite and chlorite; Fine-grained (0.025mm) calcite and quartz. Sericite (30%) , Plagioclase (15%), Biotite (15%), Chlorite (5%), Calcite(20%), Quartz (~15%).	 D18a: XPL	 D18
67.40	67.60	DB3S20	Tuff	Tuff with strong foliation and frequent calcite and quartz-calcite veins.		Fine-grained (0.084-0.20 mm) plagioclase, fine grained (~0.042 mm) sericite, biotite and chlorite; Fine-grained (0.044mm) calcite and quartz. Sericite (20%) , Plagioclase (20%), Biotite (15%), Chlorite (5%), Calcite(20%), Quartz (~20%).	 D139d: XPL	 D139
67.40	67.60	DB3S14	Tuff	Tuff with calcite veins are oxidized to brown.				
75.04	75.24	DB3S15	Tuff	Tuff characterized by with dark grey, thin mafic foliated layers and frequent calcite and quartz-calcite veins.		Fine-grained (0.088-0.25 mm) plagioclase, fine grained (~0.041 mm) sericite, biotite and chlorite; Fine-grained (0.044mm) calcite and quartz. Sericite (20%) , Plagioclase (15%), Biotite (10%), Chlorite (15%), Calcite(25%), Quartz (~15%).	 D142: XPL	 D142

From (m)	To (m)	Spl No.	Lithology	Lithological Description	Sample Picture	Microscopic Description (Texture and Mineralogy)	Thin Section Photomicrograph	Scanned Thin Section
76.24	76.44	DB3S16	Tuff	Tuff with dark grey, thin mafic foliated layers.				
77.50	77.70	DB3S17	Chlorite Schist	Chlorite schist with weak foliation and frequent quartz-calcite veins.		Fine-grained (0.088-0.25 mm) plagioclase, fine grained (~0.041 mm) sericite, biotite and chlorite; Fine-grained (0.044mm) calcite and quartz. Sericite (25%), plagioclase (15%), Biotite (10%), Chlorite (15 %), Calcite (20%), Quartz (15%).		 D143
85.60	85.80	DB3S18	Tuff	Tuff with thin mafic foliated layers, frequent calcite veins and subordinate quartz veins.		Fine-grained (0.020 mm) plagioclase, Fine grained (<0.050 mm) sericite, biotite and chlorite; Fine-grained (0.065 mm) calcite and quartz. Sericite (25%), plagioclase (15%), Biotite (10%), Chlorite (15 %), Calcite (20%), Quartz (15%).	 D19b: XPL	 D19
89.50	89.70	DB3S19	Tuff	Tuff with white spotty appearance due to the ubiquitous quartz-calcite and calcite veins.		Fine-grained (0.018 mm) plagioclase, Fine grained (<0.076 mm) sericite, biotite and chlorite; Fine-grained (0.044 mm) calcite and quartz. Sericite (30%), plagioclase (5%), Biotite (10%), Chlorite (10 %), Calcite (30%), Quartz (15%).	 D145a: XPL	 D145

Appendix B
Sulphur Isotopic Data

Sulphur isotope ratios ($\delta^{34}S_{CDT}$) were determined on 13 sulphide mineral separates of chalcopyrite, pyrite and galena at the Ithemba Labs, University of the Witwatersrand, South Africa. The sulphide samples were taken from the Deblin Copper Mine and Kombat deposit. The measurements of the isotope ratios ($\delta^{34}S$ values) are reported relative to the Cañon Diablo Troilite (CDT) standard.

Table B-1.

Laboratory Number	Sample No.	Borehole ID	Depth (m)	Host Rock	Mineralization Type	δ34S (Chalcopyrite)	δ34S (Pyrite)	δ34S (Bornite)
WITS 1203	DB2S9	DBDD0002	59.87-60.07	Silicified Dolomite	Disseminated	3.63		
WITS 1204	DB2S7	DBDD0002	59.36-59.56	Silicified Dolomite	Vein	3.73		
WITS 1205	DB2S17	DBDD0002	137.22-137.42	Silicified Dolomite	Disseminated	-9.99		
WITS 1206	DB1S18	DBDD0001	137.73-137.93	Agglomerate	Disseminated		-8.46	
WITS 1207	DB1S22	DBDD0001	157.50-157.70	Agglomerate	Vein		-4.88	
WITS 1208	DB1S16	DBDD0001	136.61-136.81	Silicified Dolomite	Vein	-4.93		
WITS 1209	DB2S8	DBDD0002	59.67-59.87	Silicified Dolomite	Vein	6.04		
WITS 1210	DB2S12	DBDD0002	73.40-73.60	Silicified Dolomite	Disseminated	-4.17		
WITS 1211	DB1S17	DBDD0001	137.22-137.42	Silicified Dolomite	Disseminated	-6.14		
WITS 1212	Kombat 2	Kombat		Limestone	Massive	18.72		
WITS 1213	Kombat 1	Kombat		Limestone	Massive	18.65		
WITS 1214	Kombat 3	Kombat		Limestone	Massive			18.61
WITS 1215	Kombat 4	Kombat		Limestone	Massive			18.58

Appendix C

Whole Rock Geochemical Data

A total of 15 samples of the metavolcanic rocks were selected for geochemical analyses of which 9 and 6 samples were taken from drill cores and outcrops, respectively. These selected rock samples were analyzed for their whole rock major and, trace and rare earth elements (REE) contents by X-ray fluorescence spectrometry (XRF) and Inductively Coupled Plasma-Mass Spectrometry (ICP-MS) methods, respectively at the Earth Laboratory, University of the Witwatersrand, Johannesburg, South Africa.

Table C-1. Major Element Geochemical Data.

Sample	DB3S14	DB3S19	DB3S9	DB3S20	DB3S16	DB1S19	DB1S20	DB8a	DB7a	DB3S8	DB1b	DB3S7	DB10h	DB10a	DB10b
SiO_2	48.67	43.73	40.85	41.97	44.73	44.49	42.28	37.92	45	31.08	37.33	33.11	35.07	44.18	41.74
Al_2O_3	11.98	12.22	12.76	12.87	14.35	14.47	16.61	10.97	14.44	11.68	6.77	9.47	7.43	9.13	9.93
$Fe2O_3$	1.35	1.6	1.47	1.03	1.28	0.55	0.87	0.98	0.95	0.9	0.49	0.6	0.61	0.83	0.9
FeO	10.89	12.93	11.95	8.37	10.38	4.46	6.99	7.92	7.71	7.28	3.97	4.86	4.92	6.77	7.28
MnO	0.12	0.16	0.16	0.2	0.18	0.12	0.13	0.14	0.12	0.58	0.25	0.61	0.29	0.14	0.12
MgO	5.77	3.01	1.48	0.91	7.95	1.96	2.72	7.24	9.03	4.51	4.76	6.1	1.97	7.05	7.36
CaO	5.11	7.93	10.32	13.66	4.55	10.77	9.57	12.01	7.59	16.33	22.46	17.29	24.99	10.37	12.04
Na2O	4.05	5.04	3.15	5.71	4.27	0.09	0.05	0.07	0.03	0	0.04	0	0	0.03	0.05
K2O	1.53	1.53	4.07	1.27	1.37	5.07	5.49	3.3	2.16	4.98	0.94	3.95	2.5	2.94	2.14
TiO2	1.91	2	2.85	2.26	1.99	2.75	3.49	2.28	1.58	2.03	0.96	1.84	1.24	1.64	1.29
P2O5	0.28	0.21	0.4	0.29	0.21	0.35	0.6	0.24	0.33	0.26	0.16	0.25	0.17	0.2	0.19
Cr2O3	0.01	0.02	0.01	0.02	0.02	0.02	0.03	0.03	0.02	0.02	0.02	0.02	0.03	0.02	0.02
NiO	0.01	0.01	0	0	0.01	0.01	0.01	0.01	0.01	0.01	0.01	0	0	0	0.01
LOI	8.48	9.77	10.11	11.86	8.98	7.9	9.48	16.84	11.07	20.22	20.36	22.1	20.75	16.56	16.94
Total	100.16	100.16	99.58	100.42	100.27	93.01	98.32	99.95	100.04	99.88	98.52	100.20	99.97	99.86	100.01

Table C-2. Trace and REE Geochemical Data

Sample	DB3S14	DB3S19	DB3S9	DB3S20	DB3S16	DB1S19	DB1S20	DB8a	DB7a	DB3S8	DB1b	DB3S7	DB10h	DB10a	DB10b
Li	42.23	12.25	23.81	11.44	51.72	60.23	59.44	23.89	83.17	66.88	36.41	48.73	21.22	17.50	46.20
Sc	26.84	24.57	23.16	25.69	30.31	33.96	32.97	22.65	22.71	23.12	12.85	16.58	16.80	18.41	18.57
Ti	10333	10463	15893	11411	10946	17163	20314	13127	9354	11565	5628	10112	6741	9259	7321
V	272	197	198	167	283	309	360	235	220	228	131	180	131	167	157
Cr	29.89	19.80	6.47	32.09	79.40	107	87.77	118	66.94	56.47	55.02	58.52	80.12	76.04	63.57
Co	57.99	29.46	33.55	18.80	72.72	45.90	14.72	25.33	26.41	16.85	29.80	27.76	22.83	13.81	19.61
Ni	39.98	43.16	36.51	27.51	64.28	102	59.04	55.22	42.76	59.18	50.07	34.77	37.56	31.59	63.23
Cu	10.67	7.70	8.84	8.87	8.48	79.37	11.01	8.06	33.31	33.41	5153	30.25	383	6.33	109
Zn	237	100	97.40	57.35	300	37.28	85.18	59.75	93.20	92.88	63.54	58.70	50.82	41.71	80.99
Ga	16.84	15.45	20.65	15.19	19.92	19.68	25.48	14.91	19.45	17.27	9.66	13.29	10.23	12.58	13.37
Rb	99.44	59.02	195	74.29	73.47	164	219	122	109	283	56.33	190	122	102	64.52
Sr	57.38	83.22	93.71	152	55.07	63.40	63.55	74.58	31.75	103	111	90.20	166	76.98	56.29
Y	13.55	18.06	26.96	24.97	10.12	23.38	29.17	22.48	20.49	24.37	19.04	23.34	22.75	19.00	16.47
Zr	167	145	288	180	146	230	403	173	198	158	101	140	126	133	119
Nb	22.23	23.32	42.91	28.99	22.50	35.61	48.45	29.33	31.63	26.82	15.76	22.59	15.68	21.16	18.05
Ba	358	627	1675	691	496	4058	3652	684	254	580	180	337	437	368	268
Cs	5.85	1.92	1.83	1.19	4.79	1.85	3.07	8.84	1.83	3.63	1.01	2.60	1.12	6.24	3.66
La	17.14	16.55	21.67	14.61	13.45	17.96	36.98	24.02	28.44	17.29	18.91	12.67	19.52	20.97	17.94
Ce	39.13	34.16	47.35	33.11	30.57	48.60	81.23	51.89	61.57	37.63	37.69	29.86	39.04	44.58	39.29
Pr	5.50	4.50	6.71	4.81	4.29	7.02	11.37	6.63	7.71	5.11	4.79	4.02	4.89	5.72	4.87
Nd	23.81	18.95	28.15	22.18	19.11	31.74	47.95	27.42	31.02	21.91	19.12	17.66	20.37	23.15	19.79
Sm	5.25	4.55	7.43	5.67	4.54	9.00	12.17	5.86	6.04	5.16	3.72	4.63	4.46	4.88	4.03
Eu	1.48	1.49	2.51	1.92	1.37	2.91	4.61	1.75	1.51	1.93	0.85	1.72	1.32	1.42	1.07
Gd	4.69	4.34	6.52	5.22	3.73	6.36	9.19	5.42	5.81	4.89	3.75	4.88	4.61	4.85	4.02
Tb	0.62	0.62	0.96	0.76	0.48	0.90	1.20	0.76	0.76	0.72	0.55	0.76	0.67	0.69	0.57
Dy	2.87	3.30	5.01	4.22	2.23	4.62	5.89	4.08	3.98	3.99	3.15	4.47	3.83	3.66	3.11
Ho	0.48	0.62	0.92	0.75	0.40	0.85	1.01	0.76	0.72	0.79	0.62	0.86	0.72	0.66	0.57

Er	1.31	1.64	2.44	2.03	1.11	2.24	2.78	2.07	2.11	2.19	1.78	2.26	1.97	1.89	1.59
Tm	0.20	0.24	0.37	0.31	0.18	0.33	0.41	0.31	0.33	0.32	0.26	0.33	0.29	0.28	0.24
Yb	1.47	1.63	2.54	2.19	1.28	2.12	2.78	1.98	2.08	2.08	1.70	2.00	1.75	1.80	1.53
Lu	0.24	0.25	0.39	0.34	0.22	0.33	0.45	0.29	0.32	0.31	0.26	0.29	0.27	0.28	0.23
Hf	3.69	3.49	6.40	4.18	3.72	5.49	8.77	4.42	5.02	3.79	2.48	3.43	3.02	3.47	3.04
Ta	1.24	1.35	2.77	1.64	1.30	2.12	3.14	1.70	2.03	1.52	0.94	1.31	0.88	1.28	1.13
Pb	7.35	9.84	22.84	20.28	7.08	4.00	4.09	2.15	7.12	20.34	10.35	16.06	6.31	1.95	2.21
Th	2.60	2.62	3.66	2.89	2.43	2.96	7.00	5.33	8.97	2.36	3.82	2.17	2.68	5.42	3.50
U	0.54	0.56	1.03	0.77	0.48	0.89	1.19	1.33	1.41	0.72	2.23	0.59	0.73	0.83	1.26

Appendix D

Table D-1. List of structural readings (foliation) collected during field work.

Easting (m)	Northing (m)	Lithology	Strike	Dip	Dip Direction
758361	7814949	Phyllite	264	59	174
758329	7814972	Chlorite Schist	290	53	200
758750	7814860	Chlorite Schist	110	44	200
759552	7814663	Mafic Metavolcanic	120	67	210
759567	7814763	Agglomerate	89	67	179
759558	7814742	Mafic Metavolcanic	98	87	188
759557	7814720	Mafic Metavolcanic	80	84	170
759554	7814668	Mafic Metavolcanic	120	78	210

Table D-2. List of structural readings (bedding) collected during field work.

Easting (m)	Northing (m)	Lithology	Strike	Dip	Dip Direction
758320	7814913	Dolomite Breccia	270	53	180
758323	7814929	Dolomite Breccia	275	51	185
758322	7814950	Grey Limestone	270	64	180
758326	7814955	Phyllite	115	75	205
758505	7814889	Grey Limestone	120	24	210
758490	7814832	Grey Limestone	105	55	195
759641	7814738	Grey Limestone	110	85	200
759659	7814688	Silicified Dolomite	80	90	170
759679	7814622	Grey Limestone	110	53	200
759746	7814543	Banded Limestone	100	37	190
759611	7814222	Pyritic Dolomite	114	70	204
759531	7814557	Grey Limestone	50	35	140
759842	7814523	Grey Limestone	120	75	210
760024	7814513	Silicified Dolomite	95	60	185

759985	7814520	Banded Limestone	95	54	185
758304	7814965	Silicified Dolomite	100	52	190
759553	7814613	Grey Limestone	85	46	175
759587	7814529	Grey Limestone	25	30	115
759474	7814207	Diamictite	115	53	25
759438	7814538	Grey Limestone	134	85	224
759531	7814491	Banded Limestone	115	77	205

Table D-3. List of structural readings (strike and dip) taken from the geological map of the southern Otavi Mountain Land of Smit (1959).

Easting (m)	Northing (m)	Strike	Dip	Dip Direction	Easting (m)	Northing (m)	Strike	Dip	Dip Direction
752279	7818964	60	50	150	767141	7818043	90	60	180
751411	7818438	48	45	135	753121	7814913	82	50	172
750938	7818017	10	50	140	754568	7815018	70	60	160
750228	7817254	71	65	155	756356	7814782	80	60	170
750648	7816939	55	60	150	758250	7814966	88	50	178
749912	7816176	165	45	135	758645	7814887	131	80	221
751674	7816781	73	60	150	759697	7814466	82	60	172
752884	7816702	57	65	147	761696	7814782	72	60	162
755304	7817149	92	20	182	760486	7814624	74	70	164
756698	7816518	3	40	93	762222	7814940	83	50	173
758698	7817202	76	70	166	764616	7813388	96	50	186
761486	7817123	92	80	2	764563	7814571	106	55	196
762748	7817044	92	60	2	765063	7814256	92	70	182
763906	7817096	91	80	1	767299	7814177	99	75	189
762459	7817728	92	50	182	768325	7814256	95	80	185
764248	7817886	86	45	176	766904	7813309	103	65	193
752858	7811625	82	50	172	770798	7813756	95	80	185

752884	7809547	47	60	137	771403	7813151	89	90	179
752358	7809337	32	60	302	754121	7813440	76	45	166
752937	7808995	113	60	23	754094	7813335	142	30	52
751359	7808811	92	70	182	754541	7812020	68	60	158
754804	7809758	95	60	185	756672	7813519	85	60	175
755725	7809679	100	60	190	759145	7813309	112	55	202
761986	7812546	103	45	193	750517	7812072	105	70	195
765931	7811125	104	70	194	751858	7811967	108	65	198
766931	7812125	120	40	30	766904	7807495	92	40	182
766405	7807890	82	75	352					

Appendix E

Magnetic Data

Magnetic Susceptibility data for DBDD0001.

Table E-1. Magnetic Susceptibility data for DBDD0001.

Depth (m)	x10^{-3} SI Units	Depth (m)	x10^{-3} SI Units	Depth (m)	x10^{-3} SI Units	Depth (m)	x10^{-3} SI Units	Depth (m)	x10^{-3} SI Units	Depth (m)	x10^{-3} SI Units	Depth (m)	x10^{-3} SI Units	Depth (m)	x10^{-3} SI Units	Depth (m)	x10^{-3} SI Units	Depth (m)	x10^{-3} SI Units
0.00	-0.235	12.85	-0.539	30.69	-0.828	45.00	0.024	55.63	0.043	80.26	-0.005	98.86	0.055	120.62	-0.009	138.17	0.075	160.07	0.274
0.33	-0.018	13.23	0.028	30.99	1.04	45.17	-0.381	55.90	0.019	80.84	-0.053	99.27	0.01	121.06	0.042	138.61	0.037	160.69	0.148
0.66	-0.043	13.60	-2.06	31.29	-0.42	45.33	-0.079	56.16	0.047	81.42	0.034	99.68	-0.004	121.50	0.049	139.05	0.042	161.30	0.211
0.99	-0.056	13.97	-0.036	31.59	-0.034	45.50	-0.253	56.42	0.052	82.00	0.063	100.09	-0.023	121.93	0.051	139.49	0.002	161.91	0.35
1.32	-0.153	14.34	-1.58	31.89	-0.853	45.67	-0.091	56.69	0.78	82.18	0.04	100.50	0.006	122.37	0.027	139.93	0.015	162.53	0.261
1.65	-0.387	14.71	-0.02	32.19	-0.198	45.83	-0.127	56.95	0.027	82.35	0.042	100.94	-0.2	122.81	0.04	140.37	0.034	163.14	0.221
1.98	-0.033	15.08	-1.53	32.49	-1.26	46.00	-0.43	57.21	-0.086	82.53	-0.091	101.37	-0.208	123.25	0.035	140.81	0.052	163.75	0.223
2.31	-0.043	15.45	-0.195	32.79	-0.253	46.17	-0.298	57.48	-0.116	82.70	0.015	101.81	0.031	123.68	0.047	141.24	0.057	164.37	0.291
2.64	-1.83	15.82	-0.07	33.09	-0.176	46.33	0.015	57.74	0.02	83.05	0.038	102.25	-0.002	124.12	-0.002	141.68	0.058	164.98	0.023
2.97	-0.151	16.19	-0.144	33.39	-0.472	46.50	0.47	58.00	-0.097	83.40	0.013	102.69	0.044	124.56	0.031	142.12	0.056	165.59	0.365
3.30	-0.166	16.57	-0.033	33.69	-1.49	46.67	-0.015	58.27	-0.029	83.75	-0.06	103.12	0.008	124.99	0.034	142.56	0.502	166.21	0.465
3.49	-0.17	16.94	-0.711	33.99	-0.152	46.83	0.039	58.53	-0.68	84.10	-0.042	103.56	0.016	125.43	-0.094	143.00	0.846	166.82	0.338
3.67	-1.57	17.31	-1.37	34.29	-0.431	47.00	0.35	58.79	-0.073	84.45	0.035	104.00	0.05	125.87	0.026	143.44	0.748	167.43	0.348
3.86	-1.49	17.68	0.007	34.59	-1.28	47.21	-0.69	59.06	-0.008	84.80	0.059	104.44	0.006	126.31	0.028	143.88	7.92	168.05	0.408

4.04	-0.107	18.05	-0.467	34.88	-0.073	47.43	-0.1	59.32	0.004	85.14	-0.15	104.87	-0.008	126.74	0.029	144.32	21.4	168.66	0.425
4.23	-0.086	18.42	-1.87	35.18	-0.399	47.64	-0.058	59.90	0.009	85.49	-0.021	105.31	0.015	127.18	-0.168	144.76	94.7	169.27	0.307
4.41	-0.555	18.79	0.002	35.48	-0.076	47.86	-0.006	60.48	0.021	85.84	0.022	105.75	0.023	127.62	0.018	145.20	43.9	169.89	0.355
4.60	-1.08	19.16	-1.99	35.78	-0.046	48.07	0.034	61.06	-1.94	86.19	0.025	106.19	0.021	128.06	0.019	145.64	134	170.50	0.492
4.79	-0.001	19.54	-1.91	36.08	-0.031	48.29	-0.447	61.65	0.007	86.54	0.027	106.62	0.019	128.49	-0.032	146.08	150		
4.98	0.026	19.91	-0.009	36.38	-0.016	48.50	0.007	62.23	-0.014	86.89	0.025	107.06	0.014	128.93	0.02	146.52	137		
5.17	0.003	20.28	-0.583	36.68	0.022	48.71	0.024	62.81	-0.415	87.24	0.001	107.50	0.055	129.37	-0.003	146.96	84.3		
5.36	-1.66	20.65	-1.07	36.98	-0.009	48.93	-0.132	63.39	0.031	87.59	0.019	107.94	0.029	129.81	0.002	147.40	139		
5.55	-0.935	21.02	-0.003	37.28	0.567	49.14	-0.051	63.97	-0.018	87.94	0.023	108.37	-0.003	130.24	0.055	147.83	181		
5.75	0.16	21.39	-0.004	37.58	-0.085	49.36	0.027	64.55	-0.542	88.29	-0.0289	108.81	0.85	130.68	0.011	148.27	95.1		
5.94	-0.103	21.76	-1.39	37.88	0.023	49.57	0.042	65.14	-0.415	88.64	0.015	109.25	0.052	131.12	0.013	148.71	130		
6.13	-1.71	22.13	-1.37	38.18	0.031	49.79	-0.537	65.72	-0.007	88.99	-0.111	109.69	0.035	131.56	0.03	149.15	82.7		
6.32	-1.49	22.50	0.006	38.48	-0.771	50.00	0.196	66.30	-0.288	89.33	0.037	110.12	0.026	131.99	-0.121	149.59	58.3		
6.51	-0.107	22.88	-0.281	38.78	0.007	50.21	0.01	66.88	-0.374	89.68	0.055	110.56	0.023	132.43	0.006	150.03	84.2		
6.70	-0.004	23.25	-0.717	39.08	0.013	50.43	0.053	67.46	0.02	90.03	0.01	111.00	0.005	132.87	0.009	150.47	6.17		
6.85	0.009	23.62	0.037	39.37	-0.699	50.64	0.052	68.04	-0.246	90.38	-0.004	111.44	0.037	133.31	0.045	150.91	70.7		
7.00	0.003	23.99	-1.95	39.67	0.041	50.86	-0.049	68.62	-0.013	90.73	-0.023	111.87	0.017	133.74	-0.134	151.35	17.2		
7.14	-1.29	24.36	0.012	39.97	0.025	51.07	-0.141	69.21	0.023	91.08	0.022	112.31	0.041	134.18	-0.005	151.79	46.9		
7.29	-0.152	24.73	-0.199	40.27	-0.221	51.29	-0.058	69.79	-0.083	91.49	0.034	112.75	0.034	134.62	0.016	152.23	6.37		
7.44	-0.033	25.10	-0.763	40.57	-0.011	51.50	-0.012	70.37	-0.124	91.90	0.009	113.18	-0.168	135.06	0.033	152.67	0.562		
7.59	-0.06	25.47	0.014	40.87	0.03	51.71	-0.096	70.95	-0.06	92.31	-0.078	113.62	0.017	135.49	0.22	153.11	10.1		
7.73	-2.13	25.84	-1.84	41.17	-0.241	51.93	-0.095	71.53	0.035	92.72	-0.019	114.06	0.037	135.93	-0.021	153.55	0.678		

7.88	-0.524	26.22	-1.06	41.47	0.029	52.14	0.037	72.11	-0.239	93.13	-0.006	114.50	0.026	136.09	-0.02	153.99	0.349		
8.03	-1.56	26.59	0.023	41.72	-0.09	52.36	-0.4	72.70	0.014	93.54	0.006	114.93	0.033	136.26	-0.005	154.42	15		
8.40	-0.041	26.96	-1.47	41.97	0.015	52.57	-0.71	73.28	0.022	93.95	-0.144	115.37	0.021	136.42	-0.252	154.86	0.342		
8.77	-0.034	27.33	0.8431	42.23	0.005	52.79	-0.55	73.86	0.016	94.36	0.022	115.81	0.01	136.58	-0.106	155.30	0.36		
9.14	-0.023	27.70	-0.02	42.48	-0.235	53.00	0.047	74.44	-0.011	94.77	0.025	116.25	0.027	136.70	0.029	155.74	0.293		
9.51	-0.01	28.00	0.003	42.73	0.006	53.26	-0.0298	75.02	0.06	95.18	0.027	116.68	0.039	136.81	0.01	156.18	0.156		
9.89	-0.338	28.30	-1.77	42.98	-0.101	53.53	0.052	75.60	-0.088	95.59	0.025	117.12	-0.139	136.93	-0.067	156.62	0.425		
10.26	-0.504	28.60	-0.006	43.24	-0.558	53.79	-0.143	76.18	-0.365	95.99	0.001	117.56	0.05	137.04	-0.002	157.06	0.325		
10.63	-0.058	28.90	-1.74	43.49	-0.002	54.05	0.005	76.77	0.027	96.40	0.019	118.00	0.04	137.16	0.052	157.50	0.081		
11.00	-0.058	29.20	-1.51	43.74	0.017	54.32	0.059	77.35	0.033	96.81	0.023	118.43	0.05	137.27	0.048	157.56	0.294		
11.37	-0.003	29.50	-0.004	43.99	0.031	54.58	-0.837	77.93	0.012	97.22	-0.0289	118.87	0.041	137.39	0.075	157.62	0.298		
11.74	-0.041	29.80	-0.356	44.24	-0.72	54.84	0.046	78.51	-0.024	97.63	0.015	119.31	0.036	137.50	0.067	158.23	5.71		
12.11	-1.03	30.09	-1.99	44.50	0.02	55.11	0.005	79.09	-0.033	98.04	-0.111	119.75	0.021	137.62	0.074	158.85	13.1		
12.48	0.024	30.39	-0.003	44.75	-0.057	55.37	-0.922	79.67	-0.076	98.45	0.037	120.18	0.032	137.73	0.036	159.46	0.596		

Table E-2. Magnetic Susceptibility data for DBDD0002.

Depth (m)	x10^{-3} SI Units	Depth (m)	x10^{-3} SI Units	Depth (m)	x10^{-3} SI Units	Depth (m)	x10^{-3} SI Units	Depth (m)	x10^{-3} SI Units	Depth (m)	x10^{-3} SI Units
0.00	-0.136	29.55	0.027	55.93	-0.17	74.37	0.011	90.84	-0.002	110.15	48.7
0.57	-0.002	30.33	0.074	56.42	-0.223	74.65	-0.139	91.20	-0.052	110.59	115
1.14	-0.055	31.11	0.006	56.91	0.075	74.92	-0.029	91.55	0.279	111.04	109
1.72	0.006	31.89	0.033	57.39	-0.135	75.20	-0.026	91.91	-0.268	111.49	80.5
2.29	-0.211	32.67	0.039	57.88	-0.193	75.47	-0.086	92.27	-0.058	111.94	97.1
2.86	0.014	33.44	0.038	58.37	-0.195	75.56	-0.006	92.62	0.016	112.39	6.05
3.43	-0.0922	34.22	-0.147	58.85	-0.403	75.66	0.015	92.98	0.045	112.83	2
4.00	0.047	35.00	-0.013	59.34	0.014	75.75	-0.034	93.33	0.007	113.28	0.173
4.58	-0.745	35.49	-0.023	59.51	-0.089	76.10	-0.024	93.69	-0.008	113.73	0.248
5.15	0.01	35.97	-0.167	59.68	-0.008	76.44	-0.004	94.05	-0.014	114.18	0.204
5.72	-0.731	36.46	0.021	59.84	-0.026	76.79	0.008	94.40	0.019	114.63	-0.071
6.29	0.013	36.95	-0.077	60.01	-0.348	77.14	0.009	94.76	0.12	115.07	0.307
6.86	0.82	37.43	-0.046	60.18	0.039	77.48	-0.011	95.11	0.003	115.52	-0.717
7.43	0.011	37.92	0.014	60.35	0.02	77.83	-0.012	95.47	-0.048	115.97	0.401
8.01	-0.799	38.41	-0.0286	60.51	-0.106	78.17	-0.143	95.82	-0.1	116.42	0.189
8.58	0.044	38.89	0.014	60.68	0.02	78.52	-0.02	96.18	0.051	116.86	-0.913
9.15	-0.737	39.38	-0.057	61.17	-0.18	78.87	-0.045	96.29	0.103	117.31	0.234
9.38	0.025	39.87	-0.019	61.66	-0.107	79.21	-0.003	96.39	0.151	117.76	-0.85
9.61	0.047	40.35	-0.017	62.15	-0.069	79.56	-0.036	96.50	0.109	118.21	-0.697
9.83	-0.825	40.84	-0.095	62.64	-0.035	79.91	-0.312	96.60	0.405	118.66	0.067
10.06	0.018	41.33	-0.336	63.12	-0.024	80.25	-0.037	96.71	0.284	119.10	0.14
10.29	-0.01	41.82	0.006	63.61	-0.19	80.60	-0.154	97.16	0.429	119.55	-0.12
10.52	-0.195	42.30	-0.003	64.10	-0.01	80.95	-0.005	97.61	0.345	120.00	0.2
10.75	-0.746	42.79	-0.107	64.59	-0.018	81.29	-0.042	98.05	0.388		
10.98	0.002	43.28	-0.043	65.08	-0.009	81.64	-0.067	98.50	0.411		
11.20	-0.09	43.76	-0.037	65.57	-0.157	81.98	-0.125	98.95	0.789		
11.43	-0.771	44.25	-0.304	66.06	-0.128	82.33	-0.044	99.40	0.499		

11.66	-0.717	44.74	-0.022	66.55	-0.396	82.68	-0.121	99.85	0.205		
12.44	-0.35	45.22	-0.039	67.04	-0.027	83.02	-0.063	100.29	11.5		
13.22	-0.018	45.71	-0.018	67.53	-0.01	83.37	-0.212	100.74	1.53		
13.99	-0.756	46.20	-0.172	68.01	-0.271	83.73	-0.012	101.19	0.428		
14.77	-0.709	46.68	-0.228	68.50	0.006	84.08	-0.229	101.64	37.7		
15.55	-0.02	47.17	-0.098	68.99	-0.007	84.44	-0.118	102.08	41.3		
16.33	-0.089	47.66	-0.127	69.48	0.043	84.79	-0.154	102.53	106		
17.11	-0.633	48.14	-0.169	69.97	-0.028	85.15	-0.009	102.98	46.3		
17.88	-0.06	48.63	-0.106	70.25	-0.001	85.51	0.041	103.43	88.7		
18.66	-0.336	49.12	-0.118	70.52	-0.005	85.86	-0.01	103.88	13.8		
19.44	-0.19	49.60	-0.088	70.80	-0.012	86.22	0.056	104.32	46.6		
20.22	-0.237	50.09	-0.208	71.07	-0.028	86.57	-0.314	104.77	88.2		
21.00	-0.963	50.58	-0.036	71.35	-0.012	86.93	-0.075	105.22	80.7		
21.77	-0.24	51.06	-0.032	71.62	0.028	87.28	-0.52	105.67	27.7		
22.55	-0.743	51.55	0.012	71.90	0.163	87.64	-0.005	106.12	43.4		
23.33	-0.118	52.04	-0.017	72.17	-0.054	88.00	-0.163	106.56	0.442		
24.11	-0.719	52.52	-0.238	72.45	-0.018	88.35	-0.134	107.01	19.2		
24.89	-0.179	53.01	0.023	72.72	0.01	88.71	0.059	107.46	63.6		
25.66	-0.019	53.50	-0.002	73.00	0.024	89.06	-0.128	107.91	86.7		
26.44	-0.003	53.99	-0.005	73.27	0.026	89.42	-0.045	108.36	50.1		
27.22	0.016	54.47	-0.177	73.55	0.021	89.78	-0.03	108.80	113		
28.00	-0.126	54.96	0.012	73.82	-0.0165	90.13	0.058	109.25	74.8		
28.78	-0.757	55.45	0.005	74.10	0.005	90.49	0.021	109.70	167		

Table E-3. Magnetic Susceptibility data for DBDD0002.

Depth (m)	x10^{-3} SI Units	Depth (m)	x10^{-3} SI Units	Depth (m)	x10^{-3} SI Units	Depth (m)	x10^{-3} SI Units	Depth (m)	x10^{-3} SI Units	Depth (m)	x10^{-3} SI Units
0.00	0.23	15.83	0.174	27.45	-0.486	39.85	0.077	57.92	-0.794	77.29	-0.057
1.35	0.127	16.16	0.157	27.76	0.076	40.16	-0.063	58.45	-0.66	77.71	-0.275
2.70	0.169	16.50	-1.76	28.07	0.163	40.48	0.008	58.98	-1.2	78.13	-0.004
3.15	-0.045	16.83	-0.009	28.37	0.163	40.80	-1.151	59.51	0.16	78.55	0.146
3.61	0.206	17.17	-0.031	28.68	0.197	41.14	-0.831	60.04	0.13	78.97	-0.631
4.06	-0.966	17.50	0.132	28.98	-0.4	41.47	0.109	60.57	0.192	79.39	-1.16
4.51	-1.08	17.84	0.04	29.29	-0.064	41.81	-0.37	61.10	-1.29	79.81	-0.219
4.96	-1.05	18.17	-0.736	29.59	0.037	42.14	0.288	61.60	0.016	80.23	0.136
5.42	0.12	18.51	0.034	29.92	0.64	42.48	-0.848	62.09	-0.445	80.65	-0.451
5.87	-0.594	18.85	-0.146	30.25	-0.503	42.81	-0.067	62.59	-1.19	81.07	-1.4
6.32	0.681	19.18	0.037	30.57	0.034	43.15	-0.505	63.08	-0.643	81.49	-0.356
6.77	0.325	19.52	-1.26	30.89	-1.04	43.48	0.328	63.58	0.05	81.91	-1.58
7.23	-1.09	19.85	-0.596	31.21	-1.21	43.82	-0.402	64.07	-0.69	82.33	-0.248
7.68	0.213	20.19	-1.35	31.54	0.087	44.15	0.278	64.57	-0.16	82.75	0.432
8.13	-1.09	20.52	-1.29	31.86	-0.834	44.68	0.213	65.06	0.183	83.19	0.383
8.58	0.213	20.86	-1.91	32.18	-1.76	45.21	-0.555	65.56	-0.347	83.62	-0.979
9.04	-1.65	21.20	-0.269	32.51	0.203	45.74	-1	66.05	0.153	84.06	-0.656
9.49	1.5	21.53	0.07	32.83	-1.66	46.27	-0.824	66.55	-0.153	84.49	-0.02
9.94	0.412	21.87	-0.181	33.15	-1.39	46.80	0.217	67.04	-0.578	84.93	0.278
10.39	0.315	22.20	-1.05	33.47	0.171	47.33	-1.12	67.54	0.132	85.37	-2.18
10.85	-1.1	22.54	0.185	33.80	-0.898	47.86	0.352	68.03	-0.8	85.80	0.292
11.30	0.41	22.87	-1.31	34.12	-0.863	48.39	-0.533	68.53	-1.72	86.24	-2.03
11.75	-0.262	23.21	0.475	34.44	0.21	48.92	-2.01	69.02	0.072	86.68	0.218
11.91	-0.132	23.55	1.51	34.76	-1.67	49.45	-0.446	69.52	-1.69	87.11	-2.21
12.07	-0.811	23.88	-0.963	35.07	-1.15	49.98	-0.625	70.01	-1.01	87.55	0.052
12.23	0.095	24.07	0.781	35.39	0.196	50.51	-0.514	70.51	-0.223	87.98	-1.65
12.38	0.036	24.25	0.13	35.71	-1.2	51.04	0.288	71.00	-2.03	88.42	0.221

12.54	-0.672	24.44	-0.865	36.03	-1.23	51.57	0.335	71.50	-1.19	88.86	-1.2
12.70	-2.26	24.62	-0.632	36.35	0.19	52.10	-0.117	71.99	-2.14	89.29	0.288
12.99	-0.69	24.81	0.252	36.66	-1.06	52.63	0.239	72.49	-1.15	89.73	-0.283
13.28	0.201	24.99	0.153	36.98	-1.53	53.15	0.35	72.98	0.218	90.16	-0.644
13.57	-1.33	25.18	-0.347	37.30	0.243	53.68	-1.44	73.48	-0.245	90.60	0.317
13.86	-0.729	25.32	0.273	37.62	-1.54	54.21	-0.137	73.97	0.032		
14.15	0.164	25.62	-0.416	37.94	-1.32	54.74	-0.863	74.47	0.194		
14.45	-1.19	25.93	0.254	38.26	0.253	55.27	0.044	74.96	-1.1		
14.74	0.333	26.23	0.216	38.57	0.341	55.80	-1.43	75.46	-0.9		
15.03	0.072	26.54	-0.69	38.89	-0.966	56.33	0.065	75.95	0.186		
15.32	-0.247	26.84	0.191	39.21	0.251	56.86	-0.272	76.45	0.012		
15.61	0.135	27.15	0.201	39.53	-1.62	57.39	-0.147	76.87	-0.186		

Table E-4. Magnetic Susceptibility data from the outcrops in the study area.

Easting (m)	Northing (m)	Lithology	x10^{-3} SI Units	Easting (m)	Northing (m)	Lithology	x10^{-3} SI Units	Easting (m)	Northing (m)	Lithology	x10^{-3} SI Units
758505	7814768	Silicified Dolomite	-0.093	758409	7814945	Grey Limestone	-0.029	758751	7814851	Chlorite Schist	8.53
758528	7814771	Silicified Dolomite	0.054	758813	7814800	Grey Limestone	0.021	758737	7814858	Chlorite Schist	86.4
758561	7814861	Silicified Dolomite	0.144	758799	7814805	Grey Limestone	0.153	758734	7814859	Chlorite Schist	47.6
758562	7814862	Silicified Dolomite	0.033	758798	7814808	Grey Limestone	4.97	758598	7814887	Agglomerate	34.2
758548	7814790	Silicified Dolomite	0.049	758791	7814814	Grey Limestone	0.061	758595	7814887	Agglomerate	53.3
758604	7814782	Silicified Dolomite	0.024	758790	7814816	Grey Limestone	0.09	758592	7814888	Agglomerate	47.6
758620	7814780	Silicified Dolomite	0.005	758755	7814848	Grey Limestone	7.13	758589	7814888	Agglomerate	28.6
758580	7814790	Silicified Dolomite	-0.03	758728	7814857	Grey Limestone	2.33	758581	7814886	Agglomerate	53

759361	7814340	Silicified Dolomite	0.007	758727	7814856	Grey Limestone	0.061	758586	7814898	Agglomerate	34.3
759364	7814343	Silicified Dolomite	0.011	758728	7814857	Grey Limestone	0.146	758587	7814900	Agglomerate	69.4
759355	7814344	Silicified Dolomite	-0.029	759545	7814781	Grey Limestone	0.631	758871	7814798	Agglomerate	43.9
758587	7814783	Dolomite Breccia	0.027	759567	7814785	Grey Limestone	2.14	758874	7814802	Agglomerate	21.2
758587	7814787	Dolomite Breccia	0.081	759551	7814690	Grey Limestone	0.136	758586	7814902	Agglomerate	91
758634	7814803	Diamictite	0.023	759559	7814689	Grey Limestone	0.03	758588	7814901	Agglomerate	41.4
758655	7814815	Diamictite	0.04	759559	7814680	Grey Limestone	0.15	758588	7814901	Agglomerate	42
758667	7814816	Diamictite	0.049	759554	7814672	Grey Limestone	0.147	759553	7814664	Mafic Metavolcanic	0.293
758671	7814818	Diamictite	0.045	758516	7814867	Pyritic Dolomite	0.11	759557	7814660	Mafic Metavolcanic	0.305
758691	7814822	Diamictite	0.056	758499	7814880	Pyritic Dolomite	0.051	759556	7814659	Mafic Metavolcanic	0.462
758706	7814818	Diamictite	0.061	759574	7814757	Pyritic Dolomite	0.07	759555	7814656	Mafic Metavolcanic	0.494
758705	7814810	Diamictite	0.031	759558	7814758	Pyritic Dolomite	0.041	759542	7814665	Mafic Metavolcanic	0.646
758721	7814794	Diamictite	0.048	759555	7814718	Pyritic Dolomite	0.199	759705	7814668	Mafic Metavolcanic	0.267
758753	7814790	Diamictite	0.046	759551	7814717	Pyritic Dolomite	0.371	759551	7814644	Mafic Metavolcanic	0.244
758796	7814797	Diamictite	0.135	759544	7814718	Pyritic Dolomite	0.232	759542	7814642	Mafic Metavolcanic	0.255
758800	7814800	Diamictite	0.231	759544	7814716	Pyritic Dolomite	0.153	759536	7814641	Mafic Metavolcanic	0.369
758809	7814798	Diamictite	0.055	759539	7814706	Pyritic Dolomite	0.149	759547	7814651	Mafic Metavolcanic	0.579
758809	7814787	Diamictite	0.044	759532	7814708	Pyritic Dolomite	0.355	759558	7814651	Mafic Metavolcanic	0.37
758813	7814800	Diamictite	0.091	758222	7814931	Chlorite Schist	0.281	758342	7815086	Felsic Volcanic Breccia	0.14

759007	7814143	Diamictite	-0.005	758226	7814929	Chlorite Schist	0.201	758342	7815083	Felsic Volcanic Breccia	0.256
759010	7814147	Diamictite	0.141	758228	7814926	Chlorite Schist	0.341	758342	7815078	Felsic Volcanic Breccia	0.233
759014	7814150	Diamictite	-0.011	758236	7814926	Chlorite Schist	0.184	758338	7815078	Felsic Volcanic Breccia	0.057
759023	7814149	Diamictite	0.04	758271	7814967	Chlorite Schist	0.071				
759060	7814114	Diamictite	0.049	758320	7814996	Chlorite Schist	0.097				
759073	7814129	Diamictite	0.014	758321	7815002	Chlorite Schist	0.005				
758536	7814883	Diamictite	0.058	758753	7814849	Chlorite Schist	75.6				

Appendix F

New Local Geological Map of the Deblin Copper Mine

